Universidad de Valparaíso

PhD. Thesis

Searching for gaseous giant planets around debris disks

Author:
Nicolás Godoy Barraza

Supervisors:
Dr. Johan Olofsson
Dr. Amelia Bayo(Co-S)

Committee:
Dr. Johan Olofsson
Dr. Amelia Bayo
Dr. Gaël Chauvin

A thesis submitted in fulfilment of the requirements
for the degree of PhD. in Astrophysics

in the

INSTITUTO DE FÍSICA Y ASTRONOMÍA

December 2022

Acknowledgements

The acknowledgements and the people to thank go here, don't forget to include your project advisor :)

Contents

List of Figures

List of Tables

Abstract

The past decades have clearly demonstrated that planet formation is an efficient process and that it can lead to a vast variety of planetary systems. Since then, understanding how to form this enormous population of extrasolar planets has been an important question for modern astrophysics. It has been possible to formalize different theories of planetary formation trying to explain the populations of planets that we observe. Direct imaging has provided important hints that help to confront and challenge these theories from the characterization of planets as well as their detectability. Despite the significant advances in technological terms (new instruments and techniques have been developed in recent years), and the great relevance of several discoveries (e.g., PDS70), direct imaging still has great challenges that must be faced.

In this thesis, we first provide some context on what we know about planetary formation and detection techniques, with an emphasis on direct imaging and its challenges in Chapter 1. We then investigate how to improve direct imaging data reductions and which are the main sources of improvement, when using the NaCo instrument. To do this, we developed a pipeline called CenteR within the ISPY consortium, to investigate the effects of centering and frame selection in sequences of thousands of frames. Our new reduction strategy and the main conclusions are presented in Chapter 2. In addition, we focused on searching for giant planets using the SPHERE instrument. Our sample was built based on hints of possible planet-disc interactions. Such interactions, complemented with information about the location of the disk from SED analysis, the proper motion anomaly, and recent planet-disk interaction models, provided us with important constraints on the presence of possible planets. Chapter 3 shows the target selection, the treatment carried out on the data, and the main conclusions of the analysis of our sample and our non-detections of planets. In Chapter 4 we present a brief conclusion on the work of this thesis and in Chapter 5 the future perspective on this work in the context of new instruments and archival data.

For/Dedicated to/To my...

Chapter 1

Introduction

1.1 Star formation: from clouds to debris disks

It is agreed that stars are born in clouds of gas and dust in so-called star formation regions. Broadly, stars are formed from the gravitational collapse of the dense nuclei into molecular clouds (Shu et al. 1987), which due to conservation of angular momentum results in the formation of a disk around the protostar (Terebey et al. 1984). The disk, rich in gas and dust (a proportion of 1:100 is usually assumed, e.g., Trapman et al. 2017), is usually called the protoplanetary disk, in which gas is rapidly depleted and removed from the disk as the star formation process proceeds. The evolution of the protoplanetary disk is generally well-understood, however, intermediate steps are a matter of discussion and are still under study due to the complexity of the phenomena and interactions with the protostar, planetesimals, planet in formation, or even surrounding stars. The process that started with the collapse of the molecular cloud ends up forming a system composed of a star (or more) supported by thermonuclear reactions, possible planets formed during the evolution of the disk, and a remnant of the disk called debris disk (e.g., our own solar system). The star formation process will be briefly described below, and the planet formation process will be presented later in section 1.2.

Observationally, the evolutionary stages of the young stellar objects (YSOs) can be separated into 5 phases. This classification stems from infrared observations of the spectral energy distribution (SED, see Figure 1.1) of the YSOs, where initially the classes correspond to I-III (Lada 1987), and later were incorporated Class 0 (Andre et al. 1993), and the initial phase of cloud collapse. Figure 1.1 shows an evolutionary scheme of the YSOs, where the evolutionary process of the protostar and its disk is exemplified, showing the most common features in the SED. The curve filled with light blue represents the contribution of the protostar, and the curve filled with yellow the contribution of the surrounding material on top of the contribution from the protostar (it can be the envelope in the prestellar core, or the debris disk in Class III). This process can also be divided into three stages: pre-stellar phase, protostellar phase, and pre-main-sequence phase.

Pre-stellar phase: The collapse phase can be understood as the formation of pre-stellar cores (see Figure 1.1, upper-left side). The cloud must be massive enough to initiate the collapse, and the force of gravity must be large enough to compensate for the thermal gas pressure, rotation, and magnetic fields.

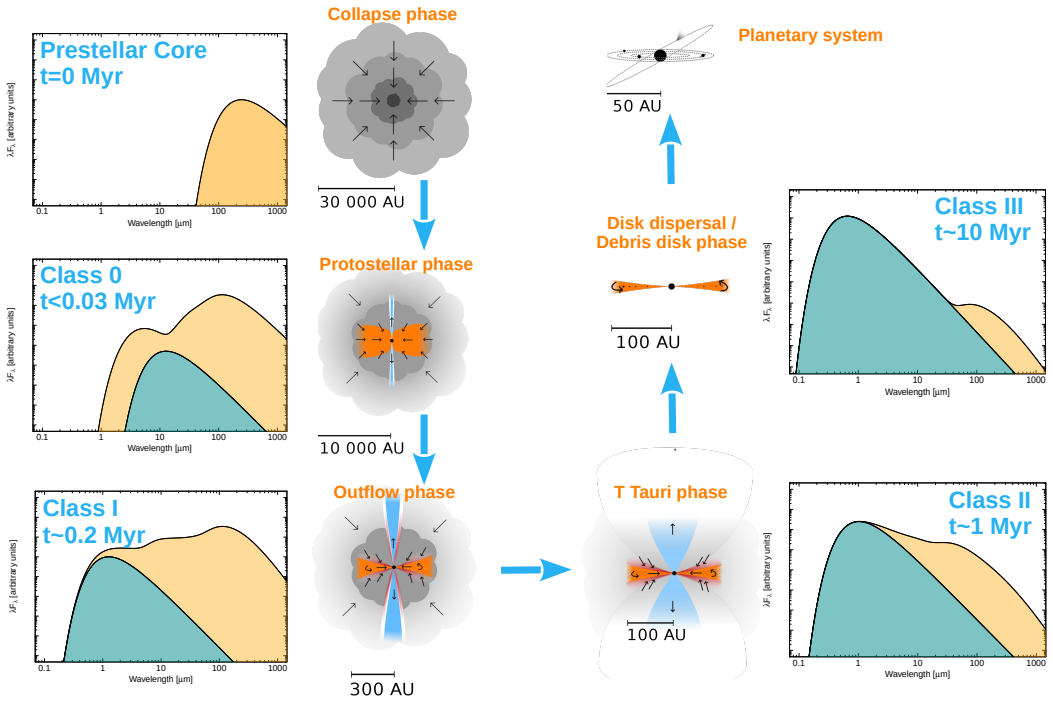

FIGURE 1.1: Schematic representation of the protostar evolution and their disks (drawings), and its relation to observations using SEDs (panels at the side of each drawing). Figure taken and modified from "Persson, Magnus Vilhelm (2014): Current view of protostellar evolution (ENG). Figure. https://doi.org/10.6084/m9.figshare.654555.v7".

For a cloud in equilibrium, the virial theorem dictates that the cloud will collapse if the gravitational potential energy is greater than twice the kinetic energy (mostly composed of thermal energy, if the cloud is not too turbulent or rotating too fast). This relationship gives a minimum mass to initiate cloud collapse, which depends on density and temperature (critical mass decreases for dense and/or low-temperature regions, typically 10-20K). As the cloud collapses, different regions within the cloud may meet the minimum mass criteria locally, initiating a local collapse that fragments the cloud. This process results in a distribution of less massive protostar seeds.

Protostellar phase (left side on Figure 1.1): Composed of classes 0 and I, characterized by the fact that the protostar has not yet decoupled from its birth cloud so that the extinction by the envelope is significant. Class 0 or protostar phase is characterized by rapid accretion of material towards the protostar leading to rapid gain mass, with an accretion rate of $10^{-5} M_{\odot}$/yr (e.g., Vorobyov & Basu 2010). The protostar is still completely obscured by its envelope (Evans et al. 2009), so the infrared emission is dominated by nebula heated by the forming protostar, the hot inner disc, and outflows. The typical timescale of Class 0 is $< 30\,000$ years. Class I objects are still deeply embedded within the molecular clouds and this phase is dominated by an enlarged circumstellar disk, a remaining envelope, and a moderately extinct protostar, with a typical accretion rate below $10^{-6} M_{\odot}$/yr (Vorobyov & Basu 2010). The characteristic timescale of Class I objects is around 500 000 years, which ranges from 0.2 to 1 Myr.

Pre-main sequence phase (right side on Figure 1.1): Composed of classes II and III, for which the photosphere dominates the SED and is much less affected by extinction from an envelope remnant (if any). Class II is characterized by having an actively accreting star surrounded by a protoplanetary disk.

Emission from the disk and protostar can be observed, as the envelope is expected to have dissipated due to outflows (van der Marel 2015). In addition, at this stage, the disk undergoes photoevaporation for instance, which leads to a gradual decrease in the amount of gas in the protoplanetary disk. The timescale of Class II is $\sim 5\,\mathrm{Myr}$, with ages over 1 Myr that last for several Myr (e.g., $\sim 10\,\mathrm{Myrs}$ old). Class III is characterized by a depleted disk, with very weak emission at infrared wavelengths, whose entire emission is strongly dominated by the photosphere of the protostar. This phase is known as the debris disk phase, and it is expected that the disk is depleted of gas (although it is possible that it has gas due to other processes, such as the sublimation of comets, and gas generated by collisions of icy bodies in the disk itself). The timescale of Class III is $\geq 10\,\mathrm{Myrs}$ and older.

It is worth noting that stars do not form in an isolated environment, so their formation process can be altered by external processes (e.g., stellar encounters, and photoevaporation by external radiation, multiplicity).

1.2 Planet formation

According to the International Astronomical Union (IAU), there is no global and official definition that describes what an exoplanet is. The definition provided by IAU (resolution B5[1]) defines the planets in our solar system as celestial objects that orbit the Sun, have sufficient mass to assume a spheroidal shape in hydrostatic equilibrium, and have cleared the neighborhood around their orbits. However, this definition does not apply to extrasolar planets. Nonetheless, there is a working definition, and currently the IAU defines exoplanets as objects with masses below the deuterium-burning mass limit (nominally $13 M_{Jup}$) that orbit a star, brown dwarf, or stellar remnant (Lecavelier des Etangs & Lissauer 2022). However, other studies prefer to link an exoplanet to its formation rather than just refer to the deuterium-burning mass limit (for example, because the deuterium burning depends on metallicity and time, Spiegel et al. 2011). Motivated by this, Currie et al. (2022) defines a planet separating it from what is considered a brown dwarf as objects with masses less than $25 M_{Jup}$, mass ratios with their central stars below 0.025, and semi-major axis $\leq 300\mathrm{au}$. Therefore, in this thesis, a planet will be understood in general terms as an object that orbits its star, whose mass is less than $25 M_{Jup}$ and greater than the lower limit imposed by the IAU for our own solar system.

Theories of planetary formation aim at either explaining the observed planetary systems in statistical terms, or to study individual systems using observational data to constrain their possible evolutionary path. There are two main models of giant planet formation, and they can be understood as bottom-up and top-down scenarios that mainly differ on the kind of process to form planets. The core accretion model (Pollack et al. 1996) starts with embryos or seeds of planets that accrete solids and gas, while gaining mass and atmosphere. While the disk instability model (Boss 1997; Mayer et al. 2002) starts by fragmenting the protoplanetary disk to generate clumps, from which planets will form in a way quite comparable to star formation.

The core accretion theory relies on building a planet via the accretion of material in the disk. This process starts by forming small embryos coming from the aggregates of small dust grains and ends with a fully-formed planet. The formation process itself is mainly characterized in the literature by the type

[1] https://www.iau.org/static/resolutions/Resolution_GA26-5-6.pdf

of accretion: pebble accretion and planetesimal accretion (e.g., Liu & Ji 2020). The main difference between both models is regarding the type of material that is accreted by the protoplanet. For pebble accretion, most of the material is assumed to be in pebble form, which means that the gas in the disk plays an important role in the accretion process. Pebble can be defined as particles that are marginally coupled to the gaseous disk, which at distances of 1 au corresponds to centimeter-sized particles, being able to be even smaller at larger distances from the host star. On the other hand, planetesimal accretion assumes that all material is mostly composed of planetesimals. Planetesimals are defined as bodies with sizes ranging from ~ 100 m to even kilometer-sized, whose interaction with the gas is negligible or null. Therefore, the difference between both types of accretion lies in whether the gas plays an important role or not in the process. The accretion process has to face different barriers related to the prevalence of particles of different sizes that coagulate and end up forming a planet. The dust grows into pebbles by accreting material from the disk, but they can be severely impacted by radial drift, for example. This barrier refers to the loss of angular momentum of dust aggregates because of their interaction with the gas, resulting in their efficient inward migration onto the star. Other barriers in the dust evolution are, for example, the bouncing and fragmentation barriers, for which the velocity of the particles plays a crucial role in the dust evolution, usually called the threshold velocity. A favorable formation of pebbles allows them to grow to larger particles, in a runaway and oligarchic growth process (see for instances, Kokubo & Ida 2002; Ormel & Klahr 2010; Ormel et al. 2010; Drazkowska et al. 2022). Both the pebble and planetesimal accretion also differ in the isolation mass reached by the protoplanet. This isolation mass is a critical mass for which the planetary embryo is isolated from the pebbles or planetesimals, opening a gap in the disk (for the pebble isolation mass see Lambrechts & Johansen 2014; Bitsch et al. 2018; Ataiee et al. 2018). The isolation mass from planetesimal accretion can be a few orders of magnitude smaller than the pebble isolation mass (Drazkowska et al. 2022).

Once the isolation mass is reached, the embryonic planet begins to accrete gas (e.g., Pollack et al. 1996; Ayliffe & Bate 2012). There is a critical mass for which the planet embryo can accrete gas in a more efficient way, the "critical metal mass", which depends on the disk and envelope parameters (Mizuno 1980), such as solid accretion rate (e.g., Lambrechts et al. 2019), and solid composition (e.g.,Brouwers & Ormel 2020). To effectively form a planet, it is essential that the embryo reaches this critical mass when there is still gas in the disk, in order to become a gas-giant planet. Only objects that accrete efficiently and rapidly, and migrate very slowly, can become cold[2] gas giants. On the contrary, if the gas accretion process is less efficient and the embryonic planet migrates quickly, it may instead end up as a sub-Neptune very close to the star. The accretion energy of solids and gas, the contraction of the gas in the atmosphere, and the irradiation of the planet (cooling process) determine the energy balance of the envelope. This energy balance will govern the accretion rate and the amount of gas that the planet can capture (e.g., Mordasini et al. 2012). All the accreted material starts falling onto the core of the protoplanet, forming a liquid/solid core of metals[3]. When the core of the planet embryo reaches a certain mass (which also depends on the energy released by and stored in the embryo of the planet), the accreted solids and gas begin to be deposited in the atmosphere instead of falling onto the core since the temperature and pressure gradients affect the composition and physical state of the metals. The metals sublimate, polluting the atmosphere or envelope of the protoplanet. The atmosphere becomes rich in metals, creating gradients and clouds at different depths depending on temperature and pressure

[2] "cold" refers to gaseous planets far enough from their stars to be cold (usually distances greater than the ice line) and is often used to distinguish them from their counterparts, the hot Jupiters which are much closer to their stars.

[3] Unlike chemical terminology, metals refer to anything other than H or He.

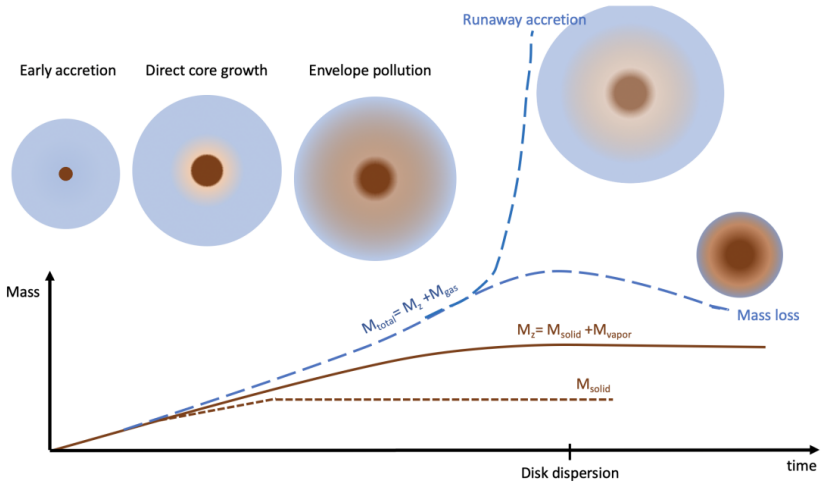

FIGURE 1.2: Formation scheme of gas-dominate, polluted giant planets, and sub-Neptune. Initially, the solids fall into the core, forming a dense core of metals (early accretion, direct core growth). Then, as the protoplanet accretes more material, the temperature and density of the envelope increase, and the solids start to sublimate. This sublimation enriches the envelope in metals. As the temperature continuously increases, all the accreted solids are vaporized, polluting the envelope (envelope pollution). A gas-giant planet starts to form when the protoplanet reaches the critical mass, which leads to accreting gas in a runaway process. Otherwise, the protoplanet will end up forming a sub-Neptune. After the disk dispersal, the stellar irradiation generates a loss of envelope (in particular, gas). The coffee short dashed line signifies the mass of solids, the coffee solid line of the metals (solid and vapor), and the blue dashed line the total mass. Figure taken from Drazkowska et al. (2022).

gradients, density, and energy released by the protoplanet, for instance. This gradient distribution of metals has an important impact on the thermal evolution of the planet and derived properties (Stevenson 1985; Vazan et al. 2016), and can even decrease the critical metal mass for runaway gas accretion (e.g., Hori & Ikoma 2011; Venturini et al. 2016). Figure 1.2 shows the process of planet formation, starting with the early accretion, the direct core growth, the formation of the polluted envelope, and the runaway accretion of gas to form gas-dominated or solid-dominated planets formed. It should be noted that the gas-dominated planet formation process is closely related to the metallic environment, where a metal-rich environment can produce giant planets without the need to form very massive embryos because the pebble accretion becomes much more efficient as more pebbles are available for the accretion (Bitsch et al. 2015; Ndugu et al. 2018; Drazkowska et al. 2022). Both pebble and planetesimal accretion form planetary populations that can be vastly different depending on the initial conditions of the models. For this reason, it renders the comparison with observations even more challenging, given the complexity of the planet formation process (e.g., Chambers 2018, Mulders et al. 2019, Drazkowska et al. 2022).

The formation of rocky planets can take place following different paths. In general, the embryo planet does not end up being a gas-dominated planet due to its slow accretion of pebbles, therefore reaching the isolation mass much later. As a consequence, it cannot accrete much gas, and ends up being a planet dominated by solids. Another way to form these planets is in stages after the gaseous disk has dissipated, where collisions are essential to form sub-Neptunes, for example. Furthermore, super-Earth may form at even later stages by accretion of planetesimals in the inner regions of the disk (Chiang & Laughlin 2013; Ogihara et al. 2015).

On the other hand, the gravitational instability scenario posits that giant planets form from early-stage gravitational collapses in the disk. One of the requirements is that the disk should be massive and cool

enough to be affected by self-gravity and to trigger clump formation via disk instabilities (e.g., Deng et al. 2017). This model forms giant planets beyond a separation larger than ~ 10 au, with masses above the mass of Jupiter. Explaining the formation of less massive planets (sub-Jupiter or sub-Neptune) is a challenge for this model, due to the rapid accretion of material accumulated in the clumps. Another problem with this theory is that these supermassive planets should migrate toward the inner regions of the disk very quickly, hindering their prevalence at large separations (Baruteau et al. 2011). However, it is very helpful in explaining the formation of super Jupiters, and the formation of planets far away from their stars where the core accretion process is too slow to form gaseous planets that are too massive, in a few Myrs (Schlaufman 2018).

Interestingly, the formation of planets, whether rocky or gaseous, is closely related to the amount of solids/metals available in the disk (e.g., Santos et al. 2004, Fischer & Valenti 2005, Fulton et al. 2021). Several studies have shown that metal-rich stars host more giant planets, recovering the relation even in different theoretical models and simulations (e.g., Ida & Lin 2008, Mordasini et al. 2012, Bitsch & Johansen 2017, Ndugu et al. 2018).

Planet formation is still not fully understood and far from having a unified model to explain all the observed planetary systems. There are factors such as chemical composition, disk properties, initial conditions of the molecular cloud, different interactions and possible evolution of aggregated particles, the lifetime of the gas in the disk, outflows, magnetic activity of the star, multiplicity, surrounding environment (e.g., close O-type stars that can evaporate the disk quickly), planetary feedback, amongst others that have an important impact on the formation of planetary systems. To face these difficulties and challenges, it is important to study a robust statistical sample of planets in different configurations and environments, to better understand the key factors that influence most the formation of planets and to challenge different formation theories.

1.3 Detection techniques of extra-solar planets

To date we know 5 141[4] extrasolar planets and about 2 600 candidates. However, if we apply the definition of a planet given by Currie et al. (2022), applying the mass ratios filter when possible (since not all stars in the catalog have a measured mass) this number is reduced to 2 069 confirmed extrasolar planets and 102 candidates. Following the definition used in this thesis for what is considered a planet, i.e. objects with masses below $25 M_{Jup}$, we know 2 480 extrasolar planets and about 200 candidates. We can distinguish two groups of techniques to detect these planets: indirect and direct. The indirect techniques are those by which we infer the presence of the planet (e.g. transits), while in the direct ones we can see the planet in situ (we do not have to infer its presence). The vast majority of them have been discovered with indirect detection techniques and, due to the limitations of these techniques, the population of planets (and their characteristics) is quite biased. Direct techniques help reduce this bias, however, due to their current limitations and the type of planets they aim to detect, their contributions in terms of discoveries are much lower (around 2% considering the entire catalog from *exoplanet.eu*, $\sim 2\%$ using the Currie et al. 2022 definition of exoplanet, and about 5% applying our criteria).

[4] At 04-08-2022 from `http://exoplanet.eu/`

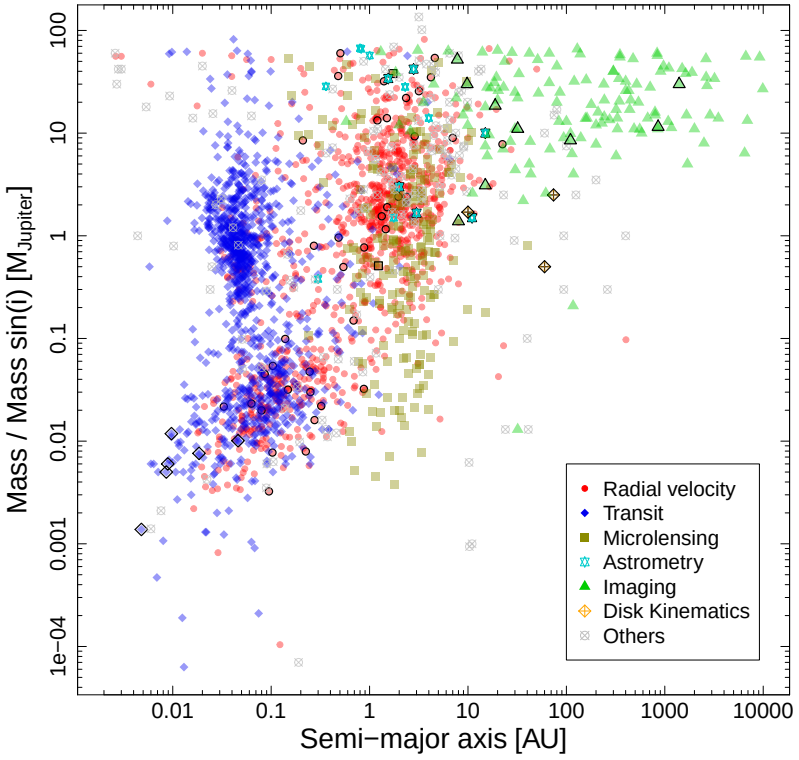

FIGURE 1.3: Masses of the known extrasolar planets and sub-stellar objects as a function of their semi-major axis. Different symbols and colors represent the different observational techniques used for their detection. Solid red circles for radial velocities; solid blue diamonds for transit; dark yellow squares for microlensing; open cyan 6-points star for astrometry; green solid triangles for direct imaging; open diamond with an orange cross for disk kinematics; and gray open circle with a cross for others techniques. The black outlines of the symbols on each technique correspond to planet candidates.

Figure 1.3 shows the masses[5] of currently known and candidates extrasolar planets versus their semi-major axis. The colors and symbols represent the different and main techniques used to detect these planets, while the black outline in each symbol marks the candidates for each technique. Some of these detection techniques are listed and explained below, and the direct imaging technique is further detailed in Section 1.4 as it is the basis for this work.

- **Radial velocity**

  This technique corresponds to an indirect detection method (red solid circles in Figure 1.3). The first detection of an extrasolar planet using this technique around a solar-type star was the system 51 Pegasi (Mayor & Queloz 1995a), Nobel Prize in Physics in 2019. It is based on the study of spectroscopic lines arising from the stellar atmosphere to determine changes in these lines due to the Doppler effect. In a system of multiple bodies, in which the mass of the secondary is not negligible (for example, a planet), the center of rotation of the system (barycenter) no longer is the center of the central star. This causes the more massive body to orbit around the center of mass (reflex motion). In the case of planetary systems, this effect translates into a redshift and blueshift of the lines we observe from the star. For a given inclination, the smaller the difference between a planet and its host star masses, the greater the observed Doppler shift. Figure 1.4 schematically

[5]Or $M_{\text{planet}} \sin(i)$, with "i" being the inclination of the planet's orbit, yielding to a lower limit for the planet mass.

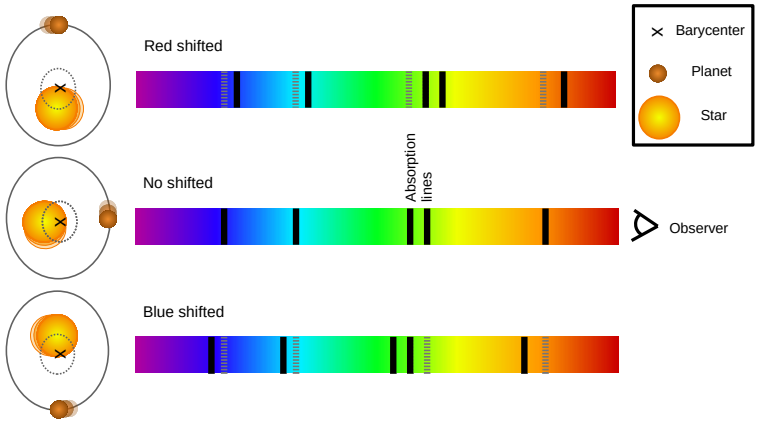

FIGURE 1.4: A scheme of a planetary system with a single planet. From top to bottom: the blue-shifting effect observed in the stellar lines, the no-Doppler effect, and the red-shifting of the stellar lines.

exemplifies the Doppler effect of a star with a single planet. With this technique, it is possible to determine some of the planetary parameters such as the observable velocity semi-amplitude, orbital period, eccentricity, orientation angle, and knowing the stellar mass, the $M_{\text{planet}}\, sin(i)$, and the semi-major axis (e.g. Jeong et al. 2022).

The limitations of this technique are the inclination of the planet's orbit. It is expected that 87% of the detected planets have inclinations between 30 and 90 degrees (Lovis & Fischer 2010). In addition, these planets must have a short orbital periods, of the order of months, so that we can observe multiple cycles and determine whether or not the planet in question exists. One of the most common source of confusion is related to the observed lines themselves. Changes due to the presence of spots can affect the shape of the absorption line, making it difficult to measure the center of the line and may lead to an erroneous inference of a planet. Other sources of confusion are stellar oscillations (P-mode), and magnetic activity (see Lovis & Fischer 2010). On the other hand, the technical limitations are related to the measurement of the spectrum itself which must have a good signal-to-noise ratio and a very high spectral resolution (typically greater than $R \sim 20,000$), in order to make very precise fitting to the lines (Spanò et al. 2012). Due to these limitations, this technique detects planets very close to their stars, whose masses range from Earth masses to several Jupiter masses. Different instruments have been designed to meet the requirements to detect even terrestrial planets in the habitable zone[6], such as ESPRESSO (Pepe et al. 2021), HARPS (Mayor et al. 2003), and CRIRES (Kaeufl et al. 2004; Dorn et al. 2014).

Figure 1.5 shows an example of a radial velocity diagram for the system HD 22532 (Pezzotti et al. 2022), and its modeling. The complexity of the modeling increases if more planets are present around the star (e.g. Lubin et al. 2022).

- **Transit**

  The transit technique (blue diamonds in Figure 1.3), is an indirect technique that uses light curves to detect "planetary transit". The first system detected with this technique was HD 209458 (Henry et al. 2000; Charbonneau et al. 2000). This technique measures the decrease in the light of the

[6]The habitable zone is defined as the region where H_2O remains in its liquid state. A planet very close to its star will have water vapor, while if it is very far away it will have water in an ice state.

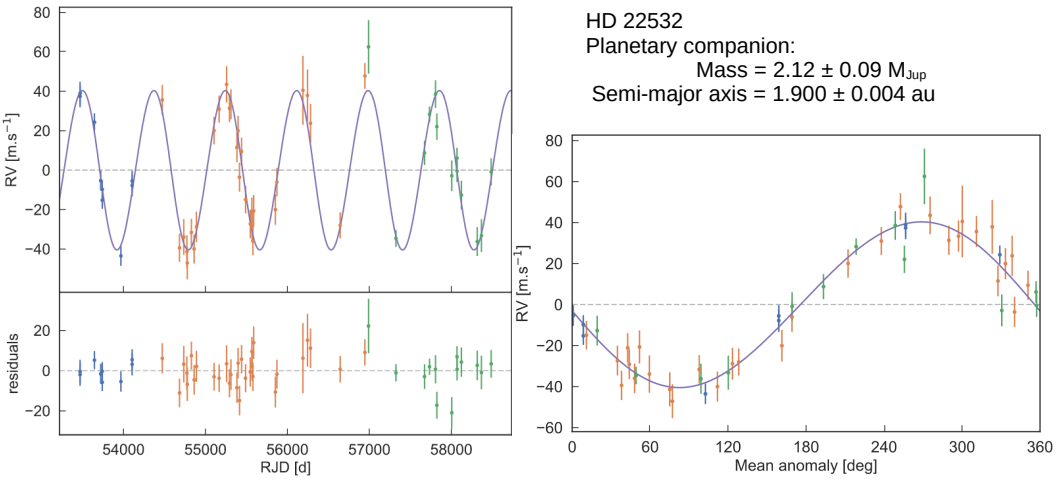

FIGURE 1.5: Radial velocity study of the planetary system HD 22532 from CORALIE. Left: radial velocity measurements as a function of time. Right: Radial velocity measurements in phase. Colored dots are the different CORALIE instrument upgrades, while the solid black line corresponds to the best Keplerian model. Figures were taken and modified from Pezzotti et al. (2022).

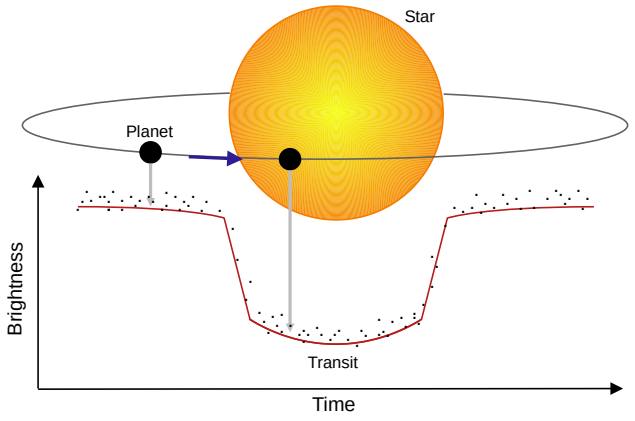

FIGURE 1.6: Schematic drawing of a planet transiting in front of its star (primary transit), along with an example of how the photometry varies due to the planetary transit.

studied star due to a planet passing in front of it, blocking part of the light that reaches us. Also, it is possible to see the reflected light when the planet moves behind the star (secondary eclipse). This phenomenon occurs periodically because the planet rotates around its host star in a favorable configuration for the eclipse (depending on the inclination and semi-major axis of the planet, for instance). The depth of the transit is related to both the size of the planet and its proximity to the star and the presence of an atmosphere (and its composition), while the transit time is more related to its semi-major axis. With this technique, it is possible to determine some of the planetary parameters such as radius, mass ($m\,sin(i)$), mean density, and semi-major axis (e.g. Henry et al. 2000). For a Jupiter-sized planet transiting a Sun-like star, the depth of the primary transit is $\sim 1\%$ of the stellar flux, and for an Earth-sized planet it is $\sim 0.01\%$ (Winn 2010). This means an accuracy better than 0.01 mag is required to detect such planets around a sun-like star at 10 pc.

The study of light curves at different wavelengths helps to better constrain the effective size of the planet and its composition since the atmosphere affects the amount of stellar light that is blocked hence affecting the depth of the transit, helping to study the so-called transmission spectra of the planet (e.g. Esparza-Borges et al. 2022). Different surveys aim detecting planets using this technique, for example, WASP (Collier Cameron et al. 2007), HATNeT (Bakos et al. 2007), Kepler (Borucki et al. 2010), CoRoT (Barge et al. 2008), and TESS (Ricker et al. 2014). About 45% or $\sim$ 1 100 of the known extrasolar planets have been detected using this technique[7], which has revolutionized our way of thinking about statistical samples of planets and their potential for understanding the formation and evolution of planetary systems.

The main limitations are clear, the planet's orbit must have a high inclination favorable for the eclipsing of the host star. Planets with large radius are more likely to be detected in transits, as well as planets that are closer to their host star. When increasing the semi-major axis, the probability that a planet transits in front of the star, decreases significantly. In addition, we must have a short period of a few days to months to be able to observe the transit more than once. The latter is an important factor both to better constrain the modeled parameters, especially the period, and to confirm the veracity of the transiting planet. One of the most common source of confusion is the presence of stellar spots. These spots are produced in magnetically active stars, and because they rotate with the star and they are cold they effectively decrease the stellar flux. As a consequence, it is very easy to confuse them with planetary transits (e.g., Collins et al. 2018). This is why it is extremely important to determine the rotation period of the star, to rule out these spots as candidates for planets. The "blending" is also a common source of confusion in which a second star is contaminating the stellar light that reaches us (can be a background star in the same light of sight). On the other hand, the technical limitations are linked to the cadence of the observations, which must be in some cases less than a minute, as well as the precision to measure the stellar flux (low uncertainties in magnitude are required). Depending on the geometrical configuration of the system, the transit duration can be of a few hours or even less.

Figure 1.7 shows an example of the phase folded and detrended light curve of the primary transit of planet TOI-1259Ab with $\sim 0.44 M_{\text{Jupiter}}$ (Martin et al. 2021). Recent theoretical works can add even more complexity to the modeling of these transits. For example, it could be possible to detect rings around these planets in transit and/or scattered light (e.g. Sucerquia et al. 2020a), and even "exomoons" (Sucerquia et al. 2020b).

- **Microlensing**

  Microlensing also belongs to the category of indirect techniques. The planetary system OGLE-2003-BLG-235/MOA-2003-BLG-53Lb was the first detection using this technique (Bond et al. 2004). This technique is based on the deformation of the space produced by a massive and relatively compact object. Microlensing happens when a star crosses in front of a background source within $\sim 1''$on the plane of the sky, with both sources at different distances (Gaudi 2012). This star (massive object), usually called a lens, generates two effects on the source (distant object): it amplifies the light that reaches us and increases the apparent angular size of the source. Depending on the configuration, it is possible to see duplicates of the source instead of the "true" one, called images[8],

[7] Note that this number is quite larger if we consider the entire catalog from *exoplanet.eu*: 70% or $\sim$ 3 600 extrasolar planets.

[8] Note that due to the current instrumental limitation, it is not possible to resolve the different images in a microlensing event at this scales.

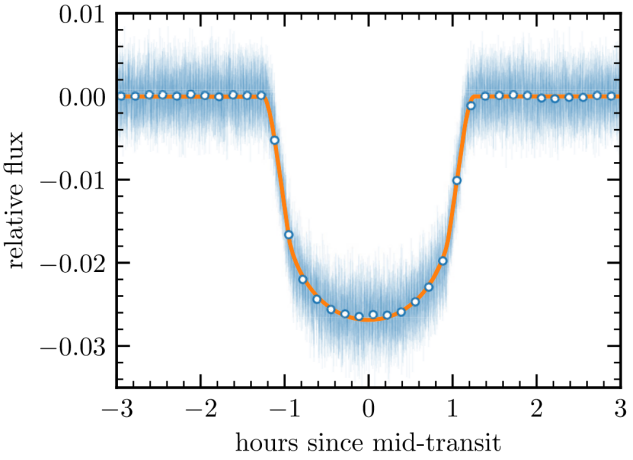

FIGURE 1.7: An example of a transiting planet, TOI-1259Ab of about $\sim 0.44 M_{\text{Jupiter}}$. The blue dots and lines correspond to the unbinned data, and the 10 minutes binned data are in blue-contours white solid points. The orange line shows the best-fit model. Figure taken from Martin et al. 2021.

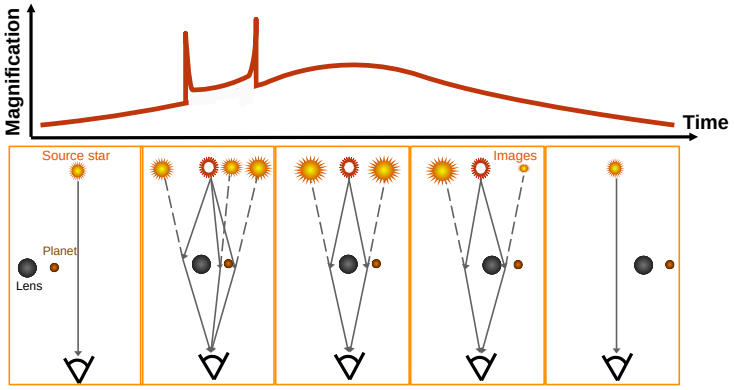

FIGURE 1.8: Illustration of the planetary microlensing event for a lens with a single planet. The diagram shows the configuration and temporal evolution of one possible scenario for the event, reflected in the observed light curve of the source (top panel). Likewise, the images produced from the source due to the transit of the lens are illustrated, even though it is currently not possible to resolve the images.

or even the Einstein ring when the lens and the source are (approximately) perfectly aligned (Chwolson 1924; Einstein 1936, among others). The microlensing effect, in practice, generates an increase in the brightness of the source as a function of time. When the lens has a second object orbiting it (in this case a planet), it results in an extra amplification of brightness. A schematic of this phenomenon is shown in Figure 1.8. This profile is particular to this type of magnification as shown in Bond et al. (2004). With this technique, it is possible to obtain the planet-star mass ratio, and angular separation of the planet with respect to the Einstein ring (Gaudi 2012), only possible if we know both the mass and distance of the lens. It is also possible to improve the microlensing model by calculating the angular size of the source using the color-magnitude diagram (Yoo et al. 2004), or even using the microlensing parallax (Gould et al. 1994).

One of the fundamental limitation of this technique is that it is not possible to observe the same phenomenon again. This is why the best way to detect galactic microlensing events is with constant monitoring, at a very good cadence since the time of microlensing produced by a planet is short (1 to 2 days in the case of Jupiter-mass planets, and less than an hour in case of Earth-mass

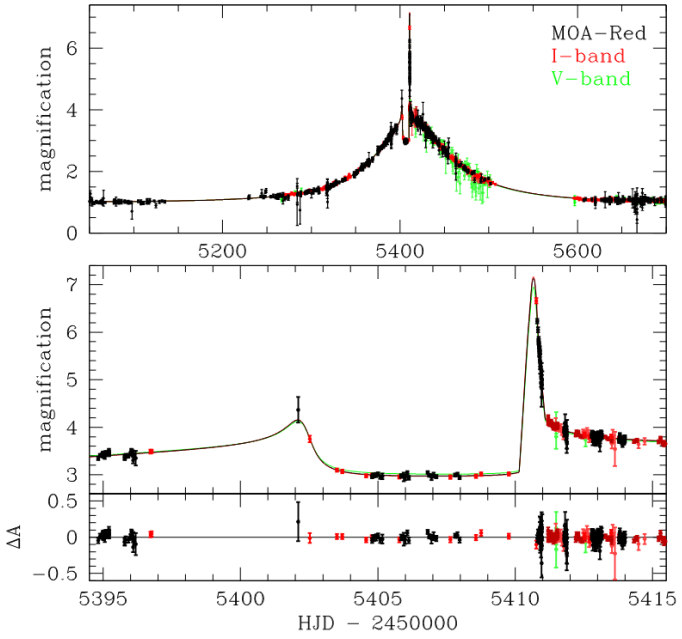

FIGURE 1.9: The light curve of the microlensing event MOA-2010-BLG-117. The configuration corresponds to a source composed of a binary system and a planet-star lens system. Different colored dots are marking different instruments and bands; for I-bands: SAAO in dark red, OGLE in red, and CTIO in light red; for V-band: OGLE in green, and CTIO in light green; the MOA-Red band is plotted in black. The best-fit models are plotted in each band color. Figure taken from Bennett et al. (2018).

planets). Several surveys point to this type of study, such as OGLE (Udalski 2003), and MOA (Bond et al. 2004). Other limitations are related to the configuration of the lens (i.e., planet and its star), where the degeneracies increase for some configurations (e.g. Skowron et al. 2011). Also, the orbital motion of the lens can affect the magnification (e.g., Albrow et al. 2000), the starspots can generate important changes in the light-curve adding to the complexity of having a proper model of the planet lens (e.g., Gould et al. 2013), or even the system can be confused with a binary system (Hwang et al. 2013). Depending on the sensitivity of the observations and their precision, it is possible to detect low-mass planets.

Unlike the other techniques, this method covers a very wide space of orbital parameters, being able to observe from planets very close to their stars, or planets on wide orbits (always at projected separations on the order of the Einstein ring size), for a very wide range of masses. However, a very particular configuration is required for this type of phenomenon to occur, both for the microlensing and planetary microlensing events. This is why the detection rate is low (for more details see Gould et al. 2010, and Cassan et al. 2012).

Figure 1.9 shows the case of the planetary system MOA-2010-BLG-117 hosting a planet of $\sim 0.5 M_J$ presented by Bennett et al. (2018), where the planet-induced brightness increase is clearly visible. Even though microlensing is an achromatic phenomenon, as mentioned before, the size of the planet can depend on the wavelength of observations, leading to different light curves at different wavelengths (e.g., Sajadian & Jørgensen 2022).

- **Astrometry**

The astrometry technique is an indirect method of detection that provides us with reliable information on the presence of "invisible" companions. The term astrometry is related to the study and measurement of the position of a star with respect to a reference system (usually the background sky, or even QSOs, Fischer et al. 2014). By studying the astrometric motion of a star, we can infer the presence of an unseen companion as it causes a shift of the motion of the barycenter. The first detection of a sub-stellar object was a BD orbiting an M dwarf (Pravdo et al. 2005). The first detection of a planet exclusively using this technique was in the HD 176051 system, an exoplanet of several Jupiter masses orbiting an unresolved binary using interferometric astrometric measurements (Muterspaugh et al. 2010). This method is particularly sensitive to wide planetary orbits since the center of mass of the system is mostly displaced with respect to the star center. In other words, the greater the orbital period of the companion, the more reliable the measurement of its perturbation in the system. The two main measurable properties correspond to the dynamical mass of the system as well as the mass ratio given by $M^3_{\rm planet}/(M_\star + M_{\rm planet})^2$, meaning that if we know the mass of the star $M_\star$, it is possible to infer the mass of the companion without ambiguities.

One of the great advantages is that this technique allows for studies of planets with long periods, and that it is possible to know their masses without the ambiguity of the $\sin(i)$ as is the case for the radial velocity technique. Furthermore, stellar activity affects this technique to a much lesser extent than radial velocity and transits (e.g. Lagrange et al. 2011). It also allows us to search for planets around nearby stars, regardless of stellar mass or age. Among the main limitations, to detect an Earth-like planet a precision of the order of 1μarcsec is mandatory, on top of a long period of observations. Precision is fundamentally limited by our ability to measure the star position on the detector and is related to the wavelength, the telescope aperture size D, and the S/N of the object in question. In the case of ground-based telescopes, this limitation is accompanied by the effect of the atmosphere which, thanks to the excellent adaptive optics systems, is limited only to D (Cameron et al. 2009). However, the precision of around $0.1mas$ has been recorded for the case of optical images (Lazorenko et al. 2009), well above that required to detect Earth-like planets. On the other hand, the precision has been improved using techniques such as interferometry, where precisions of $0.01mas$ can be achieved in the measurement of relative positions between two stars (Shao & Colavita 1992). Many programs have been launched for astrometric studies in the search for extrasolar planets (e.g., Launhardt et al. 2008; Sahlmann et al. 2013a). While the technique alone turns out to be very impressive in terms of determining planetary parameters, it is heavily impacted by the parameters that need to be tuned (at least 12, compared to radial velocity which requires at least 6; Wright & Howard 2009). The combination with other techniques such as radial velocity has shown much more robust results, where the correlation between parameters is minimized. With Gaia it is also possible to have this synergy between different techniques. So far, about 1 900 sub-stellar object (72 with masses less than $20M_{Jup}$) have been reported (Gaia Collaboration et al. 2022). Of this sample, 9 of these are known companions from radial velocity and 63 from astrometry, which helped to validate the sample of candidates. It is expected that Gaia will provide thousands of candidates and confirmed exoplanets in the near future.

Figure 1.10 shows an example of the L1.5 dwarf system $DENIS-PJ082303.1-491201$ harboring a planet of $\sim 28M_J$ discovered with astrometry (Sahlmann et al. 2013b). The Figure shows the motion of background stars with respect to the field (panel a), and the astrometric motion of the

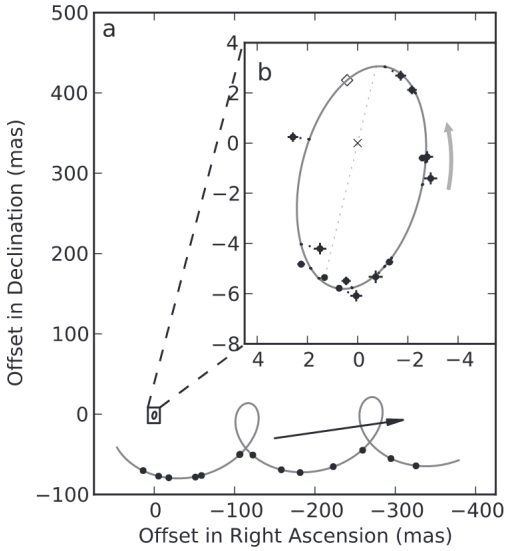

FIGURE 1.10: An example of an astrometric study of the system $DENIS - PJ082303.1 - 491201$, composed of an ultracool dwarf and a planet of $\sim 28 M_{\text{Jupiter}}$. Panel a) shows the proper and parallactic motion of background stars (field stars). Panel b) shows the motion of the dwarf around the barycenter. The black dots are the different measured epochs, the gray line to the best-fit model, the cross marks the barycenter, and the open diamond the periastron position. The dotted line represents the line of nodes. Figure taken from Sahlmann et al. (2013b).

ultracool dwarf and its barycentric orbit over 14 epochs between October 2010 and January 2013 (panel b).

"Disk kinematics" is a new technique that has led to the inference of possible protoplanets and planets in formation in direct interaction with the surrounding protoplanetary disk. Since this technique is still in its early stages (it is a very young technique), and the presence of any planet has not yet been fully confirmed (so far they are referred to as candidates instead of confirmed planets), we decided not to include a detailed description in this thesis. Lastly, since the direct imaging technique is the basis of this work, even though it is part of the detection methods, it is further presented in the next section.

1.4 Direct imaging

In this section, we further talk about the direct imaging technique, since it is the main focus of this doctoral thesis. We start by explaining the method itself, and briefly describe the different post-processing tools in Sec. 1.4.1. Then, we discuss how the detection of candidates is performed and the steps to follow for their confirmation as companions and planets, as well as their characterization in Sec. 1.4.2. Finally, the current knowledge and implications of the surveys and what we managed to understand about them from a statistical point of view are described in Sect. 1.4.3.

1.4.1 Technique and post-processing

The direct image technique (green solid triangles in figure 1.3) allows us to directly observe the light coming from an extrasolar planet, which cannot be done for planets detected with other techniques.

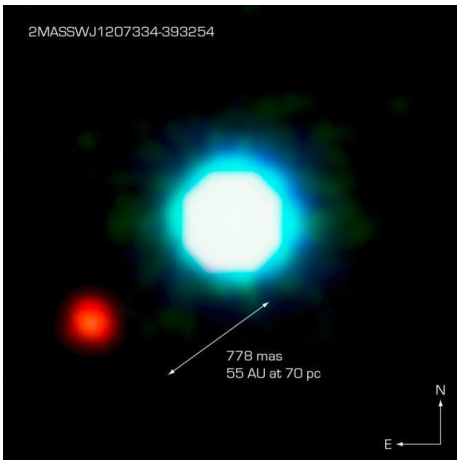

FIGURE 1.11: First direct imaged extrasolar planet $2MASSWJ1207334-393254$ by Chauvin et al. (2004) using the NaCo instrument, at the Very Large Telescope, Paranal Observatory. Credit: ESO - https://www.eso.org/public/images/eso0515a/.

The direct imaging technique therefore brings something unique to the table, helping to inform models of planet formation. Since we "see" the planet and do not infer its presence, this technique is considered as a direct one. The first detection of a planet using direct imaging was in the planetary system $2MASSWJ1207334-393254$, a planet orbiting a brown dwarf, by Chauvin et al. (2004) using the NaCo instrument (see figure 1.11). This technique is, in essence, taking an image of a planet orbiting its star. However, this comes with a series of challenges, limitations, and several tools had to be developed to overcome them. We can separate these challenges and tools into two groups: those related to the observations themselves, and post-observation data processing.

Direct imaging requires separating the light from the host star from the light emitted by the exoplanet. The planet-to-star contrast ratio at a given angular separation is a good metric to understand how deep the observations have to be to detect a planet and properly separate both light sources. The level of starlight suppression required to detect a planet is closely related to whether the detection is in reflected light or thermal emission, and to the mass of the planet, the age, and angular separation, among others (see Fischer et al. 2014). For example, to detect in reflected light a Jupiter-like planet orbiting a star similar to our Sun, but at 10 pc, a contrast of 10^{-9} at $0.5''$would be needed, well outside current observational capabilities (e.g., SPHERE reaches $\sim 10^{-6}$ at $0.5''$; Langlois et al. 2021a). On the other hand, young planets cool down and contract over time, releasing this energy as thermal emission (e.g. Burrows et al. 2001). A young self-luminous giant planet of about $10 M_{\rm Jupiter}$ around a 10 Myr old Sun-type star, would yield to a contrast of $10^{-3} - 10^{-5}$ (Launhardt et al. 2020a). Figure 1.12 shows how the contrast varies using some examples of planets at different ages, masses, and effective temperatures (Currie et al. 2022). The younger the planets, the hotter and brighter they are at infrared wavelengths, which facilitates and lessens the requirements necessary for their detection. This is why the direct imaging technique focuses on searching and detecting young self-luminous planets in thermal emission (infrared observations), around young stars. Studying this type of planetary population is crucial for understanding the different processes of planetary formation confronting the observations with the different theories (e.g., Vigan et al. 2021a), usually a population difficult to access with other techniques such as radial velocity and transits.

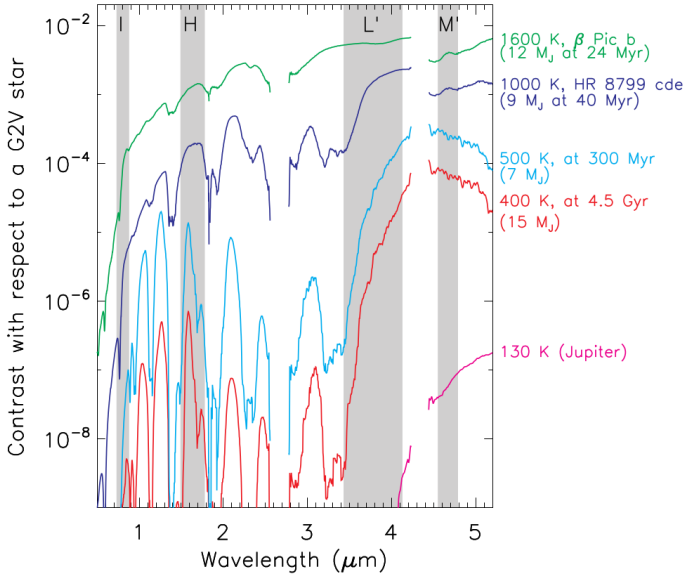

FIGURE 1.12: Contrast as a function of wavelength for 4 passbands from optical to mid-IR (grey shaded areas), for models of known directly imaged planets. Models considered from young and hot, to old and cool planets at different masses. A G2V primary star is assumed in all cases to compute the corresponding contrast curves. Figure taken from Currie et al. (2022).

Starlight suppression is crucial to improve contrasts, and this is why various ways of dealing with this problem have been implemented over the years. For example, the implementation of adaptive optics systems (from the first instruments with non-AO to the new ones with extreme-AO systems with the use of sensors, deformable mirrors, and computing hardware), helps to correct the effects of the atmosphere and to correct internal imperfections of the telescope/instrument. The use of coronagraphs helps to remove the light coming from the star and control the diffraction pattern without affecting too much the light coming from the planet. Different types of coronagraphs have been designed based on different suppression strategies (phase and amplitude mask coronagraph, see for example Kuchner & Traub 2002; Sivaramakrishnan et al. 2005; Guyon et al. 2006; Kenworthy et al. 2007; Mawet et al. 2010; Otten et al. 2017). Furthermore, improvements in software and hardware for better performance yielded faster correction, more efficient wavefront corrections, enabling its use not only for the control but also for suppression of speckles - residuals of the starlight in the image - (e.g., Gerard et al. 2018; Bos et al. 2021).

The use of AO systems, coronagraphs, and advanced software/hardware is still not sufficient for optimal suppression of starlight, as it can only reach contrast values of about 10^{-3} (see Currie et al. 2022). The so-called speckles are quasi-static and are due to nanometer imperfections in the optical path of the telescope, poor alignment between the star and the coronagraph, and even environmental factors such as low-wind effect (e.g., Cantalloube et al. 2018; Cantalloube et al. 2020). All this results into a pattern of speckles that is far from being simple white photon noise (Hinkley et al. 2007), but with a distribution much more complex and which can lead to erroneous planet detections (or false positives, Soummer et al. 2007; Marois et al. 2008a). This is why post-processing techniques are crucial in order to decrease the noise level and thus improve the final contrast. Usually, the post-processing techniques are related to specific observation modes, however, they are not mutually exclusive. There are different implementations, the most common being listed below:

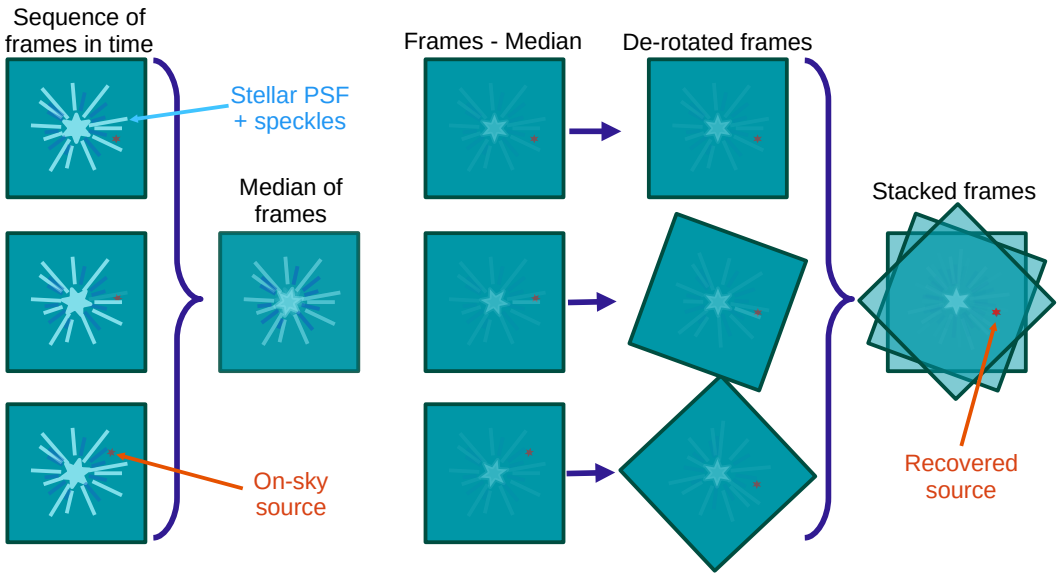

FIGURE 1.13: Scheme of the classical ADI approach. From left to right: the observation sequence (data cube) of the star observed using both a coronagraph and the natural rotation of the sky; then a reference image is calculated (median between all images) to later subtract it in the sequence; residual images are de-rotated using the parallactic angle and true north corrections; and finally, a stacking of all the residual images is performed, usually calculating the median.

- *Angular Differential Imaging* (ADI, Marois et al. 2006), is one of the most widely used techniques and takes advantage of two properties: the quasi-static nature of the speckles, and the natural motion of the sky (for ground-based observations). Indeed, the artifacts created in the optics of the telescope remain quasi-invariant (from seconds to minutes, depending on each instrument, environmental conditions, and stellar brightness, among others), while any astrophysical signal is expected to rotate on the sky during the observing sequence. In observations from the ground, many images are usually taken over a typical duration of 30-60 minutes, at the point of maximum on-sky rotation (meridian cross-passage). In its classic version, the ADI algorithm takes the median between all the images, to construct a reference point spread function (PSF). This PSF is then subtracted from each individual frame, which are then de-rotated to account for the parallactic rotation and finally median-combined. Figure 1.13 shows a scheme of how classical ADI is performed. This technique allows for the suppression of speckles without completely suppressing the signal from the planet (or any astronomical object in the field of view). The main limitation is the effect of self-subtraction of the planet which can be significant at small separations since the planet is not moving much during the observing sequence. In addition, extra corrections are required to compensate for this loss of flux.

- *Spectral Differential Imaging* (SDI, Marois et al. 2000; Sparks & Ford 2002a; Biller et al. 2004), relies on the fact that the halo of speckles scales as a function of wavelength in the radial direction. For observations made in more than one bandpass (for example dual-band imaging or integral field spectrograph - IFS), a PSF model can be made by readjusting the size or scale of the halo of speckles before subtracting it to the observations. Since this scaling occurs in the optical path that produces the speckles, astronomical signals are not affected by this correlation with wavelength. As for ADI, SDI is affected by self-subtraction and is less efficient at small angular separations from

the center. In addition, throughput corrections represent a greater challenge than other techniques (Pueyo 2016a).

- *Reference Differential Imaging* (RDI, Smith & Terrile 1984a), the idea of this technique is to use a reference star, different from the science one, and use those calibration frames to suppress the halo of speckles. Originally, the reference star was observed before or after the science sequence, but this was vulnerable to observing condition changes (e.g., seeing, coherence time). More recently, progress have been made at the telescope to quickly hop back and forth between the reference and the science stars to maximize the gain in contrast (e.g., Wahhaj et al. 2021). However, it requires the observing conditions to be very stable during the whole sequence, and the selection of the reference star is crucial for a good PSF match (in terms of brightness, color, and airmass, see Krist et al. 1998). One of the main advantages is that the final image is no longer affected by self-subtraction, so it is possible to go much deeper at small angular separations (e.g., star-hopping RDI technique at SPHERE yields ~ 2 mag deeper than ADI at $0.1''$, Wahhaj et al. 2021).

Combinations of these different techniques have also been studied (e.g., Kiefer et al. 2021):

- *Combined Differential Imaging* (CODI, Kiefer et al. 2021), which combines the use of ADI and SDI at the same time. Briefly, halo speckles are scaled to be removed using, for example, principal component analysis (Amara & Quanz 2012a) in the same manner as for ADI, then scaled back and de-rotated, before combining all the images.
- *SADI* (SDI + ADI), is based on first performing the SDI to remove part of the speckles, then using ADI to remove persistent residual speckles, and then combining the images. The difference with CODI is that SADI uses PCA twice, once for SDI and once for ADI, while CODI only uses it for SDI.
- *ASDI* (ADI + SDI), in the same way as SADI is used, but this time starting with ADI and then with SDI.

While CODI, SADI, and ASDI are interesting approaches that showed better performance compared to ADI and SDI alone, CODI proved to be a much more optimal combination for the case of SPHERE/IFS (Kiefer et al. 2021).

For each of the techniques (ADI, SDI, RDI, CODI, ASDI, SADI) there are also different implementations that are offered in pipelines. Some of these state-of-the-art post-processing techniques and pipelines are: PynPoint (Stolker et al. 2019), VIP (Gomez Gonzalez et al. 2017a), SpeCal (Galicher et al. 2018), vltsphere (Vigan 2020), among others. A series of algorithms for speckle suppression has been introduced within these pipelines, for example, the already mentioned principal component analysis (PCA, Amara & Quanz 2012a), the locally optimized combination of images (LOCI, Lafrenière et al. 2007b), the template LOCI for SDI (TLOCI, Marois et al. 2014), the Karhunen-Loève image projection (KLIP, Soummer et al. 2012), the Karhunen-Loève eigenimages forward modeling (KLIP-FM, Pueyo 2016a), the local low-rank, sparse, and Gaussian noise component decomposition (LLSG, Gomez Gonzalez et al. 2016), the maximum likelihood-based ANDROMEDA (Mugnier et al. 2009; Cantalloube et al. 2015a), the exoplanet detection based on patch covariance (PACO, Flasseur et al. 2018, Flasseur et al. 2020), the temporal causal regression model (lightcurve) approach (TRAP, Samland et al. 2021). In addition,

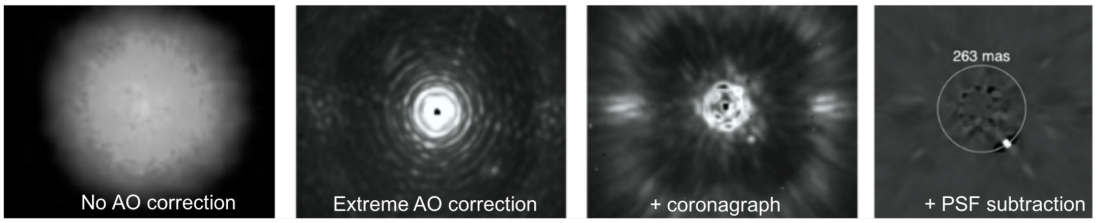

FIGURE 1.14: Demonstration of the impact in direct imaging for the use of non-atmospheric correction (left), the extreme-adaptive optic systems (middle left), the coronagraph blocking the starlight (middle right), and the use of post-processing algorithms for speckle suppression (right). Figure taken from Currie et al. (2022).

some dedicated PSF reference library construction (e.g., Xuan et al. 2018a, Ruane et al. 2019a, Bohn et al. 2019a) are used to perform reference differential imaging (e.g., Lafrenière et al. 2009a, Soummer et al. 2011a, Gerard & Marois 2016a, Xie et al. 2022).

Figure 1.14 shows how the performance of direct imaging improves from the seeing-limited point-spread function (left), the use of AO systems (middle left), the use of a coronograph (middle right), and the application of post-processing speckle suppression techniques (right).

1.4.2 Detection and characterisation of companions

Although both observational and post-processing techniques help to obtain contrasts at the level of detection of young planets of some Jupiter masses, the detection of a point source in the vicinity of the star does not guarantee that the candidate is a planet or even a substellar object. It is necessary to understand the nature of these candidates, and for this, it is possible to carry out a series of different studies based on, for example, the color-magnitude diagram, the spectral energy distribution, low-resolution spectra, proper motion diagrams, and orbital motion.

With direct imaging we can ultimately have access to the orbital solution of a planet, with which we can independently constrain its orbital parameters such as the mass. Given the large orbital period of the planets detectable with direct imaging (about decades, for example the period of HR 8799 e is $\sim 50\,yrs$, Zurlo et al. 2022), this has only been possible for some systems (e.g. β Pictoris, Lagrange et al. 2019a, Lagrange et al. 2020). Figure 1.15 shows an example of astrometric orbital characterization of the planetary system HR 8799 (Wahhaj et al. 2021). However, candidates can be ruled out as background or foreground contaminants by demonstrating that the candidate shares the same proper motion as the host star (e.g., PDS 70, Keppler et al. 2018). Figure 1.16 shows an example of a proper motion diagram where a candidate planet moves along with the star after showing that it shares the same proper motion as the star. The expected motion of a perfectly static background source is shown with red circles (Keppler et al. 2018). The co-moving nature is crucial to constrain some of the planetary parameters since the planet and its host star would share similar properties, the age being the most critical one given the sensitivity of the models to this parameter.

Color-magnitude diagrams also help to understand the nature of the candidate. For example, Figure 1.12 shows different absorption bands where the color of substellar objects varies depending on the atmospheric composition, temperature, and pressure, among others (other absorption features of interest

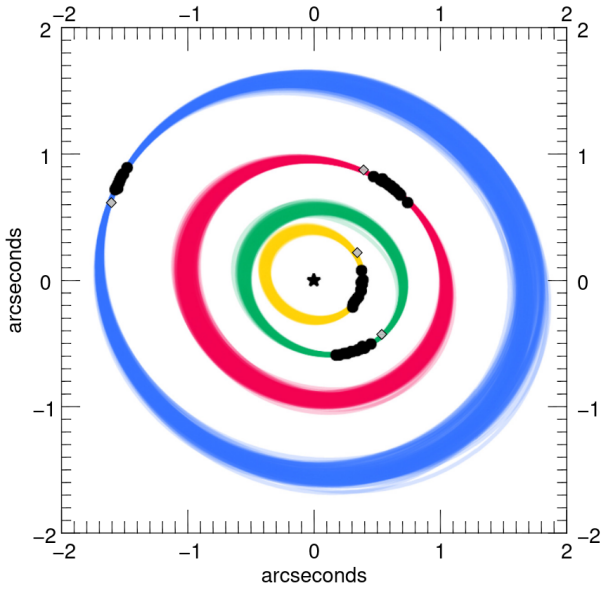

FIGURE 1.15: Orbital models of the planetary system HR 8799. Black dots correspond to different measurements of the astrometric position of the planets *bcde* using different instruments, and the gray diamonds are the new astrometric points presented in the publication (November 1st, 2019). The different colored lines correspond to the different orbital solutions (yellow, green, red, and blue lines corresponding to planets b, c, d, and e, respectively). Figure modified from Wahhaj et al. (2021).

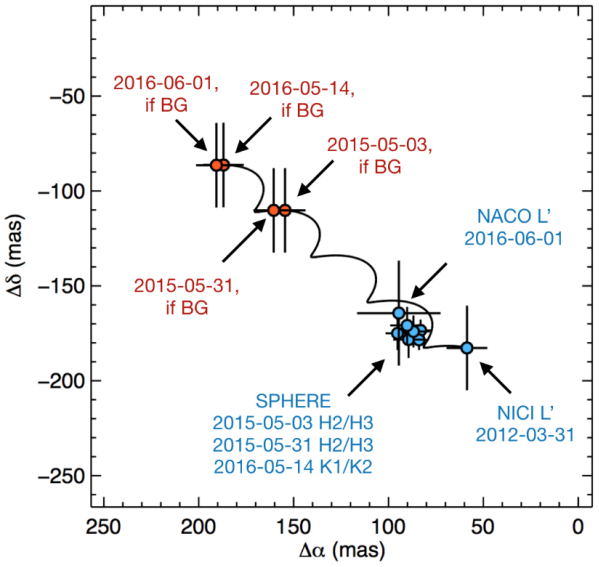

FIGURE 1.16: Proper motion diagram diagnostic for the PDS 70 system. The solid black line corresponds to the expected motion of a background source due to the proper and parallax motions of the star. Red circles are highlighting the expected location of a background, perfectly static source at each epoch, while the blue circles mark the location of the planet PDS 70 b at each epoch, demonstrating that the point source is moving along with the star. Figure taken from Keppler et al. (2018).

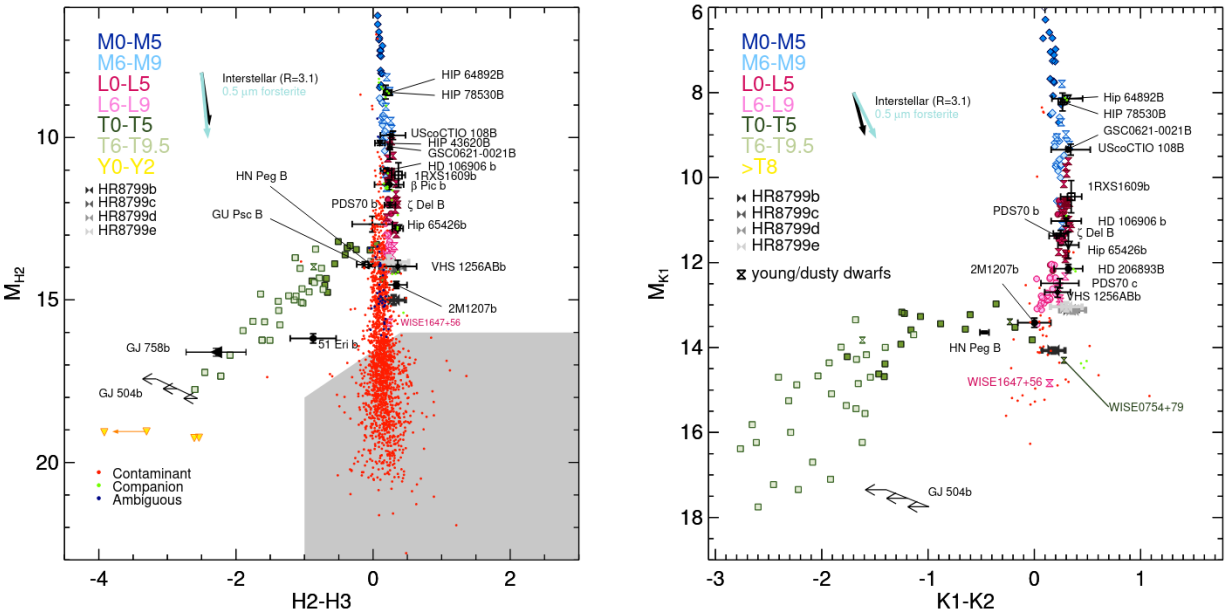

FIGURE 1.17: Color-magnitude diagrams of 159 stars observed with the SPHERE instrument from the SHINE program. Figures correspond to M_{H2} vs $H2-H3$ (left) and M_{K1} vs $K1-K2$ (right) color-magnitude diagrams. The spectral types are highlighted with different colors and symbols: blue and light-blue diamonds mark the M, the solid pink and light-pink circles the L, the green and light-green squares the T, and the yellow inverted triangle the Y. The contaminants, companions, and ambiguous nature unclear, unknown, or unconfirmed) are marked with red, green, and blue dots, respectively. The known planetary-mass objects are marked with black symbols with their respective planet name. The interstellar extinction vector is also plotted with black and light blue arrows. The grey area in the left panel corresponds to the excluded zone (background-like point sources). The Figure was taken from Langlois et al. (2021a).

are also shown in Figure 1.19 - see next paragraph). The narrow band filters have been designed to better identify these molecules and absorption features in the planetary spectrum, such as CH_4, CO, NH_3, KCl, and H_2O, for example (see right side of Figure 1.18). Molecular absorptions provide important clues about the nature of the candidate, thus being able to reject with a certain degree of confidence those that do not follow this trend (e.g. Langlois et al. 2021a). However, some of the detected planets show extreme reddening colors that make it difficult to easily distinguish them from the background stellar population. This is why the study of color-magnitude diagrams rather allows us to rule out candidates instead of confirming them. Figure 1.17 shows three examples of color-magnitude diagrams where the populations of M, L, T, and Y spectral types are highlighted with different colors and symbols, on top of the known direct imaged planets and planetary mass objects (Langlois et al. 2021a).

Using multiple wavelengths in narrow bands, broadbands, and low-resolution spectra (from IFS, for example) helps to better constrain the true nature of the candidates. Planets and planetary mass objects display distinctive absorption bands and shapes, which facilitate the determination of some of their fundamental properties. Figure 1.18 shows an example of typical spectra of directly imaged planets (right side) and brown dwarfs (left side), and their more prominent absorption bands, shapes, and molecules (Guillot et al. 2022). For example, L-spectral types with very red colors in the near-IR and silicate condensed clouds (Kirkpatrick 2005), T-spectral types with bluer colors in the near-IR, and considerable absorption of methane at, for example, $\sim 1.6\mu m$ (Kirkpatrick 2005), and the Y-spectral type beyond the T-types (also cold with blue colors, dominated by absorption mainly of methane, Cushing et al.

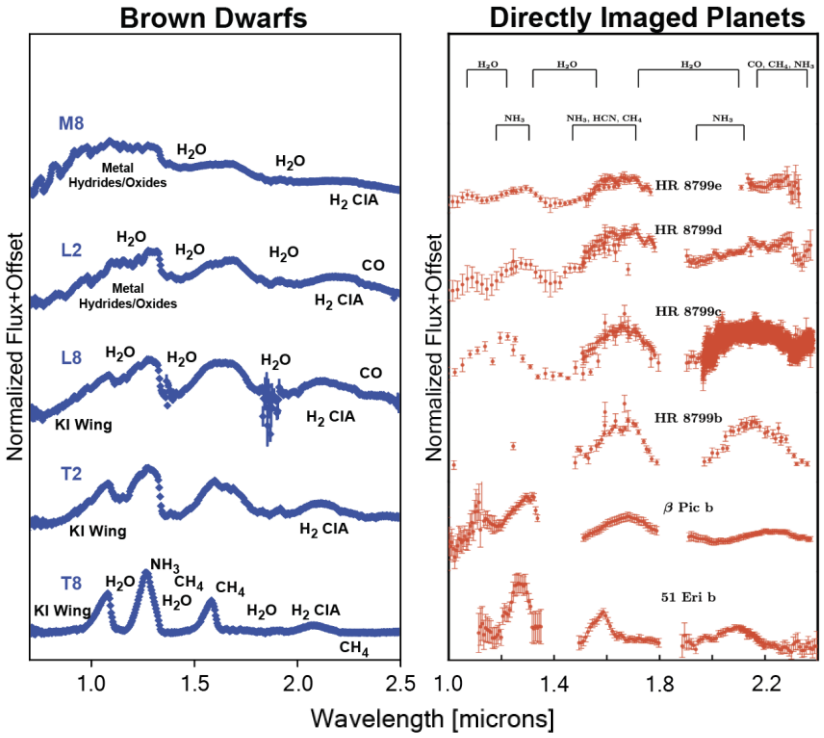

FIGURE 1.18: Example of typical spectra of some young stellar objects and their most common absorption features. The left panel shows the typical spectra of brown dwarfs from the SpeX Prism Library. The right panel shows spectra of some self-luminous giant planets observed with direct imaging. Figure taken and modified from Guillot et al. (2022).

2011). Planets are affected by distinctive signs from clouds/dust, chemistry, and gravity (e.g., Bonnefoy et al. 2014), which is why planets with very red colors are observed in the color-magnitude diagram (e.g., PDS 70 system). Figure 1.19 shows an example of spectro-photometric observations and characterization of two companions using the JWST, the planet HIP 65426 b (top panel) with $T_{eff} \approx 1660K$, $log\, g \approx 4.0$, and $R \approx 0.95 R_{Jup}$ using BT-SETTL atmospheric forward model[9] (Carter et al. 2022), and the planetary-mass companion $VHS\,J125601.92 - 125723.9\,b$ (bottom panel) with silicate clouds, water, methane, carbon monoxide, and carbon dioxide, and $M < 20 M_{Jup}$ (Miles et al. 2022). The spectra (broad and narrow bands, and low-resolution spectra), can provide strong evidence to affirm that they are exoplanets and not background stars (e.g., 51 Eridani b, Macintosh et al. 2015).

Regarding evolutionary models, there are several factors that can greatly impact the atmosphere and the evolution of the planet, such as non-equilibrium chemistry, dust, and clouds formed at different layers. For example, we can consider two planets with the same internal temperature profile (T=T(P)); one with an optically thin cloud-free atmosphere, while the other one has a considerable opacity (cloudy). Convection will be one of the favorable energy transport in both cases to carry the energy released from the planet's interior to atmospheric layers where photons can escape. The planet without clouds will have a more constant radiative flux without interruptions, while the planet with clouds will require additional convective motions to transport the energy to the upper layers of the atmosphere. This is because the energy is re-processed by clouds and dust and is re-emitted at longer wavelengths. This process also causes energy to escape less efficiently, leading to a much slower cooling process, and much redder

[9] In contrast with values obtained from evolutionary models and bolometric luminosity: $mass \approx 7 M_{Jup}$, $T_{eff} \approx 1280K$, and $R \approx 1.45 R_{Jup}$, see Carter et al. 2022.

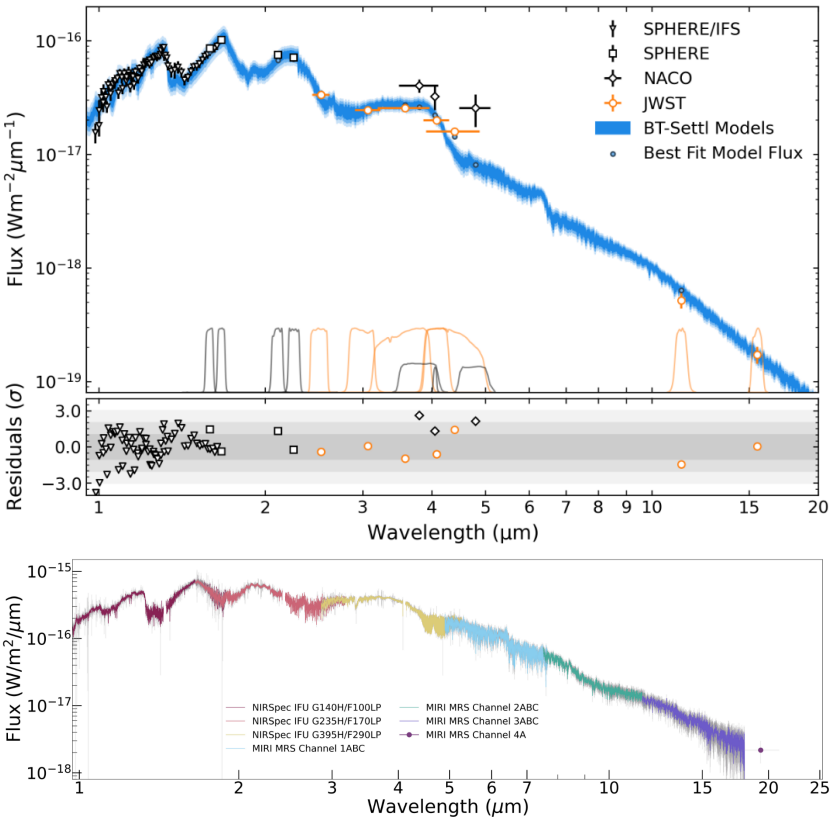

FIGURE 1.19: ***Top panel:*** a collection of all spectroscopic and photometric observations of HIP65426b obtained from SPHERE (IFS in triangles, IRDIS in squares), NaCo (diamonds), and JWST (circles). The best BT-SETTL atmospheric forward models from the modeling are plotted in blue dashed lines and the respective model for each filter is in small blue circles. Additionally, the throughput profiles for all photometric observations are shown. The bottom of this panel shows the residual values. ***Bottom panel:*** Spectrum of VHS1256b using NIRSpec-IFU and MIRI-MRS observations from the JWST. Each filter/bandpass is plotted with different colors, with the respective uncertainties displayed in grey. Figures taken from Carter et al. (2022, top panel), and Miles et al. (2022, bottom panel).

planets on color-magnitude diagrams. Therefore, two identical planets but one with a cloudy and dusty atmosphere will have different "apparent" effective temperatures and colors, the cloudless planet being bluer with larger effective temperatures (see Crivellari et al. 2019). Infrared observations are especially helpful in studying the clouds in the planetary atmospheres. Near-IR observations probe deeper into the cloud surfaces, while mid-IR wavelengths probe higher-up, cooler cloudtops (e.g., Manjavacas et al. 2021). Figure 1.20 shows the example of the atmospheric modeling of planet HR 8799 d (Currie et al. 2011; Currie et al. 2022), in which two models of thick and thin clouds are fitted. From the Figure the effect of the different clouds is clear, as they can re-process the energy to mid-IR wavelengths. Also, Figure 1.19 (bottom panel) shows an example of spectra that, for a proper match between models and data, two types of clouds are required with a sedimentation parameter of $f_{sed} = 0.6$ and $f_{sed} = 1$ in a ratio of $1:9$ (see Miles et al. 2022).

So-called "hot" and "cold" start models are used to convert the observable luminosity of the planet into a mass. These models assume certain initial properties to predict the luminosity evolution of the planet as a function of time. For instance, the "hot" start model assumes a high initial entropy, resulting in very bright planets at ages of a few Myrs (Baraffe et al. 2002, Burrows et al. 2001, Burrows et al. 2003), while the "cold" start model assumes lower values of the initial entropy, forming planets with very small

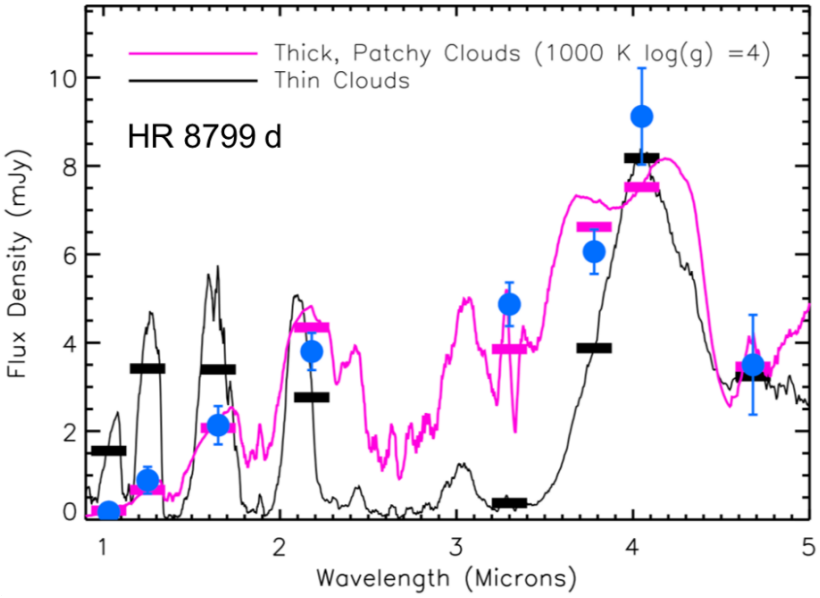

FIGURE 1.20: Flux density as a function of wavelength of the planet HR 8799 d. The figure shows an example of two different atmospheric models that include thick (magenta line) and thin (black line) clouds. Blue dots correspond to observations of HR 8799 d using different bandpasses and instruments. The horizontal magenta and black lines identify the flux of the model in the photometric filters convolved over the filter function. Figure taken from Currie et al. (2022).

brightness at the same ages (Marley et al. 2007). However, there is a strong degeneracy between the mass, the age, and the temperature, which makes it very difficult to convert the luminosity into physical properties of the planet (for example, its mass), and the age of the planet is the most sensitive parameter in the models. This is why the study of members of young moving groups and stellar associations whose age is relatively well determined has been preferred. In cases for which an age estimate of this kind is not available, it is still possible to narrow down the age using stellar rotation and activity (e.g, Angus et al. 2019). However, as mentioned above, age is a key factor in deriving the mass of a self-luminous planet. There are emblematic cases, such as GJ504B, a companion with a planetary mass of $3-9M_{Jup}$ with an age of $100-510Myr$ (Kuzuhara et al. 2013). However, the age of the star was later revised to $3-6Gyr$. As a result, the newly estimated mass rather falls into the brown dwarf regime (D'Orazi et al. 2017). Figure 1.21 shows an example of atmospheric characterization of the planet 51 Eri b, in which a variety of observations were used to study the spectral energy distribution of the planet, deriving some of the planetary properties: $T_{eff} \approx 760K$, $log\, g \approx 4.2$, $Fe/H \approx 1$, $R \approx 1R_{Jup}$, and sedimentation parameter of $f_{sed} \approx 1.2$ (Samland et al. 2017).

It should be noted that all the works previously mentioned rely on observations taken at different dates, and therefore we are making the implicit assumption that the object remains the same over time. In addition, for each observation, we are not considering each individual frame as an individual measurement but the combination of the entire sequence. Indeed, the average of the observing sequence does not allow us to study the variations in the luminosity of the planet during the observing time. However, time series observations can in principle allow us to study the rotation of sub-stellar objects as well as their variability. For example, Bryan et al. (2020) derived the rotation periods of 27 planets ranging from 4 to 22 hours. Snellen et al. (2014) presented a study of the spectral-line broadening of β Pictoris b, inferring a rotation period of 7-9 hours. If we consider the fact that the planets can have randomly distributed

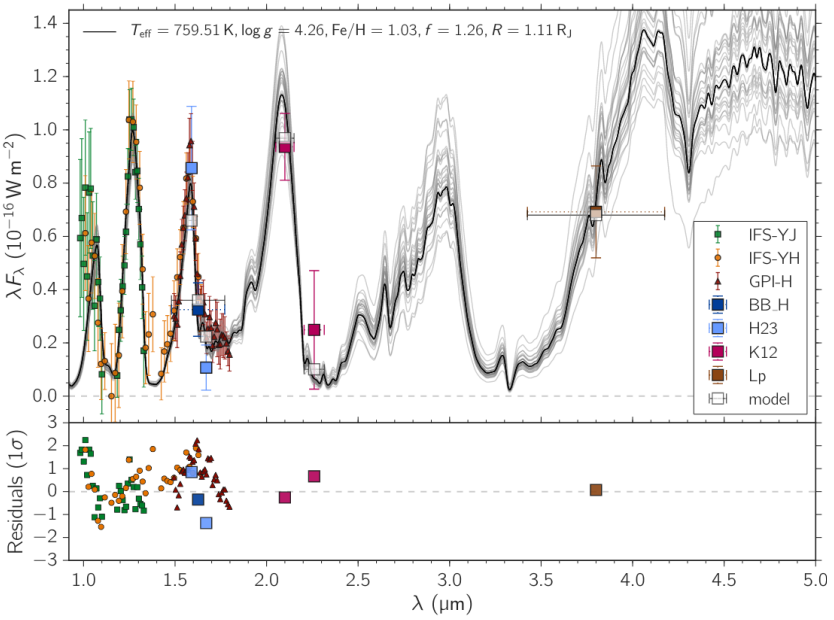

FIGURE 1.21: Atmospheric characterization of the planet 51 Eri b. The colored symbols correspond to different observations taken with different instruments (narrow- and broad-bands, and IFS observations). The black open squares correspond to the best fit to the model. Gray lines are the different models that fit the data, with the black one corresponding to the median of the models. Figure taken from Samland et al. (2017).

clouds and added to their fast rotation periods, it is possible to measure variability because they can appear brighter depending on the number of layer clouds they exhibit at a given phase. However, these temporal variations in brightness have not been measured for planets studied with direct imaging, but it might become possible to do it for some cases using the JWST.

In addition to the challenges in terms of atmospheric characterization and astrometry, there are other factors that make it difficult to assess the true nature of a planet candidate. The most common one would be to confuse structures of the protoplanetary disk with a planet in formation (Currie et al. 2017). The disk can display clumps of gas and dust that can be confused with an embedded protoplanet instead of a spiral produced by an inner companion (Norfolk et al. 2022). For instance, when using PCA to post-process the observations, some disk structures can appear as "bubbles" or "point-like sources" in the final image and can be easily confused with planets. For example, a point-like source was identified in the protoplanetary disk around HD 34282 but was later discarded as a feature of the disk produced by the PCA post-processing, which acts as a spatial filter (ISPY consortium internal discussion).

1.4.3 Surveys and statistics

Numerous campaigns and surveys have been carried out for the detection of young giant planets. The selection of targets has been carried out strategically and focused on young stars whose characteristics should be favorable for the detection and characterization of planets. However, this unfortunately leads to an observational bias that must be considered when reaching conclusions regarding the complete sample. The selection criteria are mostly based on targeting young moving groups, since their members share the same kinematics and origin; young star formation regions, since it is favorable when searching

for protoplanets and being able to study the early stages of planet formation. Surveys have also focused very heavily on the Scorpius-Centaurus association, given its high rate of planet detection as well as the detection of many debris disks, which could be a signpost for the presence of massive planet(s) (e.g., HR 8799 and $\beta\,Pic$). The association also contains many type A and B stars, which were originally deemed favorable targets to search for planets at infrared wavelengths, since planets and sub-stellar objects seem to be more common than around FGKM-type stars (e.g., Nielsen et al. 2019a). Furthermore, there are also a number of accelerating stars, for which we can measure the indirect effect of unseen companions. For instance, monitoring the proper motion anomaly (e.g., Brandt 2018; Kervella et al. 2019; Fontanive et al. 2019; Brandt 2021) has been shown to be a good tool for unseen companion detections, where astrometric comparison between the Hipparcos and Gaia catalogs has helped to check the effectiveness of this method with, for example, the systems with proper motion anomaly HR 8799, β Pic, and HD 206893 that harbor already known planets (Brandt et al. 2021b; Nielsen et al. 2019a; Grandjean et al. 2021).

Although it has been shown that the planet detection rate is very low in direct imaging surveys, since one planet is detected for every 100 stars (e.g., meta-analyses by Bowler 2016a, Bowler & Nielsen 2018), the contrast curves have been fundamental to carrying out statistical studies and comparisons with models of planetary formation. The incorporation of various tools in direct imaging (see Section 1.4.1), has been improving the sensitivity of these surveys, hence improving the final contrast curves. For example, with an AO-enabled 8m telescope a $\Delta mag \sim 8$ at $0.5''$was achieved (e.g., Masciadri et al. 2005 with the VLT; Chauvin et al. 2003, ESO 3.6m; Lowrance et al. 2005 with HST). For 8m telescopes, with an AO system, and speckle suppression we can reache a contrast of $\Delta mag \sim 10$ at $0.5''$(e.g., Biller et al. 2007 with the VLT and MMT; Lafrenière et al. 2007a with Gemini; Chauvin et al. 2010 with the VLT). For an 8m class telescope with an AO system, speckle suppression, and a coronagraph, a contrast of $\Delta mag \sim 11-12$ at $0.5''$is achieved (e.g., Desidera et al. 2015, Chauvin et al. 2015, Vigan et al. 2017 with NaCo-large programme; Biller et al. 2013 , Wahhaj et al. 2013, Nielsen et al. 2013 with Gemini NICI Science campaign; Vigan et al. 2012, Galicher et al. 2016 for IDPS; Tamura 2016, Brandt et al. 2014 for SEEDS; Skemer et al. 2014a, Stone et al. 2018a for LEECH). Finally, for 8m telescopes with extreme-AO system, more sophisticated speckle suppression, and coronagraphs, a contrast of $\Delta mag \sim 13-14$ at $0.5''$can be obtained (e.g., Nielsen et al. 2019a with the Gemini-GPIES; Vigan et al. 2021a, Desidera et al. 2021a, Langlois et al. 2021b for SPHERE-SHINE; Asensio-Torres et al. 2018 and Bonavita et al. 2016 for SPOTS large survey at Gemini; Janson et al. 2021 for BEAST survey; Bohn et al. 2020a, Bohn et al. 2020b, and Bohn et al. 2021 for YSES; Currie et al. 2020 for SCExAO/CHARIS HGCA survey ; Launhardt et al. 2020a for ISPY survey). It should be noted that these surveys focus on searching for planets mostly in H-band, while some of them have done it in mid-IR, in particular $L\prime$-band (e.g., LEECH and ISPY). The contrast curve changes as a function of wavelength, depending on the type of planet it aims at detecting. Launhardt et al. (2020a) shows that, in fact, observations at mid-IR wavelengths are more favorable for the detection of planets compared to near-IR wavelengths (see Figure 1.22). To be able to detect the same planet, it is not necessary to go as deep in contrast in $L\prime$-band compared to H-band. In addition, observations in mid-IR have fewer stellar contaminants (background or foreground stars) compared to near-IR wavelengths. Figure 1.23 shows two examples of sensitivity reached for some of these surveys (GPIES and SHINE), where the contrasts were transformed into probability map detection for planetary mass as a function of semi-major axis (sensitivity of a survey), in addition to the planetary companions that have been detected (Nielsen et al. 2019a; Vigan

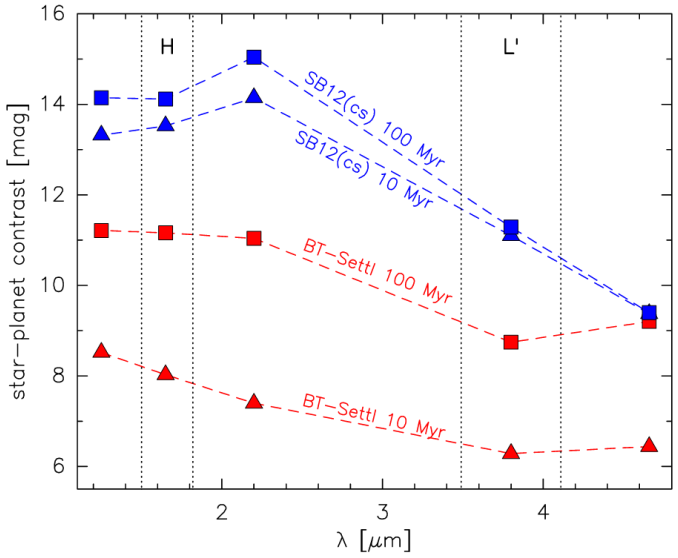

FIGURE 1.22: Star-to-planet contrast as a function of wavelength for a $1\,M_{\odot}$ star and a giant planet of $10\,M_{\rm Jupiter}$. The red color corresponds to the "hot start" model (Allard 2014a), and the blue to the "cold start" model (Spiegel & Burrows 2012). The triangle and squares are the two different ages used in the models (10 and 100 Myr, respectively). The symbols mark the location of J, H, K, L', and M bandpasses. Figure taken from Launhardt et al. (2020a).

2020). Contrast curves are fundamental to understand the occurrence rate of gas giant planets, and this is why the improvements from the first surveys to today have been fundamental not only to going deeper into the images (improving the contrast) but also to carrying out statistical studies that help understand the most favorable scenario for the formation of gas giant planets.

Regarding studies on the occurrence rate of giant planets, the first surveys carried out their analysis assuming some distributions for the semi-major axis and mass of sub-stellar objects (e.g., Masciadri et al. 2005, Lafrenière et al. 2007a, Nielsen & Close 2010), concluding that the occurrence rate of giant planets ($> 1 M_{\rm Jupiter}$) in wide orbits ($> 10\,$au) is relatively low ($< 10\%$). Subsequent surveys showed a similar occurrence rate, in addition to the fact that wide-separation giant planets are more likely to be found around higher-mass stars (e.g., Lannier et al. 2016), and that the occurrence rate may also be higher for stars hosting debris disks (e.g., Meshkat et al. 2017). The latest generation of surveys confirm the low occurrence rate of planets in direct imaging for which the frequency of systems with at least one substellar companion[10] are $\sim 23\%$, $\sim 5\%$, and $\sim 12\%$ for AB, FGK, and M -type stars, respectively (Vigan et al. 2021a), concluding that wide-separation giant planets of $2-13 M_{\rm Jupiter}$ at $10-100\,$au have a much higher occurrence rate of $\sim 8.7\%$ around higher-mass stars ($> 1.5 M_{\odot}$), compared to $\sim 0.7\%$ around Solar-like stars (Vigan et al. 2021a; Nielsen et al. 2019a). Nielsen et al. (2019a) parameterized the distribution of sub-stellar objects as a function of their mass m, semi-major axis a, and host star mass M_* as $d^2N/dm\,da = C\,f_p\,m^{\alpha}\,a^{\beta}\,(M_*/1.7M_{\odot})^{\gamma}$, where f_p is the occurrence rate and C a normalization factor. For giant planets ($5-13\,M_{\rm Jupiter}$), their found that $\alpha = -2.27$, $\beta = -1.68$, and $\gamma = +2.03$, which means that the occurrence rate decreases as the mass of the planet or semi-major axis increase, and increases with the host star mass. On the other hand, for sub-stellar objects of larger masses ($13 - 80 M_{\rm Jupiter}$), their found that $\alpha = -0.47$, $\beta = -0.65$, and $\gamma = -0.85$, which means that it has a mass distribution concentrated in the upper part (more massive objects), a semi-major axis distribution more concentrated

[10] For masses between 1 and 75 $M_{\rm Jupiter}$ and semi-major axis in the range of $5-300\,$au.

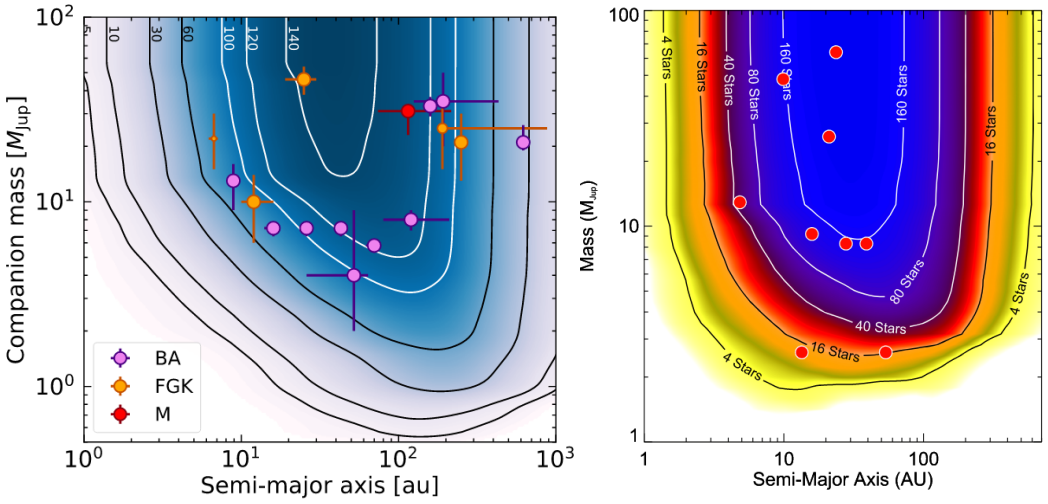

FIGURE 1.23: Probability detection maps for sub-stellar companions as a function of mass and semi-major axis. The contours give the number of stars to which each survey is complete or sensitive to. ***Left panel:***: map of the SHINE survey for the 150 stars in their sample. The contrast curves were converted into mass using the BEX-COND-hot evolutionary models (Marleau et al. 2019). The colored symbols represent the detected sub-stellar companions in the sample. The different colors indicate the spectral type of the targeted star (BA, FGK, and M). ***Right panel:***: map of the GPIE survey for the 300 stars in their sample. The contrast curves were converted into mass using the CIFIST2011 BT-Settl atmosphere models (Caffau et al. 2011; Allard 2014b; Baraffe et al. 2015). The red circles are the detected sub-stellar companions at each projected separation. Figures taken from Vigan (2020, left panel) and Nielsen et al. (2019a, right panel).

towards 100 au, and a small dependence with the mass of the host star. Considering the semi-major axis range between 10 and 100 au, and host star mass between 0.2 and 5 $M_{\odot}$, the occurrence rate of planets is 3.5% (68% confidence interval of $2.1\% - 5.4\%$), and 0.8% (68% conf. int. of $0.3\% - 1.6\%$) for brown dwarfs. Nielsen et al. (2019a) concluded that the occurrence rates are consistent with different formation mechanisms, being pebble accretion in the case of planets, and gravitational instability and fragmentation of circumstellar disks in the case of brown dwarfs.

Since planets are affected during and after their formation by different mechanisms, such as interactions with the disk, migrations, and even scattering (e.g., Morbidelli et al. 2009; Johansen & Lambrechts 2017; Emsenhuber et al. 2021), it is important to test the models and theories to determine key parameters essential to reproduce the observed planet population. Demography of exoplanets in direct imaging (supported by the occurrence rate and contrast curve/sensitivity) provides critical tests that help test the different theories of planet formation and migration, determining which of them dominates the observed population. These theories (core accretion and disk instabilities, for instance, see Section 1.2) predict different distributions of planet populations with different properties and at different distances from their stars. Disk instability predicts giant planet formation in wide-separations with more high-mass planets than low-mass ones without substantial dependence on stellar mass. On the other hand, core accretion predicts more giant planets closer to the star, and more low-mass planets than higher-mass ones. Rameau et al. (2013) defines regions in semi-major axis and mass in which formation by disk instability would be possible. However, given the non-detection of planets in this region, they set upper limits on the frequency of giant planets formed by disk instability. Statistical studies from the Gemini-GPIES and SPHERE-SHINE surveys (Nielsen et al. 2019a; Vigan et al. 2021a), suggest that core accretion is the dominant mechanism for the formation of giant planets observed with direct imaging. Figure 1.24 shows

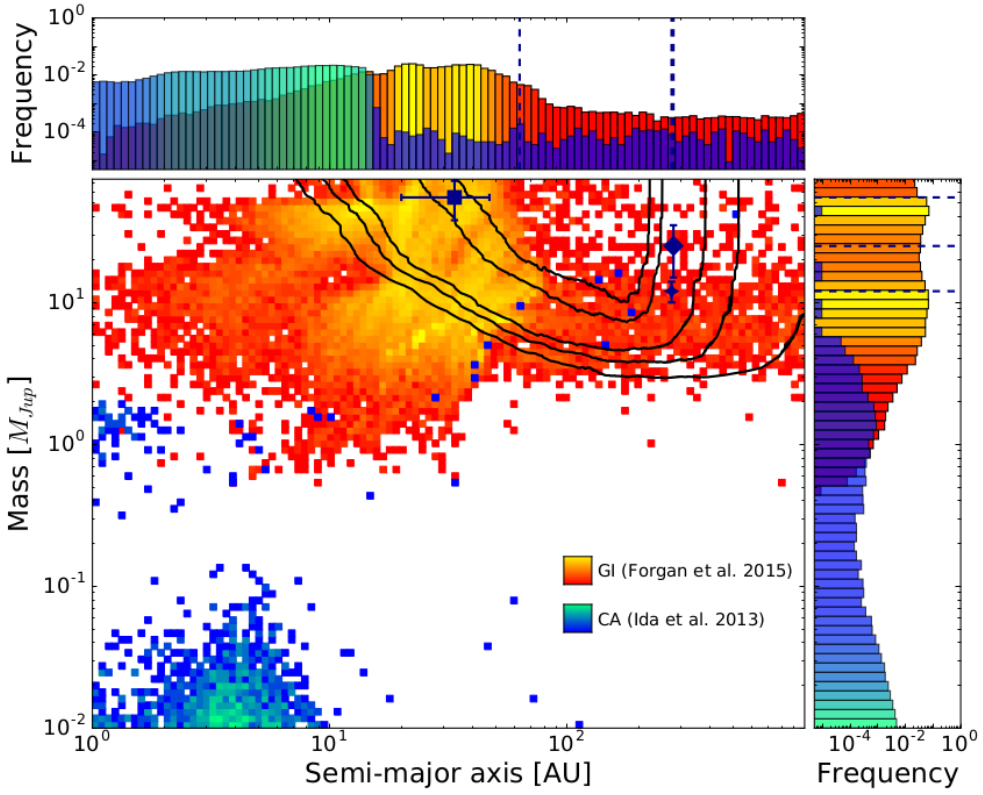

FIGURE 1.24: Probability map detection for planetary mass vs semi-major axis. The density-colored points are the scattered population for gravitational instability formation (red to yellow color gradient, Forgan & Rice 2013; Forgan et al. 2015), and core accretion formation (dark blue to cyan color gradient, Ida et al. 2013). The density colors go from low occurrence (dark blue, red) to high occurrence (cyan, yellow). The black contours are the mean detection probability of NaCo campaign observations and are highlighted the 5%, 25%, 50%, 90%, and 95%, respectively. The histograms on the right and top represent the relative frequency per bin of the semi-major axis and planetary mass, respectively. The histograms take into account the entire synthetic sample, not only the visible in the plot. Figure taken from Vigan et al. (2017).

a comparison of populations of planets formed via core accretion (Ida et al. 2013) shown in red and yellow tones, and disk instability (Forgan et al. 2015) shown in blue and green tones, whose evolution starts from embryos of planets that are then affected by migration and scattering (Vigan et al. 2017). The Figure also shows the histograms of planet populations for the semi-major axis and mass distributions, as well as the contrast curves in terms of sensitivity for the case of NaCo (black contour curves). From figures 1.24 and 1.23, if planet formation via disk instability was the main mechanism, we would expect to have a larger detection rate. On the other hand, the population of planets in the core accretion shows a very small population of planets in the medium and high sensitivity regions, which, when compared to the low detection rate of giant planets, results in a better agreement with the observations. However, this does not imply that all observed planets can be explained by core accretion. Furthermore, the 2M1270B (Chauvin et al. 2004) system can best be explained with disk instability instead of core accretion.

1.5 Main challenges in direct imaging

The complementarity between the different theories of planet formation (Section 1.2), and the observational techniques (Section 1.3) and direct imaging in particular (Section 1.4) provide important constraints to better understand the population of planets observed. Direct imaging helps very directly to determine the most likely mechanism for the formation of icy giant planets and to understand the global statistics of the population of these planets. However, as previously mentioned, even with all the advances in theory, instrumentation, and post-processing techniques, we are far from having a unified theory that explains all observed planetary systems. Furthermore, direct imaging still presents challenges, such as data reduction and improvements in contrast curves (e.g. Xie et al. 2022), especially for new instruments and capabilities (e.g., JWST). For this, it is crucial to carry out different tests, implement new algorithms, and even carry out new observation and post-processing strategies that help improve the contrast obtained by the observations. Since there are a few number of giant planets detected with direct imaging, we want to maximize the chances of detecting them. To do this, we need to test different selection criteria based on some properties of the star and surrounding debris disks. This thesis focuses on these two points, the improvement in data reduction techniques (Chapter 2), and searching for gas giant planets in systems whose properties suggest the presence of a massive perturber, i.e., an exoplanet (Chapter 3). The summary and conclusions of this thesis are presented briefly in Chapter 4. Finally, we talk about the future perspective and possible projects to carry out with the new generation of instruments and archival data in Chapter 5.

Chapter 2

Improvements in the data reduction of NaCO ISPY observations

This chapter corresponds to the paper: N. Godoy, J. Olofsson, A. Bayo, A. C. Cheetham, R. Launhardt, G. Chauvin, G. M. Kennedy, S. S. Brems, G. Cugno, J. H. Girard, Th. Henning, A. Müller, A. Musso Barcucci, F. Pepe, S. P. Quanz, A. Quirrenbach, S. Reffert, E. L. Rickman, M. Samland, D. Ségransan, T. Stolker (2022). "ISPY - NaCo Imaging Survey for Planets around Young stars. CenteR: The impact of centering and frame selection", published in Astronomy & Astrophysics, Volume 663, id.A53, 25 pp.

2.1 Introduction

Thousands of exoplanets have been discovered in the past decades using a variety of observational techniques. Directly measuring the brightness of the planets using high-contrast imaging techniques, provides crucial information on their temperatures and chemical compositions, and therefore on their possible formation history. This is particularly achievable when using spectro-photometry in the near- and mid-infrared (e.g., Samland et al. 2017). In addition, it allows us to probe a unique parameter space, in particular at large orbital separations (typically ¿10 au for nearby stars). Several dedicated surveys aim to find young giant gaseous planets using the direct imaging technique (see Bowler 2016b for an overview of previous large imaging surveys). Such surveys take advantage of the fact that gaseous giant planets at an early age ($< 100\,\mathrm{Myr}$) are bright at infrared wavelengths because of the energy released during the contraction of their atmospheric envelope (see, e.g., Marley et al. 2007). For this reason, many of the recent, present, and future direct imaging instruments focus on near- and mid-infrared observations (e.g., SCExAO, Jovanovic et al. 2015; MagAO-X, Males et al. 2018; SPHERE Beuzit et al. 2019; GPI, Macintosh et al. 2014). In particular, the NaCo Imaging Survey for Planets around Young stars (ISPY, Launhardt et al. 2020b) is a survey whose aim is to find new young ($< 100\,\mathrm{Myr}$) substellar ($\lesssim 72 M_{\mathrm{Jup}}$) companions at L' filter ($\sim 3.8\,\mu\mathrm{m}$) using the NaCo instrument (NAOS+CONICA, Rousset et al. 2003, Lenzen et al. 2003) at the Very Large Telescope (VLT), Paranal Observatory, Chile.

The main challenge in detecting and characterizing faint companions around bright stars is to reach very high contrast values in the immediate vicinity of the star. Using a coronagraph to block the stellar light has proven to be a reliable strategy, improving the contrast by several orders of magnitude (e.g., Chauvin 2018) as close as a few λ/D from the star (typically >100 mas with current planet imagers). In addition, as mentioned in Launhardt et al. (2020b), the contrast between a planet and its host star is more favorable at mid-infrared wavelengths. However, the observations are still largely dominated by the stellar halo and the point spread function (PSF), obscuring the planet signal in the images, so several observational techniques were designed to tackle this challenge: angular differential imaging (ADI, Marois et al. 2006), reference differential imaging (RDI, Smith & Terrile 1984b), and spectral differential imaging (SDI, Marois et al. 2000, Sparks & Ford 2002b). Since ISPY uses only one filter and has no spectral information, it uses ADI as it allows the temporal subtraction of the PSF and the quasi-static speckles using the data of the objects themselves as reference. Since the sky rotates during the observing sequence, while the PSF and the speckles remain quasi-static, subtracting the median from the datacube essentially removes their contribution in the final image (classical ADI, Marois et al. 2006). The suppression of the stellar PSF is significantly improved by using advanced post-processing algorithms and, for the forward- modeling approaches, prior information on the noise statistics and the ADI planetary signal itself. Some of these algorithms are the locally optimized combination of images (LOCI, Lafrenière et al. 2007b); Karhunen-Loéve image projection (KLIP, Soummer et al. 2012), principal component analysis (PCA, Amara & Quanz 2012b), KLIP-forward modeling (KLIP-FM, Pueyo 2016b); the maximum likelihood-based ANDROMEDA (Mugnier et al. 2009; Cantalloube et al. 2015b), local low-rank, sparse, and Gaussian noise component decomposition (LLSG, Gomez Gonzalez et al. 2016); a dedicated PSF reference library construction (e.g., Xuan et al. 2018b, Ruane et al. 2019b, Bohn et al. 2019b) used to perform reference differential imaging (RDI, Lafrenière et al. 2009b, Soummer et al. 2011b, Gerard & Marois 2016b); exoplanet detection based on patch covariance (PACO, Flasseur et al. 2018, Flasseur et al. 2020); and more recently the temporal causal regression model (lightcurve) approach (TRAP, Samland et al. 2021).

Surveys with very large samples allow us to put statistically robust constraints on the occurrence of giant planets around young stars, and therefore provide critical inputs to inform and refine planet formation models (see, e.g., Vigan et al. 2020). As many bright stars (L <6 mag) were included in the ISPY sample, it was possible to observe a large fraction of them ($\sim$ 70%) using the annular groove phase mask (AGPM) vector vortex coronagraph (Mawet et al. 2013, Absil et al. 2014). The position of the star is a crucial parameter in the post-processing of ADI observations since it is the reference center to align and combine all the images. However, as soon as the star is placed behind the AGPM, its exact position can no longer be measured accurately, and this represents a challenge for high-resolution imaging observations, especially for first-generation direct imaging instruments such as NaCo. Second-generation instruments tackle this problem by using the deformable mirror to produce diffractive attenuated copies of the stellar PSF, called satellite spots (SPHERE, Beuzit et al. 2019; SCExAO/CHARIS, Groff et al. 2015) or by using diffracted images of the star produced by a reference grid inside the optical path of the instrument (GPI, Macintosh et al. 2014), to determine the position of the star behind the coronagraph with subpixel precision (reaching $0.1 - 0.2$ pixels in the case of SPHERE in H band[1]).

Ground-based observations at mid-infrared wavelengths are performed with a very short detector integration time (DIT) to avoid saturating the detector, because of the significant sky thermal emission.

[1] According to Appendix A.12, page 116 in the VLT/SPHERE User Manual Issue: 106

The typical on-source time per target for the ISPY observing strategy is between 2 and 4 hours, leading to 10,000 to 30,000 frames per target. Because the observing conditions vary throughout the night, or the coronagraph is slightly drifting (see Section 2.3.1), the quality of these thousands of frames will significantly vary. It is therefore relevant to assess whether removing the worst frames while keeping the most homogeneous ones can improve the final reduction. Different frame selection techniques have been proposed to try and improve the contrast or increase the S/N of any point source detection at different wavelengths. For example, Stolker et al. (2019) used a selection based on the sky brightness, Keppler et al. (2018) used the PSF variation of the stars in the field of view, while Bohn et al. (2020c) discarded images with poor AO correction. There are therefore several approaches to performing some sort of frame selection, but overall they are usually on the conservative side, and there has not been an in-depth study of the potential benefits of performing more aggressive frame selection on large datacubes.

In this paper we present a new technique that aims to accurately find the position of the star behind the coronagraph for the particular case of NaCo observations with the AGPM. A good determination of the position of the star is essential for astrometric studies and a better extraction of the flux of potential companions. We also present our approach to registering the quality of the science frames, and to studying the impact of performing frame selection on the final reduction.

The paper is structured as follows. Section 2.2 summarizes the observation strategy and data reduction. In Section 2.3 we explain the new centering technique and the determination of the position of the star behind the coronagraph. We also explain our approach to registering and selecting the science frames. In Section 2.4 we benchmark our centering technique using observations of a star with a known companion. We apply our pipeline to two known companions (β Pictoris b and R CrA b), and present in Section 2.5 the improvements in the S/N of these point sources. In Section 2.6 we summarize our findings and conclusions on the importance of centering and frame selection for ADI observations.

2.2 Observations and data reduction

In this section we describe the observing strategy, the standard (cosmetic) reduction steps, and the post-processing used to obtain the final images. In addition, we describe the effective shape of the coronagraphic image in the corrected science data that is described later on for the centering algorithm and registration of frames.

2.2.1 Observational strategy

The stars HD 34282, R CrA, and HD 104237 were observed as part of the ISPY program (Launhardt et al., 2020b), during the nights 2016 November 07, 2017 May 19, and 2017 May 16, respectively. The observations were performed under different weather conditions varying from good to bad seeing (ranging between 0.34″ and 1.54″), as summarized in Table 2.1. We used the L27 camera (pixel scale $\sim$ 27.2 mas pix^{-1}) with the L' filter (λ_c = 3.8 μm, $\Delta\lambda$ = 0.62 μm) and the AGPM coronagraph for all three stars. The observing strategy was already described in Launhardt et al. (2020b), but as a brief summary, it consists in obtaining multiple datacubes of 100 images each with the star manually placed behind the AGPM (hereafter science sequence). At the end of each science sequence the field

Table 2.1: Log of the observations.

	HD 34282	R CrA	HD 104237	β Pictoris
Obs. date	2016-11-07	2017-05-19	2017-05-16	2013-02-01
Wind Speed[a] [m/s]	2.15-5.18 (4.00)	5.03-7.80 (6.09)	12.98-17.08 (15.43)	0.53-4.28 (2.28)
Coherence time[a] [ms]	4.8-17.3 (10.7)	2.9-5.8 (4.2)	1.8-3.7 (2.3)	1.03-2.43 (1.76)
Seeing[b] [″]	0.69-1.29 (0.87)	0.67-0.92 (0.77)	0.97-1.43 (1.21)	0.84-1.57 (1.13)
Field Rotation [deg]	118.26	35.86	45.18	82.97
DIT[c] [sec]	0.25	0.35	0.35	0.2
NDIT	100	100	100	200
Total exposure time [min.]	$\sim$ 135	$\sim$ 70	$\sim$ 152	$\sim$ 114
Total number of Frames	32500	12100	26100	34277
Program ID	198.C-0612(A)	199.C-0065(A)	199.C-0065(A2)	60.A-9800(J)

Notes. The minimum and maximum value registered are tabulated for the wind speed, coherence time, and seeing, while the median registered value is in parentheses. [(a)] DIMM measured values during the observations. [(b)] Seeing measured on the image analysis detector (at the pointing location). [(c)] DIT = detector integration time.

of view is shifted so that it does not include the star (hereafter sky sequence). The purpose of the sky sequence is to estimate the thermal background and subtract it from the science observations. Each science-sky sequence lasts between three and five minutes, and is repeated tens of times for each star. At the beginning and end of every observation, we also obtained a separate set of images with the star placed at different regions of the detector (far from the AGPM), with shorter exposure times to measure the stellar PSF for photometric calibration (hereafter photometry frames or images). Since the third quadrant (bottom left corner of the camera) contains persistent bad columns, it was not used for the photometry observations.

β Pictoris was observed on 2013 February 01 (observations not part of the ISPY program), with the AGPM, under rather poor conditions. The data were presented in Absil et al. (2013) and re-reduced in Stolker et al. (2019), using the same strategy as used within ISPY, but for those observations the DIT was set to 0.3 s and the number of exposures per science cube was set to 200. The flux calibration strategy was also slightly different: in ISPY the star is moved to the three good quadrants of the detector, but for those observations sky measurements were taken between the photometry frames. The observations were executed using a window size of 768×770 pixels, which, in combination with the DIT, lead to a loss of $\sim 10\%$ of the frames. The total number of science sequences, the exposure times and the weather conditions are summarized in Table 2.1 for all stars.

2.2.2 Cosmetic corrections

To prepare the data for the analysis, it is necessary to perform cosmetic corrections. First, we corrected the images for the dark current subtracting the suitable master darks. Master darks were produced by calculating the median of the dark frames grouped by the different exposure times used in an observing sequence (photometry, science, sky, flat field). Every image was corrected by the corresponding master dark by subtracting it from the image. The second correction corresponds to normalizing the response of all pixels. To this end, we constructed a master flat field by median averaging all the sky flat images (flat images are usually taken once per observing run and correspond to sky flats), and dividing by the mean value of counts. The correction for the flat field is done simply by dividing every image by its respective master flat field. At the end, all science, sky, and photometry images were corrected by

master dark and master flat field. We also created a bad pixel map using the master dark and performing σ-clipping to select the outlier pixels (with $\sigma = 5$). The bad pixels were then corrected for by using a bicubic interpolation for every image. In the end, the sky mean was computed for every sky datacube using all available images. Then, the science images were sky-subtracted using the sky observations that are closest in time. We note that performing the sky subtraction this way is possible because of the negligible motion of the circular aperture and of the AGPM between consecutive science-sky sequences (see Appendix 2.7.1).

2.2.3 Effective shape of the coronagraphic image

When we subtract the sky background from the science images, we are also removing the thermal contribution of the AGPM (see Absil et al., 2016) and dust and debris located in the optical path of the telescope and instrument. A bright torus becomes visible around the coronagraphically rejected central star image. This torus is the result of the finite bandwidth of the AO, both spatial and temporal. Wavefront aberrations outside this bandwidth are not corrected for and lead to off-axis modes that are not rejected by the AGPM. Although the AGPM efficiently cancels out the on-axis light from the star, its transmission rapidly increases for off-axis light (see Fig. B.1 in Launhardt et al., 2020b). The shape of the torus strongly depends on the alignment between the star and the AGPM, the performance of the adaptive optics system, and in general, the weather conditions. Both the AGPM and the star can move during an observing sequence (see Section 2.3), with the motion of the AGPM being negligible for consecutive science-sky frames (see Fig. 2.19 and Fig. 2.20 in Appendixes 2.7.1 and 2.7.2, respectively). For this reason it is important to find the center position of the AGPM on the detector and to find the star position with respect to the AGPM center.

2.2.4 Principal component analysis

The PCA and the derotation processes were performed using the `PynPoint`[2] package (Amara & Quanz, 2012b; Stolker et al., 2019). The PCA process consists of creating an orthonormal basis of images (or eigenimages) representative of the ensemble of frames. Ultimately, the goal is to build an accurate representation of the stellar PSF and quasi-static speckles, which will be subtracted from each individual frame. Ideally, due to the sky rotation during the pupil-stabilized observations providing angular diversity with respect to the speckle noise, any real astrophysical signal should survive the process. Once the estimated PSF and quasi-static speckles have been removed, each frame is derotated according to its parallactic angle and all the frames are median-combined to recover the signal in the field of view (for more details, see Amara & Quanz, 2012b and Hunziker et al., 2018). For the method to work, there is a compromise between the total field rotation (effective rotational angle) and the minimization of the flux loss of the astrophysical signal. The final images are obtained using a specific number of principal components. Given that the computational time necessary for the entire process is proportional to the size of the datacube, we performed our tests using different image sizes, between 39×39 and 121×121 pixels. For a given star, several images are produced, with different numbers of principal components to find the maximum S/N of the point sources in the field of view (if any) and to study the impact of the

[2]PynPoint version 0.6.2: `https://pynpoint.readthedocs.io/en/latest/`

frame selection process as a function of the number of principal components. Their number varies in the range 1 to 30 or 1 to 150 (depending on the size and total number of frames).

2.3 CenteR algorithm

In this section we introduce a new algorithm, CenteR[3], designed to try to improve the data reduction process for angular differential imaging observations, focusing on observations taken with a coronagraph (AGPM). Our approach is twofold: first, we aim to estimate more accurately where the star lies behind the AGPM; second, we perform frame registration to characterize the quality of the science frames in order to perform frame selection later on.

2.3.1 Calibrating the AGPM detector location

One critical aspect when performing high-contrast imaging with ADI, is to accurately determine the position of the star behind the coronagraph. This is an especially challenging problem for first-generation instruments such as NaCo since Mawet et al. (2013) and Huby et al. (2015) showed that the location of the AGPM is not always the same as that registered on the detector, physically on top of a less stable and dynamic adaptive optics correction. We therefore present here a new method to determine the position of the star behind the AGPM. When the star is aligned behind the AGPM, the resulting shape is similar to a torus for sky-subtracted science images (see Section 2.2.3 and Figure 2.5). Therefore, the most straightforward way to obtain the position of the star is to fit a positive and a negative 2D Gaussian profile, modeling the aforementioned torus profile. However, the problem is highly degenerate if all the parameters are free to vary (around 13, depending on the assumptions), leading to poor constraints on the position of the star (uncertainty on the order of 0.65 pixels when considering all the parameters as free). We present a novel approach that helps determine the position of the star by fixing some of the free parameters, hence alleviating the degeneracies of the modeling. In particular, we fix some parameters of the negative 2D Gaussian profile related to the AGPM.

Our approach consists in finding the position of the AGPM independently, to keep it fixed during the rest of the modeling of the torus later on. In the sky images the AGPM is bright (see Fig. 2.3.1) due to its thermal emission, and as noted by Absil et al. (2016), it directly corresponds to the vortex center, which is not contaminated by the contribution of the star. By fitting a positive 2D Gaussian profile, for example, it is possible to accurately determine its position. However, for the science frames, the star is behind the AGPM, making it more difficult to determine the position of the AGPM. In Figure 2.3.1, the AGPM is clearly visible close to the center, along with the borders of a circle that correspond to the edges of the 15″circular aperture of the coronagraphic mask. We can correlate the center of this circular aperture with the position of the AGPM in the sky images. It is then possible to find the position of the AGPM in the science images by measuring the center of this circular aperture, following these steps:

1. Measure the AGPM position in the sky frames;
2. Measure the center of the circular aperture in the sky frames;

[3]Available at https://github.com/Nico-Godoy/CenteR.git

3. Relate both centers to obtain the transformation between the position of the AGPM with respect to the center of the circular aperture;

4. Measure the center of the circular aperture in the science frames without correcting for the thermal sky emission;

5. Use the transformation found in (3) to obtain the AGPM position in the science frames.

We use the sky images to estimate the relationship between the position of the AGPM with respect to the position of the center of the circular aperture. Using the collapsed frames helps increase the signal of both the aperture and AGPM, therefore minimizing the final uncertainty. This can only be achieved because of the lack of significant motion of both positions in one sequence (for ISPY, 100 frames per sequence). The AGPM position is fitted by collapsing the image along the X- and Y-axes to obtain a more robust solution for the position, increasing the signal of the AGPM and making the modeling faster (see Fig. 2.2). However, 2D fitting is also possible, and depending on the model used and the number of free parameters, uncertainties on the order of 0.07 to 0.15 pixels can be reached, while our approach yields uncertainties of $0.1 - 0.15$ pixels. In addition, we find that the 1D and 2D models are both consistent. The solution using the 1D model is obtained by fitting two normal distributions using a nonlinear least-squares method, minimizing the following equation:

$$\eta = \sum_{i=1}^{M} \left(Z_{\rm i} - I_1 \exp\left[-\xi_1\right] - I_2 \exp\left[-\xi_2\right] - Z_{\rm Bkg}\right)^2 . \tag{2.1}$$

The value $Z_{\rm i}$ corresponds to the normalized sum of counts per column (or row), $\xi_1 = (X_{\rm i} - \mu_{\rm AGPM})^2/2\sigma_1^2$, $\xi_2 = (X_{\rm i} - \mu_{\rm AGPM})^2/2\sigma_2^2$, and $X_{\rm i}$ the position of each column (or row); $\mu_{\rm AGPM}$ corresponds to the position of the AGPM; σ_1 and σ_2 are the standard deviations of the two Gaussians, I_1 and I_2 the scaling factor for the two profiles, and $Z_{\rm Bkg}$ is the background level, all of which are free parameters. The variable M corresponds to the number of columns (or rows). The modeling uses two Gaussians to account for the thermal emission of the AGPM and its halo (see Fig. 2.2). The results show that the movement of the AGPM during a normal sky sequence of 100 images remains negligible.

To estimate the position of the circular aperture, we first identified the pixels that reside inside the aperture. To this end, we compute both the median absolute deviation (MAD, $\sigma_{\rm image}$) and the median using the entire image, and then for each column along the X-axis X_i (or row along the Y-axis, respectively), we count the total number of pixels $N_{\rm i}$ that are three times $\sigma_{\rm image}$ above the median[4]. If we were to use a linear sampling along the X-axis, the wings of the distribution would be undersampled, which would then bias the fitting results. The sampling therefore follows a cosine distribution to more evenly distribute the number of points in polar coordinates. To find the coordinate $X_{\rm CA}$ and radius $R_{\rm CA}$ of the aperture, we then minimize the quantity

$$D = \sum_{i=1}^{N} \sqrt{(X_i - R_{\rm CA}\cos(\alpha_i) - X_{\rm CA})^2 + (N_i/S_{\rm CA} - R_{\rm CA}\sin(\alpha_i))^2}, \tag{2.2}$$

[4]Or 10 times $\sigma_{\rm image}$ below the median when the observations are performed with windowing. In this case, there are many fewer pixels outside the aperture, and therefore the median is no longer representative of the background level.

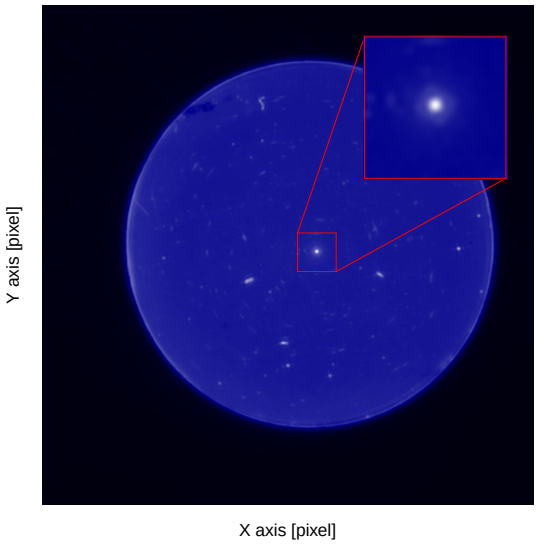

FIGURE 2.1: Example of a sky image showing the circular aperture in blue (observing date 2016 November 08. The top right inset shows a zoom-in on the central part, with the AGPM thermal emission in the center. The white elongated spots correspond to dust or dirt in the optical path of the instrument or on the camera, and are emitting at near-IR wavelengths.

where $S_{\rm CA}$ is a scaling factor to account for slightly elongated shapes (i.e., the aperture is not perfectly circular) and $\alpha_i = \arctan[(X_i - X_{\rm CA})S_{\rm CA}/N_{\rm i}]$. This transformation allows us to work in polar coordinates from the center of the aperture, and the fitting is performed for the X- and Y-axes independently. Figure 2.2 shows examples of fitting the AGPM position in a sky frame (left panel) and of the circular aperture (right panel).

Figure 2.3 shows the position of the center of the circular aperture for science and sky images (blue triangles and red circles, respectively) for the observations of HD 34282 and R CrA (left and right, respectively). For HD 34282, the observing sequence was interrupted, which explains the two separate blocks of points, indicating that the coronagraphic mask actually moves between observing sequences. The figure shows that the centers of the apertures for the science and the sky frames follow the same path, but also that the center of the circular aperture slightly shifts during the observing sequence.

For the sky frames only, figure 2.4 shows the position of the AGPM and the center of the circular aperture for the same three targets. It is important to note that the AGPM and the center of the circular aperture move following the same path in both cases. To estimate the relationship between the two positions, we make the simplest assumption (i.e., a constant value), which is evaluated for each observing sequence. We find no evidence of a more complex relationship between the two positions than this one (e.g., a time dependence; see Appendix 2.7.2). These constant values are determined as

$$\Delta X = \overline{X_{\rm AGPM} - X_{\rm CA}} \pm \delta(X_{\rm AGPM} - X_{\rm CA}), \tag{2.3}$$

$$\Delta Y = \overline{Y_{\rm AGPM} - Y_{\rm CA}} \pm \delta(Y_{\rm AGPM} - Y_{\rm CA}), \tag{2.4}$$

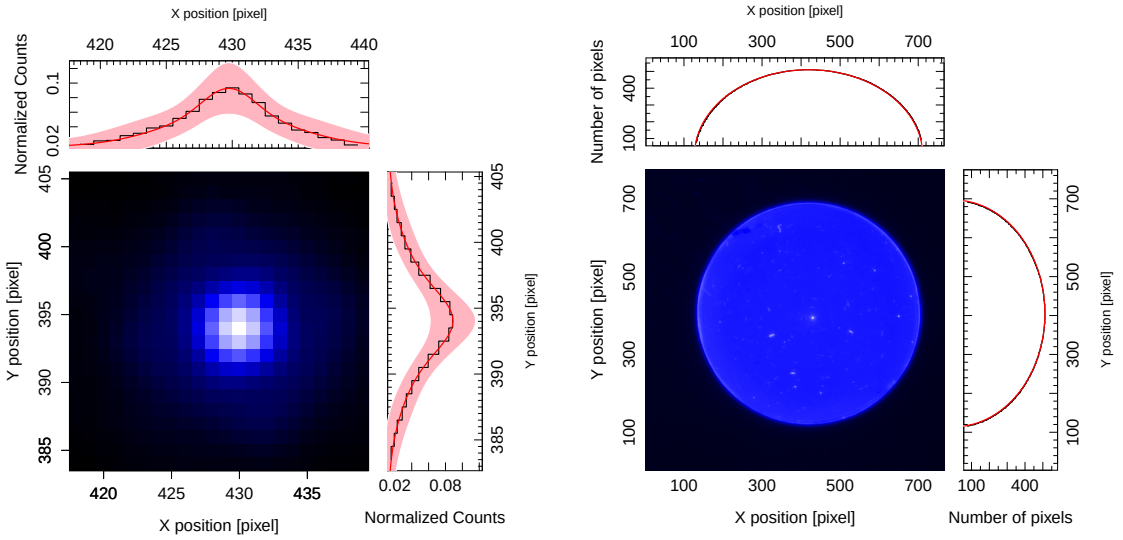

FIGURE 2.2: Examples of what the AGPM and the circular aperture look like in a sky image. *Left*: Modeling of the thermal emission profile of the AGPM along the X- and Y-axes to obtain the coordinate center for a cleaned sky image. *Right*: Modeling of the circular aperture along the X- and Y-axes to estimate the coordinates of its center in the same image. The colored area corresponds to a 95% confidence interval.

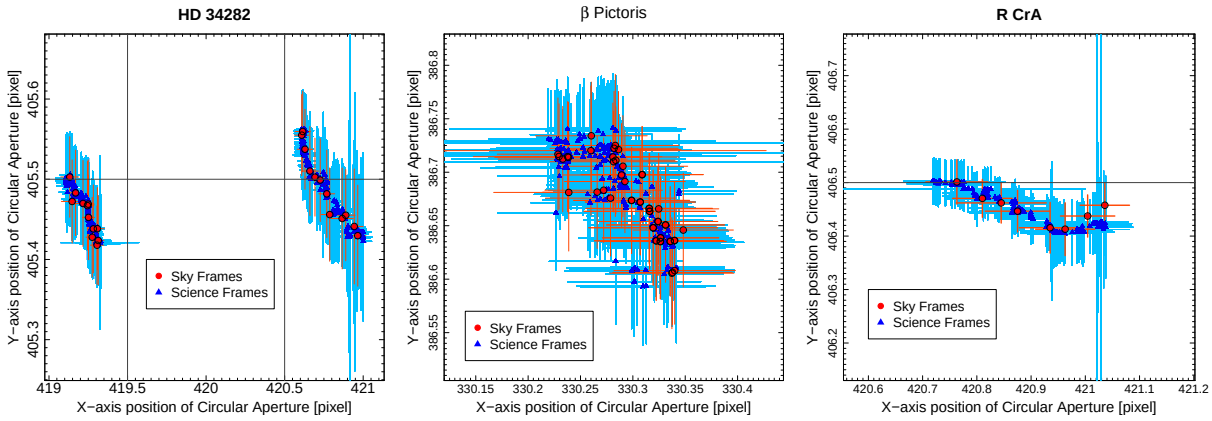

FIGURE 2.3: Position of the center of the circular aperture (with respect to the camera) during the observation sequence for sky and science images (red and blue, respectively), for HD 34282 (left), β Pictoris (middle), and R CrA (right); the axis scales are 1:5, 1:1, and 1:3, respectively. The grid represent pixels, and the colored crosses correspond to the uncertainty obtained in the fit.

where X_{AGPM} and Y_{AGPM} correspond to the measured position of the AGPM on the X- and Y-axes for every individual sky frame, $\overline{X_{\mathrm{AGPM}} - X_{\mathrm{CA}}}$ and $\overline{Y_{\mathrm{AGPM}} - Y_{\mathrm{CA}}}$ correspond to the mean value of the difference between the AGPM position with respect to the center of the circular aperture for the X- and Y-axes, and $\delta(X_{\mathrm{AGPM}} - X_{\mathrm{CA}})$ and $\delta(Y_{\mathrm{AGPM}} - Y_{\mathrm{CA}})$ are the standard deviations of these relative positions. For each science frame, knowing the position of the center of the circular aperture and using those two equations, it becomes possible to determine the position of the AGPM with a precision better than 1 pixel (on the order of 0.1 pixels). The accuracy of 0.1 pixels in the position of the AGPM contributes directly to the final uncertainty in the star position, and it is the same order of accuracy as second-generation instruments (e.g., SPHERE or GPI).

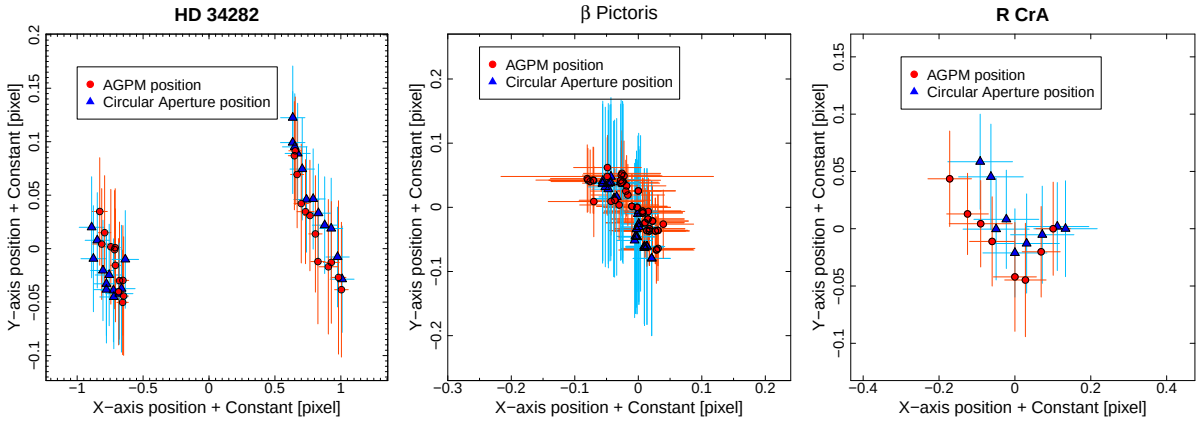

FIGURE 2.4: Position of the center of the circular aperture (blue triangles) and AGPM (red circles) with respect to their median value, for sky frames only. *Left:* Position for HD 34282. *Middle:* Same, but for β Pictoris. *Right:* Same, but for R CrA. The axis scales of the left, middle, and right panels are 1:8, 1:1, and 1:3, respectively. The colored crosses correspond to the uncertainty obtained on the fit.

2.3.2 Estimating the stellar location

With the position of the AGPM known, it becomes easier to determine the location of the star behind it. With our approach we can accurately determine the location of the AGPM if we know the center of the circular aperture. In Fig. 2.19 in Appendix 2.7.1 we furthermore show that the latter does not significantly move during an observing sequence, meaning that we are able to know the location of the AGPM for all frames without assuming for instance that the AGPM is located at the local minimum in the sky-subtracted frames. The frames are cropped into 23×23 pixel images, centered on the AGPM position to minimize the computational time. Then, each cropped science frame is fitted with a model that has three different contributions to reproduce the torus: a positive 2D Gaussian distribution representing the imperfectly AO-corrected non-attenuated star image on the detector $V_{\rm Star}$, a negative 2D Gaussian function accounting for the cancellation of the on-axis star light produced by the AGPM $V_{\rm AGPM}$, and an estimate of the background level Z_0. The last is estimated in an annulus outside of the AGPM between 5 and 11 pixels accounting for the halo generated around the AGPM, while the 2D (negative or positive) Gaussian profile takes the general following form:

$$V = A \frac{\exp\left[-\frac{1}{2}(X-\mu)^{\rm T} R(\theta) \times \Sigma^{-1} \times R(\theta)^{\rm T}(X-\mu)\right]}{\sqrt{(2\pi)^2 ||\Sigma||}}. \tag{2.5}$$

Here A is the amplitude, μ is the center of the distribution (fixed to $X_{\rm AGPM}$ and $Y_{\rm AGPM}$ for the AGPM), X are the pixel coordinates $[x, y]$, $\boldsymbol{\Sigma}$ is the covariance matrix (a 2D diagonal matrix with $\sigma_{\rm x}^2$ and $\sigma_{\rm y}^2$ along the diagonal, allowing for elongated profiles), and $\boldsymbol{R(\theta)}$ is a rotation matrix that depends on the angle θ. For the distribution that represents the stellar contribution, the free parameters are $A_{\rm Star}$, $\mu_{\rm Star}$, $\boldsymbol{\Sigma_{\rm Star}}$ (both $\sigma_{\rm x,Star}$ and $\sigma_{\rm y,Star}$), and $\theta_{\rm Star}$. For the AGPM, $\mu_{\rm AGPM}$ is fixed to the positions found previously using the circular aperture, and the free parameters are the amplitude $A_{\rm AGPM}$ and $\boldsymbol{\Sigma_{\rm AGPM}}$ (assuming that $\sigma_{\rm x,AGPM} = \sigma_{\rm y,AGPM}$, and therefore $\boldsymbol{R(\theta)}=\mathbb{I}$ and $\theta_{\rm AGPM}$ is set to zero). One possible caveat is that for frames where the star is slightly off-center with respect to the AGPM, our assumption that the negative Gaussian profile is centered at $X_{\rm AGPM}$ and $Y_{\rm AGPM}$ may not be entirely

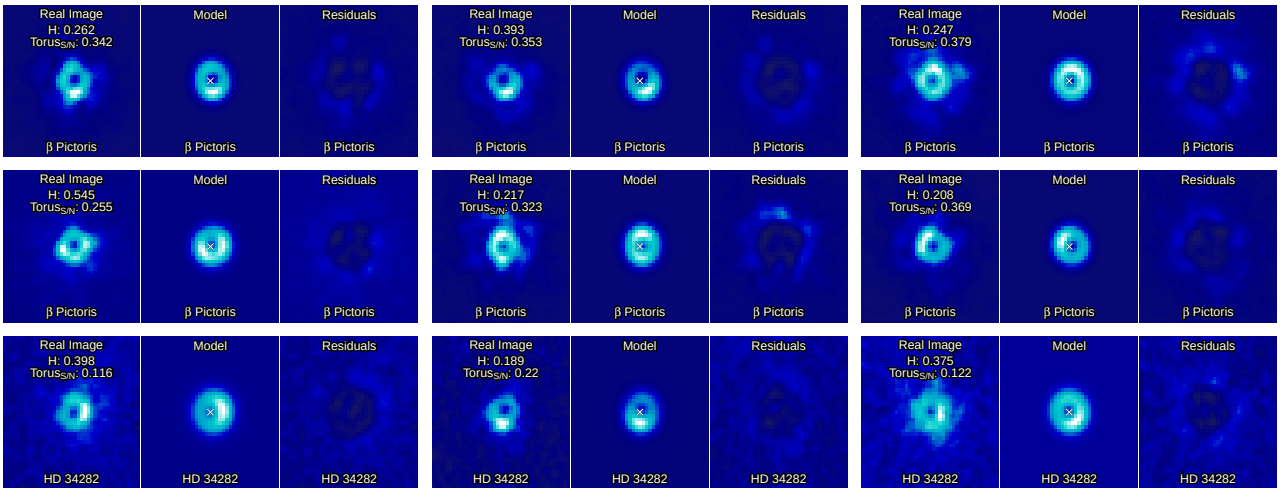

FIGURE 2.5: Modeling example of sky-subtracted science images for HD 34282 and β Pictoris using both the negative and positive 2D Gaussian. For each sub-panel, the observations are shown on the left, while the best-fit model is shown on the middle, and the residuals in the right. The homogeneity (H) and the S/N of the torus (Torus$_{S/N}$) is labeled for each frame. The color scale is the same for each subpanel. The white cross for each center panel marks the location of the AGPM.

correct. Indeed, subtracting a negative profile in the wings of a positive profile may slightly shift the position of the minimum. Nonetheless, this remains a good first-order approximation, and our approach is further tested in Section 2.4.

When minimizing the χ^2 to model the sky-subtracted science frames, they are first cropped to a size of 41×41 pixels, centered on the position of the AGPM. Furthermore, we impose that the variable $\sigma_{x/y,AGPM}$ (i.e., the 2D Gaussian σ of the AGPM) cannot be greater than the value of $\sqrt{\sigma^2_{x,Star} + \sigma^2_{y,Star}}$. We also consider the following constraints: for both the star and the AGPM, μ and σ cannot be greater than the actual size of the cropped frame. For σ_{AGPM}, its value is constrained from fitting the sky frames, and it can vary but cannot be greater than 2.5 pixels[5]. Considering the original set of 13 unconstrained free parameters, we have now 8 free parameters in our modeling. In the end, for each individual frame, we store the location of the center of the circular aperture, as well as the eight fitted free parameters, and their associated uncertainties. Examples of the negative and positive 2D Gaussian fitting are shown in Fig. 2.5, showing the sky-subtracted science frames, the models, and residuals. In the model images we also give the location of the AGPM, showing that it does not necessarily correspond to the location of the minimum flux. Overall, with our approach, we are able to accurately find the position of the star behind the AGPM in the sky-subtracted science images with typical uncertainties of 0.20 and 0.19 pixels on the X- and Y-axes (see Section 2.4).

2.3.3 Frame registration and selection

The motivation behind frame registration is to characterize every individual image to identify subsamples that worsen some aspect of the reduction in order to remove those frames in the datacube later on, performing frame selection. Depending on the objective, there are different ways of performing this registration and selection of frames that will affect the final noise distribution, the signal of the candidate,

[5]We consider the previous fit done using eq. 2.3.1 and their uncertainties to constrain the σ_{AGPM}.

and/or its position. For example, when we are interested in obtaining the position and flux of a candidate, it would be ideal to be able to maximize the signal of the object and/or minimize the residual noise of speckles. For this, we can discard those frames whose speckles and stellar PSF/halo distributions are very different from the rest of the frames, for example. Another need could be trying to maximize the S/N of the candidate, where the idea is to minimize the noise at the same angular separation to be sure that the signal is not being considerably contaminated by speckles. To this end, it could be possible to use frames whose statistical properties of noise are very similar as a function of angular separation, discarding those whose distributions are considerably different. Or even when we only want to increase the signal of the object, eliminating frames where the signal of the object has been very diluted due to a poor AO correction or changing weather conditions. In practice, there is no unique way to do the frame registration and selection. The most common approaches are carried out either visually when the total number of images remains small (e.g., Samland et al., 2017) or using simple criteria such as the background level (see Stolker et al., 2019 and Cugno et al., 2019), the AO performance and correction (Hagelberg et al., 2016), or by studying the photometric variability of the point sources in the field of view (Keppler et al., 2018).

To quantify the degree of similarity among frames it is necessary to characterize the torus shape described in previous sections. One way to do this is by measuring the distribution of speckles and inhomogeneities generated around the AGPM, produced by a misalignment between the star and the AGPM, the weather conditions, and/or a poor AO correction, for instance. Similarly, the ring-shaped contribution (torus with isotropic distribution) formed due to the star–AGPM combination, can give us information mostly about the centering. The best way to measure both is by using image reconstructors, such as the pseudo-Zernike moments. The pseudo-Zernike moments were defined in Teh & Chin (1988) as a tool to obtain information about images and their reconstructions. The pseudo-Zernike moments are defined from the (pseudo-)Zernike polynomials (Zernike 1934, Bhatia & Wolf 1954), and they comprise a complete set of orthogonal functions on the unit disk. Teh & Chin (1988) showed that pseudo-Zerinke moments are less sensitive to image noise than the conventional Zernike moments. They are routinely used in optics, atmospheric sciences, and atmospheric turbulence corrections using adaptive optics systems (see, e.g., Noll, 1976, Ma et al., 2017, Fusco et al., 2006, or Sauvage et al., 2016).

One of the main benefits of using the pseudo-Zernike moment is its fast computational analysis when performing such decomposition, making it possible to analyze quickly over thousands of frames. We use the package `IM` (Rajwa et al., 2013) from R Core Team (2019) to obtain the pseudo-Zernike moments for a specific order n and repetition m on the sky-subtracted science frames, where n= 0, 1, 2, ... ∞ and $|m| \leq n$. The order n is related to the complexity of the reference image (pseudo-Zernike moment) and m to the azimuth distribution. We note that $m = 0$ is purely related to radial profiles, and therefore it is not representative of anisotropies in the reconstruction. With the coefficients obtained from the moment decomposition (hereafter ζ), it is possible to define two criteria: the homogeneity H and intensity (S/N) of the torus formed around the AGPM in the science frames. The homogeneity of an image is related to the distribution of the light around the coronagraph; an image is classified with a high H value when the brightness distribution is homogeneously distributed as a function of the azimuth. For each frame H is calculated combining the information of the second and third repetitions (denoted $m = \pm1$ and $m = \pm2$) of the pseudo-Zernike moments as

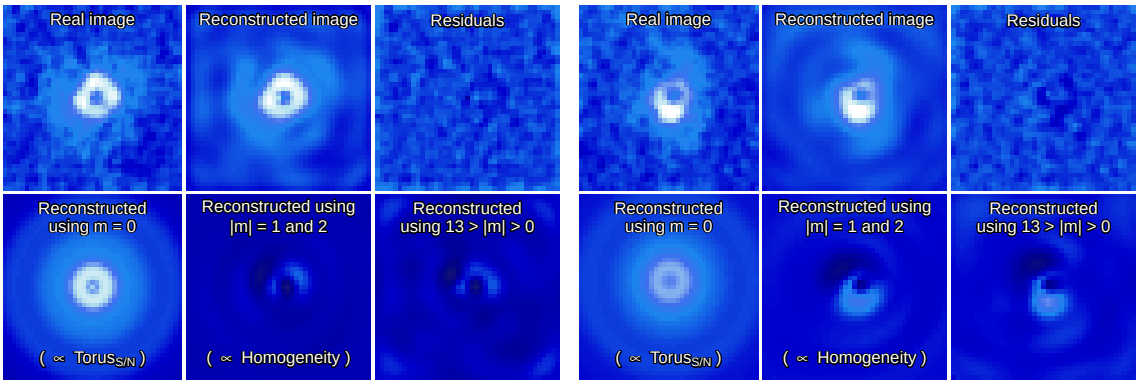

FIGURE 2.6: Two examples of reconstructed images using the pseudo-Zernike moments. For each panel (made up of six subpanels): *top left:* Observations; *top center:* Reconstructed image using m up to 12; *top right:* Residuals of the modeling; *bottom left:* Reconstruction of the image using only $m = 0$, related to radial and uniform azimuthal distribution; *bottom center:* Reconstruction of the image using $|m| = 1$ and 2, corresponding to the adopted inhomogeneous contribution; *bottom right:* Reconstruction of the image using $1 \leq |m| \leq 12$, related to all the azimuthal contributions. For each subpanel the color scale is the same.

$$H = 1 - \sqrt{|\sum_{n=1}^{5}(|\zeta_n^{m=\pm1}|)|^2 + |\sum_{n=1}^{5}(|\zeta_n^{m=\pm2}|)|^2}. \tag{2.6}$$

Both repetitions are related to the azimuthal brightness distribution with respect to the AGPM; therefore, large values of both repetitions implies a rather inhomogeneous frame. The S/N of the intensity of the torus is calculated using the first repetition ($m = 0$) of the pseudo-Zernike moments as

$$\text{Torus}_{\text{S/N}} = \frac{\sqrt{\sum_{n=1}^{5}(|\zeta_n^{m=0}|^2)}}{\sigma(25 < r < 35)}, \tag{2.7}$$

where r is the distance from the location of the AGPM in pixels. To estimate the S/N of the torus, its intensity is divided by the noise, which is the standard deviation measured in a ring between 25 and 35 pixels in radius. This region was chosen as it is free of speckles since we want a S/N measure that reflects only the intensity of the torus and the background noise of the image not affected by residual speckles. The numerator of the previous equation corresponds to the intensity of the torus, but preliminary tests suggest that it is not by itself an ideal parameter to classify the science frames. The first repetition $m = 0$ is purely related to the radial and isotropic distribution of rings, and consequently it is azimuthally homogeneous. Therefore, any inhomogeneity of the torus would not be reflected in $\text{Torus}_{\text{S/N}}$. Figure 2.6 shows two examples of reconstructed images and their respective residuals using the pseudo-Zernike moments. In addition to the reconstruction using only $m = 0$, which corresponds to the torus intensity (without azimuthal components), the figure also shows the reconstruction using $|m| = 1$ and 2 corresponding to the homogeneity as well as the reconstruction using $1 \leq |m| \leq 12$. Both values, H and $\text{Torus}_{\text{S/N}}$, are also normalized between 0 and 1, for all the frames and for each object individually.

With the results from the 2D negative and positive Gaussian profile fitting and with the information from the pseudo-Zernike moments, it is possible to further inspect the parameter space to distinguish between

the most homogeneous well-centered frames and the bad ones. Different combinations of parameters can be used to separate the good and bad frames. However, the parameter space strongly depends on the observing conditions. Therefore, we need to adapt the selection criteria for each dataset. We find that the most crucial parameters to identify the set of good frames are the following:

1. The separation between the estimated locations of both the star and the AGPM;
2. The S/N of the torus;
3. The background level and its standard deviation;
4. The goodness of fit of the torus (from the 2D positive and negative Gaussian fitting);
5. The ratio of the estimated uncertainties to the corresponding best-fit values for each of the free parameters.

The separation between the star and the AGPM provides a direct estimate of the quality of the centering during the observations. The S/N of the torus can indirectly provide comparable information: we find that when the S/N of the torus is high, the star is usually well-centered and the surface brightness is homogeneously distributed around the AGPM (in comparison with a misaligned case under same conditions). However, the value of the S/N is also affected by the weather conditions (e.g., clouds), decreasing the overall signal of the torus even if it is symmetric around the AGPM. The background level and the background noise level around the AGPM give us information about the strength of the speckles produced (e.g., their magnitudes and radial distribution), and as a consequence the quality of the AO correction. A poor AO correction usually generates many speckles, thus decreasing the contrast close to the AGPM. The ratio of the uncertainty to the estimated parameter serves as a filter to identify the frames where the fitting procedure was not successful. Other parameters, such as H, provide similar information and we note that their incorporation in the analysis does not necessarily improve the frame selection process (see Appendix 2.7.3). However, its use can be beneficial for the characterization of frames in instruments whose modeling of the torus can be very complicated or even when the torus is not clearly detected.

Our approach for the frame selection is shown in Fig. 2.7, for HD 34282, showing in the left panel the S/N of the torus as a function of the separation between the star and the AGPM positions along the X-axis. The right panel shows the separation between the star and the AGPM for both axes. For both panels, the points are color-coded according to the goodness of fit when modeling the torus with two 2D Gaussian profiles (i.e., the sum of the squared residuals within the 23 central pixels). The vertical cluster of points that appears on the left side of Figure 2.7 can be explained as follows. When the star is well aligned with respect to the AGPM, the S/N of the torus increases as the starlight is more homogeneously distributed around the AGPM. We find that in these cases the fitting process yields better results (smaller residuals). When the separation between the star and the AGPM increases, the S/N of the torus decreases leading to higher values for the residuals. Therefore, the resulting distribution, as shown in Fig. 2.7, shows a relatively wide ring of points, with low S/N values, as well as a narrower cluster of points with higher S/N values. However, the torus is also affected by the weather conditions and the AO performance. Even if the star is well centered behind the AGPM, if the observing conditions degraded, the S/N of the torus will also decrease. The resulting distribution is therefore a mix between well or poorly centered frames, all of them affected by the observing conditions and AO performance.

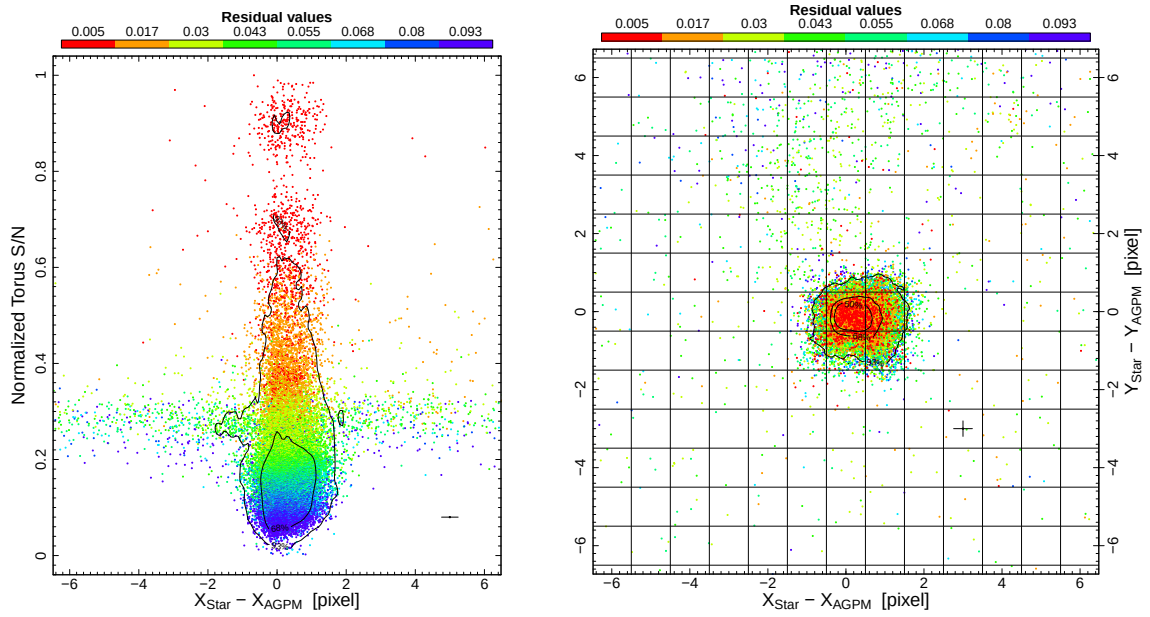

FIGURE 2.7: Examples of the distribution and registration of frames as a function of different parameters. *Left*: S/N of the torus as a function of the difference between the positions of the star and of the AGPM along the X-axis. *Right*: Relative position of the star with respect to the position of the AGPM. For both panels the star is HD 34282 and the color-coding corresponds to the goodness of fit. The crosses in both panels correspond to the typical uncertainties. The contours contain 93% and 68% of the data in the left panel, and 93%, 68%, and 50% of the data in the right panel.

In the left panel of Fig. 2.7 the horizontal plane formed around the normalized S/N value of 0.3 is most likely related to poor AO correction. When this happens during the observations the background level around the AGPM increases due to the stellar leakage, and more speckles appear close to the AGPM. The algorithm can then only poorly constrain the position of the star given the overall lower quality of the AO correction. It can even find the brightest speckle next to the AGPM as the best approximation for the star location (top right panel of Fig. 2.8). Therefore, the intensity of the torus is dominated by the stellar leakage background, which is much larger than for other frames as the stellar light is much more diluted and less affected by the AGPM obstruction. As a result, we observe this relatively constant level in the measured S/N when the AO correction is not working optimally. In these cases, we find that the speckles are randomly distributed in intensity and separation, and the fitting procedure finds separations up to several pixels between the location of the star and of the AGPM (instead of a fraction of a pixel).

The next step is to design the criteria that will be used for the frame selection. The goal is to select the most homogeneous frames of the sequence, the ones that share the most common features, which can then be removed using a principal component analysis (PCA), for instance. To this end, it is possible to reject the outliers in some of the distributions (e.g., star to AGPM separation, background level). This can be done by rejecting all the frames that are 5×MAD away from the median. In addition, it is also possible to fine-tune the acceptance level for the S/N of the torus. This can be done by rejecting the frames that comply with being less than $\phi \times MAD + \tau$, where τ is the median and MAD is the median absolute deviation for the S/N of the torus, while ϕ being a free parameter that can take values from $-\infty$ to $+\infty$, in principle. It is possible to also consider the ratio of the estimated uncertainty to the best-fit value for each of the parameters used when modeling the torus with the positive and negative

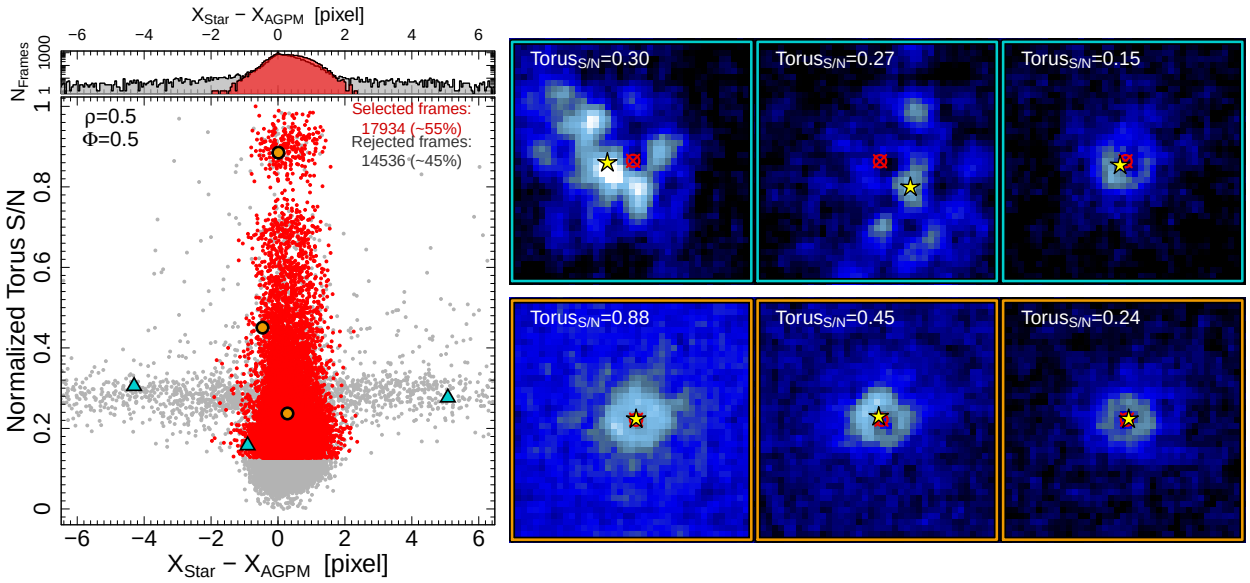

FIGURE 2.8: Examples of selected or rejected frames after applying our selection criteria. *Left*: Normalized $\text{Torus}_{\text{S/N}}$ as a function of the difference between the positions of the star and the AGPM along the X-axis. The color-coding corresponds to the frame selected using $\phi = 0.5$ and $\rho = 0.5$ (red dots) and rejected frames (gray dots). The orange circles correspond to three examples of frames selected and the cyan triangles to examples of rejected frames. The small panel at the top of shows the histogram of both distributions in logarithmic scale. *Right*: Three examples of rejected frames (top row) and selected frames (bottom row). The red crossed circles correspond to the position of the AGPM, while the yellow star gives the derived position of the star obtained from the negative and positive 2D Gaussian fitting. The color scale is the same for all six images.

Gaussians. For each frame, if the ratio is higher than ρ (being the second free parameter, with ρ between 0 and $+\infty$), then the frame is not considered in the rest of the analysis.

Figure 2.8 shows an example of the frame selection for HD 34282 using $\phi = 0.5$ and $\rho = 0.5$, keeping $\sim 55\%$ of the frames equivalent to 17 934 frames. The left panel shows the normalized $\text{Torus}_{\text{S/N}}$ as a function of the separation between the star and the AGPM location along the X-axis, with the red dots corresponding to the selected frames and the gray dots to the rejected ones. The histogram at the top of the left panel shows the distribution of the selected and rejected frames. The orange circles correspond to examples of selected frames, while the cyan triangles examples of rejected frames, and these examples are shown on the right side of the figure (bottom and top, respectively). The red crossed circles give the location of the AGPM, while the yellow stars are the estimated position of the star. As mentioned previously, the horizontal cloud of gray dots at 0.3 in $\text{Torus}_{\text{S/N}}$ corresponds to frames where the AO system was not working nominally.

For our frame selection method the most important parameter is ϕ as it directly relates to the percentage of frames that will later on be used in the PCA. Figure 2.9 shows an example of the number of selected frames as a function of ϕ for HD 34282. The parameter ρ helps us determine the fitted parameters that are poorly constrained and, according to Figure 2.9, it has a rather marginal effect on the number of frames selected. For this reason, we prefer to use $\rho = 0.5$ as reference value.

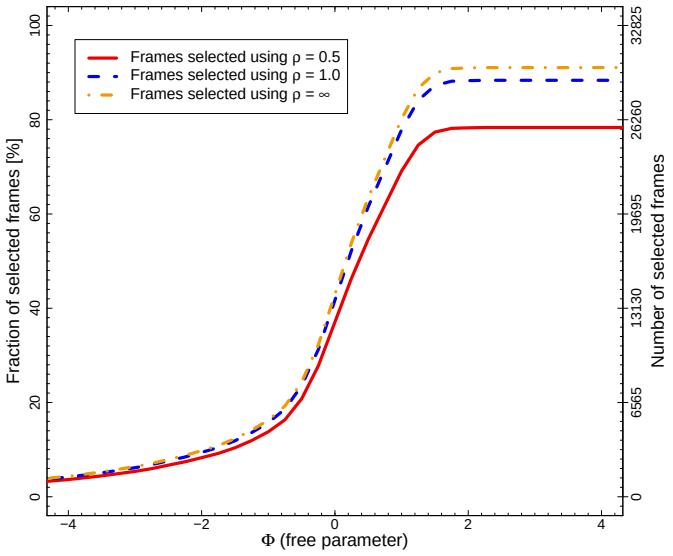

FIGURE 2.9: Percentage of selected frames as a function of the free parameter ϕ for HD 34282. The different lines show the behavior for three different values of ρ.

2.4 On-sky validation: Benchmarking the centering algorithm

In this section we present a test on the robustness of our method to recover the true position of the star behind the AGPM. Given that there is no direct and model-independent way to measure the true position of the star behind the AGPM for NaCo, the best way to validate our method is to use pair(s) of stars whose angular separations are known or measurable. Therefore, we analyze observations of a target with a bright nearby known companion. The central star is HD 104237 and its companion, HD 104237 B, which lies in the field of view of $\sim 3.29 \times 3.29''$(or 121×121 pixels), is detected in all the individual science and photometric frames. Using the photometric frames, in which the central star is $> 1.6''$ from the AGPM center and unsaturated, we are able to measure the separation and position angle of the companion with respect to HD 104237. We can therefore use this information later on to estimate the location of the central star in the science frames, correcting the position angle for changes in the parallactic angle.

The angular separation and the position angle are measured as follows. First, we fitted 2D Gaussian profiles to obtain the positions of both point sources in the reduced photometric frames. This was done by cropping the frames to smaller windows and centering them on both components. To avoid being biased by the Airy rings or being limited by low number statistics, we chose different sizes when cropping the images (10×10, 15×15, and 20×20 pixels) and calculated the mean weighted by the respective uncertainties. Then we measured the angular separation and position angle, propagating the estimated uncertainties on the final values. For each photometric integration we used the median stacked image over the 400 frames, calculating the median parallactic angle and its range as uncertainty. The photometric sequence is performed three times at the beginning and three times at the end of the observations, leading to six measurements for the angular separation and position angle. However, since the first sequence was observed with a poor AO correction (the stellar flux was completely diluted in the image), we discarded these bad-quality frames. We obtained the following results: 50.69 ± 0.20 pixels and $254.633 \pm 0.122°$ for

TABLE 2.2: Astrometric measurements of HD 104237 B.

	Grady et al. (2004)	This work
Obs. date	2003-06-10	2017-05-16
Position angle [°]	254.586 ± 0.350	255.027 ± 0.245
θ_0 [″]	1.365 ± 0.019	1.379 ± 0.007

Notes. The position angle and the angular separation (θ_0) were both measured with respect to HD 104237 A.

the separation and position angle, respectively. With a pixel scale of 27.212 ± 0.096 mas pixel^{-1} and a true north of $0.394 \pm 0.212°$ (see Launhardt et al. 2020b), the projected separation measured corresponds to $1.379'' \pm 0.007$ and position angle of $255.027 \pm 0.245°$.

HD 104237 (DX Cha) is an accreting Herbig Ae spectroscopic binary (A or AaAb, Böhm et al., 2004, Garcia et al., 2013) with a circumstellar disk. Four stars are surrounding HD 104237 A within 15″, labeled with letters from B to E (Feigelson et al. 2003), forming a kind of mini-cluster (Grady et al. 2004). The five sources (A-E) are confirmed members of the ϵ Cha association (Murphy et al. 2013), while HD 104237 A is the only early-type star of the association (3-5 Myr, Feigelson et al. 2003). Grady et al. (2004) reported that HD 104237 B ("source B" in Feigelson et al. 2003, or "star-2" in Grady et al. 2004), is a M 3-4 star with an angular separation of $1.365'' \pm 0.019$ and position angle of $254.586° \pm 0.350$ with respect to HD 104237 A (observing date 2003 June 10). Our measurements (ISPY observations, 2017 May 16) of position angle and angular separation (Table 2.2) both agree well within the uncertainties with the values presented in Grady et al. (2004).

The next step is to estimate the position of the star behind the AGPM, in a model-independent way, using the position of the companion. For each individual science frame we measure the location of the companion by fitting a 2D Gaussian profile. With the parallactic angle, the position angle, and the angular separation we can infer the true location of the star behind the coronagraph without any assumption about the reference center. We note that during the observing sequence, there were some technical problems and the observations had to be stopped. As a consequence, there is a jump in the sequence, leading to two separate distributions. In addition, the observations were executed under variable weather conditions (see Table 2.1).

To estimate the robustness of our method in finding the position of the star using the 2D negative and positive Gaussian profiles, we performed two different tests. The first consists of directly comparing the position of the close companion with the previously inferred position of the star and AGPM (see Section 2.3). The purpose of this test is to estimate the impact of using either the star position or the center of the AGPM as the center of rotation. We derotate each frame to align the position of the close companion to the north using both its position angle and the parallactic angle of the frame. This is done in two separate ways: (i) using the AGPM as the rotation center and (ii) using the stellar position derived in section 2.3.2 as the center of rotation. To center the 2D distribution around zero, we then compute the difference between the location of the companion and the location of the star (or AGPM) and subtract the angular separation of the companion measured in the photometric frames. Measuring the dispersion of the final density distribution allows us to test whether the center of rotation is the correct one. For this test we kept $\sim 93\%$ of the data as we only removed the frames for which we could not determine accurately the positions of the companion and of the star (uncertainties larger than 1 pixel). The results

are shown in Figure 2.10. The left panel shows the density contours when the derotation is performed centered on the modeled position of the star, while the right panel shows the results when centered on the position of the AGPM. The median absolute deviation correspond to 0.20 pixels for the X- and Y-axes using the star position as reference center. When using the AGPM as the reference center we measure dispersions of 0.22 and 0.27 pixels. If we assume that the chosen center is correct, we expect to obtain a distribution centered around zero with low dispersion. Since we derotated the companion to the north, dispersion on the X-axis is dominated by uncertainties on the parallactic and position angles, while the dispersion along the Y-axis is dominated by the uncertainty on the angular separation, as shown in the left panel of Figure 2.10 where the position of the star was used as the center. However, when the position of the AGPM is used as a reference center, the distribution is elongated along the Y-axis, suggesting that the angular separation between the AGPM and the companion varies. We therefore conclude that using the AGPM as the rotation center can introduce additional biases in the reduction process, while using the position of the science target leads to a smaller dispersion of 0.20 pixels.

The second test consists in directly comparing the true position of the central star (inferred from the position of the companion) with respect to the position of the star obtained with our method, without performing any derotation, and therefore without having to assume a center. Figure 2.11 shows the relative position of the central star using the two methods. The MAD corresponds to 0.21 and 0.19 pixels on the X- and Y-axis, respectively. Compared with the first test, the results strongly suggest that our method agrees well with the true position of the star within a dispersion of 0.20 pixel.

From both tests we can therefore conclude that our approach to finding the position of the star behind the AGPM agrees with the true position of the star estimated using its companion (within an uncertainty of 0.20 pixel), and to the same order of accuracy as second-generation instruments (e.g., SPHERE or GPI). Huby et al. (2015, 2017) demonstrated that there are some nonlinear effects when the star is close to the center of the coronagraph installed for Keck/NIRC2, which we do not take into account with our approach. These effects can introduce a slight shift or increase the dispersion in our measurements on the position of the star. However, we do not observe this effect for NaCo (see Figure 2.11), or at least it is not measurable considering our uncertainties.

2.5 Applications

Ultimately, the goal of performing frame selection is to try to improve the contrast in the innermost regions, increasing the probability of detecting faint point sources. To quantify the effects of our centering and the frame selection approaches, we studied two targets with known companions that are located at different projected separations from their host star.

2.5.1 Signal-to-noise ratio improvements

2.5.1.1 The case of β Pictoris b

β Pictoris is a young star that hosts a gas-bearing debris disk (Smith & Terrile, 1984b, Mouillet et al., 1997a; Dent et al., 2014). The star is located at a distance of 19.45 ± 0.05 pc (van Leeuwen, 2007a)

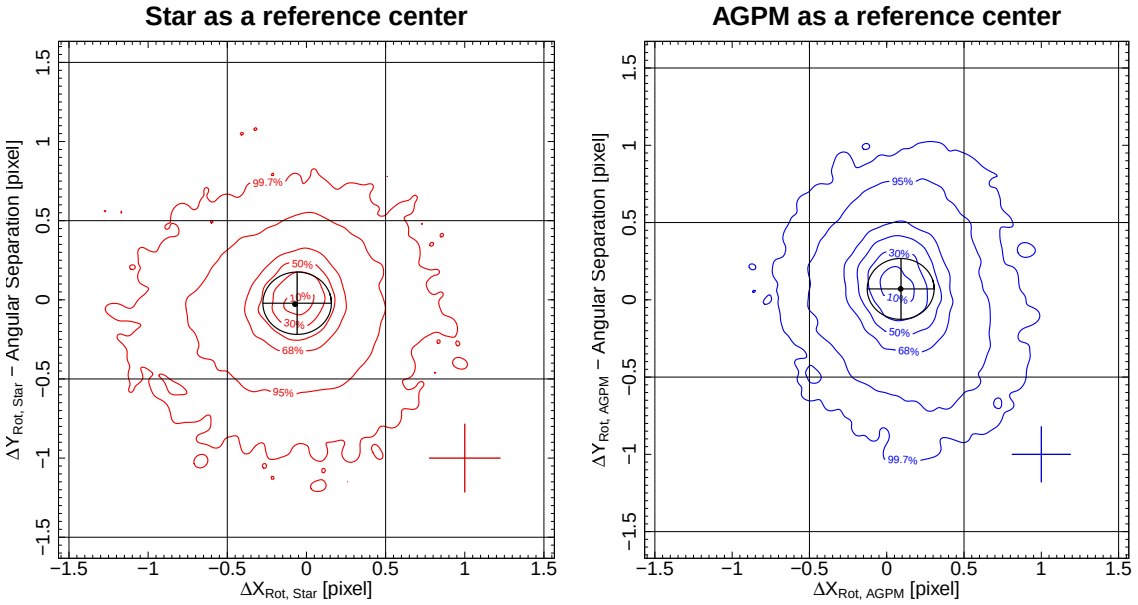

FIGURE 2.10: Density contours of the position of the close companion after derotating each frame by the parallactic angle and the position angle of the companion, and after subtracting its angular separation. The derotation is either done at the position of the star inferred from our modeling (left) or at the position of the AGPM (right). The black circle corresponds to the uncertainties on the angular separation and the position angle of the companion at the peak of the distribution. The grid shown in each panel represent pixels, and the colored crosses correspond to the typical uncertainty. The contour lines in each panel enclose the areas containing 99.7%, 95.5%, 68.5%, 50%, 30%, and 10% of the sample with respect to the maximum of the distribution.

and is a member of the β Pictoris moving group with an estimated age of 22 ± 6 Myr (Shkolnik et al., 2017). β Pictoris hosts at least one young giant planet, β Pictoris b, discovered in 2008 via direct imaging (Lagrange et al., 2010, 2009a). More recently the presence of another planet, β Pictoris c, has been suggested (Lagrange et al., 2019c). The planet β Pictoris b is located at $8.90^{+0.23}_{-0.41}$ au; it has a period of $20.29^{+0.86}_{-1.35}$ yrs (Lagrange et al., 2019b) and a mass of $9.3^{+2.6}_{-2.5}\,M_{\rm J}$ (see Brandt et al., 2021a, Snellen & Brown, 2018).

Observations with VLT/NaCo and the AGPM were carried out on 2013 February 01 (ESO program ID: 60.A – 9800(J)). They were first presented in Absil et al. (2013), and processed again in Stolker et al. (2019). The summary of the observations is presented in Table 2.1. It should be noted that the observations were performed under poor weather conditions, which gave us the opportunity to test the effect of frame selection and centering under less than ideal conditions.

The observations were reduced as described in Section 2.2, including our approach for the centering of the science frames. The frame selection is performed following the workflow presented in Section 2.3.3. We tried with different values of ϕ, from +1 to −1 in steps of 0.25. These values, combined with $\rho = 0.5$, provide us with a wide range of frame selection efficiency, from $\sim 9\%$ to $\sim 65\%$ of the total number of frames (34 277). With these cubes, as well as the complete dataset (i.e., without frame selection), we are able to compare our approach with other state-of-the-art post-processing techniques. In this case, we compare our results with those presented in Stolker et al. (2019). We worked with the same frames as in Stolker et al. (2019) to directly compare the effect of the centering on the final images. Stolker et al. (2019) performed a first frame selection where the frames with an unusually high background level

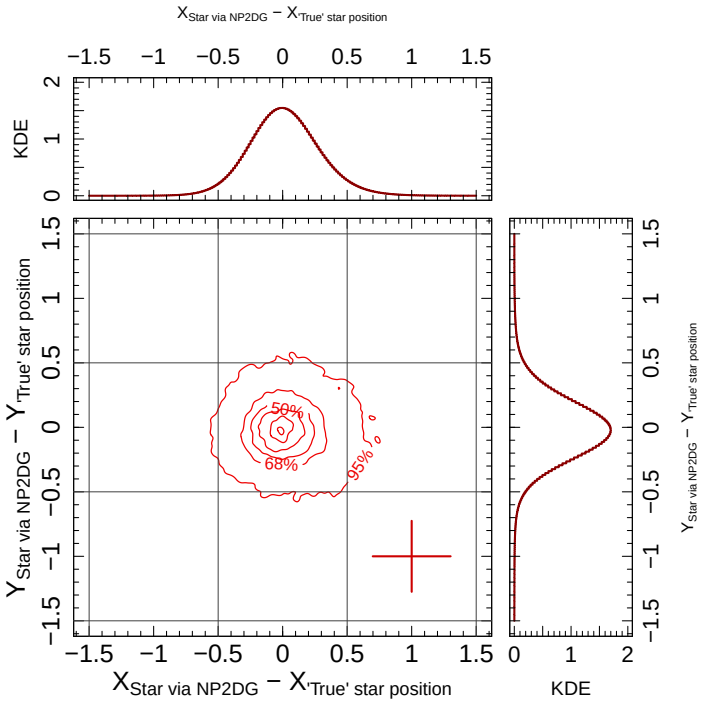

FIGURE 2.11: Comparison of the star positions derived from the close companion and those obtained by our fitting approach (negative and positive 2D Gaussian fitting labeled NP2DG in the figure). The small top and side panels show the kernel density estimators (KDE) for the X- and Y-axes, respectively. The grid represent pixels, and the colored cross corresponds to the typical uncertainty. The contour lines enclose the areas containing 95.5%, 68.5%, 50%, 30%, 10%, and 1% of the sample with respect to the maximum of the distribution.

were removed from the cube just before aligning the images. Consequently, we used 29 681 frames out of the original 34 277 to compare the effect of different centering techniques. In addition, we also used the entire sequence of 34 277 frames in order to compare the effect of rejecting those frames. In the rest of this work all images are cropped to 45×45 pixels.

For each cube of data we measured the S/N of β Pictoris b for a different number of principal components, ranging between 1 and 120 in steps of 1. The signal was measured using an aperture with a radius equal to the FWHM of the PSF measured on the photometric frame, and the noise was estimated using other apertures placed at the same distance to the center of the image. To compute the S/N of the point source, we used the `python` pipeline module called `FalsePositiveModule` from the `PynPoint` package (Amara & Quanz 2012b, Stolker et al. 2019), which accounts for low number statistics (Mawet et al., 2014). To better characterize the point-source in every reduced image, we fitted a 2D Gaussian profile to obtain the coordinates of the companion. With these coordinates, weighted by their respective uncertainties, we estimate the mean position to be used in the `PynPoint` routine.

When performing the principal component analysis we consider three cases for the centering of the science frames. We center them in the position of the AGPM (to later be derotated and stacked) using either the position of the AGPM or of the star as the center of rotation; we also center them at the position of the star for both the principal component analysis and the derotation and stacking processes. The S/N as a function of the number of principal components for the three centering strategies using the full and matched datacubes are presented in Figure 2.12. The same figure, but for the frame selection with four different selection criteria, is presented in Figure 2.13. It is worth noting that the sky subtraction for

the data presented in Stolker et al. (2019) was performed differently than in this work. They estimated the sky contribution using a principal components analysis while we use the sky frames that are closest in time to correct each science frame. Therefore, it is not surprising that the S/N curves show some differences for certain numbers of components used, while the overall trend remains the same.

The S/N estimation does not include an estimate of its uncertainty and the measure of the S/N may vary due to the fluctuation of the noise when removing the stellar PSF and combining the images together. To obtain a first-order estimate of this uncertainty, we first fit a polynomial of degree $N_{\rm degree}$ to the values of S/N as a function of the number of components. $N_{\rm degree}$ is fixed using the Bayesian information criterion (BIC, Schwarz, 1978). The BIC is a criterion for model selection among a finite set of models (in this case a family of polynomials of maximum degree 50), where the increased complexity of the model is penalized (i.e., models with a small number of free parameters are preferred). The model with the lowest BIC value is selected, and then we subtract the resulting polygon from the S/N curve, and measure the standard deviation as an uncertainty estimator from the residuals.

Overall, we find that for β Pictoris b we reach a better S/N (higher values) when the centering used for the principal component analysis is located at the AGPM position, followed by the derotation at the location of the star. This combination of centers for the entire sequence of frames provides the highest S/N, with an improvement of 19.5% ± 4.2% with respect to the analysis presented in Stolker et al. (2019). We note that if we compare the matched dataset (29 681 frames) to this combination of centers, we obtain a slightly higher S/N than presented in Stolker et al. (2019), but within the uncertainties.

Concerning the S/N when applying frame selection, we first note that the S/N agrees with the reduction presented in Stolker et al. (2019) with an increase in the S/N between 40 and 60 principal components. Except for values of ϕ of 1 and 0, and using only the star position in the post-processing analysis, overall we obtain significant improvements in the S/N of β Pictoris b. The best S/N values are 23 ± 1 when using only the star as a reference center, and 22.6 ± 0.6 when using the combination of AGPM and star positions as reference centers. However, considering the uncertainties, we conclude, and in agreement with the full dataset, that the combination of the AGPM and star positions provides the best reduction.

When we set the center for the principal component analysis at the location of the AGPM, we are aligning the torus and the speckles together in all frames. Therefore, the speckles and stellar PSF subtraction become more efficient and result in cleaner individual images. The improvements are most notable in the innermost regions, close to the AGPM, compared to regions that are less affected by speckles and the stellar PSF. This results in higher S/N values, and can also be seen when comparing the final images in Figure 2.14. We also note that selecting the location of the AGPM to perform the principal component analysis seems to reduce the self-subtraction effect around the companion, but we do not investigate this further in this study. Our approach to performing the derotation centered at the location of the star is justified by the fact that the rotational center of NaCo, when performing ADI observations, is the central star according to the manual of the instrument[6]. Derotating at a different location would lead to smearing effects on potential companions when mean- or median-stacking the dataset.

[6] According to Section 5.8, page 64 in the VLT/NACO User Manual Issue: 102

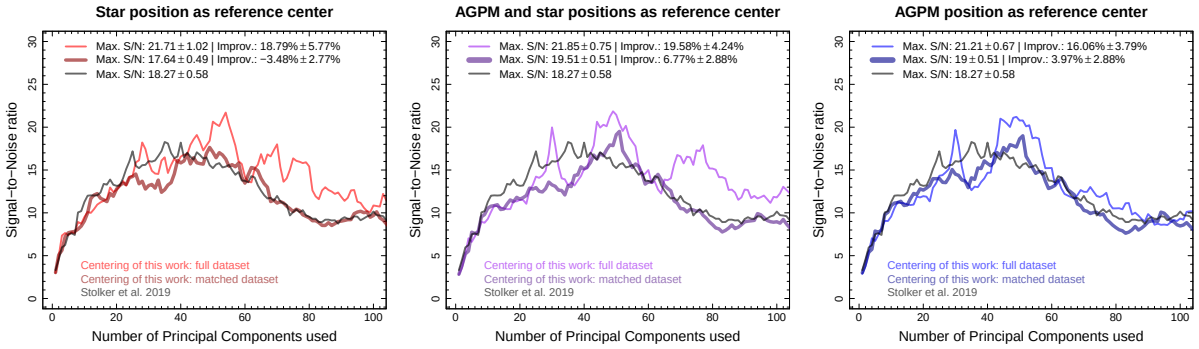

FIGURE 2.12: S/N of β Pictoris b as a function of the number of principal components used. The solid black line corresponds to the S/N from the data reduction presented in Stolker et al. (2019). The thin solid lines correspond to the full dataset, while the thick solid lines correspond to the same frames used in Stolker et al. (2019) (matched dataset), but both with our different centering options (depending on the panel). In the left panel the frames are processed using the star position as the reference center for the full analysis. The middle panel shows the results when using the AGPM position for the principal component analysis and the star position for the derotation and stacking of the frames. In the right panel the center is located at the position of the AGPM for the full analysis.

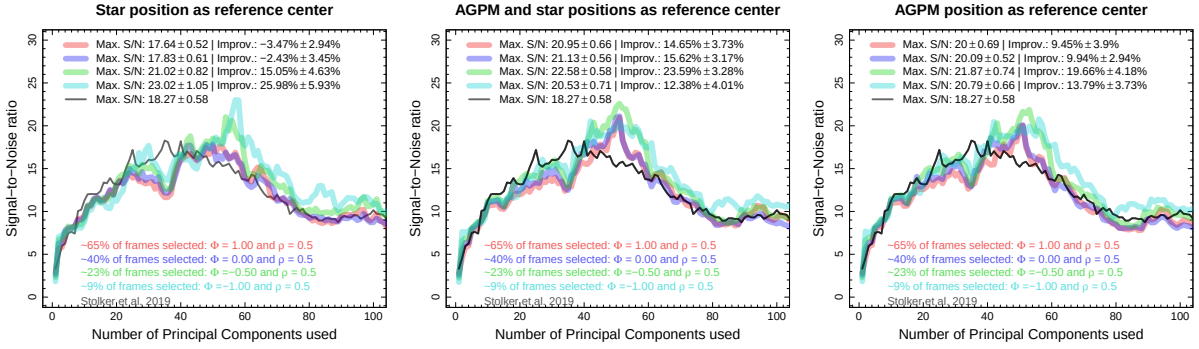

FIGURE 2.13: Similar to Figure 2.12, but here the thick transparent lines correspond to the reduction with frame selection using ϕ equal to 1 (red), 0.0 (blue), −0.5 (green), and −1.0 (cyan). For all the reductions, $\rho = 0.5$.

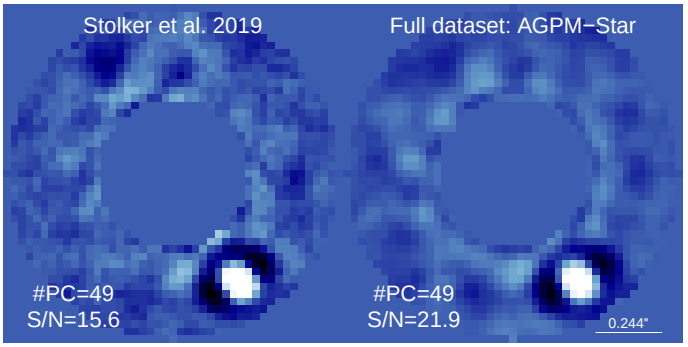

FIGURE 2.14: Final images of β Pictoris b using different approaches for the data processing. *Left*: Images of β Pictoris b using the reduction from Stolker et al. (2019), using 49 principal components. *Right*: Same as the left panel, but with our approach for the centering using the entire dataset, using the AGPM position for PCA, and using the star position for the derotation and stacking of the frames. The color scale is linear and is the same for both images.

2.5.1.2 The case of R CrA b

R Coronae Australis (R CrA - HIP 93449) is a HAeBe star, one of the brightest in the very young, compact, and obscured Coronet protostar cluster (Taylor & Storey, 1984). The star is at an early evolutionary stage and is still embedded in its dusty envelope (Kraus et al., 2009). There are some discrepancies in the estimation of the age, which varies between 0.3 to 3.1 Myr (e.g., Bibo et al., 1992, Forbrich et al., 2006, Meyer & Wilking, 2009, Sicilia-Aguilar et al., 2011). The distance to the Corona Australis region is estimated to 154 ± 4 pc in Dzib et al. (2018) using mean trigonometric parallax obtained from Gaia Collaboration et al. (2018). Cugno et al. (2019) and Mesa et al. (2019) identified a close companion in the R CrA envelope: R CrA b. Cugno et al. (2019) reported a mass for the companion in the range $0.10 - 0.63\,M_{\odot}$ at an angular separation of 196.8 ± 4.5 mas (using the first epoch of NaCo L' observations taken on 2017 May 19), while Mesa et al. (2019) estimated a mass of $0.29 \pm 0.08\,M_{\odot}$ with an angular separation of 184 ± 4 mas (using SPHERE observations, K1-K2 dual band imaging, 2018 August 16). In addition, Sissa et al. (2019) reported that the star is a spectroscopic binary, with masses for the primary and secondary of $3M_{\odot}$ and $2.3M_{\odot}$, respectively, and a period of ~ 60 days.

The target was observed as part of the ISPY program, and the observations were presented in Cugno et al. (2019). Here we used the first of the two epochs published in Cugno et al. (2019). It is important to note that the star saturated around the AGPM during the observing sequence (fully saturated at $\sim 19\,000$ counts, see Appendix 2.7.5). We reduced the observations and estimated the S/N the same way as for β Pictoris b. We used the same central mask to block the central region as in Cugno et al. (2019, $0\farcs05$ in radius), and the frames were cropped to the same size (39×39 pixels). Even though the target was observed under good weather conditions (see Table 2.1), we find that for at least half of the time the star is shifted toward a preferential direction with respect to the AGPM, which suggests rather poor centering (see Fig. 2.22 in Appendix 2.7.4, and Appendix 2.7.5 for examples of frames with different centering).

We produced cubes similar to those for β Pictoris, and we similarly considered three different centering strategies; using solely the AGPM, solely the star, or both as reference centers (see Section 2.5.1.1). For each centering strategy we produced datacubes for the full dataset, or for subsets after performing frame selection. The frame selection was performed using ϕ values between 1 and -1 in steps of 0.25. In the end, a total of 30 different cubes were built, in addition to the cube presented in Cugno et al. (2019) where the authors used a different centering strategy. We produced the final images using a number of principal components between 1 and 40 in steps of 1, for each datacube, since for large numbers of components self-subtraction can become important. Then the S/N of the companion was estimated for all the different reductions in the same way as described for β Pictoirs b in Section 2.5.1.1. In the end, we obtain 31 different S/N curves, one per datacube, and Figure 2.15 shows a selection of them for the full dataset and when performing frame selection (keeping $\sim 70\%$, $\sim 55\%$, and $\sim 47\%$ of all frames).

From Figure 2.15 we highlight that using the AGPM as the center for the entire process (right panel) yields the worst S/N curve, with a maximum S/N on the order of 10 whether we use frame selection or the full dataset (similar values were obtained by Cugno et al. 2019). In the other two cases (either using the position of the star only, or both the positions of the AGPM and of the star) we note significant improvements on the estimated S/N. For all the cases we find that the S/N is higher in the principal component range of 13 to 25. In particular, when we use both the AGPM and the star positions in the

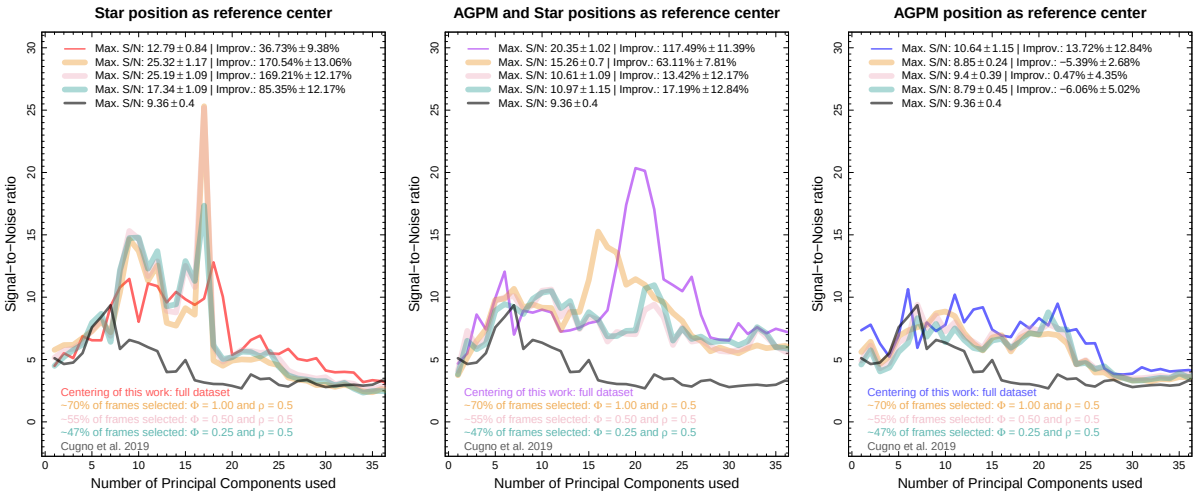

FIGURE 2.15: S/N of R CrA b as a function of the number of components used. The solid black line corresponds to the S/N from the data reduction presented in Cugno et al. (2019). The thin solid lines correspond to the full dataset. The thick transparent lines correspond to the reduction with frame selection using ϕ equal to 1 (orange), 0.5 (pink), and 0.25 (cyan). For all the reductions, $\rho = 0.5$. In the left panel the frames are processed using the star position as the reference center for the full analysis. The middle panel shows the results when using the AGPM position for the principal component analysis and the star position for the derotation and stacking of the frames. In the right panel the center is located at the position of the AGPM for the full analysis.

post-processing analysis, the peak broadens, reaching a maximum S/N of 20.3 when using the full dataset (middle panel of Fig. 2.15). This broadening of the peak suggests that not only is the noise lower, but also that self-subtraction effects become less significant as the number of principal components increases. In contrast, when using only the star as the center for the entire process, we find that the S/N of the companion is overall lower, suggesting that the PSF subtraction is less adequate in this case despite a narrow peak when using 17 principal components. Given the narrowness of this peak, the result should be taken with caution.

The negative patterns, due to self-subtraction effects, appear more symmetric when we use only the star position or both the star and AGPM positions as the center (see Figure 2.16 to compare the images with the best S/N). In Appendix 2.7.4 we show the distribution of relative positions between the star and the AGPM (for all the targets), and as mentioned above the distribution for R CrA is not centro-symmetric with respect to the position of the AGPM. If only the AGPM is used as the center of reference, for instance, the signal of the object might be more diluted in the final image, due to the choice of center for the derotation. For R CrA we conclude that this is the most critical point when post-processing the observations as it can significantly improve the results in the inner regions. Regarding the impact of frame selection, we find that overall the improvements are marginal at best for this specific target.

2.5.2 Effects on astrometric measurements

Astrometric measurements are critical for assessing the co-moving nature of candidate companions. The astrometric position as a function of time allows us to study the orbital motion of giant gaseous planets around their host stars, helping to better constrain their orbital parameters and masses (see, e.g., Wang et al. 2018, Nielsen et al. 2020, and Brandt et al. 2021a). For this reason, we attempt to quantify here

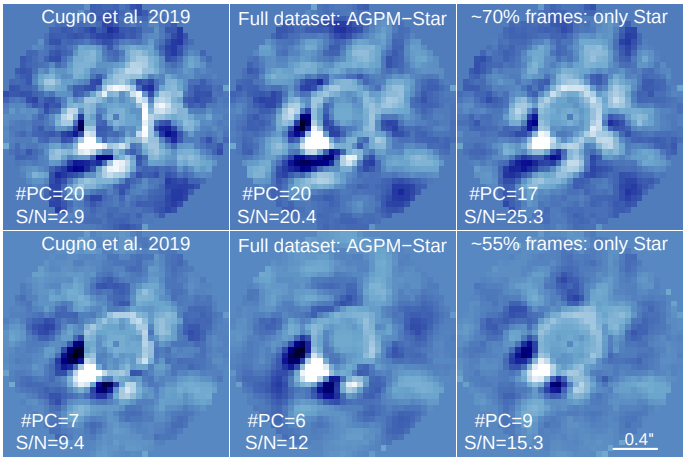

FIGURE 2.16: Final images with the highest S/N for R CrA b using different approaches for the data processing. *Top row*: Images using principal components from 13 to 35. *Bottom row*: Same as the top row but for principal components between 1 and 13. Shown are the best S/N for Cugno et al. (2019) (left), for the entire dataset using our centering approach with the combination of the AGPM and star positions (middle), and the frame selection using only the star position as reference center (right). The top and bottom rows have different color scales, but the subpanels in each row are consistent.

(at least to first order) the effect of the centering and the frame selection on the astrometry of point sources.

The positions of β Pictoris b and R CrA b can be obtained following different approaches. For example, the negative fake companion technique (Lagrange et al. 2010, Marois et al. 2010), which consists of injecting a negative signal at the approximate location of the source of interest in the frame sequence at each parallactic angle. The technique aims to cancel out the companion as much as possible in the final post-processed image and has been used for instance in Stolker et al. (2019) and Cugno et al. (2019) (see Sect. 3.5.2 of Stolker et al. 2019 for further information). There are other methods to determine the astrometric position of companions, for example using the ANgular Differential OptiMal Exoplanet Detection Algorithm (ANDROMEDA, Cantalloube et al. 2015b) or the Vortex Imaging Processing (VIP, Gomez Gonzalez et al. 2016), which have been applied in Biller et al. (2021),Jorquera et al. (2021), and Langlois et al. (2021b). However, all these methods require considerable computing power, proportional to the size of the field of view and the number of frames. In the case of NaCo we have $10\,000 - 30\,000$ frames per target, making these procedures very challenging to carry out. Stolker et al. (2019) and Cugno et al. (2019) addressed this problem by stacking several images together, reducing the number of frames from thousands to hundreds. When using frame selection, we remove frames that are not necessarily consecutive in time, which means we cannot easily stack the images in a similar manner; we therefore opted for the simpler approach of fitting 2D Gaussian profiles to the images.

For each dataset (β Pictoris and R CrA, with or without frame selection, different centering, or original reductions), we computed the final images using a different number of principal components (between 1 and 35 for R CrA, and between 1 and 120 for β Pictoris). For each image we then fitted a 2D Gaussian profile to find the location of the companion (see Appendix 2.7.6, figures 2.24 and 2.25 for the position of the companion as a function of the number of principal components for β Pictoris b and R CrA b, respectively). The free parameters are the amplitude, center, rotation angle, and width for both axes. For each dataset we then computed the mean value for the X and Y positions, weighted by their corresponding uncertainties. Residual speckles systematically affect the position of the companion in an image

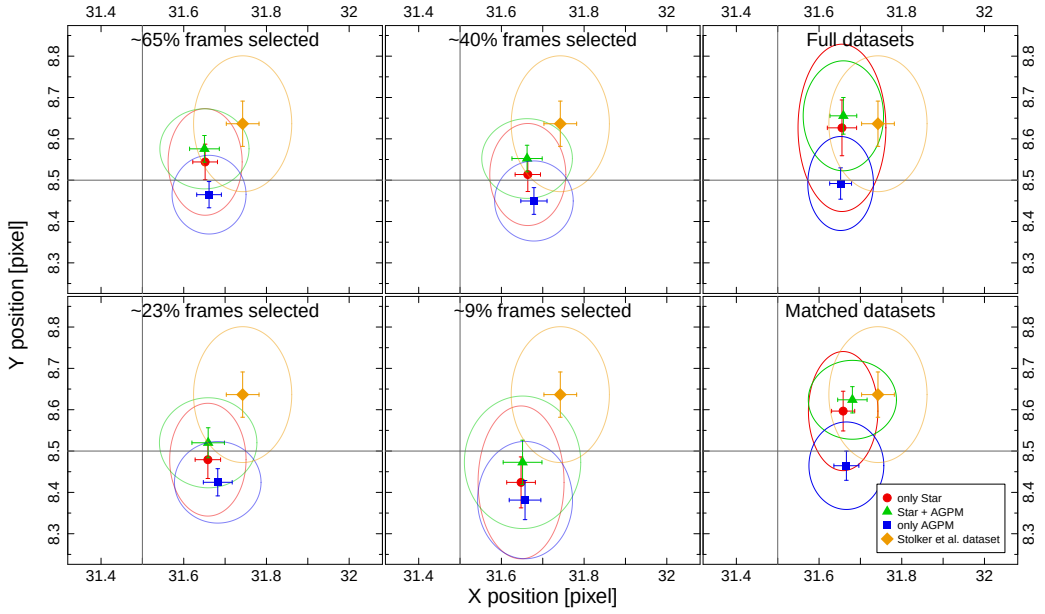

FIGURE 2.17: Position in the final image (45×45 pixels) of β Pictoris b. Each subpanel corresponds to a specific dataset (frame selections, full dataset, and matched dataset). The solid red circles correspond to the datasets that use the position of the star as the reference center, while the solid blue squares use only the AGPM, and the solid green triangles use both (star + AGPM). The orange diamond corresponds to the reduction of Stolker et al. (2019). The ellipses correspond to 3σ uncertainties, while the error bars 1σ uncertainties.

using a certain number of components. However, these residuals change while increasing the number of components used, affecting the observed position in a different manner. In this way we can obtain a better approximation of the position of the companion (least affected by this systematic) by calculating the median between all the positions obtained using a wide range of principal components.

Figures 2.17 and 2.18 show the results for β Pictoris b and R CrA b where we plot the results for different datasets. Despite small differences, the astrometry remains consistent for all the datasets on each companion (including the dataset from Stolker et al. 2019 and Cugno et al. 2019) at the 3σ level. The figures show that, overall, frame selection reduces in some cases the uncertainties on the astrometric measurements when compared to the reductions for the full datasets. For the astrometry of R CrA b, the dataset from Cugno et al. (2019) agrees better with our solution using only the AGPM. The same is observed when comparing the S/N where both follow the same trend (see Fig. 2.15). The astrometry uncertainties for R CrA b are larger than for β Pictoris b and, even though all the datasets are consistent with each other, differences of ~ 0.7 pixels are registered corresponding to the magnitude of the asymmetry on the distribution of the differences between star and AGPM positions. Overall, we do not observe significant differences in the final astrometry at the 3σ level. This is the case even without accounting for additional uncertainties, for example on the pixel scale (typically 27.2 ± 0.1 mas/pixel) or the true north (0.4 ± 0.2 deg.). We therefore conclude that the centering approach seems to primarily have an impact for the S/N of the detection, and can reduce the uncertainties associated with the astrometry, but marginally affects the astrometric measurements themselves.

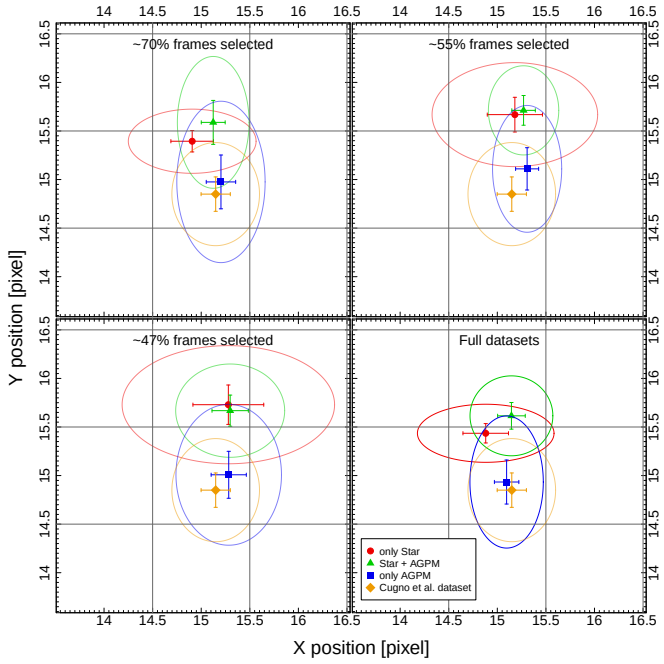

FIGURE 2.18: Similar to Fig. 2.17, but for R CrA b (compared with Cugno et al. 2019).

2.6 Summary and conclusions

In this paper we presented the new CenteR algorithm to improve the performance of coronagraphic NaCo observations at L' band. One of the fundamental challenges of such observations is to find the location of the star behind the coronagraph (AGPM). Our method makes use of the sky frames to determine the location of the AGPM in the science frames, thus alleviating the degeneracy when modeling the contributions from the central star and AGPM to infer the positions of either. The method described in this paper can be applied to any instrument for which the circular aperture of the coronagraphic mask is visible in all the frames and where the AGPM emits thermally. We also presented an in-depth analysis of the impact of frame selection when dealing with datasets containing tens of thousands of frames. Our approach is based on the modeling results of the star and AGPM and on the pseudo-Zernike moment decomposition of the sky-subtracted frames to select the most homogeneous images. We also investigated the impact of choosing different centers for the principal component analysis and the derotation of an angular differential imaging sequence. Our pipeline is tested on two different stars harboring known companions at short and intermediate separations (R CrA and β Pictoris). We also tested our pipeline on a star that hosts a bright circumstellar disk (HD 34282, see Appendix 2.7.7). However, the analysis of the disk and its detectability and S/N improvements is beyond the objectives of this article.

Using observations of a star with a bright nearby companion, HD 104237, we demonstrated that our approach can successfully recover the true position of the star behind the AGPM, with a ~ 0.20 pixel dispersion, even if the observing sequence is interrupted. Since our method provides the positions of the AGPM and of the star, we showed that performing the PCA centered at the location of the AGPM followed by the derotation at the location of the star yields better results compared to using only one single position (either the star or the AGPM). Performing PCA at the location of the AGPM removes the diffracted starlight and speckles more efficiently, but the derotation and stacking of the frames should

be performed centering at the location of the star to avoid smearing the flux from any nearby point sources. For NaCo the center of rotation coincides with the science target, so that no shifts have to be applied beforehand. We find that for point sources the flux is less smeared, yielding better detections and higher S/N values. Regarding the astrometry, we find that all the centering strategies are consistent with each other within 3σ, while the corresponding uncertainties are smaller when using both the star and the AGPM positions. We compared our reductions with published results, reduced with state-of-the-art pipelines, and found that we are able to improve the S/N of the detection of point sources around β Pictoris and R CrA by $24 \pm 3\,\%$ and $117 \pm 11\,\%$. This may also be related to the intrinsic quality of the centering during the observations. Our method yields higher S/N values when the star is poorly centered behind the AGPM and the distribution of the difference between the star and AGPM positions is not centro-symmetric. In contrast, our method reaches similar or slightly better S/N values when the distribution of the difference between the star and the AGPM positions is centro-symmetric.

To the best of our knowledge, this study is the most thorough investigation of the impact of frame selection for datasets consisting of thousands of images. We concluded that frame selection, at best, marginally improves the final reduction. We find that frame selection is most useful when either the observing conditions or the AO correction degraded during the observing sequence. The frames taken under such conditions would dilute the astrophysical signal, and removing them does help decrease the noise, especially in the innermost regions that are more likely to be dominated by speckles. Regarding the astrometry, we find that frame selection can slightly decrease the uncertainties depending on the centering strategy and the percentage of frames kept, but overall provide consistent solutions when compared with the full datasets. On the other hand, in cases for which the centering is poor and anisotropic (i.e., the star moved in a preferential direction during the observing sequence), the centering strategy using the full dataset can have an impact on the astrometry. R CrA is a clear example of this situation, where we estimated a possible bias in the position of about 0.7 pixels or $\sim$19 mas when using only the AGPM centering in the entire processing. Nonetheless, for this particular case, the different centering strategies implemented provide results that are consistent with each other within $3\,\sigma$.

There is a wealth of archival data obtained with an AGPM vector vortex coronagraph. First- and second-generation instruments that use an AGPM, such as VLT/NaCo (Rousset et al. 2003;Lenzen et al. 2003), LBT/LMIRCam (Skrutskie et al. 2010; Defrère et al. 2014) or Keck/NIRC2 (Vargas Catalán et al. 2016; Serabyn et al. 2017) and its previous and ongoing surveys (e.g., LEECH Skemer et al. 2014b; Stone et al. 2018b), may benefit from a reanalysis using the method described in this study. New generation instruments, VLT/ERIS or ELT/METIS among others, may benefit from the use of an AGPM and the centering method and techniques described in this study. Thanks to the improved centering of the whole dataset, our approach yields better results closer to the AGPM, in the typical range $10 - 50$ au from the star, where the population of giant planets is still poorly constrained.

2.7 Appendix of the article

2.7.1 Motion of the circular aperture as a function of time

Figure 2.19 shows the motion of the center of the circular aperture as a function of time for all four targets. The science frames (colored solid circles) and the sky frames (colored solid triangles) move on

the same random path as a function of time. Even with that random path the motion of the circular aperture in consecutive science-sky frames is less than 0.1 pixels.

2.7.2 AGPM: Circular aperture motion as a function of time

Figure 2.20 shows the difference between the AGPM position and the circular aperture center as a function of time for the X- and Y-axes. The relation shows small deviations of higher polynomial order than a constant behavior, but which are within the data uncertainties at the 2σ level. To avoid overfitting, we chose the simplest solution and adopted a constant value calculated from the mean weighted by the respective uncertainties. In addition, Figure 2.20 shows the calculated value for every target that provides the direct transformation between the center of the circular aperture and the AGPM position. In the case of HD 104237 we calculated two different transformations for each of the observing sequences (before and after the interruption). We further note that as the center of the AGPM is located near the center of the circular aperture, a possible rotation of the circular aperture in time (instead of a linear shift) will not have a strong impact on the differential motion between the circular aperture and the AGPM.

2.7.3 The effect of H in frame selection

The homogeneity parameter H is obtained using the reconstruction of pseudo-Zernike moments for the nonradial and azimuthal components (see Eq. 2.6 and Fig. 2.6). The reconstruction is a linear combination where the base corresponds to the pseudo-Zernike moments. For this reason, it is possible to consider the square root sum of the coefficients as a constant (e.g., normalizing the root square sum to 1). When the star is well centered behind the AGPM, the torus formed is mostly homogeneous, where the radial component dominates (larger values for $|m| = 0$ coefficients and therefore for $\text{Torus}_{\text{S/N}}$, see Eq. 2.7 and Fig. 2.6 left panel). When the star is misaligned with respect to the AGPM, the azimuthal components dominate in the reconstruction (higher values for $|m| = 1$ and 2 coefficients, lower H values, see Eq. 2.6 and Fig. 2.6 right panel). Then, H and $\text{Torus}_{\text{S/N}}$ are correlated with each other and both provide similar information. Figure 2.21 shows the normalized $\text{Torus}_{\text{S/N}}$ as a function of the star position with respect to the AGPM center along the X-axis in the left panel, and in the right panel the values for H with the same horizontal axis. The red dots correspond to the selected frames ($\sim 55\%$), the gray dots to the rejected ones ($\sim 45\%$), and the blue dots are the frames that, having been selected in the original frame selection (red dots), are excluded when we also consider the H parameter for the selection, using a cutoff value below 0.6. We note that both selection criteria are mutually consistent, with a 3.6% discrepancy (corresponding to $\sim 2\%$ of all the frames). The location of these blue dots in both graphics shows that both $\text{Torus}_{\text{S/N}}$ and H classify those frames as low-quality frames with respect to the other ones. Therefore, the incorporation of the H parameter does not have a strong impact on data processing since it provides information similar to and consistent with $\text{Torus}_{\text{S/N}}$.

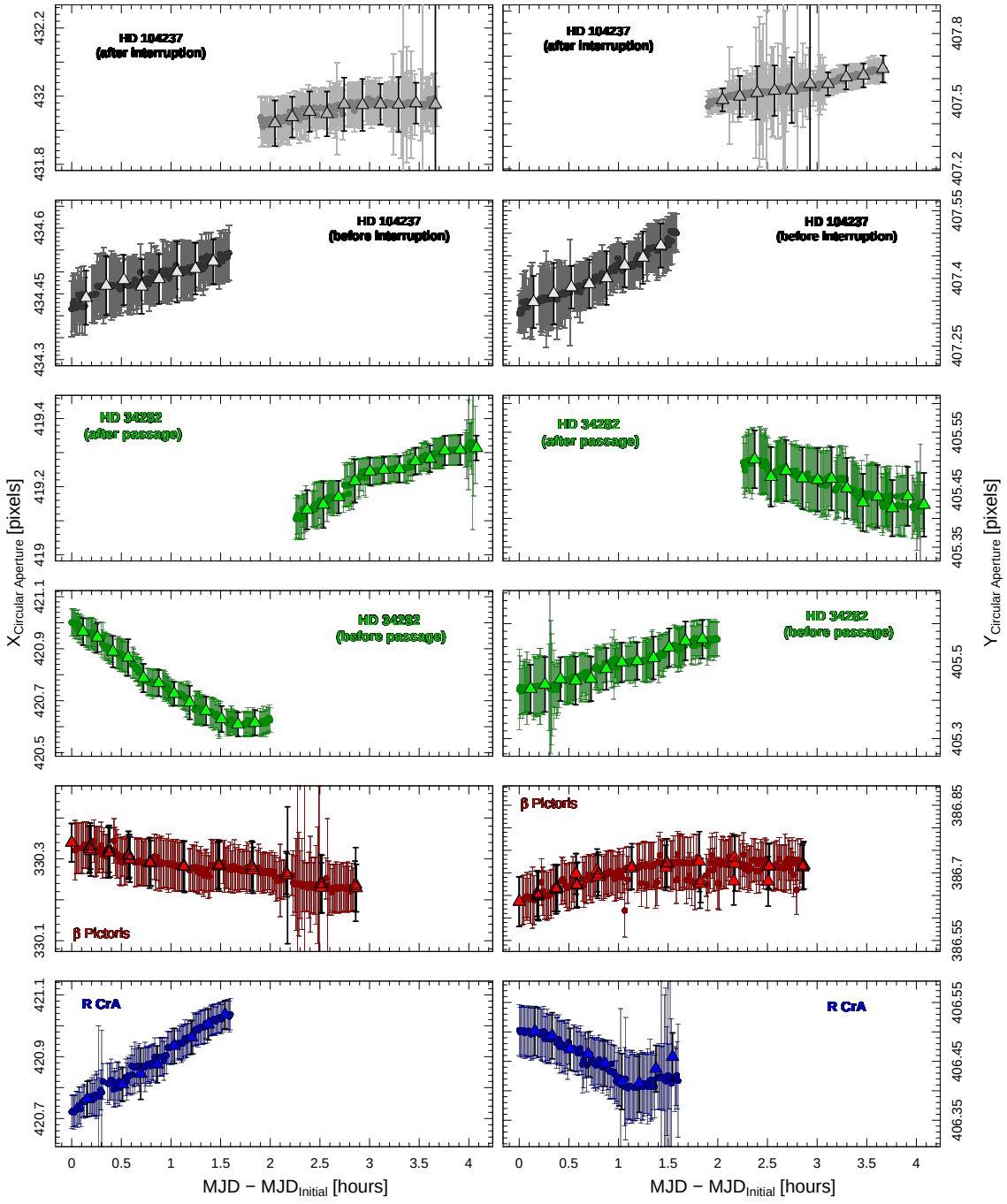

FIGURE 2.19: Motion in time of the circular aperture for the four stars studied in this work. *Left panel*: Position of the center of the circular aperture along the X-axis as a function of time for all four targets. If the sequence was interrupted (because of an instrumental problem or zenith avoidance region), each sequence is plotted in a different panel. The error bars correspond to the 1σ uncertainties. The colored solid circles correspond to science frames and the colored solid triangles to the sky frames. *Right panel*: Same as the left panel, but for the Y-axis.

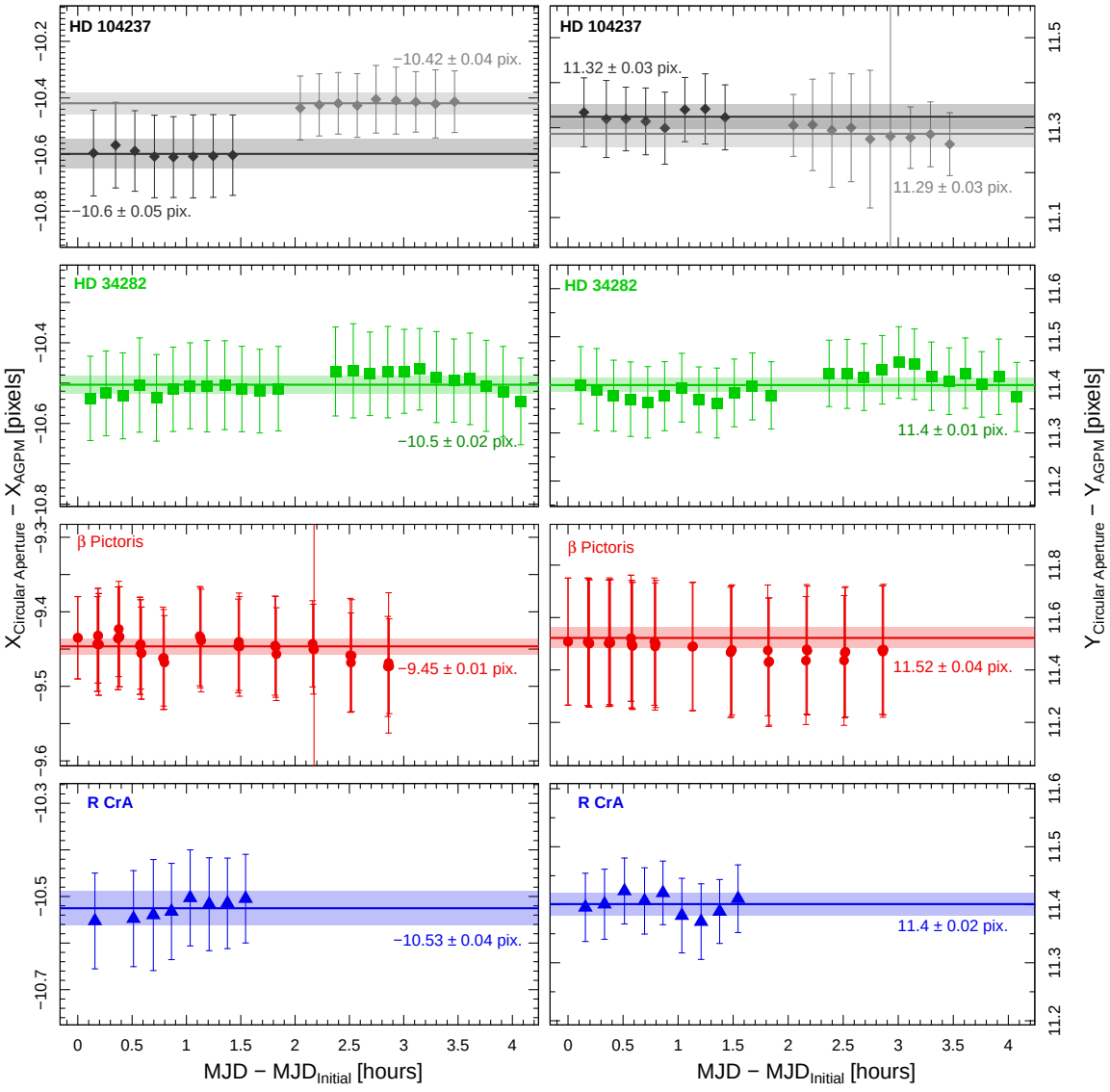

FIGURE 2.20: Differences between the position of the AGPM and the center of the circular aperture as a function of time (sky frames only), for the X- and Y-axis (left and right, respectively), for all four targets. The error bars shown represent the 1σ uncertainties. The solid horizontal lines correspond to the mean weighted by the uncertainties, and the colored areas correspond to the 1σ uncertainty.

2.7.4 Relative positions and torus S/N

The left panel of Fig. 2.22 shows the position of the stars with respect to the AGPM for all the sources. The right panel shows the de-normalized $\text{Torus}_{\text{S/N}}$ for a more direct comparison between all the observations at different weather conditions. In particular, R CrA shows a distribution that is not centro-symmetric. This implies that the choice of the center becomes more critical, affecting the S/N and the astrometric measurements of the companion. In contrast, β Pictoris shows a more uniform distribution (azimuthally homogeneous) where we do not observe significant differences in the results for the S/N and positions of the companion.

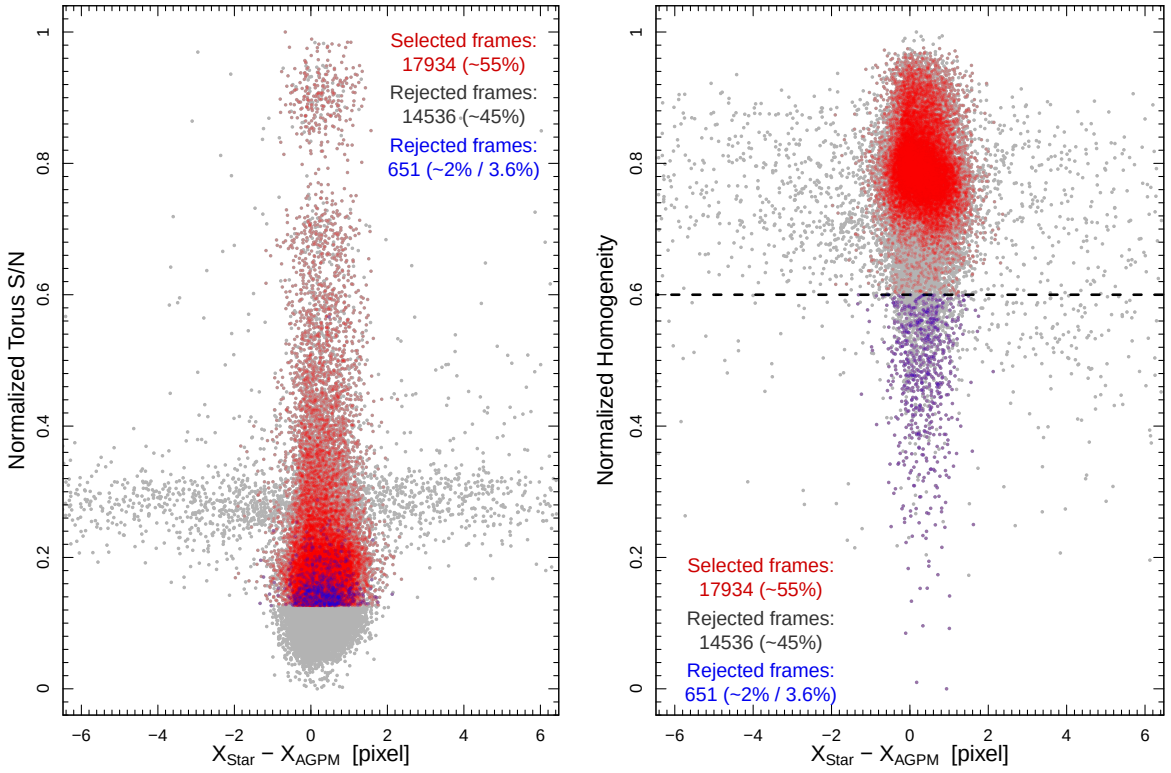

FIGURE 2.21: Example of registration and selection of frames with and without considering the H parameter for HD 34282. *Left:* $\text{Torus}_{\text{S/N}}$ as a function of the difference between the star position and AGPM center along the X axis. *Right:* H as a function of the difference between the star position and AGPM center along the X axis. The red dots correspond to the frame selection presented in this work, using $\phi = 0.5$ and $\rho = 0.5$ corresponding to $\sim 55\%$ of the frames, while the gray dots are the rejected frames. The blue dots are the additional rejected frames when H is also considered in the frame selection criterion. The number of blue dots corresponds to 3.6% and 2% of the first selection (red points) and the full dataset, respectively.

2.7.5 Frames of R CrA

Regions of the frames of R CrA are saturated, especially close to the AGPM in the entire observing sequence, resulting in a stronger signal of the torus and speckles around the AGPM. Figure 2.23 shows the distribution of the star position with respect to the center of the AGPM along both axes (top left panel) and with respect to the $\text{Torus}_{\text{S/N}}$ and homogeneity H (top right and bottom left panel, respectively). Examples of the different images at different separations are shown in the bottom right panel, corresponding to examples from good to poor centering (red triangles, green squares, and cyan circles, respectively). In this particular case, both $\text{Torus}_{\text{S/N}}$ and H are less informative in distinguishing between frames with good and poor centering. However, the distribution of the star position with respect to the AGPM is a more robust criterion to select the most homogeneous and well-centered frames.

2.7.6 Position of companions as a function of number of components

We made a 2D Gaussian fitting to each of the companions (β Pictoris b and R CrA b) to know their approximate positions in each of the post-processed images according to the number of components

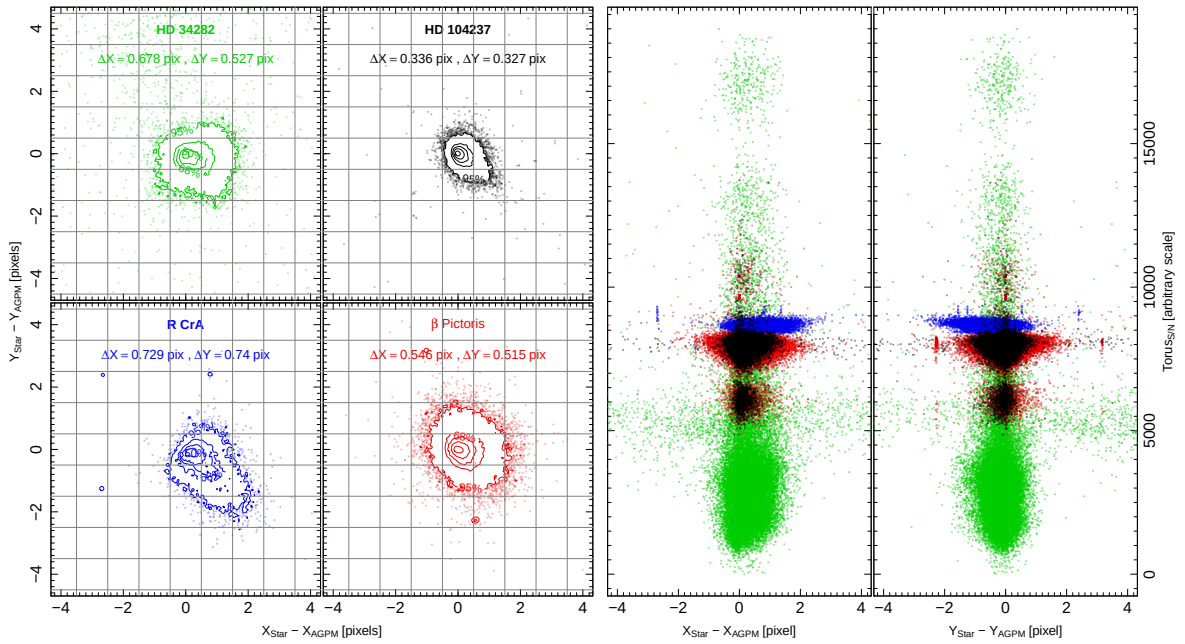

FIGURE 2.22: Distribution of the frame registration and density distribution of the relative positions for each star. *Left panel*: Distribution of the difference between the positions of the star and of the AGPM for all four stars included in this study. The ΔX and ΔY correspond to ∼ 1.5 times the median absolute deviation. *Right panel*: $\text{Torus}_{\text{S/N}}$ for all the targets in a common reference frame. The contours contain 10%, 30%, 50%, 68%, and 95% of the data.

used. Since this method of knowing the position of the object in question is very sensitive to residual speckles and then to the number of components used, we took all the images to calculate the weighted average by the uncertainties associated with each position. Figure 2.24 shows an example for β Pictoris b of the results of our fitting for the X- and Y-axis (solid points with their error bars), as well as the calculated average position and its associated uncertainty (horizontal solid line and the colored area, respectively), for the case of full datacubes. Figure 2.25 shows an example for R CrA b in the same format. These figures show the trend of the positions of each of the objects as a function of the number of components. It is noticeable that as the number of components increases, the associated uncertainty also increases due to the fact that there is less flux available for the fitting (effect of self-subtraction).

2.7.7 Extended sources

The advantage of using direct imaging, compared with polarimetric observations, is that it is possible to obtain the full intensity of extended structures. However, it is usually a challenge for angular differential imaging as it removes part of the flux and can introduce dark regions at the edges. In most cases the circumstellar disks are significantly removed in the final image especially for disk with inclinations lower than 60° (see Milli et al. 2012) as a disk with low inclination will be incorporated in the reference PSF to be subtracted. Different efforts have been put into addressing and solving this problem, either from the observations themselves (e.g., RDI, Smith & Terrile 1984b) or in post-processing techniques (see, e.g., LOCI, Lafrenière et al. 2007b). More recently, Ren et al. (2020, 2018) implement a new algorithm, the data imputation using sequential non-negative matrix factorization (DI-sNMF), which is a model-free solution in a post-detection disk scenario. Broadly speaking, the idea is to transform the signal

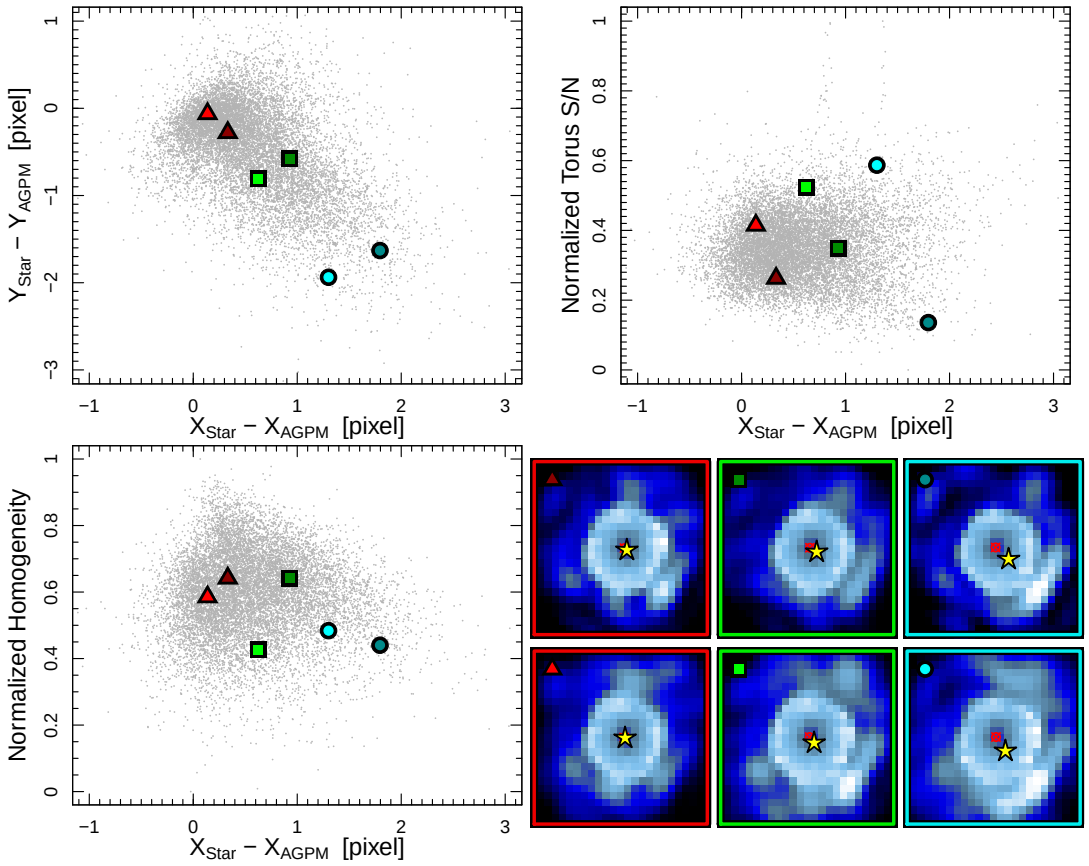

FIGURE 2.23: Frame registration for R CrA for six of the parameters used in the frame selection, and examples of frames with different centering. *Top left*: Distribution of the star position with respect to the AGPM center along both axes. *Top right*: $\text{Torus}_{\text{S/N}}$ as a function of the star position with respect to the AGPM center along the X-axis. *Bottom left*: Homogeneity H as a function of the star position with respect to the AGPM center along the X-axis *Bottom right*: Examples of images with good (red triangles), intermediate (green squares), and poor (cyan circles) centering. The yellow stars correspond to the star position, while the red crossed circles give the AGPM position. The images have the same color scale.

(disk or point sources) into a missing data problem, assigning to that region the PSF signal (following the statistical properties). Then it should be possible to remove both the stellar PSF and the speckles in every image, avoiding problems of self-subtraction. However, none of these studies investigate the effect of the centering or frame selection on the properties of the resulting disk image (signal, structure, self-subtraction), and detectability (e.g., noise distribution, significance of the detection).

We study here the impact of both the centering and frame selection when the target shows extended emission in its vicinity. From the previous sections, we know that the centering has a significant impact on the results for point sources, but the effect of frame selection is marginal. However, frame selection may improve the speckle suppression in the case of disks. If we keep the most homogeneous, well-centered frames, we should be able to decrease the number of components needed, overall decreasing the contribution of residual speckles in the inner regions. Furthermore, by removing the frames with a poor quality (poor centering or weather conditions) the contrast should improve in the inner regions where the disk is located. We tested our reduction strategy on the HAeBe star HD 34282. The star is located at a distance of 359 ± 5 pc (Gaia Collaboration et al., 2018), with an age of $6.41^{+1.92}_{-2.58}$ Myr (Merín et al., 2004). The disk was first resolved with ALMA observations (van der Plas et al., 2017), and first imaged

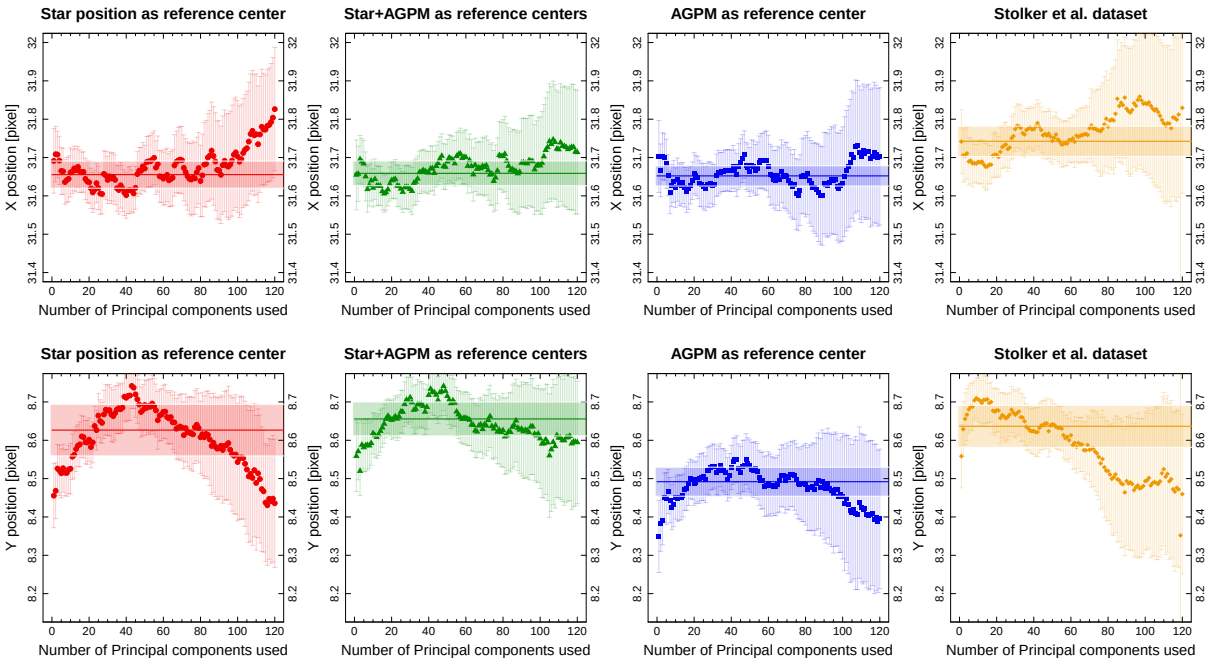

FIGURE 2.24: Each panel shows the position for X (top panels) and Y (bottom panels) using our 2D Gaussian fitting for β Pictoris b. From left to right, the center used for our reduced data correspond to: only the star, the star and the AGPM, only the AGPM, and at the end the dataset from Stolker et al. (2019). The solid horizontal line corresponds to the weighted mean by the respective uncertainties (the vertical line in each solid point), with the respective associated uncertainty (colored horizontal area).

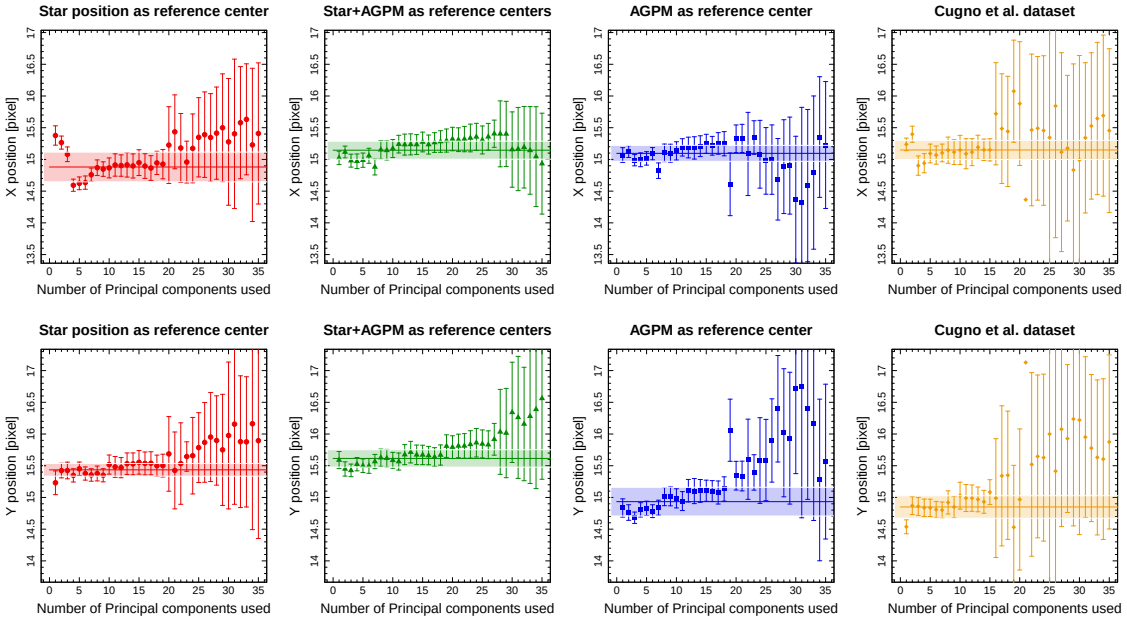

FIGURE 2.25: Same as Fig. 2.24, but for R CrA b.

at infrared wavelengths by Launhardt et al. (2020b) as part of the ISPY program using VLT/NaCo, and by de Boer et al. (2021) as part of the DISK program in polarimetric mode at near-infrared using VLT/SPHERE. The reduction is performed in the same way as for the previous targets in this paper. The details related to the observations are summarized in Table 2.1. We performed the frame selection using ϕ and ρ as 0.5, keeping $\sim 50\,\%$ of the 32 825 available frames.

Figure 2.26 shows reduction examples for three different centering configurations (top to bottom), using 18 principal components. From left to right, we show the final images when using the full dataset, with our frame selection, and a control reduction, selecting at random the same number of frames as for the middle column. Quantifying the S/N for extended emission is more difficult than for a point source; therefore, we just compare the images visually, paying special attention to the noise level and to self-subtraction effects. For instance, when using the full dataset the dark pattern caused by self-subtraction is quite significant, along with spots toward the east. In contrast, the reduction using frame selection shows a better removal of several speckles, consequently the structure of the disk is overall better recovered. This can be explained by the presence of a significant number of poorly centered frames in the entire dataset, which increases the noise in the innermost regions and dilutes the faint signal from the disk.

When performing frame selection we may remove a significant number of frames, and we therefore introduce gaps in the sequence of frames. These gaps correlate with the observing condition or the AO performance. As a consequence, we most likely remove series of consecutive frames, which may act as a protection angle[7] (see LOCI, Lafrenière et al. 2007b), therefore decreasing the effect of self-subtraction. To understand whether the result presented in Figure 2.26 (middle panel) is due to the frame selection or the result of a nonhomogeneous sampling in time, we carried out the following test. First, from the cube with frame selection (using $\phi = 0.5$ and $\rho = 0.5$), we counted the number and sizes of the gaps introduced in the sequence. We then cloned this distribution to obtain a new sample of gaps, which we could randomly introduce in the entire dataset. This new subsample had the same number of frames as the previous one. The result is shown in Figure 2.26 (right column). Overall, the signal from the disk appears fainter, the western side seems to be more disconnected from the trace of the disk, and the speckles on the eastern side are still visible, while they had disappeared when using our frame selection approach. This result strongly suggests that our strategy to perform frame selection does improve the final reduction, and that it is not solely related to the sampling of frames as a function of time. We also note that, in agreement with the previous section, using only the AGPM position as the reference center does not yield the best final image. Without a proper quantification of the S/N of the disk, it remains difficult to estimate which of the other centering strategies provides the best reduction.

[7]The protection angle consists of removing some of the adjacent frames in the time series. For the ith frame in the sequence, only the frames for which the paralactic rotation is larger than $\Delta\theta$ are used to build the reference, where $\Delta\theta$ depends on the angular size of the PSF at a specific separation from the center. The selected frames are used in the ADI, and this approach minimizes the effect of self-subtraction.

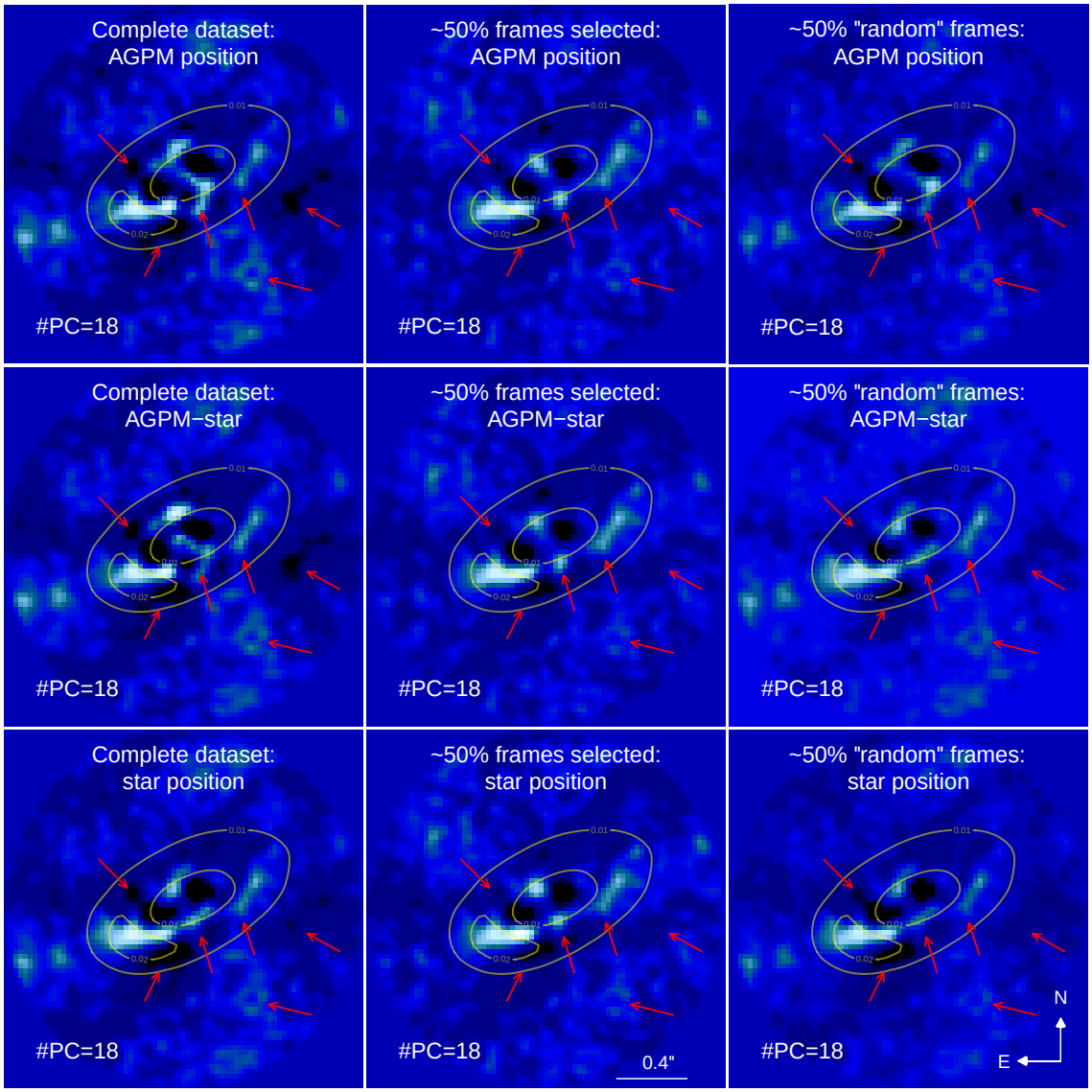

FIGURE 2.26: Comparison of the final images for the disk around HD 34282 using 18 principal components for the full dataset, frame selection, and random selection of frames. *Left panel*: Final images using the entire dataset, but implementing three different centers: the AGPM position only, both the AGPM and the star positions, and only the star position. *Middle panel*: Same as the previous panel, but with frame selection, using $\sim$ 50% of the data. *Right panel*: Same as the middle panel but with a random selection of frames (see text for details). Red arrows indicate the most noticeable lingering shadows and speckles, as well as the most notable disk features. The yellow contours correspond to the continuous image of the observations made with ALMA (van der Plas et al. 2017), and correspond to 10 and 20 mJy levels.

Chapter 3

Searching for planets in systems with signs of planet-disk interactions

This chapter is based on a paper in preparation (Godoy et al. in prep.), which has already been sent to collaborators (in its early version) and reviewed by some of them. This paper is planned to be published in early 2023.

3.1 Introduction

Since the detection of the first extrasolar planet around a sun-like star (Mayor & Queloz 1995b), substantial progress has been made in the past decades on our understanding of planet formation. Two robust theories have emerged, the core accretion and disk instability scenarios (see Drazkowska et al. 2022 for a recent review). Core accretion (Pollack et al. 1996) explains the formation of planets as a bottom-up scenario. The small particles in the protoplanetary disk grow over time, forming embryos that later on will eventually become planets. Disk instabilities (Boss 1997; Mayer et al. 2002) on the contrary, can rather be understood as a top-down scenario. These instabilities trigger clumps formation that will collapse forming a planet in a way very similar to star formation. Both scenarios predict a very different kind of planetary population. For example, core accretion predicts more planets of intermediate and low masses concentrated at distances below 10 au. While disk instability predicts more massive planets concentrated at larger separations.

The already large sample of known extrasolar planets (about 5600 and 200 candidates[1]), is key to better characterize formation models. However, this planet population is quite biased due to the different detection techniques used. The direct imaging technique is the one with the lowest detection rate (e.g., **?**), however it gives us access to a planet population that is otherwise difficult, if not impossible, to observe with other techniques. With direct imaging it is possible to characterize these planets by observing the light coming from the planet itself through different filters. The data obtained with, for example, integral field units and narrow and broad-band filters can be used with evolutionary models

[1] According to http://exoplanet.eu/

to obtain, for example, the planetary mass (e.g., Samland et al. 2017). In addition, it is possible to constrain the orbital parameters of the planet (over several years) which can provide dynamical masses (e.g., Zurlo et al. 2022). This population of cold giant planets at wide orbital separation is crucial to challenge the different planet population theories (e.g., Nielsen et al. 2019a, Vigan et al. 2021a), and they are of great importance for planetary formation as a whole.

During the last decade, numerous surveys have been carried out with the goal of detecting this population of cold gas giants (e.g., SPHERE-SHINE, Desidera et al. 2021a, Langlois et al. 2021b, Vigan et al. 2021a; Gemini-GPIES, Nielsen et al. 2019a; SPOTS, Asensio-Torres et al. 2018, Bonavita et al. 2016; SCExAO/CHARIS HGCA survey, Currie et al. 2020; NaCo-ISPY, Launhardt et al. 2020a). The selection criteria are usually based on the properties of the stars themselves rather than on possible indicators of the presence of planets (e.g., SHINE, Desidera et al. 2021a). Most of the surveys are focusing on the following stellar properties: age, distance, and to some extent spectral types. Age is key in searching for giant planets since they are more luminous at early stages. For this reason young association and star-forming regions are often part of the samples (e.g., β Pic, Tucana, Columba, Argus, among others). Also, young moving groups are also included since their members share the same kinematics and, therefore, they come from the same parent cloud and share similar ages. The distance is important since we want to observe the inner regions close to the star. This is why a cutoff is usually set at 160 pc to achieve reasonable spatial resolution (e.g.,Launhardt et al. 2020a). The spectral type is taken into account because there could be a correlation in which more massive stars harbor more giant planets (e.g., Nielsen et al. 2019a).

Other dedicated surveys made use of complementary features that could serve as tracers of planetary formation. For example, the presence of double-belt in debris disks (Matthews et al. 2018), the presence of sub-structures in disks observed in scattering light (Asensio-Torres et al. 2021), the presence of ring and gaps in planet-forming disks (Jorquera et al. 2021), among others. In addition, the new era of Gaia (Gaia-2016) provides us with unprecedented astrometry, which is revolutionizing the way in which we can build samples. A clear example is the proper motion anomaly (Brandt 2018; Kervella et al. 2019; Fontanive et al. 2019; Brandt 2021), which gives us information about possible unseen companions. However, this new information has only became available very recently, but will most likely be a key feature for upcoming new large surveys.

In this paper, we present a different approach for sample selection. We based our selection on the characteristics of the debris disks that surround the stars, which can be interpreted as hints of planet-disk interactions. We incorporated different diagnostics such as warm debris, falling evaporating bodies, exozodiacal dust grains, and planet-induced stirring. These interaction mechanisms have been observed and studied in other systems with known planets. A clear example of this is β Pictoris. The presence of a massive planet was predicted to explain the warp of the inner disk (Mouillet et al. 1997b). Years later, this hypothesis was confirmed after the discovery of β Pic b with direct imaging (Lagrange et al. 2009b). Furthermore, the strong exocometary activity of β Pic can be attributed to its giant planet (e.g., Tobin et al. 2019). The HR 8799 system is known to harbor 4 giant planets (Marois et al. 2008b) and two debris belts (e.g., Su et al. 2009). The hot belt component was studied with simulations, concluding that the disk is truncated and the dust production happens in the outer part of the belt, both attributable to the presence of HR 8799e (Contro et al. 2016). In addition, the characteristics of the outer disk (cold belt) cannot be explained only with a self-stirred evolutionary model, suggesting that the outer planets

interact with the planetesimals in the disk (Krivov & Booth 2018). The planet around HD 4113 could be responsible for the hot exozodi dust in the system. The planet interacts with the outer belt (reservoir of planetesimals) sending them towards the inner region where their sublimate later on (Absil et al. 2021). In short, the different perturbations (warm disk component, exozodi, exocometary activity) could be attributed to the presence of one or more giant planet(s) and can therefore be used as criteria for the sample selection.

In this paper, we first explain each selection criteria and the final sample in Section 3.2. We discuss the observational strategy and data reduction in Section 3.3. In Section 3.4 we present the sources that we identified, analyze the color-magnitude diagrams and proper motions, to better constrain their natures. We discuss the predictions from the theoretical counterpart and the limits imposed by the observations in Section 3.5. We then estimate the possible and most likely planetary mass if it should exist in the system (outside our detection capabilities) also in Section 3.5. Finally, we summarize and conclude our findings in Section 3.6.

3.2 Selection sample

We here present a sample of 21 stars hosting debris disks, around which we searched for giant planets. The stars were selected using four different criteria, all of them related to the properties of the disks. Out of the four selection criteria, two are related to directly constrainable properties of the disk, and the other two to hints that suggest that additional instabilities (other than secular evolution) may be or have been at play in the evolution of these disks.

3.2.1 Warm and stirring samples

The first half of the sample was drawn from a curated list of 301 debris disks, all of them having been observed with the *Spitzer*/IRS instrument (Houck et al. 2004; Werner et al. 2004). Literature search yielded an original list of $\sim$ 500 systems, out of which 301 were retained as they show significant infrared (IR) excess in their IRS spectra (3σ excess above the photospheric model at wavelengths larger than 20 μm). This list was designed circa 2014-2015 and we gathered far-IR photometric points from *Spitzer*/MIPS (Werner et al. 2004; Rieke et al. 2004) and *Herschel*/PACS (Poglitsch et al. 2010; Pilbratt et al. 2010). For this sample, we originally used distances coming from the Hipparcos catalog (van Leeuwen 2007b). The stellar parameters ($T_{\rm eff}$, log$g$) were estimated using VOSA (Bayo et al. 2008). The stellar radii were estimated using the distances and the dilution factor, and a rough estimate of the stellar mass was derived from the radii and log$g$, assuming the stars have reached the main sequence and are no longer contracting.

With the stellar parameters determined, the first sub-sample of "warm debris disks" was selected. We inspected the residuals between the IRS spectrum and the stellar model (examples shown in Fig. 3.1), focusing on the region around 10 μm. As mentioned in Ballering et al. (2014), the detection of an emission feature in this wavelength range is indicative of warm μm-sized dust grains (see Henning 2010 for a review and Olofsson et al. 2012 for extreme examples) in the innermost regions, at a few au from the central

star. Since the presence of an inner disk can be the signpost of one or more planets in the system, we identified 5 interesting candidates.

The second sub-sample, the "stirring" one, was designed based on the results of the spectral energy distribution (SED) modeling. The IR excess was fitted following an approach similar to the one presented in Olofsson et al. (2016). Briefly, after subtracting the photospheric model to the observations, we computed the thermal emission of a series of 20 concentric "shells" (the emission being optically thin, the geometry of the disk is not relevant) between $r_{\rm in}$ and $r_{\rm out}$. Each cell has the same grain size distribution between $s_{\rm min}$ and $s_{\rm max}$ following a differential power-law form, $\mathrm{d}n(s) \propto s^{-3.5}\mathrm{d}s$ (Dohnanyi 1969). The optical constant for the dust grains are the astro-silicates from Draine (2003), and for each grain size, in each cell, we computed the thermal equilibrium temperature by equating the energy received and emitted by the dust grain (see App. A of Olofsson et al. 2016 for more details). We then integrated the total thermal emission for each individual shell, and iterated over the 20 shells, to find the one that can best match the IR excess. Starting from the innermost shell, we find the best scaling factor that minimizes the residuals (since the emission is optically thin, we can scale the flux up or down) and compute the goodness of fit for this first shell. We then iterated in a similar fashion for the remaining 19 shells, and the best fit solution is the one with the smallest χ^2, thus providing a radial distance of the disk. There is a known degeneracy between the radial distance r of the disk and the minimum grain size $s_{\rm min}$ and to circumvent this issue, we set $s_{\rm min}$ to the radiation pressure blow-out size (since smaller particles should be set on unbound orbits and quickly removed from the system). While this approach makes some crude (but not necessarily unrealistic) assumptions about the distribution of the dust grains (a narrow range of distances r) it allows for a fast modeling of the SED, well suited for a large sample.

Kenyon & Bromley (2008) proposed a model for the evolution of a debris disk, in the absence of additional external perturbers. Such a model, also revisited in Krivov & Booth (2018), suggests that the evolution of a disk should be an inside-out process, as the dynamical timescales are shorter the closer to the star. Therefore, one might expect a possible relationship between the radius of the disk and its age, with a dependency on the initial mass of the disk. By comparing the radius of the disk to the stellar age, we can identify outliers that cannot be easily explained by this so-called "self-stirring" model. Those outliers most likely need additional perturbations to explain the radius of their disks, and giant planets are good candidates for this source of additional stirring of the planetesimals.

We used the membership to moving groups and young associations to gather the stellar ages for part of our sample, those ages being the most reliable ones. This was further motivated by the fact that members of such groups are usually young ($\leq 100\,$Myr old), which is the ideal age range to search for giant planets with direct imaging. We then used the results of the SED modeling and identified systems for which the radius of the disk is larger than expected for the age of the star, even if the disk was initially very massive. We identified seven targets and we will refer to this sub-sample as the "stirring" sample.

However, since the database was built and the fitting of the SEDs performed, there has been several Gaia Data Releases, and the distances of all the stars in the sample have been revised. The distances have an impact on the stellar radii and masses, and therefore on the value of $s_{\rm min}$ set by the radiation pressure. Consequently, in this paper, we updated the stellar masses based on Kervella et al. (2019, 2022) as well as revised the modeling of the SED for the stars that were originally selected. We followed the same

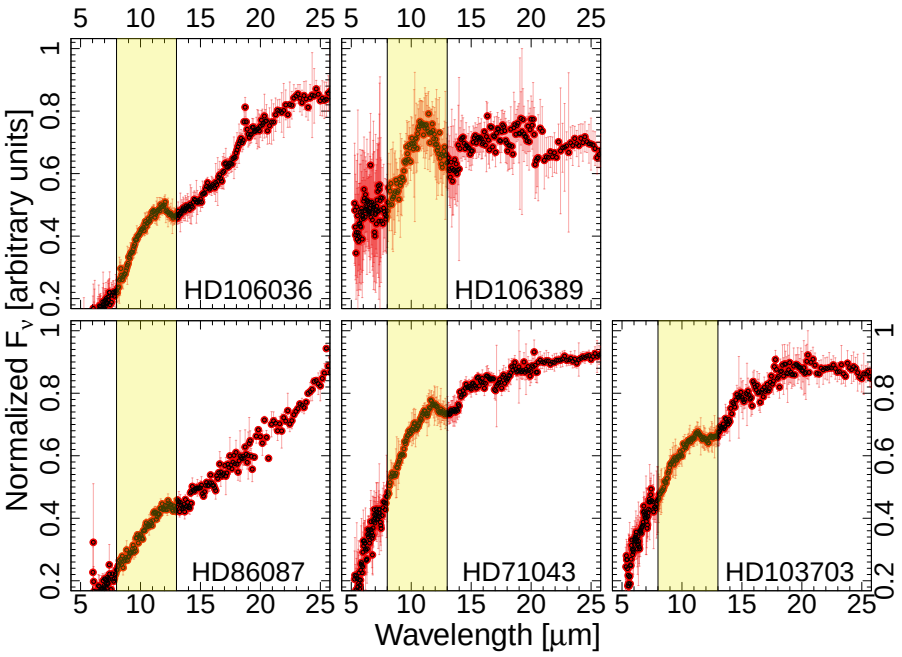

FIGURE 3.1: The "warm debris disks" sample, in which the residual spectrum between the IRS spectrum and the best stellar model as a function of wavelength is plotted for each target. Red dots are the IRS residual spectrum, and the red bars are the related uncertainties. The yellow region highlights the $\sim 10\mu m$ emission feature, indicative of warm small dust grains.

modeling approach as the one discussed above, but we additionally modeled the SEDs using a Planck function with a single temperature to reproduce the IR excess (similarly to e.g., Pearce et al. 2022).

Figure 3.2 shows the expected stirring timescale from Kenyon & Bromley (2008) and Krivov & Booth (2018) for the stirring sample. We used equations 34 from Kenyon & Bromley (2008, filled light red area) and 33 from Krivov & Booth (2018, filled red area) to highlight the expected evolution of the disk ring. We adopted the same default values for the density of the grain, the maximum size of the planetesimals, and we used three values for the mass scaling factor $x_{\rm m}$ of 1, 3, and 10 (solid, dashed, and dotted lines, respectively). However, we have used $x_{\rm m}$ of 1 and 3 for our selection since they better reflect what is expected for a "normal" disk. The stellar masses were taken from Table 3.2. We used our results from the SED modeling for the disk location (from now on, a_{SED}) using conservatively 30% of the value as uncertainty from Table 3.2, and the ages from Table 3.1 to show the disk location in the Figure 3.2 (gray rectangle).

3.2.2 FEB and exozodi samples

The second part of our sample was selected based on possible signs of planet-disk interactions, such as falling evaporating bodies (FEBs) and exozodiacal dust (exozodi hereafter). FEBs are related to exocometary activity and are interpreted as debris/material falling towards the star (Beust & Morbidelli 2000). It is thought that such exocometary activity is due to instabilities in the main reservoir of the debris disk. A possible cause for such instabilities could be the presence of a larger body like a planetesimal or a planet disturbing the disk. For instance, β Pictoris is a clear example of intense exocometary activity (e.g., Kiefer et al. 2014, Tobin et al. 2019) possibly triggered by the presence of, at least, one massive

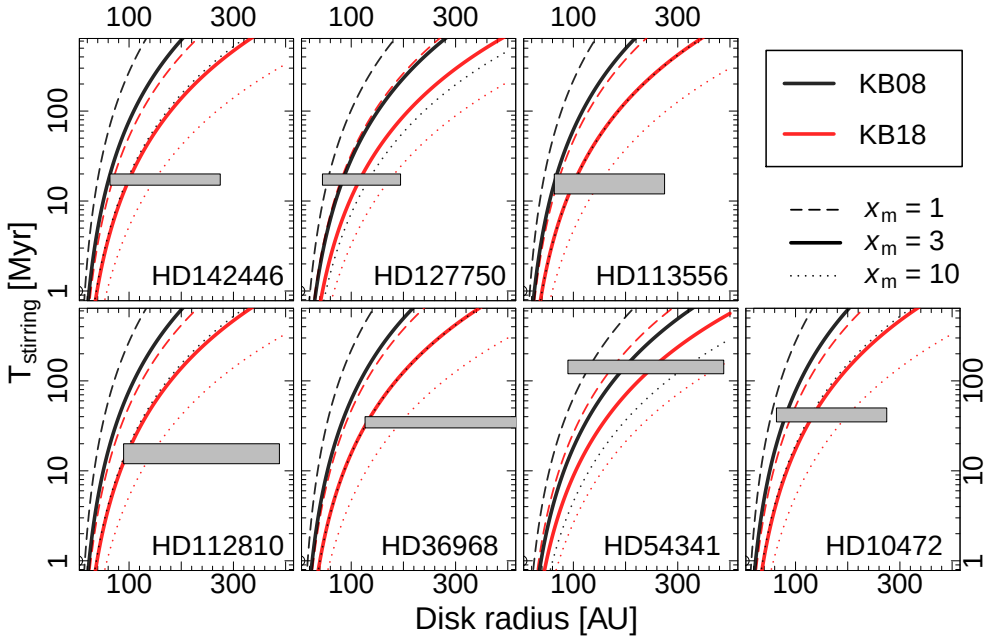

FIGURE 3.2: Expected stirring timescale as a function of semi-major axis for the "stirring" sample. Red and black lines correspond to the models from (Kenyon & Bromley, 2008, KB08) and (Krivov & Booth, 2018, KB18), respectively. The solid, dashed, and dotted lines correspond to three different values for the scaling of the initial mass of a protoplanetary disc progenitor $x_{\rm m}$ (1, 3, and 10, respectively). The grey rectangles mark the debris disk location and expected width on the x-axis and the age of the system and uncertainties on the y-axis.

planet (β Pic b, Lagrange et al. 2009a). We recompiled the stars with FEBs activity from Kiefer et al. (2014), Iglesias et al. (2018, which was based on the same original sample of 301 debris disks as in this study), and Rebollido et al. (2018), leading to four stars that have been observed by our team ("FEBs" sample), out of the 20 that are part of this sample.

The term exozodi is used to refer to warm and hot dust ($T > 300\,\mathrm{K}$) orbiting a star, in the innermost regions. Warm exozodi are typically detected at mid-IR wavelengths ($\sim 10\,\mu\mathrm{m}$), while hot exozodi are detected at near-IR wavelengths (H and K bands, usually using an interferometer). Fomalhaut is an excellent example of a system composed of both kind of exozodi: a hot belt ($\sim 200\,\mathrm{K}$) dominated by submicron-sized grains located at short distances ($\sim 0.2\,\mathrm{au}$), and warm dust ($\sim 400\,\mathrm{K}$), dominated by micron-sized grains at $\sim 2\,\mathrm{au}$ (see Lebreton et al. 2013). Explaining the survival of exozodi at different ages remains a challenge since the lifetime of the dust is of about a few hundred years. Kral et al. 2017 summarized different possible mechanisms that help to either increase the lifetime of the particles (e.g., magnetic fields, trapping with gas), or quickly replenish the material that is expelled (e.g., dynamical instabilities, eccentric planets, scattered material by planets, comets). The systems part of our "exozodi" sample were compiled from Ertel et al. (2014), and correspond to two objects already observed from the original list of 14 targets of our sample.

3.2.3 Main properties of the sample

In summary, all of the 19 stars in this sample share the following features: they harbor a debris disk (or circumstellar dust of some sort), and some of their properties (warm dust, distance of the disk, FEBs,

or exozodi) strongly suggest the presence of at least one massive perturber. We therefore observed them using the *Spectro-Polarimetric High-contrast Exoplanet REsearch* instrument (SPHERE, Beuzit et al. 2019), knowing that all the stars have high to moderate proper motions and $R < 13$ mag, in order to properly discriminate the companion nature of any possible candidate point sources.

Tables 3.1 and 3.2 summarize the main properties of the stars in our sample. As previously mentioned, parallaxes are compiled from Gaia DR3 (Gaia Collaboration et al. 2016; Gaia Collaboration et al. 2021a; Gaia Collaboration et al. 2021b). The proper motion anomalies were obtained following Kervella et al. (2022). The stellar masses and radius are obtained also following Kervella et al. 2022 (see also Kervella et al. 2019). The radial distances ($a_{\rm SED}$) of the debris disks to their host star come from our SED modeling. Note that due to the degeneracies in the modeling approach, we assumed a 30% uncertainty for $a_{\rm SED}$.

3.3 From observations to data products

3.3.1 Observational strategy

We performed observations with the SPHERE planet-finding instrument mounted at the VLT. The observational strategy consists of placing the star under a coronagraph and using the Angular Differential Imaging technique during the integration (ADI, Marois et al. 2006). ADI takes advantage of the natural rotation of the sky to suppress, in post-processing, the stellar point spread function (PSF) and the speckles produced within the optical path. The combination of using ADI and a coronograph yields an exquisite contrast of 13-14 magnitudes at angular separations typically of 0.5″. We used the IRDIFS and IRDIFS_ext observing modes which split the light into two subsystems: a differential imager and spectrograph (IRDIS, Dohlen et al. 2008), and an integral field spectrometer (IFS, Claudi et al. 2008). We used IRDIS in both dual-band and broad-band imaging (Vigan et al. 2010; Dohlen et al. 2008), with the H23 (λ_{cen}=1.5859μm, $\Delta\lambda_{Weff}$=0.0533μm, and λ_{cen}=1.6660μm, $\Delta\lambda_{Weff}$=0.0561μm), K12 (λ_{cen}=2.1029μm, $\Delta\lambda_{Weff}$=0.1009μm, and λ_{cen}=2.2554μm, $\Delta\lambda_{Weff}$=0.1100μm) filter pairs, and H filter (λ_{cen}=1.6259μm, $\Delta\lambda_{Weff}$=0.286.1μm). The IFS observations were done in the YJ mode, which spans the range 0.95-1.35 μm and has 39 wavelength channels (Mesa et al. 2015). Plate scale are typically 12.250 ± 0.004, 12.258 ± 0.004 and 12.246 ± 0.009 mas/pixel for H2, K1, and H respectively (see Maire et al. 2021 and table 3.4).

The typical observing sequence is as follows: flux frames, centering, science observations, centering, flux frames, and lastly sky thermal emission. The flux frames correspond to unsaturated stellar PSF outside the coronagraph (usually using a neutral density filter to avoid saturation and non-linear regime), which is later on used for the flux calibration. During the centering step the star is put behind the coronagraph, and the deformable mirror is shaped so that satellite spots are created. Those spots can then be used to precisely estimate the location where the star is behind the coronagraph. The centering step is repeated at the end of the observing sequence to monitor whether the star drifted during the observations. The science observation consists of 32 to 2048 frames per target with individual exposure times (DIT) of 0.8 to 64 seconds. Finally, the sky is observed at the very end of the sequence to remove its thermal emission from the science frames. Table 3.4 shows a summary of the observing conditions, filters, exposure times, and the number of frames per target.

TABLE 3.1: Summary of target properties.

Name	RA [hh:mm:ss]	DEC [dd:mm:ss]	Distance [parsec]	μ_α [mas/yr]	μ_δ [mas/yr]	Sp. type	Selection criteria	Age [Myr]	Association	Ref.
HD112810	12:59:59.93	-50:23:21.20	133.7 ± 0.3	-29.403 ± 0.013	-12.367 ± 0.013	F3/5IV/V	Stirring	16 [12-20]	LCC	1
HD36968	05:33:23.93	-39:27:02.20	148.6 ± 0.3	-7.582 ± 0.013	16.515 ± 0.014	F2V	Stirring	35 [30-40]	Octans	2
HD54341	07:06:20.99	-43:36:36.90	101.5 ± 0.9	4.64 ± 0.09	12.91 ± 0.111	A0V	Stirring	185 [120-170]	-	3
HD10472	01:40:24.49	-60:59:53.90	71.3 ± 0.1	60.882 ± 0.017	-10.275 ± 0.017	F2IV/V	Stirring	45 [35-50]	Tuc-Hor	1
HD142446	15:56:05.59	-36:53:34.30	135.6 ± 0.4	-18.835 ± 0.023	-26.6 ± 0.017	F3V	Stirring	17 [15-20]	UCL	1
HD127750	14:34:37.31	-46:17:34.70	144.4 ± 0.7	-21.811 ± 0.036	-21.501 ± 0.032	A0V	Stirring	17 [15-20]	UCL	1
HD113556	13:05:32.62	-58:32:06.00	100.5 ± 0.2	-39.615 ± 0.016	-16.628 ± 0.019	F2V	Stirring	16 [12-20]	LCC	1
HD86087	09:54:51.03	-50:14:37.10	99.2 ± 0.4	-37.034 ± 0.041	6.859 ± 0.046	A0V	Warm debris	237 [40%]	Field	4
HD71043	08:22:55.41	-52:07:22.90	72.1 ± 0.2	-22.862 ± 0.034	19.588 ± 0.039	A0V	Warm debirs	45 [35-50]	Tuc-Hor	1
HD103703	11:56:26.66	-58:49:14.00	107.2 ± 0.2	-36.276 ± 0.017	-8.444 ± 0.019	F3V	Warm debris	16 [12-20]	LCC	1
HD106036	12:12:10.21	-63:27:13.00	99.8 ± 0.2	-40.782 ± 0.021	-9.974 ± 0.023	A2V	Warm debris	16 [12-20]	LCC	1
HD106389	12:14:28.25	-47:36:42.00	146.0 ± 0.7	-28.119 ± 0.028	-8.373 ± 0.023	F6IV	Warm debris	16 [12-20]	LCC	1
HD36546	05:33:30.76	24:37:43.73	100.2 ± 0.4	7.508 ± 0.041	-41.305 ± 0.029	B8	FEBs	6.5 [3-10]	TA	5
HD56537	07:18:05.58	16:32:25.39	30.7 ± 0.2	-46.157 ± 0.199	-36.007 ± 0.183	A4IV	FEBs	638 [50%]	-	6
HD37306	05:37:08.77	-11:46:31.85	69.6 ± 0.2	20.094 ± 0.033	-22.918 ± 0.031	A1V	FEBs	45 [35-50]	Tuc-Hor	1
HD38678	05:46:57.34	-14:49:19.02	22.3 ± 0.1	-14.203 ± 0.198	-0.776 ± 0.206	A2IV-V(n)	NA	350 [19-500]	-	1
HD80007	09:13:11.98	-69:43:01.95	34.7 ± 0.1	-156.47 ± 0.14	108.95 ± 0.11	A1III	FEBs	324 [50%]	-	6
HD2262	00:26:12.20	-43:40:47.40	24.0 ± 0.1	106.394 ± 0.126	32.491 ± 0.132	A5IVn	Exozodi	578 [50%]	-	6
HD102647	11:49:03.58	14:34:19.41	11.0 ± 0.1	-497.68 ± 0.87	-114.67 ± 0.44	A3Va	Exozodi	50 [40-70]	Argus	1

Notes. The astrometric parameters are from Gaia DR3 (Gaia Collaboration et al. 2016; Gaia Collaboration et al. 2021a). Literature references for ages (column Ref.) are as follows. 1: Desidera et al. (2021b). 2: Ujjwal et al. (2020). 3: Meshkat et al. (2017). 4: David & Hillenbrand (2015). 5:Lisse et al. (2017). 6: Nielsen et al. (2019b).

TABLE 3.2: Summary of target parameters.

Name	$M_\star$ $[M_\odot]$	$L_\star$ $[L_\odot]$	$R_\star$ $[R_\odot]$	$T_{\rm eff}$ [Kelvin]	$a_{\rm SED}$ [au]	$\Delta_{\rm GDR3}$
HD112810	1.40 ± 0.07	3.36	1.40 ± 0.07	6455	298.5	40.58 ± 29.58
HD36968	1.50 ± 0.10	4.62	1.45 ± 0.07	6855	421.7	–
HD54341	2.20 ± 0.11	25.58	1.83 ± 0.09	9585	298.5	254.80 ± 69.20
HD10472	1.40 ± 0.07	3.80	1.41 ± 0.07	6615	211.3	23.90 ± 10.82
HD142446	1.40 ± 0.07	3.98	1.47 ± 0.07	6520	211.3	19.12 ± 37.62
HD127750	1.90 ± 0.09	17.56	1.59 ± 0.08	9170	149.6	23.55 ± 35.45
HD113556	1.50 ± 0.07	4.66	1.49 ± 0.07	6760	211.3	28.55 ± 20.69
HD86087	2.99 ± 0.15	51.49	2.48 ± 0.12	9610	37.5	10.58 ± 29.37
HD71043	2.00 ± 0.10	21.90	1.71 ± 0.09	9300	26.6	34.31 ± 18.12
HD103703	1.40 ± 0.07	3.91	1.52 ± 0.08	6410	4.7	55.41 ± 21.58
HD106036	1.90 ± 0.09	13.59	1.60 ± 0.08	8560	6.6	32.36 ± 17.00
HD106389	1.30 ± 0.06	2.49	1.42 ± 0.07	5995	1.7	128.59 ± 40.90
HD36546	1.90 ± 0.09	14.78	1.56 ± 0.08	8945	18.8	95.53 ± 26.87
HD56537	2.50 ± 0.12	28.74	2.14 ± 0.11	8310	–	35.31 ± 39.28
HD37306	1.90 ± 0.09	15.88	1.60 ± 0.08	8935	53.1	20.71 ± 16.06
HD38678	2.00 ± 0.10	15.58	1.82 ± 0.09	8235	13.3	17.19 ± 30.24
HD80007	3.00 ± 0.10	–	6.30 ± 1.00	8925	–	–
HD2262	1.90 ± 0.09	12.21	1.72 ± 0.08	7735	37.6	31.71 ± 20.74
HD102647	2.00 ± 0.10	13.02	1.69 ± 0.22	8750	37.6	–

Notes. Δ_{GDR3} refers to the tangential velocity anomaly between the long-term Hipparcos-Gaia proper motion and the Gaia DR3 proper motion, expressed in meters per second.

3.3.2 Data reduction and products

Data reduction and post-processing tasks were performed by the SPHERE Data Center (SPHERE-DC, Delorme et al. 2017; SpeCal, Galicher et al. 2018). All the frames are first corrected for cosmetics (i.e., dark current, flat-fielding, bad pixels, distortions), then, the centering frames are used to identify the position of the star in the science frames and to align them. The photometric frames are cropped to a size of 64 by 64 pixels, the neutral density filter (if any) is accounted for, and the resulting images are normalized by the exposure time. The parallactic angle is computed for every science frame and will be used during the post-processing step, for which we use state-of-the-art algorithms (in the context of point source detection optimization) and pipelines. For IRDIS we used the PCA (Soummer et al. 2012), ANDROMEDA (Mugnier et al. 2009;Cantalloube et al. 2015a), and no-ADI reductions, while for IFS we used the PCA and ASDI reductions (Mesa et al. 2015). In this work, we mostly used the ANDROMEDA data products in our analysis for the IRDIS data, as it directly provides the detection probability and flux maps to be used for the analysis, as well as the contrast curves for all filters. The effective field of view of the outputs from ANDROMEDA was set to ~ 410 pixels in radius (or $\sim 5''$), and for objects outside this region, we used the no-ADI (i.e., only de-rotating and stacking the frames) products for the identification and extraction of point sources, since those distant regions do not suffer from self-subtraction in the post-processing using no-ADI. The PCA and ASDI data products were used for the visual inspection and verification of identified candidates (see Section 3.4.1 and 3.4.5).

3.4 Point sources identification

In this section, we describe the procedure for the identification and characterization of point sources in the IRDIS observations. We use the astrometry and photometry of the candidates to investigate their possible nature by locating them in color-magnitude diagrams (CMDs hereafter), analyze their proper motions (when a second epoch is available), and study their significance computing detection probability maps. Finally, we present and discuss the point sources that were also detected in the IFS data.

3.4.1 Astrometry and photometry of sources

We used the final products of the ANDROMEDA pipeline from the SPHERE-DC to identify and obtain the astrometry and photometry of all the point sources. The work-flow is similar to the one described in Cantalloube et al. (2015a). We used the S/N map to first identify the sources, and extract their position. To identify the point-sources, we used the tasks provided in `DAOPHOT` (Stetson 1987), which given an FWHM and a threshold returns the position at the maximum of the signal. To avoid problems identifying sources with very weak signals, we performed the procedure using the original S/N map and a smoothed version (obtained applying a 1.1 standard deviation Gaussian kernel). In both cases we set the FWHM to 4.2 pixels (the typical FWHM is ~ 4.0 pixels under an average strehl ratio of 90%, Langlois et al. 2021b) but vary the threshold according to the version of the map used and the instrumentation setup: $1.2-\sigma$ for the original map and 0.9 for the smoothed one in the case of dual-band imaging, and 1.5 and 0.9 for broad-band. The specific values of each threshold were selected by visual inspection and as a trade-off between recovering weak but real signal and the exponential identification of artifacts (i.e., speckles, noise, persistent residuals). With the point sources identified, we performed a first selection based on further analysis of their significance. We calculated for each source the noise at the same angular separation as described in Mawet et al. (2014). Then, we divided the S/N of the point source by the estimated noise, only keeping those with a ratio larger than 1.25. The motivation is to avoid selecting persistent speckles and decrease the already large number of sources identified. In the case of dual-band observations, we have one S/N map per filter, while for the broad-band observations we have two maps coming from the two sides of the camera. Therefore, we generated one list of possible point sources for each S/N map. To avoid duplication and to eliminate residual artifacts, we performed a crossmatch between the different tables with a maximum separation no greater than 1.5 pixels, keeping only those sources that appear on both sides of the camera. The list of possible sources contains the coordinates in pixel of each source at the maximum S/N and their respective S/N value.

With this first list of point-sources identified, we proceeded to obtain the precise position by modeling their morphology in the S/N map using a 2D Gaussian following Cantalloube et al. (2015a). For each point source we cropped a sub-image of 11×11 pixels centered at the maximum S/N. We used nonlinear least-squares routines to obtain all the 6 free 2D Gaussian parameters (i.e., μ_X, μ_Y, σ_X, σ_Y, θ and amplitude), and their respective uncertainties. The uncertainties of μ_X and μ_Y were set to three times the retrieved uncertainty by the modeling as suggested by Cantalloube et al. (2015a). The extraction of the flux was done on the flux map using the previously explained refined positions and the same 2D Gaussian fitting approach. The flux of each source can be measured directly from the flux map by taking the value of the fitted gaussian at the subpixel position obtained from the S/N map (see Cantalloube et al. 2015a). Note that this position is not necessarily the maximum of the 2D Gaussian in the flux map.

The flux uncertainty is then obtained by propagating the uncertainties via Monte Carlo simulation. We performed the same procedure for both pairs of maps, one S/N and flux maps for each left and right side of the camera. With this additional modeling, fluxes, positions, and residuals of the models (root squared sum of each residual image), we performed a second selection of point sources. We kept candidates which primarily meet the following criteria: low uncertainty values in positions (below 1 pixel); low elongation of the Gaussian profile (ratio between σ in X and Y less than 0.25); low normalized residual values (below 300 for S/N lower than 30); separation between both measured positions less than 0.7 pixels; minimum registered S/N above 5.

We used the noADI products to search and identify additional point sources outside the field of view of ANDROMEDA, and determine their flux and astrometry. Additionally, we also re-process point sources for which the extraction with ANDROMEDA failed or did not converge. In the former case, these point sources appear in regions far away from the part of the image dominated by speckles in the noADI products. We proceeded by fitting 2D Gaussians on the noADI maps to obtain both relative positions and fluxes. Each point source was visually verified, and was added to the list of point sources. On the other hand, point sources with unsatisfactory fits when using the ANDROMEDA products were replaced by the results from the fitting to the noADI products. We included only point sources with S/N above 5.

For each point source, we transformed the measured contrast flux to magnitude. We then added the synthetic magnitude of the central star which was determined using the VOSA[2] tool (Bayo et al. 2008) from the main stellar properties shown in tables 3.1 and 3.2. Finally, we transformed from magnitude to absolute magnitude using the distances from Table 3.1 and assigned 0.2mag as intrinsic uncertainty related to the flux variability, as discussed in Langlois et al. (2021a).

We performed a cross-match between our point-source tables for targets with a second epoch. The cross-match accounts for the proper motion of the central star and all related uncertainties. In this case, we kept both values of the cross-match since they are related to two different epochs.

In the end, a total of 104 unique point-like sources were identified. Their relative positions, absolute magnitudes[3], filters, observed dates, and central star names are presented in Table 3.5.

3.4.2 Color-magnitude diagram

The near-IR color(s) of direct imaging point sources can be a powerful tool to further characterize their nature (e.g., Samland et al., 2017, Chauvin et al., 2017). CMDs can be very helpful, especially when it comes to identifying contaminants (e.g., background stars or red giants) rather than genuine companions. For instance, Langlois et al. (2021a) demonstrated that within the SHINE survey, some point sources that follow a main sequence in the CMD can quickly be discarded. For our dual-band observations, we build the CMDs as described in Langlois et al. (2021a), accounting for the magnitude of the central star, distance and intrinsic uncertainties on the magnitudes (see Section 3.4.1 and Table 3.5 for the entire list of point sources and their magnitudes). Figure 3.3 shows the CMD for all our point sources with dual-band observations. Black dots correspond to our point sources, while the rest of the symbols and colors refer

[2]http://svo2.cab.inta-csic.es/theory/newov2/
[3]Considering the distance of the central star.

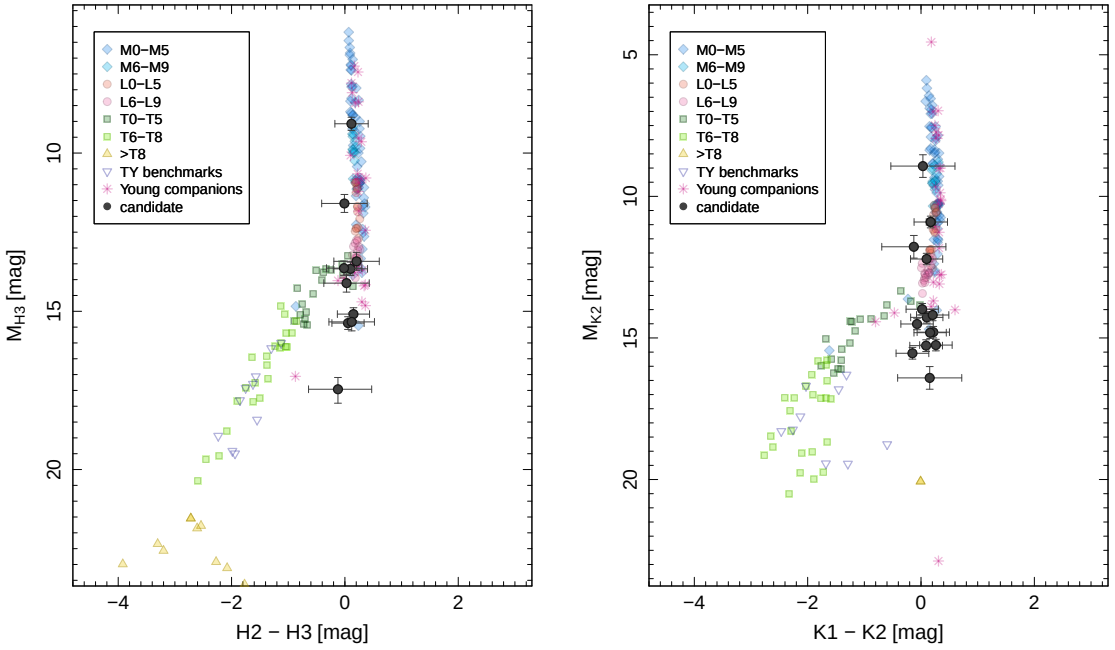

FIGURE 3.3: Photometry of the point sources (black circles) observed in our sample plotted in color-magnitude diagrams assuming a common distance with the host-star. The rest of colored symbols correspond to the sequence of stars and sub-stellar objects from M to TY spectral types. The left panel shows the color-magnitude diagram for the dual-band filters H2 and H3, and the right panel the color-magnitude diagram for K1 and K2.

to different classes of objects from M-type stars to sub-stellar objects (T-class). We discarded six point sources as stars since they follow the main sequence (they have absolute magnitudes above 12.5 in the CMD). Following Langlois et al. (2021a), we discarded one point source in the CMD with an absolute magnitude below 17. In total, we ruled out seven point sources since they have colors and magnitudes compatible with background stars, however, for the remaining sources it is not possible to confirm their nature by only studying the CMDs.

3.4.3 Proper motion diagram

By nature, bound companions should share the same proper motion as their host star. It is therefore crucial to have a good estimate of the stellar proper motions on sky, and have observations separated by a long enough baseline, to confirm (or reject) the co-moving nature of candidate companions previously identified. Thanks to the precise astrometry solution provided by Gaia DR3, and the high angular resolution of the SPHERE instrument, time baselines of months to a couple of years are often sufficient. We proceed in the same way as Langlois et al. (2021a) using the position and uncertainties of our candidates. Our campaigns did not include astrometric calibration observations, however, the SPHERE-DC uses the available public data to determine the adequate astrometric corrections. If none were available for a given point source, then the standard values taken from Maire et al. (2021) were used (see Table 3.4). We used 0.03° for the uncertainty of the pupil zero point in all our observations (Maire et al. 2021). The uncertainty for the central star position was set conservatively to 0.2 pixels, a value larger

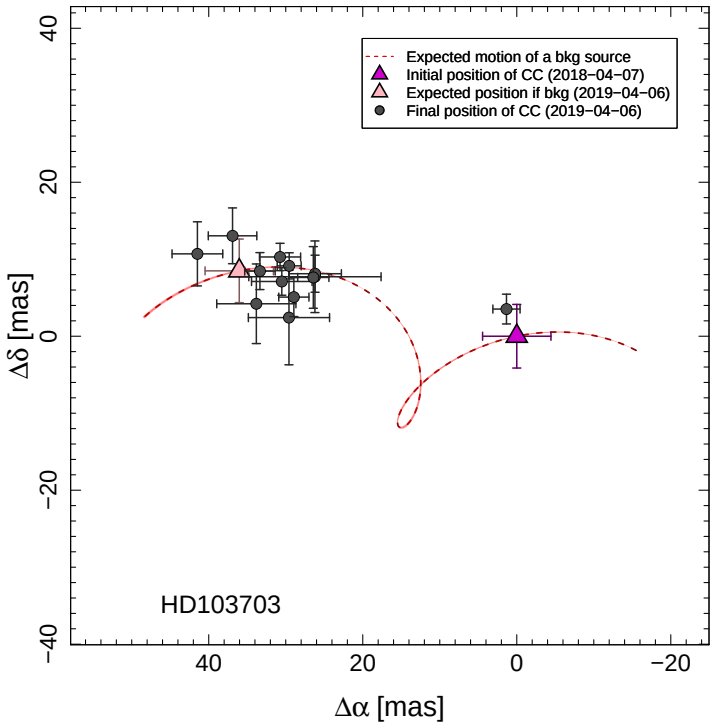

FIGURE 3.4: Example of proper motion diagram for HD 103703. The red line corresponds to the motion of a static background source with respect to the star position in the sky. The pink and light pink triangles are the positions of a background source at each observed date. The light blue circles are the positions of the point sources at the second epoch with respect to the first epoch (coordinates [0,0]). The point source with low variation in position corresponds to the known companion of the system HD 103703AB (Janson et al. 2013; Mason et al. 2001).

than (but still in agreement with) the one derived by Langlois et al. (2021a). The astrometric positions and related uncertainties are already included in Table 3.5.

Figure 3.4 shows an example of the proper motion diagram for the target HD 103703. The triangles correspond to the extreme of the expected motion of a perfectly static background source. The uncertainties of the triangles correspond to the average uncertainties of the point-like sources. The black circles correspond to the point sources at the second epoch position with respect to the first one. The zero-point of the axes corresponds to the position at the first epoch. All the proper motion diagrams are presented in Appendix 3.7.3. Two known stellar companions HD 106036AB (Kouwenhoven et al. 2005; Mason et al. 2001; PS-43 in Table 3.5) and HD 103703AB (Janson et al. 2013; Mason et al. 2001; PS-6 in Table 3.5) are presented in our sample with two epochs, clearly visible in the proper motion diagrams (Appendix 3.7.3, Figure ??)

3.4.4 Contrast curves and probability map detection

The ANDROMEDA pipeline also provides the contrast curves, which can be used to infer upper limits on the detectability of planets in our observations. We used the ATMO-weak model (Phillips et al. 2020) to convert the contrast curve from magnitude to planetary masses. We preferred to use ATMO 2020 model since it provides key updates to the grids COND and DUSTY (Baraffe et al. 2002), incorporates new

equations of state, and updates some molecular opacities, for instance. These updates can improve the modeling of the observations, however, they should also be taken with caution as discussed in Petrus et al. (2022). We used the ages and distances reported in Table 3.1, the stellar magnitude in each of the filters using VOSA, and the magnitudes from the contrast curves. We assumed that none of the parameters are correlated with each other to propagate the uncertainties via Monte Carlo simulation. We transformed the contrast to absolute magnitude in the Vega system. Then, we generated 4000 independent values for the age, and magnitude at each separation following the corresponding uncertainties. Finally, we interpolated the ages and magnitude values to obtain the corresponding mass in the ATMO-weak grids. The uncertainties in the mass estimates correspond to the 25% and 75% percentiles. With the contrast magnitude already transformed into masses, we then simulated the different planet orbital configurations. We followed the same procedure presented in Langlois et al. (2021a) and Vigan et al. (2021b), where we simulated $\sim 10^8$ orbits per map with priors in the eccentricity[4] as described by Vigan et al. (2021b). As we do not have any information about the disk inclination for all of the stars in the sample, we assumed a uniform distribution for the argument of periapsis and inclination between $0 - 360°$ and $0 - 90°$, respectively. Our sample has only one debris disk that has been spatially resolved, HD 36546, observed at near-infrared wavelengths with SCExAO/HiCIAO (Currie et al. 2017) and SCExAO/CHARIS (Lawson et al. 2021). However, we do not use the parameters obtained from these observations and modeling (e.g., inclination) in order to have a uniform treatment across the sample. We used a logarithmic scale in the planetary semi-major axis and mass from 0.1 to 10000 au and 0.1 to 113 $M_{\rm Jup}$, respectively. The realizations were done in the same manner as Bonavita (2020). This leads to a map providing the probability of detecting a planet with mass M and semi-major axis a given our observations. In cases for which a second epoch is available, the probability maps were added[5] together, re-normalizing the resulting map to unity. Figure 3.5 shows the combination of all the probability map detection for the purpose of showing the sensitivity of our sample per filter. Our observations typically cover a range from 20 to 700 au with masses over $10 M_{\rm Jup}$ at 300 au for probability detection above 50%.

3.4.5 Point sources in IFS observations

IFS observations can provide additional information and useful diagnostics in combination with IRDIS (e.g., Samland et al. 2017). We identified four point sources within the field of view of IFS, and all of them were also recovered with IRDIS. Two were identified only on stacking using the ASDI data products corresponding to the observations of HD 142446 (PS-1) and HD 86087 (PS-2), both with two epochs (see Table 3.5). These candidates were rejected as companions by the proper motion diagram analysis using the IRDIS observations (no co-moving objects, see Appendix 3.7.3). The remaining two candidates HD 103706 PS-6 and HD 106389 PS-1 are clearly identified in ASDI and PCA and correspond to known stellar companions (HD 103703AB and HD 106389AB, Janson et al. 2013, Mason et al. 2001). Since we do not have new companion candidates in the IFS observations (rejected or already known objects), we did not carry out any further analysis on the IFS data products.

[4] A Beta distribution with $\alpha = 0.95$ and $\beta = 1.30$.

[5] The multiplication of the maps would correspond to the probability of detecting a planet in both epochs. We have added the maps to obtain the probability of observing a planet in at least one of the epochs.

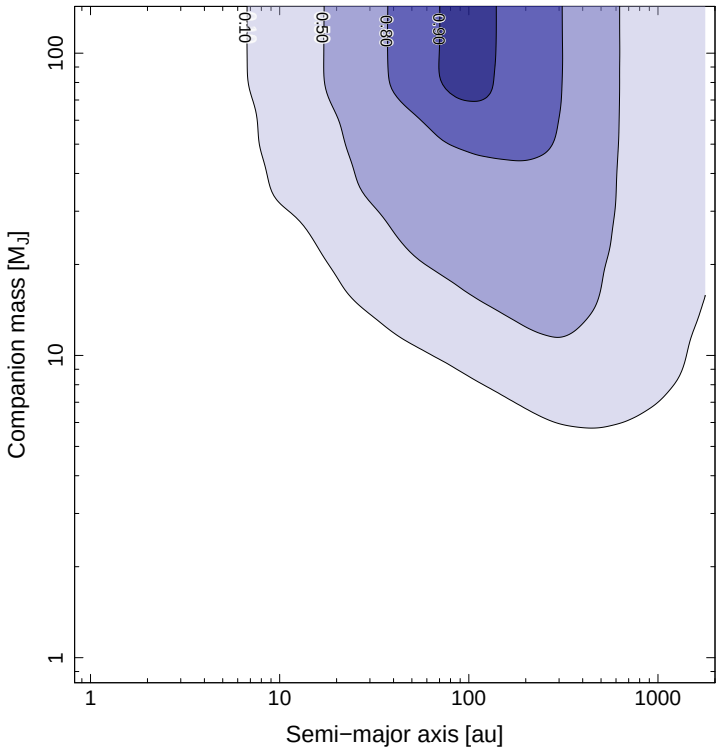

FIGURE 3.5: Mean detection probability map of our sample. Contours represent the 10%, 50%, 80%, and 90% detection thresholds.

3.4.6 Summary of the different diagnostics

We detected a total of 104 point sources around 12 of the 19 stars observed. For four of these objects (HD 113556, HD 54341, HD 112810, and HD 37306), we also used SPHERE archival data to discriminate whether or not they are background objects. From the CMDs it was possible to rule out seven of these candidates which deviate considerably from the expected region where planets should lie (e.g., Langlois et al. 2021a), or on the contrary follow the M-type branch. However, the CMD points to 18 sources with color information for which it is not possible to assess whether they are sub-stellar companions or not. In addition, there are stars observed in broad-band in our sample, and those cannot be placed in the CMD. As a second discriminant, we use the proper motion diagrams. From the complete sample of stars with two epochs in which we detect point sources, only two of them present proper motions in good agreement with the star. However, they correspond to known stellar companions (see section 3.4.3). Therefore, we have not found new companions from the proper motion diagrams diagnostic (see Appendix 3.7.3 for all the proper motion diagrams). It should be noted that four point sources detected in the first epoch around HD 113556 are not re-detected in the second one. This is because they were detected in broad-band H with a S/N below 10 in the first epoch, while the second epoch was observed in dual-band K12, which has a worse sensitivity than the H-band data. These objects are at a projected separation of more than 240 au and, if they are really gravitationally bound, they would be low-mass stellar objects according to the proper motion anomaly curve. We detected one candidate around HD 36546 for which we do not have a second epoch. However, due to its position in the CMD, and projected distance of $\sim$ 620 au, it is unlikely to be a planetary-mass object bound to the star. Finally, we detected a candidate around

HD 106389 for which we only have one epoch (PS-1 in Table 3.5). However, this candidate corresponds to a known stellar companion (Janson et al. 2013; Mason et al. 2001).

3.5 Observations versus theory

3.5.1 Prediction from theory

Different theoretical studies have explored the context of planet-disk interactions during the debris disk phase. For example, the inner edge of the disk can be used to constrain and/or predict the presence of inner planets. Its shape can provide insights into the properties of the planet shaping it (Mustill & Wyatt 2012) and its location can be used to predict the presence of unseen planets that could be stirring the disk (e.g., Mustill & Wyatt 2009). Also, it is possible to study the scenario of N equal mass planets that could produce the cavity and model the inner edge of the disk (e.g., Faber & Quillen 2007, Shannon et al. 2016). However, the predicted mass of such planet(s) responsible for the interaction strongly depends on the assumptions regarding disk properties (i.e., morphology, dust properties, density distribution, etc), history of the system, and planet orbital properties (e.g., Lazzoni et al. 2018, Morrison & Malhotra 2015). Pearce et al. (2022) derived different formulae to constrain the possible planetary masses that could be interacting with the disks. They assumed that the orbit of the planet is coplanar with the disk, and that the orbit of the planet does not change significantly over time. They formulated two different scenarios: a single planet interacting with the disk, in which the assumption is that a single planet ejects 95% of unstable debris in the inner edge of the disk; and multiple planets, in which equal mass planets with circular orbits have removed 50% of unstable debris.

We proceed in the same very way as Pearce et al. (2022). We used their equation 6, that we recall here

$$M_p \approx 8.38\, M_{\rm Jup} \left(\frac{M_*}{M_\odot}\right) \left[\frac{Q_i}{a_p + 0.4(Q_i - q_i)} - 1\right]^3 \times \left(3 - 0.4\frac{Q_i - q_i}{a_p}\right) \tag{3.1}$$

where M_* is the stellar mass, a_p the planet's semi-major axis, Q_i the apocentre of an ellipse tracing the disc inner edge, and q_i the respective pericentre. If the disk is axisymmetric, $Q_i = q_i$ and corresponds to the radius of the inner edge. With equation 3.1 we can infer the most probable mass of a single planet as a function of its semi-major axis, that is sculpting the inner edge of the disk. This equation works for planets in circular and eccentric orbits (with planet eccentric orbit $e_p < 0.3$, see Pearce et al. 2022), where the external disk may or may not be eccentric.

Additional constraints are also considered such as the ones obtained from the secular time, also taken from Pearce et al. (2022, equations 7 and 8)

$$M_p \geq 0.331\, M_{Jup} \left(\frac{a_p}{\rm au}\right) \left(\frac{Q_i}{\rm au}\right)^{-1/4} \left(\frac{t_*}{\rm Myr}\right)^{-1/2} \left(\frac{M_*}{M_\odot}\right)^{3/4} \tag{3.2}$$

and the diffusion time

$$M_p \geq 0.0419\, M_{Jup} \left(\frac{a_p}{\mathrm{au}}\right)^{-1} \left(\frac{Q_i}{\mathrm{au}}\right)^{5/2} \left(\frac{t_*}{\mathrm{Myr}}\right)^{-1} \times \left(\frac{M_*}{M_\odot}\right)^{1/2} \left[b_{3/2}^{(1)}\left(\frac{a_p}{Q_i}\right)\right]^{-1} \tag{3.3}$$

where t_* is the stellar age, and $b_S^{(j)}(x)$ the Laplace coefficient. The base of these equations is that if there is a planet, it should be massive enough to sculpt and interact with the debris within the stellar lifetime. The restriction from the secular time is that the planet removes the more distant debris more efficiently driving them onto eccentric, planet-crossing orbits in the stellar timescale. The diffusion time restricts the planet mass necessary to remove the debris close to the orbit of the planet via scattering in the stellar timescale.

Pearce et al. (2022) re-formulated the equation 15 from Mustill & Wyatt (2009) to infer the minimum mass of a single planet that can stir the debris system (equation 23 in Pearce et al. 2022). The equation takes the form of

$$M_{\mathrm{p,stir}} \geq 5.07 \times 10^{-5}\, M_{\mathrm{Jup}} \left(\frac{q_o}{\mathrm{au}}\right)^{9/2} \left(\frac{Q_i}{\mathrm{au}}\right)^{-3} \times \left(\frac{t_*}{\mathrm{Myr}}\right)^{-1} \left(\frac{M_*}{M_\odot}\right)^{1/2} \frac{(1+e_p)^3(1-e_p^2)^{3/2}}{e_p} \tag{3.4}$$

with q_o the pericentre of the disc outer edge. As in the previous equations, the idea is to obtain the minimum planetary mass for which the debris particles can be stirred. Note that this planetary mass does not necessarily sculpt the inner edge of the disk. The eccentricity of the stirring planet was conservatively set to 0.3 as in Pearce et al. (2022) since this value provides a good approximation to the minimum stirring planet mass. Pearce et al. (2022) showed that the mass of the planet is less sensitive to the choice of eccentricity for greater values in e_p, while larger values for the planet mass are obtained for $e_p < 0.3$. As for previous equations, the orbit of the planet is assumed to be coplanar with the disk.

We also analyzed the case when multiple planets with equal masses are present in the system, and in that case, we used equation 15 in Pearce et al. (2022)

$$M_{p,N} \geq 6.29 \times 10^{-3}\, M_{Jup} \left(\frac{t_*}{Myr}\right)^{-1} \left(\frac{M_*}{M_\odot}\right)^{1/2} \left(\frac{r_2}{au}\right)^{3/2} \tag{3.5}$$

where r_2 is the semi-major axis of the outermost planet, which was set to $r_2 = q_i$ following Pearce et al. (2022). The idea is to determine the minimum mass of N equal mass planets that are sculpting the inner edge of the disk and generate the cavity within the stellar lifetime. The planets have circular orbits, are coplanar with the debris disk, and they have removed the 50% of unstable debris to produce the cavity in the stellar lifetime.

Since we used the SED modeling to estimate the best disc location, we adopted $Q_i = q_i = a_{SED}$ in eq. 3.1 to 3.4 as suggested by Pearce et al. (2022). For equation 3.4 we set $Q_i = q_o = a_{SED}$ and $e_p = 0.3$ following the prescription mentioned in the paper to obtain the minimum planetary mass necessary to stir the disk, located at the inner edge of the disk.

3.5.2 Constraints from observations

Two kind of observations are available to constrain the possible mass of a single planet in the system. First, the contrast curve provides a direct observational constraint on the detectability of the planet mass as a function of the projected semi-major axis, which can be later on transformed into a probability map detection (see Section 3.4.4). Second, we also have the expected mass of a companion provided by the proper motion anomaly (see Kervella et al. 2022). Both approaches are powerful to constrain the presence of a planetary-mass companion and can be directly compared to theoretical predictions.

Figure 3.6 shows an example of the covered parameter space that the models from the previous section would yield for putative companions to HD 36546. The solid black line corresponds to the minimum mass of a planet that removes debris and sculpts the inner edge of the disk (eq. 3.1); the dashed black line shows the minimum planet mass necessary to remove the debris close to the planet orbit via scattering within the stellar timescale (diffusion time constrain); the black dotted line is the mass of a planet for which more distant debris particles were removed (secular time constrain); the gray solid line refers to the minimum planet mass in eccentric orbit $e_p = 0.3$ necessary to stir the disk (and located at the inner edge of the disk); and finally, the dashed gray line marks the minimum planet mass in a system of N equal-mass and circular orbit planets that produce the disk cavity within the stellar age. The rest of the lines correspond to the proper motion anomaly (filled yellow area and line), the best disk location from SED modeling (vertical blue line and filled area), and the probability map detection from direct imaging observations (filled green color-scales region).

To combine all the information from both theory and observation, we carried out the following exercise. We started by assuming there is a planet in the system that remains undetected with the observations available. On the part of the theory, we have different constraints that limit the regions where there could be such a planet. For example, the solid black line in Figure 3.6 related to the minimum planetary mass required to sculpt the inner edge of the disk, can be understood as two regions: above the line is the region where there could be a planet, and below where there cannot be. In this way, we can build a map similar to the probability map, marking with zeros below and ones above. Carrying out the same exercise on the rest of the theoretical lines for the single-planet case (black lines in Figure 3.6), we can define the allowed region for a planet to exist given the inferred disk location. For the observations, we treated the proper motion anomaly in the most conservative way possible, assuming that the errors are Gaussian. Although this consideration is not entirely true, it is a useful approximation to combine the different maps and does not greatly affect our findings. The curve is normalized to its maximum at each separation, to ensure that the solid line of the proper motion anomaly shown in Figure 3.6 has values of 1, decreasing to zero in regions farther away. A probability map detection can be understood as the probability of detecting a planet given the contrast curve. By performing one minus the probability from the map, we have the probability that a planet exists outside of our detection capabilities (again, assuming that a planet exists). It should be noted that the normalization to 1 of all maps is related to the most likely location to find a planet (but not that a planet is indeed there). We then multiply all the maps to obtain the region where the planet would be most likely to be found. With this approach we are effectively giving equal weights to all the different constraints we have. Figure 3.6 shows the region of most likely existence of a planet given our observational and theoretical constraints, filled with red gradient colors delimiting iso-contours corresponding to values of 0.95, 0.68, 0.50, and 0.25 respectively.

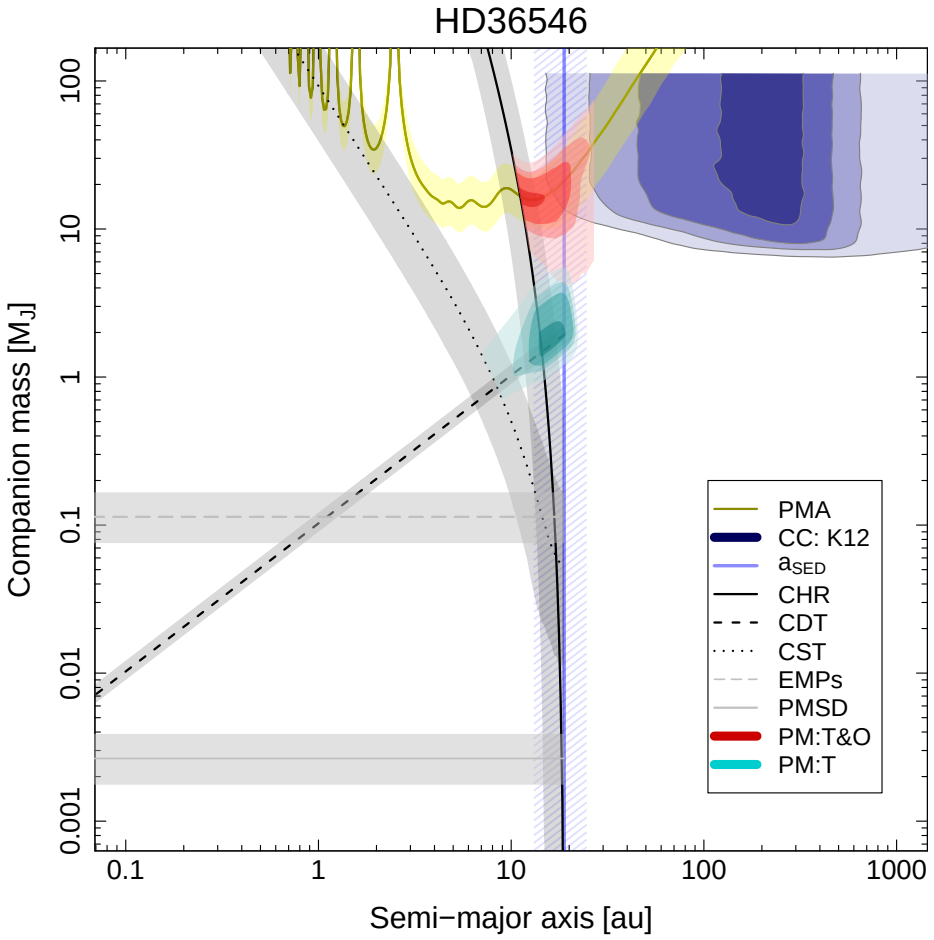

FIGURE 3.6: Planetary mass companion as a function of its semi-major axis for the case of HD 36546. The different black curves refer to the theoretical values used to constrain the minimum planet mass needed to interact in different ways with the disk. The solid black line corresponds to the Hill radius constrain (CHR). The dashed black line refers to the constraint given by the diffusion time (CDT). The dotted black line is the constraint given by secular time (CST). The solid gray horizontal line corresponds to the minimum mass of the planet to stir the disk (PMSD). The dashed gray horizontal line (EMPs) refers to the minimum mass of N planets of equal mass that interact with the disk and clear their neighborhood generating the cavity in the disk (see the text for more details about the theoretical lines). The gray areas correspond to the uncertainties on each theoretical line. The yellow line and its filled area correspond to the constraint from the proper motion anomaly (PMA). The blue filled area corresponds to the probability map detection (CC: K12), where 0.95, 0.68, 0.50, and 0.25 are marked from dark blue to light blue, respectively. The blue vertical line marks the location of the disk $a_{\rm SED}$. The red contours correspond to the zone of the greatest probability of finding a planet, given the observations, our models, and theoretical constraints (PM:T&O). Finally, the dark cyan contours corresponds to the zone of the greatest probability of finding the minimum planetary mass object given only the theoretical constrains.

The region filled with cyan colors encloses the most likely minimum mass of a planet expected from the theoretical models only (the levels are the same as for the red area).

Table 3.3 reports the values for the masses of the planet derived for all the targets in our sample. In addition, the theoretical masses (not using any of the observational constraint) are shown for the case of single-planet, multi-planet of equal masses, and the minimum mass of a planet for disk stirring, in addition to the minimum mass considering only the proper motion anomaly.

TABLE 3.3: Summary of derived masses.

Name	Selection	$a_{\rm SED}$	PMA	M_{Obs} [$M_{\rm Jup}$]	$a_{\rm Obs}$ [au]	$M_{\rm Theor}$ [$M_{\rm Jup}$]	$a_{\rm Theor}$ [au]	$M_{\rm Stir}$ [$\times 10^{-2}\,M_{\rm Jup}$]	$M_{\rm Mult}$ [$M_{\rm Jup}$]	$M_{\rm PMA}$ [$M_{\rm Jup}$]	$a_{\rm PMA}$ [au]
HD112810	Stirring	✓	✓	$7.5^{+4.6}_{-1.4}$	232^{+68}_{-45}	$5.0^{+8.6}_{-3.8}$	193^{+45}_{-35}	$5.0^{+2.0}_{-2.0}$	$2.4^{+0.9}_{-0.7}$	$5.1^{+4.5}_{-3.8}$	$6.9^{+31.1}_{-4.5}$
HD36968	Stirring	✓	✗	$8.8^{+4.2}_{-2.7}$	353^{+162}_{-95}	$4.7^{+4.8}_{-4.0}$	280^{+60}_{-64}	$4.0^{+1.0}_{-1.0}$	$1.9^{+0.6}_{-0.6}$	–	–
HD54341	Stirring	✓	✓	$8.6^{+13.2}_{-5.6}$	298^{+86}_{-100}	$2.4^{+2.5}_{-1.0}$	225^{+50}_{-40}	$0.6^{+0.3}_{-0.2}$	$0.2^{+0.1}_{-0.1}$	44^{+22}_{-14}	$8.0^{+17}_{-4.6}$
HD10472	Stirring	✓	✓	$5.8^{+3.7}_{-2.6}$	190^{+85}_{-56}	$2.5^{+2.6}_{-1.3}$	147^{+32}_{-30}	$1.2^{+0.4}_{-0.4}$	$0.5^{+0.2}_{-0.1}$	$3.0^{+1.8}_{-1.5}$	$7.0^{+17.4}_{-4.3}$
HD142446	Stirring	✓	✓	$5.3^{+4.2}_{-1.1}$	165^{+45}_{-30}	$3.9^{+4.3}_{-1.9}$	140^{+33}_{-32}	$3.0^{+1.0}_{-0.9}$	$1.3^{+0.4}_{-0.4}$	$2.3^{+5.0}_{-2.3}$	$6.8^{+15.6}_{-4.2}$
HD127750	Stirring	✓	✓	$6.7^{+6.0}_{-1.9}$	131^{+59}_{-33}	$3.8^{+7.6}_{-2.2}$	105^{+21}_{-22}	$2.1^{+0.8}_{-0.6}$	$0.9^{+0.3}_{-0.3}$	$3.5^{+5.8}_{-3.5}$	$7.5^{+17.0}_{-4.5}$
HD113556	Stirring	✓	✓	$5.8^{+3.2}_{-1.3}$	157^{+40}_{-24}	$4.0^{+4.0}_{-2.0}$	144^{+26}_{-34}	$3.4^{+1.3}_{-1.0}$	$1.5^{+0.5}_{-0.4}$	$3.6^{+3.5}_{-2.7}$	$6.8^{+32.0}_{-4.3}$
HD86087	Warm debris	✓	✓	$4.6^{+38}_{-3.9}$	37^{+12}_{-10}	$0.6^{+1.2}_{-0.4}$	31^{+15}_{-7}	$2^{+1}_{-1} \times 10^{-2}$	$1.1^{+0.5}_{-0.4} \times 10^{-2}$	$2.2^{+6.5}_{-2.2}$	$8.4^{+25.2}_{-5.2}$
HD103703	Warm debris	✓	✓	$7.2^{+6.1}_{-4.7}$	$4.1^{+2}_{-1.4}$	$0.3^{+0.5}_{-0.2}$	$3.9^{+0.8}_{-0.8}$	$1.1^{+0.4}_{-0.3} \times 10^{-2}$	$5^{+2}_{-1} \times 10^{-3}$	$6.8^{+4.2}_{-2.9}$	$6.7^{+16.0}_{-3.9}$
HD71043	Warm debirs	✓	✓	$10.1^{+11}_{-8.2}$	23^{+12}_{-7}	$0.8^{+1.3}_{-0.5}$	$21^{+6}_{-4.5}$	$6^{+2}_{-2} \times 10^{-2}$	$3^{+1}_{-1} \times 10^{-2}$	$5.4^{+3.9}_{-3.0}$	$7.6^{+22.4}_{-4.6}$
HD106036	Warm debris	✓	✓	$5.0^{+4.7}_{-3.4}$	$6.1^{+2.6}_{-1.7}$	$0.5^{+1.1}_{-0.3}$	$5.4^{+1.4}_{-1.1}$	$2.2^{+0.8}_{-0.6} \times 10^{-2}$	$9^{+3}_{-3} \times 10^{-3}$	$4.8^{+3.6}_{-2.6}$	$7.5^{+21.5}_{-4.5}$
HD106389	Warm debris	✓	✓	45^{+56}_{-24}	$1.4^{+0.8}_{-0.4}$	$0.13^{+0.16}_{-0.07}$	$1.4^{+0.3}_{-0.3}$	$2.3^{+0.8}_{-0.6} \times 10^{-3}$	$10^{+3}_{-3} \times 10^{-4}$	15^{+8}_{-5}	$6.4^{+15.2}_{-3.5}$
HD36546	FEBs	✓	✓	$16.5^{+13.5}_{-9.1}$	$13.8^{+11.2}_{-2.9}$	$1.5^{+2.8}_{-0.9}$	$14.6^{+4.3}_{-3.3}$	$2.6^{+1.2}_{-0.8} \times 10^{-1}$	$1.1^{+0.5}_{-0.3} \times 10^{-1}$	$14.0^{+7.5}_{-4.3}$	$7.3^{+15.4}_{-3.9}$
HD56537	FEBs	✗	✓	–	–	–	–	–	–	$6.4^{+8.4}_{-6.4}$	$8.0^{+21.0}_{-4.8}$
HD37306	FEBs	✓	✓	$13.4^{+13.6}_{-11.3}$	$38^{+33.5}_{-6.5}$	$1.3^{+1.9}_{-0.8}$	41^{+12}_{-9}	$1.9^{+0.6}_{-0.5} \times 10^{-1}$	$8^{+3}_{-2} \times 10^{-2}$	$3.1^{+2.8}_{-2.5}$	$7.3^{+41.4}_{-4.6}$
HD38678	NA	✓	✓	$2.2^{+8.2}_{-2.0}$	$13.3^{+4.7}_{-3.6}$	$0.2^{+0.5}_{-0.15}$	$11.7^{+5.9}_{-2.7}$	$4^{+3}_{-2} \times 10^{-3}$	$1.7^{+1.0}_{-0.6} \times 10^{-3}$	$2.7^{+5.3}_{-2.7}$	$7.5^{+24.5}_{-4.5}$
HD80007	FEBs	✗	✗	–	–	–	–	–	–	–	–
HD2262	Exozodi	✓	✓	$20.5^{+31.5}_{-18.6}$	$34.6^{+16.9}_{-13.6}$	$0.3^{+0.7}_{-0.2}$	$31.5^{+12.2}_{-6.5}$	$8^{+5}_{-2} \times 10^{-3}$	$3^{+2}_{-1} \times 10^{-3}$	$4.8^{+3.9}_{-3.2}$	$7.3^{+28.7}_{-4.5}$
HD102647	Exozodi	✓	✗	$4.5^{+11.2}_{-3.4}$	$37.2^{+14.4}_{-11.9}$	$0.9^{+2.0}_{-0.6}$	$29.8^{+13.0}_{-6.2}$	$9^{+3}_{-3} \times 10^{-2}$	$4^{+1}_{-1} \times 10^{-2}$	–	–

Notes. PMA: proper motion anomaly. $M_{\rm Obs}$ and $a_{\rm Obs}$ are the mass and semi-major axis obtained by combining theory and observations. $M_{\rm Theor}$ and $a_{\rm Theor}$ are the mass and semi-major axis obtained only from theory. $M_{\rm Stir}$ and $M_{\rm Mult}$ are the minimum masses to stir the disk, and the mass in the scenario of N equal-mass planets, respectively. $M_{\rm PMA}$ and $a_{\rm PMA}$ refer to the minimum planetary mass and semi-major axis considering only the proper motion anomaly.

3.6 Summary and Conclusions

In this paper, we presented observations of 19 stars using the SPHERE instrument, which were selected based on possible indicators of planet-disc interactions. These indicators are the presence of a warm disk, exocometary activity, exozodiacal dust grains, and planet-induced stirring. This sample is composed of spectral types ranging between F, A, and B, with A-type being the most typical, and with distances ranging between 11 and 148 parsecs. With our observations, we reach an average detection limit of $20\,M_{\rm Jup}$ at 100 au (50% detection probability). We detected 104 point sources with S/N over 5, of which we classified 96 of them as background sources using color-magnitude and proper motion diagram diagnostics. For five of the remaining point sources, we concluded that, given their angular separation and more significantly their magnitudes, they are likely to be background objects. The remaining three correspond to known stellar companions.

The observations also provided information about the detection limits in each system. We combined these limits, our best estimate of the disk location, and additional constraints from proper motion anomalies, with theoretical predictions to estimate plausible planetary-mass companions. If a planet had been detected in the sample, it would have been of great help to confront and possibly calibrate the planet-disk interaction models. However, our detection limits are an order of magnitude above the minimum masses predicted by recent theoretical models (e.g., Krivov & Booth 2018, Pearce et al. 2022, and reference therein). Therefore, with the sensitivity of our observations, we can conclude that they remain compatible with these recent models. However, these systems could be of interest for future surveys using new instruments or facilities (e.g., ERIS and JWST) whose detection limits could be of the same order of magnitude as the planetary masses estimated from the predictions presented in this paper.

3.7 Appendix of the article

3.7.1 Main observation properties.

3.7.2 List of identified point sources.

Table 3.5: Properties of identified point sources.

Name	PS#	Date [yy-mm-dd]	Sep [″]	Pos. Angle [degree]	Filter	Mag
HD106389	1	2019-04-18	0.455 ± 0.002	$+168.54 \pm 0.28$	BB_H	$5.94^{+0.14}_{-0.14}$
HD113556	1	2016-04-03	4.813 ± 0.004	-33.38 ± 0.05	BB_H	$12.34^{+0.20}_{-0.20}$
		2018-04-17	4.822 ± 0.024	-32.62 ± 0.21	DB_K1	$11.65^{+0.40}_{-0.40}$
					DB_K2	$11.78^{+0.40}_{-0.40}$

Table 3.5: Continued.

Name	PS#	Date [yy-mm-dd]	Sep [″]	Pos. Angle [degree]	Filter	Mag
	2	2016-04-03	4.521 ± 0.004	$+156.49 \pm 0.05$	BB_H	$12.71^{+0.14}_{-0.14}$
		2018-04-17	4.523 ± 0.026	$+155.51 \pm 0.18$	DB_K1	$12.31^{+0.20}_{-0.20}$
					DB_K2	$12.21^{+0.20}_{-0.20}$
	3	2016-04-03	4.930 ± 0.005	-85.31 ± 0.03	BB_H	$14.75^{+0.14}_{-0.14}$
		2018-04-17	4.867 ± 0.012	-84.86 ± 0.34	DB_K1	$14.44^{+0.20}_{-0.20}$
					DB_K2	$14.51^{+0.20}_{-0.20}$
	4	2016-04-03	5.106 ± 0.004	$+30.37 \pm 0.05$	BB_H	$9.29^{+0.15}_{-0.14}$
		2018-04-17	5.184 ± 0.022	$+30.86 \pm 0.15$	DB_K1	$8.96^{+0.21}_{-0.21}$
					DB_K2	$8.93^{+0.40}_{-0.40}$
	5	2016-04-03	4.301 ± 0.004	$+29.41 \pm 0.05$	BB_H	$15.32^{+0.14}_{-0.14}$
		2018-04-17	4.376 ± 0.021	$+29.92 \pm 0.21$	DB_K1	$15.01^{+0.20}_{-0.20}$
					DB_K2	$14.80^{+0.20}_{-0.20}$
	6	2016-04-03	4.011 ± 0.004	$+16.72 \pm 0.05$	BB_H	$15.45^{+0.14}_{-0.14}$
		2018-04-17	4.076 ± 0.023	$+17.41 \pm 0.18$	DB_K1	$14.98^{+0.20}_{-0.20}$
					DB_K2	$14.81^{+0.20}_{-0.20}$
	7	2016-04-03	3.221 ± 0.003	-168.66 ± 0.06	BB_H	$14.48^{+0.14}_{-0.14}$
		2018-04-17	3.182 ± 0.033	-170.00 ± 0.17	DB_K1	$14.37^{+0.20}_{-0.20}$
					DB_K2	$14.28^{+0.20}_{-0.20}$
	8	2016-04-03	1.989 ± 0.003	-164.49 ± 0.10	BB_H	$13.11^{+0.15}_{-0.15}$
		2018-04-17	1.943 ± 0.042	-166.32 ± 0.34	DB_K1	$14.00^{+0.20}_{-0.20}$
					DB_K2	$13.98^{+0.20}_{-0.20}$
	9	2016-04-03	3.512 ± 0.003	$+46.82 \pm 0.05$	BB_H	$15.48^{+0.14}_{-0.14}$
		2018-04-17	3.589 ± 0.021	$+47.03 \pm 0.35$	DB_K1	$15.36^{+0.20}_{-0.20}$
					DB_K2	$15.27^{+0.20}_{-0.20}$
	10	2016-04-03	3.058 ± 0.003	$+3.52 \pm 0.06$	BB_H	$15.87^{+0.14}_{-0.14}$
		2018-04-17	3.099 ± 0.027	$+4.72 \pm 0.12$	DB_K1	$15.51^{+0.20}_{-0.20}$

Table 3.5: Continued.

Name	PS#	Date [yy-mm-dd]	Sep [″]	Pos. Angle [degree]	Filter	Mag
					DB_K2	$15.25^{+0.20}_{-0.20}$
	11	2016-04-03	2.503 ± 0.003	$+139.45 \pm 0.07$	BB_H	$14.39^{+0.15}_{-0.15}$
		2018-04-17	2.530 ± 0.021	$+137.69 \pm 0.43$	DB_K1	$14.40^{+0.20}_{-0.20}$
					DB_K2	$14.19^{+0.20}_{-0.20}$
	12	2016-04-03	4.842 ± 0.005	$+102.63 \pm 0.03$	BB_H	$16.33^{+0.14}_{-0.14}$
		2018-04-17	4.903 ± 0.022	$+102.05 \pm 0.35$	DB_K1	$16.17^{+0.40}_{-0.40}$
					DB_K2	$--^{--}_{--}$
	13	2016-04-03	1.826 ± 0.003	$+126.71 \pm 0.08$	BB_H	$15.45^{+0.14}_{-0.14}$
		2018-04-17	1.859 ± 0.023	$+124.59 \pm 0.82$	DB_K1	$15.39^{+0.20}_{-0.20}$
					DB_K2	$15.54^{+0.21}_{-0.21}$
	14	2016-04-03	1.098 ± 0.003	$+99.27 \pm 0.11$	BB_H	$15.20^{+0.14}_{-0.14}$
		2018-04-17	1.147 ± 0.006	$+96.82 \pm 0.24$	DB_K1	$15.21^{+0.40}_{-0.40}$
					DB_K2	$--^{--}_{--}$
	15	2016-04-03	3.673 ± 0.004	-155.78 ± 0.05	BB_H	$16.86^{+0.14}_{-0.14}$
		2018-04-17	3.596 ± 0.039	-156.39 ± 0.41	DB_K1	$--^{--}_{--}$
					DB_K2	$16.20^{+0.50}_{-0.50}$
	16	2016-04-03	2.219 ± 0.004	-112.62 ± 0.07	BB_H	$17.36^{+0.14}_{-0.14}$
		2018-04-17	2.151 ± 0.028	-112.50 ± 0.73	DB_K1	$14.73^{+0.50}_{-0.59}$
					DB_K2	$--^{--}_{--}$
	17	2016-04-03	2.583 ± 0.004	$+131.28 \pm 0.08$	BB_H	$17.22^{+0.14}_{-0.14}$
		2018-04-17	$--\pm--$	$--\pm--$	DB_K1	$--^{--}_{--}$
					DB_K2	$--^{--}_{--}$
	18	2016-04-03	2.849 ± 0.004	$+97.89 \pm 0.07$	BB_H	$17.35^{+0.14}_{-0.14}$
		2018-04-17	2.898 ± 0.058	$+96.58 \pm 1.52$	DB_K1	$16.56^{+0.40}_{-0.40}$
					DB_K2	$16.41^{+0.40}_{-0.40}$
	19	2016-04-03	2.447 ± 0.005	$+153.75 \pm 0.11$	BB_H	$17.90^{+0.14}_{-0.14}$

Table 3.5: Continued.

Name	PS#	Date [yy-mm-dd]	Sep [″]	Pos. Angle [degree]	Filter	Mag
		2018-04-17	$---\pm---$	$---\pm---$	DB_K1	$--^{--}_{--}$
					DB_K2	$--^{--}_{--}$
	20	2016-04-03	4.291 ± 0.007	$+108.86 \pm 0.08$	BB_H	$18.33^{+0.15}_{-0.15}$
		2018-04-17	$---\pm---$	$---\pm---$	DB_K1	$--^{--}_{--}$
					DB_K2	$--^{--}_{--}$
	21	2016-04-03	4.720 ± 0.006	$+165.77 \pm 0.06$	BB_H	$18.21^{+0.14}_{-0.14}$
		2018-04-17	$---\pm---$	$---\pm---$	DB_K1	$--^{--}_{--}$
					DB_K2	$--^{--}_{--}$
	22	2016-04-03	6.162 ± 0.007	-82.41 ± 0.03	BB_H	$16.00^{+0.15}_{-0.15}$
		2018-04-17	6.111 ± 0.027	-81.91 ± 0.25	DB_K1	$14.65^{+0.40}_{-0.40}$
					DB_K2	$--^{--}_{--}$
	23	2016-04-03	5.518 ± 0.007	-15.08 ± 0.05	BB_H	$16.24^{+0.15}_{-0.16}$
		2018-04-17	5.529 ± 0.033	-14.10 ± 0.51	DB_K1	$16.87^{+0.40}_{-0.40}$
					DB_K2	$--^{--}_{--}$
HD54341	1	2015-11-18	4.404 ± 0.003	$+138.58 \pm 0.04$	DB_H2	$15.24^{+0.20}_{-0.20}$
					DB_H3	$15.09^{+0.20}_{-0.20}$
		2018-11-23	4.420 ± 0.005	$+130.00 \pm 0.07$	DB_J2	$15.83^{+0.21}_{-0.21}$
					DB_J3	$15.73^{+0.36}_{-0.48}$
	2	2015-11-18	3.108 ± 0.002	$+132.59 \pm 0.04$	DB_H2	$15.43^{+0.20}_{-0.20}$
					DB_H3	$15.37^{+0.20}_{-0.20}$
		2018-11-23	3.121 ± 0.005	$+133.09 \pm 0.10$	DB_J2	$16.13^{+0.23}_{-0.23}$
					DB_J3	$15.87^{+0.21}_{-0.21}$
HD112810	1	2016-03-16	5.788 ± 0.006	-2.01 ± 0.04	DB_H2	$13.76^{+0.22}_{-0.21}$
					DB_H3	$13.66^{+0.21}_{-0.21}$
		2020-02-18	5.823 ± 0.041	-1.16 ± 0.23	BB_H	$15.11^{+0.34}_{-0.34}$
	2	2016-03-16	6.183 ± 0.005	-75.84 ± 0.05	DB_H2	$13.62^{+0.21}_{-0.22}$

Table 3.5: Continued.

Name	PS#	Date [yy-mm-dd]	Sep [″]	Pos. Angle [degree]	Filter	Mag
					DB_H3	$13.64^{+0.22}_{-0.23}$
		2020-02-18	6.085 ± 0.006	-75.16 ± 0.05	BB_H	$13.41^{+0.27}_{-0.27}$
	3	2016-03-16	5.683 ± 0.004	-48.56 ± 0.04	DB_H2	$9.19^{+0.21}_{-0.21}$
					DB_H3	$9.07^{+0.21}_{-0.21}$
		2020-02-18	5.590 ± 0.005	-47.92 ± 0.27	BB_H	$10.05^{+0.27}_{-0.27}$
HD36546	1	2019-11-16	6.179 ± 0.007	$+169.07 \pm 0.03$	DB_K1	$11.08^{+0.21}_{-0.21}$
					DB_K2	$10.91^{+0.21}_{-0.21}$
HD142446	1	2016-05-15	0.476 ± 0.003	-140.12 ± 0.35	BB_H	$15.02^{+0.20}_{-0.20}$
		2017-05-28	0.453 ± 0.003	-140.57 ± 0.34	BB_H	$14.98^{+0.20}_{-0.20}$
	2	2016-05-15	3.823 ± 0.006	-96.67 ± 0.06	BB_H	$17.17^{+0.20}_{-0.21}$
		2017-05-28	3.801 ± 0.004	-96.38 ± 0.03	BB_H	$16.89^{+0.20}_{-0.20}$
	3	2016-05-15	4.237 ± 0.005	-119.93 ± 0.07	BB_H	$17.00^{+0.20}_{-0.20}$
		2017-05-28	4.214 ± 0.003	-119.85 ± 0.04	BB_H	$16.49^{+0.20}_{-0.20}$
	4	2016-05-15	4.114 ± 0.005	$+147.07 \pm 0.06$	BB_H	$14.76^{+0.20}_{-0.20}$
		2017-05-28	4.106 ± 0.003	$+146.72 \pm 0.04$	BB_H	$14.10^{+0.15}_{-0.15}$
HD127750	1	2016-04-14	4.341 ± 0.006	$+130.19 \pm 0.07$	BB_H	$17.38^{+0.20}_{-0.20}$
		2017-05-29	4.343 ± 0.005	$+129.72 \pm 0.07$	BB_H	$17.22^{+0.20}_{-0.20}$
	2	2016-04-14	4.193 ± 0.005	-67.02 ± 0.06	BB_H	$17.12^{+0.20}_{-0.20}$
		2017-05-29	4.182 ± 0.007	-66.61 ± 0.07	BB_H	$17.28^{+0.20}_{-0.20}$
	3	2016-04-14	3.541 ± 0.003	$+135.65 \pm 0.05$	BB_H	$15.97^{+0.20}_{-0.20}$
		2017-05-29	3.553 ± 0.003	$+135.16 \pm 0.05$	BB_H	$16.12^{+0.20}_{-0.20}$
	4	2016-04-14	2.552 ± 0.003	$+66.63 \pm 0.05$	BB_H	$15.04^{+0.20}_{-0.20}$
		2017-05-29	2.583 ± 0.003	$+66.55 \pm 0.05$	BB_H	$15.17^{+0.20}_{-0.20}$
	5	2016-04-14	4.642 ± 0.003	-143.74 ± 0.04	BB_H	$9.58^{+0.15}_{-0.15}$
		2017-05-29	4.620 ± 0.003	-143.85 ± 0.04	BB_H	$9.78^{+0.15}_{-0.15}$
HD86087	1	2015-04-11	5.055 ± 0.013	$+103.93 \pm 0.12$	DB_H2	$17.34^{+0.30}_{-0.35}$

Table 3.5: Continued.

Name	PS#	Date [yy-mm-dd]	Sep [″]	Pos. Angle [degree]	Filter	Mag
					DB_H3	$17.46^{+0.31}_{-0.39}$
		2017-05-19	5.140 ± 0.005	$+104.04 \pm 0.06$	BB_H	$17.49^{+0.21}_{-0.21}$
	2	2015-04-11	0.979 ± 0.003	-93.74 ± 0.14	DB_H2	$11.58^{+0.20}_{-0.20}$
					DB_H3	$11.59^{+0.20}_{-0.20}$
		2017-05-19	0.916 ± 0.002	-95.25 ± 0.12	BB_H	$11.18^{+0.20}_{-0.20}$
	3	2015-04-11	3.353 ± 0.006	$+2.77 \pm 0.05$	DB_H2	$14.14^{+0.20}_{-0.20}$
					DB_H3	$14.11^{+0.20}_{-0.20}$
		2017-05-19	3.345 ± 0.005	$+3.97 \pm 0.03$	BB_H	$13.60^{+0.20}_{-0.20}$
	4	2015-04-11	4.576 ± 0.006	-53.10 ± 0.08	DB_H2	$13.63^{+0.20}_{-0.20}$
					DB_H3	$13.42^{+0.20}_{-0.20}$
		2017-05-19	4.538 ± 0.004	-52.83 ± 0.06	BB_H	$13.00^{+0.15}_{-0.15}$
HD71043	1	2017-12-30	1.795 ± 0.003	-77.90 ± 0.08	BB_H	$16.30^{+0.20}_{-0.20}$
		2018-12-27	1.772 ± 0.004	-78.39 ± 0.10	BB_H	$16.49^{+0.20}_{-0.20}$
	2	2017-12-30	3.262 ± 0.003	-40.06 ± 0.05	BB_H	$15.88^{+0.30}_{-0.30}$
		2018-12-27	3.237 ± 0.003	-39.93 ± 0.05	BB_H	$15.97^{+0.20}_{-0.20}$
	3	2017-12-30	5.828 ± 0.007	-87.65 ± 0.03	BB_H	$16.38^{+0.20}_{-0.20}$
		2018-12-27	5.804 ± 0.005	-87.78 ± 0.04	BB_H	$16.54^{+0.21}_{-0.21}$
	4	2017-12-30	2.972 ± 0.003	$+150.59 \pm 0.06$	BB_H	$11.87^{+0.10}_{-0.10}$
		2018-12-27	2.988 ± 0.003	$+150.43 \pm 0.05$	BB_H	$11.92^{+0.10}_{-0.10}$
HD103703	1	2018-04-07	4.753 ± 0.014	-83.49 ± 0.10	BB_H	$17.95^{+0.21}_{-0.21}$
		2019-04-06	4.728 ± 0.009	-83.36 ± 0.06	BB_H	$17.65^{+0.20}_{-0.20}$
	2	2018-04-07	3.401 ± 0.009	$+125.15 \pm 0.15$	BB_H	$17.12^{+0.21}_{-0.21}$
		2019-04-06	3.426 ± 0.005	$+124.76 \pm 0.08$	BB_H	$17.01^{+0.20}_{-0.20}$
	3	2018-04-07	5.324 ± 0.011	$+168.78 \pm 0.10$	BB_H	$16.81^{+0.33}_{-0.38}$
		2019-04-06	5.328 ± 0.006	$+168.47 \pm 0.06$	BB_H	$16.50^{+0.22}_{-0.24}$
	4	2018-04-07	4.765 ± 0.005	$+42.70 \pm 0.06$	BB_H	$15.81^{+0.20}_{-0.20}$

Table 3.5: Continued.

Name	PS#	Date [yy-mm-dd]	Sep [″]	Pos. Angle [degree]	Filter	Mag
		2019-04-06	4.800 ± 0.005	$+42.92 \pm 0.05$	BB_H	$15.73^{+0.20}_{-0.20}$
	5	2018-04-07	4.034 ± 0.005	$+123.54 \pm 0.06$	BB_H	$15.50^{+0.20}_{-0.20}$
		2019-04-06	4.051 ± 0.004	$+123.24 \pm 0.06$	BB_H	$15.44^{+0.20}_{-0.20}$
	6	2018-04-07	0.758 ± 0.003	-42.24 ± 0.19	BB_H	$8.13^{+0.20}_{-0.20}$
		2019-04-06	0.760 ± 0.003	-41.99 ± 0.20	BB_H	$8.00^{+0.20}_{-0.20}$
	7	2018-04-07	1.440 ± 0.002	-163.33 ± 0.09	BB_H	$13.17^{+0.20}_{-0.20}$
		2019-04-06	1.423 ± 0.002	-164.37 ± 0.09	BB_H	$13.20^{+0.20}_{-0.20}$
	8	2018-04-07	4.395 ± 0.006	$+107.62 \pm 0.04$	BB_H	$16.21^{+1.49}_{-2.45}$
		2019-04-06	4.422 ± 0.005	$+107.41 \pm 0.04$	BB_H	$14.53^{+0.30}_{-0.30}$
	9	2018-04-07	2.914 ± 0.003	$+159.54 \pm 0.07$	BB_H	$14.61^{+0.40}_{-0.40}$
		2019-04-06	2.919 ± 0.004	$+158.97 \pm 0.05$	BB_H	$14.40^{+0.15}_{-0.15}$
	10	2018-04-07	2.961 ± 0.004	-106.71 ± 0.05	BB_H	$13.79^{+0.20}_{-0.20}$
		2019-04-06	2.929 ± 0.004	-106.69 ± 0.05	BB_H	$13.88^{+0.20}_{-0.20}$
	11	2018-04-07	4.672 ± 0.006	-164.94 ± 0.03	BB_H	$13.49^{+0.10}_{-0.10}$
		2019-04-06	4.657 ± 0.005	-165.23 ± 0.04	BB_H	$13.28^{+0.10}_{-0.10}$
	12	2018-04-07	5.316 ± 0.006	-33.22 ± 0.06	BB_H	$13.45^{+0.21}_{-0.21}$
		2019-04-06	5.302 ± 0.005	-32.78 ± 0.05	BB_H	$13.25^{+0.21}_{-0.21}$
	13	2018-04-07	2.848 ± 0.003	$+20.62 \pm 0.06$	BB_H	$12.44^{+0.20}_{-0.20}$
		2019-04-06	2.868 ± 0.003	$+21.18 \pm 0.05$	BB_H	$13.70^{+0.20}_{-0.20}$
HD106036	1	2019-06-08	3.433 ± 0.005	-113.34 ± 0.06	BB_H	$17.10^{+0.20}_{-0.20}$
		2020-01-29	3.432 ± 0.009	-113.09 ± 0.12	BB_H	$16.79^{+0.20}_{-0.20}$
	2	2019-06-08	3.097 ± 0.004	-94.81 ± 0.06	BB_H	$16.76^{+0.20}_{-0.20}$
		2020-01-29	3.096 ± 0.010	-94.56 ± 0.10	BB_H	$16.69^{+0.20}_{-0.20}$
	3	2019-06-08	6.064 ± 0.006	-93.32 ± 0.04	BB_H	$16.29^{+0.23}_{-0.25}$
		2020-01-29	6.060 ± 0.012	-93.18 ± 0.11	BB_H	$16.84^{+0.35}_{-0.47}$
	4	2019-06-08	5.386 ± 0.005	-73.80 ± 0.05	BB_H	$13.58^{+0.23}_{-0.23}$

Table 3.5: Continued.

Name	PS#	Date [yy-mm-dd]	Sep [″]	Pos. Angle [degree]	Filter	Mag
		2020-01-29	5.382 ± 0.012	-73.64 ± 0.11	BB_H	$13.73^{+0.33}_{-0.38}$
	5	2019-06-08	4.969 ± 0.004	$+39.28 \pm 0.04$	BB_H	$16.76^{+0.20}_{-0.20}$
		2020-01-29	4.985 ± 0.009	$+39.22 \pm 0.11$	BB_H	$17.06^{+0.21}_{-0.20}$
	6	2019-06-08	2.999 ± 0.003	$+131.37 \pm 0.06$	BB_H	$16.56^{+0.20}_{-0.20}$
		2020-01-29	2.989 ± 0.006	$+131.20 \pm 0.12$	BB_H	$16.46^{+0.20}_{-0.20}$
	7	2019-06-08	4.237 ± 0.004	-58.29 ± 0.04	BB_H	$16.67^{+0.20}_{-0.20}$
		2020-01-29	4.243 ± 0.007	-58.11 ± 0.09	BB_H	$16.61^{+0.20}_{-0.20}$
	8	2019-06-08	4.797 ± 0.005	-180.62 ± 0.11	BB_H	$16.62^{+0.20}_{-0.20}$
		2020-01-29	4.781 ± 0.017	-180.71 ± 0.25	BB_H	$16.55^{+0.20}_{-0.20}$
	9	2019-06-08	5.025 ± 0.004	-118.51 ± 0.04	BB_H	$16.41^{+0.21}_{-0.21}$
		2020-01-29	5.015 ± 0.008	-118.39 ± 0.07	BB_H	$16.80^{+0.21}_{-0.21}$
	10	2019-06-08	4.668 ± 0.004	-151.04 ± 0.04	BB_H	$16.37^{+0.20}_{-0.20}$
		2020-01-29	4.648 ± 0.009	-151.04 ± 0.09	BB_H	$16.73^{+0.20}_{-0.20}$
	11	2019-06-08	2.424 ± 0.003	$+163.05 \pm 0.05$	BB_H	$16.08^{+0.20}_{-0.20}$
		2020-01-29	2.414 ± 0.006	$+162.89 \pm 0.09$	BB_H	$16.09^{+0.20}_{-0.20}$
	12	2019-06-08	4.343 ± 0.003	$+35.25 \pm 0.04$	BB_H	$16.32^{+0.20}_{-0.20}$
		2020-01-29	4.358 ± 0.006	$+35.24 \pm 0.08$	BB_H	$16.24^{+0.20}_{-0.20}$
	13	2019-06-08	4.051 ± 0.004	-153.93 ± 0.04	BB_H	$16.12^{+0.20}_{-0.20}$
		2020-01-29	4.033 ± 0.007	-153.89 ± 0.07	BB_H	$16.40^{+0.20}_{-0.20}$
	14	2019-06-08	4.803 ± 0.004	-56.85 ± 0.04	BB_H	$16.14^{+0.20}_{-0.20}$
		2020-01-29	4.806 ± 0.006	-56.67 ± 0.06	BB_H	$16.29^{+0.20}_{-0.20}$
	15	2019-06-08	6.025 ± 0.004	-171.55 ± 0.04	BB_H	$15.58^{+0.21}_{-0.21}$
		2020-01-29	6.012 ± 0.006	-171.59 ± 0.06	BB_H	$15.89^{+0.25}_{-0.25}$
	16	2019-06-08	6.063 ± 0.004	$+10.48 \pm 0.04$	BB_H	$16.28^{+0.21}_{-0.21}$
		2020-01-29	6.077 ± 0.006	$+10.52 \pm 0.06$	BB_H	$16.52^{+0.24}_{-0.25}$
	17	2019-06-08	1.543 ± 0.003	$+154.99 \pm 0.08$	BB_H	$15.15^{+0.20}_{-0.20}$

Table 3.5: Continued.

Name	PS#	Date [yy-mm-dd]	Sep [″]	Pos. Angle [degree]	Filter	Mag
		2020-01-29	1.529 ± 0.003	$+154.49 \pm 0.11$	BB_H	$15.01^{+0.20}_{-0.20}$
	18	2019-06-08	6.552 ± 0.004	$+162.56 \pm 0.04$	BB_H	$10.53^{+0.21}_{-0.21}$
		2020-01-29	6.545 ± 0.008	$+162.50 \pm 0.06$	BB_H	$11.28^{+0.27}_{-0.29}$
	19	2019-06-08	1.179 ± 0.003	-15.49 ± 0.12	BB_H	$14.13^{+0.20}_{-0.20}$
		2020-01-29	1.186 ± 0.003	-15.10 ± 0.11	BB_H	$14.00^{+0.20}_{-0.20}$
	20	2019-06-08	5.412 ± 0.004	$+121.48 \pm 0.04$	BB_H	$15.62^{+0.21}_{-0.21}$
		2020-01-29	5.411 ± 0.005	$+121.34 \pm 0.05$	BB_H	$15.78^{+0.22}_{-0.22}$
	21	2019-06-08	5.207 ± 0.005	-12.11 ± 0.03	BB_H	$14.05^{+0.21}_{-0.21}$
		2020-01-29	5.218 ± 0.005	-11.99 ± 0.04	BB_H	$14.26^{+0.22}_{-0.21}$
	22	2019-06-08	7.555 ± 0.007	-9.91 ± 0.03	BB_H	$14.13^{+0.22}_{-0.22}$
		2020-01-29	7.574 ± 0.009	-9.84 ± 0.05	BB_H	$15.16^{+0.24}_{-0.25}$
	23	2019-06-08	4.458 ± 0.003	-132.11 ± 0.04	BB_H	$15.24^{+0.20}_{-0.20}$
		2020-01-29	4.447 ± 0.004	-132.06 ± 0.05	BB_H	$15.41^{+0.20}_{-0.20}$
	24	2019-06-08	3.757 ± 0.003	$+73.61 \pm 0.03$	BB_H	$15.19^{+0.20}_{-0.20}$
		2020-01-29	3.766 ± 0.005	$+73.47 \pm 0.04$	BB_H	$15.22^{+0.20}_{-0.20}$
	25	2019-06-08	3.756 ± 0.003	$+168.13 \pm 0.03$	BB_H	$15.10^{+0.20}_{-0.20}$
		2020-01-29	3.745 ± 0.004	$+168.01 \pm 0.03$	BB_H	$15.14^{+0.20}_{-0.20}$
	26	2019-06-08	6.717 ± 0.005	$+96.68 \pm 0.03$	BB_H	$14.33^{+0.20}_{-0.20}$
		2020-01-29	6.723 ± 0.006	$+96.59 \pm 0.03$	BB_H	$14.59^{+0.21}_{-0.21}$
	27	2019-06-08	4.906 ± 0.004	$+71.48 \pm 0.03$	BB_H	$14.98^{+0.20}_{-0.20}$
		2020-01-29	4.917 ± 0.004	$+71.38 \pm 0.03$	BB_H	$15.03^{+0.20}_{-0.20}$
	28	2019-06-08	7.328 ± 0.006	$+116.43 \pm 0.03$	BB_H	$12.84^{+0.20}_{-0.21}$
		2020-01-29	7.331 ± 0.006	$+116.33 \pm 0.03$	BB_H	$12.91^{+0.21}_{-0.21}$
	29	2019-06-08	6.229 ± 0.004	-14.48 ± 0.04	BB_H	$13.80^{+0.21}_{-0.21}$
		2020-01-29	6.240 ± 0.005	-14.38 ± 0.04	BB_H	$14.06^{+0.21}_{-0.21}$
	30	2019-06-08	4.179 ± 0.004	$+13.12 \pm 0.03$	BB_H	$14.43^{+0.20}_{-0.20}$

Table 3.5: Continued.

Name	PS#	Date [yy-mm-dd]	Sep [″]	Pos. Angle [degree]	Filter	Mag
		2020-01-29	4.194 ± 0.004	$+13.17 \pm 0.03$	BB_H	$14.46^{+0.20}_{-0.20}$
	31	2019-06-08	1.584 ± 0.002	-151.80 ± 0.07	BB_H	$12.75^{+0.20}_{-0.20}$
		2020-01-29	1.570 ± 0.002	-151.73 ± 0.07	BB_H	$12.62^{+0.20}_{-0.20}$
	32	2019-06-08	4.847 ± 0.003	-113.04 ± 0.04	BB_H	$14.69^{+0.29}_{-0.29}$
		2020-01-29	4.838 ± 0.003	-112.92 ± 0.04	BB_H	$14.91^{+0.29}_{-0.30}$
	33	2019-06-08	3.233 ± 0.003	$+33.67 \pm 0.05$	BB_H	$13.83^{+0.37}_{-0.39}$
		2020-01-29	3.247 ± 0.003	$+33.80 \pm 0.05$	BB_H	$13.89^{+0.39}_{-0.45}$
	34	2019-06-08	3.749 ± 0.003	$+111.93 \pm 0.05$	BB_H	$12.92^{+0.29}_{-0.29}$
		2020-01-29	3.749 ± 0.003	$+111.73 \pm 0.04$	BB_H	$12.97^{+0.30}_{-0.30}$
	35	2019-06-08	1.753 ± 0.002	$+62.77 \pm 0.07$	BB_H	$12.00^{+0.20}_{-0.20}$
		2020-01-29	1.767 ± 0.002	$+62.54 \pm 0.06$	BB_H	$11.80^{+0.20}_{-0.20}$
	36	2019-06-08	3.533 ± 0.003	$+89.54 \pm 0.03$	BB_H	$13.30^{+0.34}_{-0.36}$
		2020-01-29	3.540 ± 0.003	$+89.33 \pm 0.04$	BB_H	$13.33^{+0.29}_{-0.29}$
	37	2019-06-08	5.114 ± 0.004	-100.77 ± 0.04	BB_H	$13.65^{+0.21}_{-0.21}$
		2020-01-29	5.107 ± 0.005	-100.64 ± 0.04	BB_H	$13.85^{+0.21}_{-0.21}$
	38	2019-06-08	4.740 ± 0.003	$+111.81 \pm 0.04$	BB_H	$13.58^{+0.29}_{-0.29}$
		2020-01-29	4.742 ± 0.004	$+111.64 \pm 0.03$	BB_H	$13.67^{+0.30}_{-0.30}$
	39	2019-06-08	6.158 ± 0.005	-19.18 ± 0.03	BB_H	$12.48^{+0.21}_{-0.21}$
		2020-01-29	6.169 ± 0.006	-19.07 ± 0.03	BB_H	$12.73^{+0.21}_{-0.21}$
	40	2019-06-08	5.460 ± 0.004	-61.11 ± 0.04	BB_H	$12.41^{+0.20}_{-0.21}$
		2020-01-29	5.462 ± 0.004	-60.96 ± 0.05	BB_H	$12.63^{+0.21}_{-0.21}$
	41	2019-06-08	6.224 ± 0.004	-77.17 ± 0.04	BB_H	$10.87^{+0.21}_{-0.21}$
		2020-01-29	6.221 ± 0.004	-77.04 ± 0.04	BB_H	$11.17^{+0.21}_{-0.21}$
	42	2019-06-08	5.216 ± 0.004	$+99.05 \pm 0.04$	BB_H	$10.46^{+0.20}_{-0.20}$
		2020-01-29	5.221 ± 0.004	$+98.92 \pm 0.04$	BB_H	$10.58^{+0.21}_{-0.21}$
	43	2019-06-08	2.927 ± 0.006	$+26.89 \pm 0.10$	BB_H	$7.58^{+0.35}_{-0.37}$

Table 3.5: Continued.

Name	PS#	Date [yy-mm-dd]	Sep [″]	Pos. Angle [degree]	Filter	Mag
		2020-01-29	2.927 ± 0.003	$+26.94 \pm 0.05$	BB_H	$6.55^{+0.35}_{-0.35}$
HD37306	1	2015-10-28	1.357 ± 0.003	$+78.22 \pm 0.09$	DB_H2	$15.45^{+0.20}_{-0.20}$
					DB_H3	$15.33^{+0.20}_{-0.20}$
		2019-11-24	1.296 ± 0.004	$+73.34 \pm 0.12$	DB_K1	$15.18^{+0.20}_{-0.20}$
					DB_K2	$14.95^{+0.20}_{-0.20}$

Notes. The column "Mag" corresponds to the absolute magnitude of the point source assuming a common distance with the host-star. "PS#" means "Point Source number".

3.7.3 Proper motion diagrams

TABLE 3.4: Log of the observations.

Name	Program ID	Date yy-mm-dd	Filter	ΔPA [deg]	True North[a] [deg]	Pixel scale[a] [mas/pixel]	DIT[b] [sec]	N[c]	Num. frames	Coher. time[d] [msec]	Wind speed[d] [m/s]	Seeing[e] [″]
HD112810	096.C-0713(C)	2016-03-16	H23	18.54	-1.760 ± 0.040	12.247 ± 0.003	64	1	32	1.7(1.3-2.0)	9.5(9.0-9.9)	1.4(1.3-1.4)
	0101.C-0016(A)	2020-02-18	H	52.81	-1.760 ± 0.040	12.246 ± 0.009	32	14	364	5.0(2.3-12.4)	7.0(0.3-8.2)	1.0(0.3-1.5)
HD36968	096.C-0713(B)	2015-11-19	H23	30.27	-1.760 ± 0.040	12.247 ± 0.003	64	1	32	1.7(1.4-2.1)	3.6(3.1-4.2)	1.0(0.8-1.3)
HD54341	096.C-0713(B)	2015-11-18	H23	24.71	-1.760 ± 0.040	12.247 ± 0.003	64	1	32	1.9(1.6-2.3)	5.5(5.1-5.9)	1.1(1.0-1.3)
	0102.C-0188(A)	2018-11-23	J23	46.33	-1.760 ± 0.040	12.247 ± 0.013	64	4	64	5.0(3.0-6.5)	2.3(1.8-2.9)	0.9(0.9-1.1)
HD10472	096.C-0713(A)	2015-11-09	H23	13.53	-1.806 ± 0.052	12.214 ± 0.011	64	1	32	1.4(1.0-1.7)	13.8(13.0-14.5)	1.1(1.0-1.4)
HD142446	097.C-0330(A)	2016-05-15	H	33.94	-1.680 ± 0.076	12.244 ± 0.017	64	1	32	3.0(2.2-4.1)	8.7(7.9-10.4)	1.2(1.0-1.3)
	099.C-0402(A)	2017-05-27	H	70.43	-1.802 ± 0.042	12.245 ± 0.010	16	4	256	2.4(1.9-2.8)	10.5(8.8-13.0)	1.0(0.8-1.2)
HD127750	097.C-0330(A)	2016-04-14	H	20.83	-1.760 ± 0.040	12.246 ± 0.009	32	2	64	7.5(4.4-10.0)	3.8(3.0-4.9)	0.8(0.7-0.9)
	099.C-0402(A)	2017-05-28	H	44.26	-1.802 ± 0.042	12.245 ± 0.010	32	2	128	2.2(1.3-3.2)	10.7(8.0-13.2)	1.1(0.9-1.3)
HD113556	097.C-0330(A)	2016-04-03	H	14.46	-1.729 ± 0.054	12.238 ± 0.013	64	1	32	7.7(5.8-9.1)	8.1(7.8-8.7)	0.6(0.6-0.7)
	1100.C-0481(F)	2018-04-17	K12	31.00	-1.760 ± 0.040	12.255 ± 0.005	96	3	48	4.6(3.5-5.7)	6.6(5.0-7.4)	1.6(1.4-1.8)
HD86087	095.C-0274(A)	2015-04-11	H23	17.01	-1.771 ± 0.076	12.221 ± 0.027	32	2	48	2.8(1.8-4.3)	0.7(0.2-1.3)	0.9(0.9-1.0)
	099.C-0402(A)	2017-05-19	H	33.16	-1.785 ± 0.064	12.236 ± 0.016	16	4	256	6.0(3.7-8.5)	5.3(3.7-6.7)	0.8(0.7-0.9)
HD71043	0100.C-0604(A)	2017-12-29	H	28.72	-1.789 ± 0.060	12.243 ± 0.013	16	4	192	8.7(6.0-11.4)	3.7(1.4-4.3)	1.0(0.8-1.2)
	0102.C-0436(A)	2018-12-27	H	34.30	-1.769 ± 0.047	12.247 ± 0.010	4	12	768	9.6(8.0-12.1)	4.7(4.2-5.5)	0.9(0.8-1.1)
HD103703	0100.C-0604(A)	2018-04-06	H	23.01	-1.744 ± 0.066	12.237 ± 0.016	8	8	384	3.2(2.3-3.9)	13.2(11.8-14.4)	1.2(1.0-1.4)
	0102.C-0436(A)	2019-04-06	H	23.32	-1.785 ± 0.063	12.238 ± 0.014	16	12	192	7.1(3.7-11.7)	2.8(2.3-3.2)	1.2(1.0-1.4)
HD106036	0102.C-0436(A)	2019-06-08	H	23.56	-1.760 ± 0.040	12.246 ± 0.009	32	4	49	4.0(3.4-4.9)	7.3(6.9-7.7)	1.1(1.0-1.1)
	0102.C-0436(A)	2020-01-29	H	25.63	-1.760 ± 0.040	12.246 ± 0.009	4	14	280	3.6(2.7-4.5)	6.7(6.3-7.6)	1.3(1.1-1.4)
HD106389	0102.C-0436(A)	2019-04-18	H	44.13	-1.785 ± 0.063	12.238 ± 0.014	∼ 0.8	16	2048	12.3(8.4-21.9)	3.4(2.6-4.1)	0.8(0.7-1.0)
HD36546	0104.C-0093(A)	2019-11-16	K12	20.29	-1.795 ± 0.049	12.263 ± 0.011	64	4	64	5.5(4.1-6.6)	4.4(4.1-5.0)	1.7(1.6-2.0)
HD56537	0104.C-0093(A)	2019-12-03	K12	27.23	-1.760 ± 0.040	12.256 ± 0.003	4	60	880	7.5(4.4-13.1)	4.4(1.3-6.8)	1.2(1.0-1.5)
HD37306	0104.C-0093(A)	2019-11-24	K12	26.60	-1.795 ± 0.049	12.263 ± 0.011	64	4	64	5.2(3.4-8.6)	1.9(0.4-3.1)	0.9(0.7-1.0)
	095.C-0212(B)	2015-10-28	H23	29.20	-1.818 ± 0.039	12.251 ± 0.010	32	1	48	1.6(1.4-2.1)	5.0(4.0-5.9)	0.9(0.8=1.1)
HD38678	0104.C-0093(A)	2019-12-12	K12	21.97	-1.760 ± 0.040	12.256 ± 0.003	4	60	960	18.1(10.9-23.8)	1.5(0.0-2.7)	0.9(0.8-1.2)
HD80007	0104.C-0093(A)	2019-12-31	K12	25.76	-1.763 ± 0.051	12.258 ± 0.011	2	50	1600	10.0(8.2-12.8)	2.9(1.6-5.0)	1.4(1.3-1.7)
HD2262	0104.C-0093(A)	2019-10-10	K12	44.78	-1.806 ± 0.051	12.236 ± 0.009	8	30	480	10.2(5.7-16.1)	3.4(1.8-5.9)	1.0(0.9-1.1)
HD102647	0104.C-0093(A)	2020-02-22	K12	28.42	-1.795 ± 0.049	12.263 ± 0.011	2	50	1600	5.1(2.7-7.7)	5.9(4.6-7.3)	1.4(1.2-1.8)

Notes. The median value registered is tabulated for the wind speed, coherence time, and seeing, while the minimum and maximum registered values are in parentheses. All observations were made using an ND_1.0. [(a)] Values calculated by the SPHERE-DC using public astrometric observations. For those without any observation, the values provided by Maire et al. (2021) were considered. [(b)] DIT = detector integration time. [(c)] N = NDIT, number of frames per fits file. [(d)] DIMM measured values during the observations. [(e)] Seeing measured on the image analysis detector (at the pointing location).

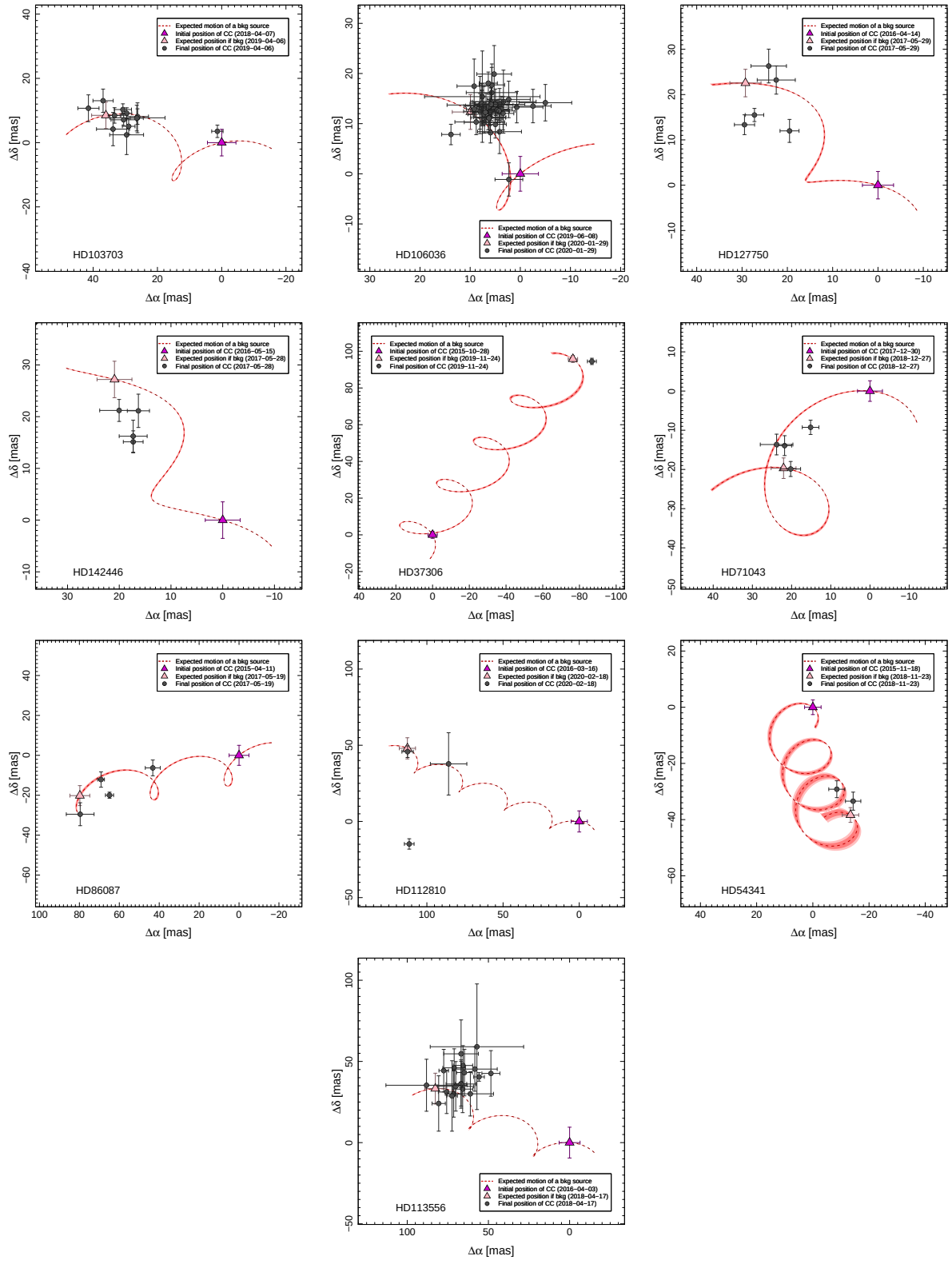

FIGURE 3.7: Same as Figure 3.4 for all the other targets with a second epoch.

Chapter 4

Summary and conclusions

In this thesis, we focused on two important challenges of direct imaging and the search for planets: improvements in data reduction, and a search for planets for systems displaying planet-disk interaction indicators. From the point of view of improvements, we have worked with the Naco instrument mounted until 2019 at the VLT. This study (published in Godoy et al. 2022) was developed as part of the ISPY consortium, to solve one of the challenges in the post-processing of the NaCo-AGPM data. These challenges are related to the centering and optimization of detections using frame selection. NaCo is a first-generation instrument designed for direct imaging, and it presented important challenges such as the correct identification of the star behind its vortex-AGPM-type coronagraph. We designed a new technique that allowed us to use the data itself to calibrate and determine the position of the star behind the AGPM in the science sequence observations. We managed to obtain the position of the star with an accuracy typically of 0.2 pixels, the same order of magnitude as second-generation instruments such as SPHERE.

In the same line, we studied how the selection of frames affects the final image and point sources. This point is extremely important given the great diversity of frames obtained per observation, the number of which can vary between 10 000 and 30 000 for observations that can last between 2 and 4 consecutive hours. For this we used the results of the centering analysis (the parameters obtained from different modeling and fitting), to characterize each of the frame (frame registration). In addition, we incorporated an extra analysis that allowed us to measure the inhomogeneities formed by the speckles around the coronagraph. With this, we then quantified the quality of the centering and the number of speckles, in the inner regions close to the coronagraph. We made this approximation using the pseudo-Zernike moments, whose decomposition gives us values on the azimuthal inhomogeneities, and radial homogeneities. Combining all the information that characterizes each frame allowed us to design selection criteria based on how similar or different the frames are.

We analyzed the effect of frame selection following different strategies for the centering; use the position of the star, the position of the coronagraph, or a combination of both. We concluded that frame selection can improve point source detection marginally, and that the choice of the centering yields the greatest source of signal-to-noise improvements. The best centering strategy was the combination of star-coronagraph positions, reaching an improvement of $\sim$ 20% in the case of β Pictoris b and $\sim$ 100% in the case of

R crA b, while the worst result was obtained by using only the coronagraph position in the entire post-processing. These procedures and approaches were published in a public pipeline called CenteR (github: https://github.com/Nico-Godoy/CenteR.git).

Regarding the second focus of this thesis, we searched for giant planets in systems that show possible signs of planet-disc interactions. The indicators considered in our study were the presence of a warm disk, exocometary activity, exozodiacal dust grains, and planet-induced stirring. We have constructed a sample of 19 stars, composed of F, A, and B spectral types, and distances ranging from 11 to 149 parsecs. This sample was observed using the SPHERE instrument with IFS and IRDIS modes, in bands H2H3, K1K2, and H (depending on each system and program). The data was reduced by the SPHERE Data Center, and we used the ANDROMEDA and no-ADI products for the characterization of our sample and point-sources detected. We identified 104 point sources, of which 96 were classified as background stars using color-magnitude and proper motion diagrams. Of the remaining point sources, 5 of them were classified as likely background stars, given their magnitudes and angular separations. The remaining 3 correspond to known stellar companions.

In addition to the identification of point-like sources and the determination of their nature (stellar companions and background stars), we used the contrast curves from our observations to obtain the most probable planetary masses in each system. We have done this using our best estimate of the position of the disk, in combination with additional proper motion anomaly data, and recent theoretical analyses. If a planet had been detected in the system, it would have been of great help to refine and better constrain the planet-disk interaction models. However, our contrast curves sensitivity lie above what was predicted by the models. We concluded that our observations are, therefore, not contradicting the theoretical models. Additionally, we estimated the most likely planetary masses given these models and our observations. These masses were estimated as the minimum possible masses according to the models, and the best estimate according to the models and our observations. These values will be of great help for future explorations of these systems and for future observation campaigns of new samples using, for example, SPHERE, ERIS, or even JWST.

Although the field of planetary formation is "only" a few decades old in astronomy, it turns out to be very dynamic and is enriched with each new discovery. The new generation of instruments (e.g., ERIS and JWST facilities) will provide us with even better images and data to work toward a unified theory of planetary formation. In addition, the combination of different tools and techniques such as Gaia, will provide us with a large number of promising candidates to observe with direct imaging (the 4^{th} Gaia data release, for instance).

Chapter 5

Future perspective

5.1 Postdoctoral position at LAM

I recently accepted a postdoctoral position at Laboratoire d'Astrophysique de Marseille, in the Research and Development Group (GRD). The topic of the postdoc position is "Analysis of GTO and ERS JWST data –Characterization of Exoplanets and Disks with JWST images", as part of the ESCAPE ERC Project. The group led by Dr. Elodie Choquet is working on improvements in the reduction and post-processing of JWST data for direct imaging. The JWST (Gardner et al. 2006) is a space telescope launched in December 2021, and has been designed to address different research fields, including instruments that can be used for searching and characterizing extrasolar planets. The telescope is hosting the following instruments, NIRCam, NIRSpec, MIRI, and FGS-NIRISS, which are briefly described below:

- ***NIRCam*** (Near-Infrared Camera, Rieke et al. 2005) is an instrument that can observe from 0.6 to 5 microns and offers imaging, coronagraphy, wide field slitless spectroscopy, and time-series monitoring both in imaging and spectroscopy. Table 5.1 shows a summary of the different observing modes and their main characteristics. In addition, it offers two types of occulting masks, three round-type and two bar-type, paired with two pupil plane Lyot stops, yielding an inner working angle of between 0.13 to 0.89 half-width at half-maximum. Each type of mask is designed to perform optimally at certain wavelengths, and they have different inner working angles (see Girard et al. 2022). NIRCam has 10 detectors or sensor chip assemblies, each with $2\,040 \times 2\,040$ pixels. Of the 10 detectors, 8 are used for short wavelengths and two for long wavelengths. It is possible to observe in full frame imaging mode, where all 10 detectors are read out every 10 sec. The smallest sub-array (similar to windowing), is 64x64 pixels with a read-out time of ∼50ms.

- ***NIRSpec*** (Near Infrared Spectrograph, Jakobsen et al. 2022) is an instrument designed for spectroscopy that can observe from 0.6 to 5.3 microns and offers micro-shutter assembly (MSA), an integral field unit (IFU), and fixed slits (FSs). The type of science that can be carried out with this facility is the study of galaxies and their evolution, characterization of stellar populations, characterization of transiting exoplanets, and study of resolved extended objects. It can ~~be~~ observe~~d~~ in four different modes: multi-object spectroscopy (with the MSA), imaging spectroscopy (with the IFU), high contrast single object

TABLE 5.1: NIRCam parameters and properties of each observing mode.

Observing mode	λ coverage [μm]	Field of view	Pixel scale [mas/pix]	Notes
Imaging	0.6-2.3	2×132″×132″	31	FWHM 2 pixels at $2\mu m$
	2.4-5.0	2×129″×129″	63	FWHM 2 pixels at $4\mu m$
Coronagraphic imaging	1.8-2.2	20″×20″	31	
	2.8-5.0		63	
Wide field slitless spectroscopy	2.4-5.0	2×129″×129″	63	R∼1 600 at $4\mu m$
Time-series imaging	0.6-2.2	129″×129″	31	
	2.4-5.0	132″×132″	63	
Grism time series	2.4-5.0	129″×129″	63	R∼1 600 at $4\mu m$

Notes. Information taken from table 1 of the web page https://jwst-docs.stsci.edu/jwst-near-infrared-camera.

TABLE 5.2: NIRSpec parameters and properties of each observing mode.

Observing mode	Aperture or slit size [″]	λ coverage [μm]	Resolving Power
MSA	0.20×0.46	0.6-5.3μm (prism) 0.7-1.27μm (f070lp) 0.97-1.89μm (f100lp) 1.66-3.17μm (f170lp) 2.87-5.27μm (f295lp)	∼100 (Prism)
IFU	3.0×3.0		∼1 000 (medium-resolution gratings)
Fixed slit	0.2×3.2		
	0.4×3.65		
	1.6×1.6		
Bright object time series	1.6×1.6		∼2 700 (high-resolution gratings)

Notes. The pixel scale is 0.1 arcsec for all the observing modes. Information taken from table 1 of the web page https://jwst-docs.stsci.edu/jwst-near-infrared-spectrograph.

(using FSs), and high throughput bright object time-series with the NIRSpec wide aperture. Table 5.2 shows a summary of the general characteristics of each observing mode.

- ***NIRISS*** (Near Infrared Imager and Slitless Spectrograph, Doyon et al. 2012) is an instrument that can observe from 0.6 to 5 microns over a 2.2 × 2.2 arcmin field of view. Among the capabilities for the different observing modes, we have slitless spectroscopy, high-contrast interferometric imaging, and imaging. The observing modes are wide-field slitless spectroscopy, single-object slitless spectroscopy, aperture masking interferometry, and imaging (for more information, see Doyon et al. 2012; Willott et al. 2022; Sivaramakrishnan et al. 2022; Kammerer et al. 2022).

- ***MIRI*** (Mid Infrared Instrument, Rieke et al. 2015) provides imaging and spectroscopic observing modes from 4.9 to 28.1 microns (Wright et al. 2015), with four observing modes: imaging, low-resolution slitted and slitless spectroscopy, medium-resolution integral field unit, and coronagraphy. The main scientific goals are related to direct imaging of warm exoplanets and atmospheric characterization, identification and characterization of first galaxies at $z > 7$, and analysis of dust and molecular gas in young stars and disks. Table 5.3 shows the main properties of each observing mode. There are two types of coronagraph for imaging (see Boccaletti et al. 2022). The 4-quadrant phase mask (4QPMs, see Rouan et al. 2000) coronagraphs are used to achieve an inner working angle of $1\lambda/D$, ideal for studies of exoplanets very close to their stars, the inner region of debris disks, very tight binary systems, and near-nuclear environments of AGN. The Lyot coronagraphs, despite having an inner working angle of $3\lambda/D$, serve to

TABLE 5.3: MIRI parameters and properties of each observing mode.

Observing mode	λ coverage [μm]	FoV or slit size [$''$]	Resolving Power	FWHM	Notes
Imaging	5-28	74×113	3.5-16.1	2 pixels at 6.25 μm	FWHM = 2 pix×(λ/6.25μm) for $\lambda > 6.25\mu m$
4QPM c.i.	10.65, 11.4 15.5	24×24	14.1-17.2	2 pixels at 6.25 μm	
Lyot c.i.	23	30×30	4.1	2 pixels at 6.25 μm	
LR spectroscopy	5-12	0.51×4.7 (slit size)	∼100 at 7.5μm	2.6 pixels at 7.7 μm	slit or slitless modes
MR spectroscopy	4.9-28.1	3.9-7.6	∼1 550-3 250	2.6 pixels at 6.2 μm	FWHM= 0.314 pix×(λ/10μm) for $\lambda > 8\mu m$

Notes. The pixel scale is 0.11 arcsec except for MR spectroscopy which is 0.196 to 0.273 arcsec. The c.i. means coronagraphic imaging. The LR and MR mean Low-resolution and Medium-resolution, respectively. Information taken from table 1 of the web page https://jwst-docs.stsci.edu/jwst-mid-infrared-instrument.

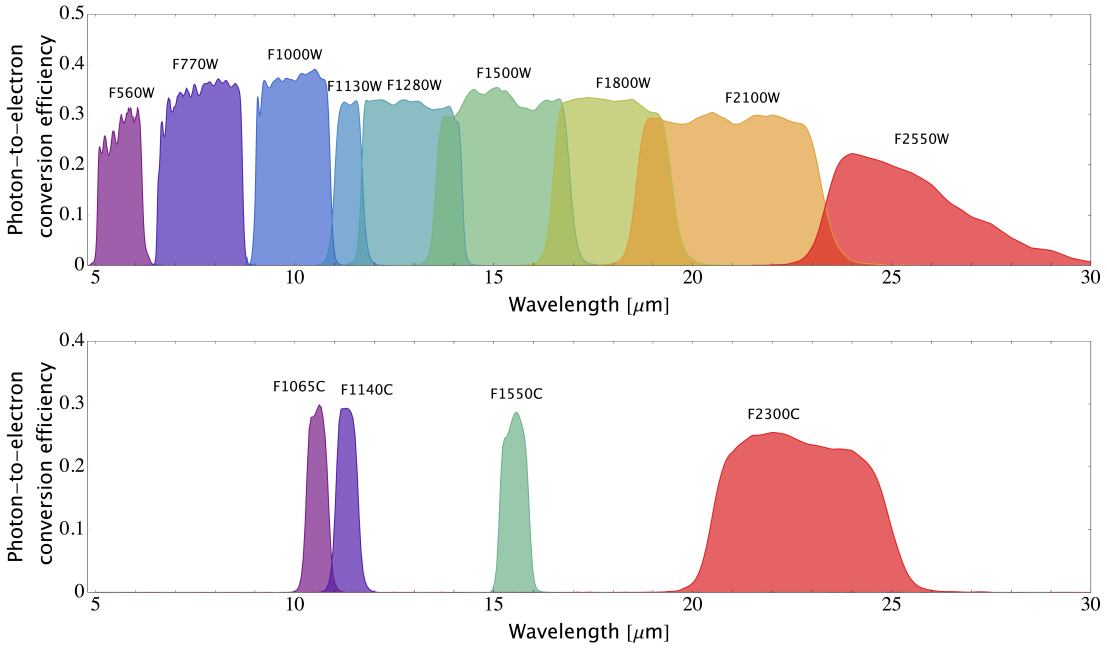

FIGURE 5.1: Transmission curves of each MIRI filter. Top panel: filter curves of MIRI imaging. Bottom panel: filters curves of MIRI coronagraphic imaging. Figures taken from the web page https://jwst-docs.stsci.edu/jwst-mid-infrared-instrument.

study the external structures of protoplanetary disks and debris disks, and extended structures around post-AGB stars, for example. The advantage of the Lyot coronagraph is that they can be used in broad-spectral bands, while the 4QPM can only operate in narrow passbands. Figure 5.1 shows the different filter transmission curves for imaging and coronagraphic imaging modes.

The medium resolution spectroscopy (MIRI-MRS, Wells et al. 2015; Labiano et al. 2021) is composed of a set of four IFU, called channels. Each channel is divided into 3 different gratings. Each grating takes a name of SHORT, MEDIUM, and LONG, alluding to its wavelength coverage. Considering all

TABLE 5.4: MIRI-MRS parameters and properties of each channel.

Channel name λ-range (μm)	FoV [″]	Number of slices	Slice width [″]	Pixel size [″]	Sub-band name	λ-range [μm]	Resolving power
Channel 1 4.88-7.52	3.2×3.7	21	0.176	0.196	SHORT (A)	4.90-5.74	3 320-3 710
					MEDIUM (B)	5.66-6.63	3 190-3 750
					LONG (C)	6.53-7.65	3 100-3 610
Channel 2 7.48-11.75	4.0×4.7	17	0.277	0.196	SHORT (A)	7.51-8.76	2 990-3 110
					MEDIUM (B)	8.67-10.15	2 750-3 170
					LONG (C)	10.01-11.71	2 860-3 300
Channel 3 11.52-18.08	5.2×6.1	16	0.387	0.245	SHORT (A)	11.55-13.47	2 530-2 880
					MEDIUM (B)	13.29-15.52	1 790-2 640
					LONG (C)	15.41-18.02	1 980-2 790
Channel 4 17.65-28.34	6.9×7.6	12	0.645	0.273	SHORT (A)	17.71-20.94	1 460-1 930
					MEDIUM (B)	20.69-24.44	1 680-1 770
					LONG (C)	24.22-28.10	1 630-1 330

Notes. Information taken from table 1 ofthe web page https://jwst-docs.stsci.edu/jwst-mid-infrared-instrument/miri-observing-modes/miri-medium-resolution-spectroscopy.

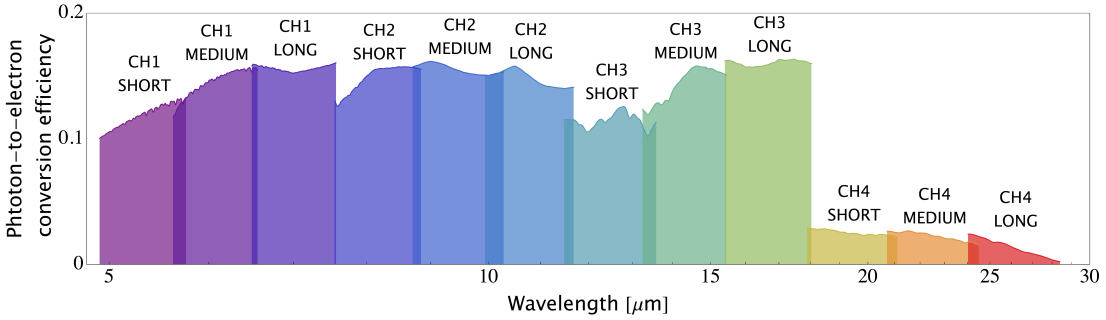

FIGURE 5.2: Transmission curves of each MIRI-MRS sub-channel. Figures taken from the web page https://jwst-docs.stsci.edu/jwst-mid-infrared-instrument/miri-observing-modes/miri-medium-resolution-spectroscopy.

the grating, we have 12 different wavelength bands. Table 5.4 shows the characteristics of each channel. As shown, each channel has a different field of view that increases as the channel increases (one FoV per IFU). Figure 5.2 shows the transmission of each channel and sub-channel of the MIRI-MRS observing mode.

This postdoctoral position is related to two main projects and a series of secondary projects (depending on the time and progress of the two projects). The first project deals with the reduction, post-processing, and characterization of GTO observations. The GTO has observed different known planetary systems using MIRI. The main objectives are to improve the existing data reductions and pipelines for optimal characterization of the planets and future observations. The base pipeline is KLIP, and the starting point is what is presented in Carter et al. (2022). The next objective is the atmospheric characterization of these planets in the same style presented in Carter et al. (2022) and Miles et al. (2022). The second project corresponds to ERS observations (led by Dr. Choquet and her group), where a series of disks have been observed using MIRI and NIRCam. The main idea is to improve the reduction and post-processing of this data to recover the disks in an optimal way. In addition, it is expected that I will be able to model the disks and characterize them (in conjunction with the working group). Secondary projects consist of exploratory mini-projects with ideas to mature and discuss. Among them is the idea of implementing

RDI for MIRI observations in the same way as Xie et al. (2022). Within JWST operations, standard stars are regularly observed for surveying and instrument testing. The main idea is to use these standard stars to build a stellar PSF library to use in RDI+ADI.

As part of my position, I will work with the team to coordinate the group meetings, create instances for example, "coffee-time" for paper discussions, organization of seminars (for example, invited speakers), and any other ideas that will benefit the working group, in terms of science, collaborations, and person-to-person contact (in particular, for the benefit of the students in the group). In addition, I will help students and work with them in conjunction with their supervisors. That is, teach them about direct imaging, data reduction, post-processing, different techniques, and enhancement strategies, among others.

5.2 An opportunity for frame selection

The case of NaCo:

We previously concluded that, for the case of NaCo, the improvements achieved with frame selection are relatively marginal, and there could be multiple reasons for this. For example, in the case of β Pictoris, even though the observing conditions were not optimal, the overall quality of the frames in time was quite homogeneous: a low-quality centering but with a star moving randomly and constantly around the coronagraph. For this kind of observation, we expect that frame selection should not have an important impact on nearby point sources. Therefore, frame selection might make a more significant difference in cases where the quality of the frames is rather changing slowly over time, or when some of the frames are clearly very different from the rest of the sequence. A clear example of this is HD 34282, where there is a wide variety of frames with very distinctive outliers. In this system, the disk is better recovered when performing frame selection, for instance.

The frame selection could therefore be important in observations during which the observing conditions change gradually over time that are neither always good nor always poor, yielding a variety of frames that are more correlated in time. Carter et al. (2022) showed the first results of HIP 65426 using observations from the JWST. These observations, together with SPHERE and NaCo data, were used for the atmospheric characterization of HIP 65426 b. However, Carter et al. (2022) reported that the NaCo observations, unlike SPHERE, do not agree with the best fit obtained from the JWST observations. One of the possible reasons would be that the observations in L', M', and N' were made under very varying observing conditions. Therefore, the photometric observations, done before and after the science sequence, might not be representative of the science sequence observations. This remains speculative at the moment, but performing frame selection on these data might improve the photometric calibration of HIP 65426 b by keeping the most homogeneous and similar frames in the science sequence (considering also the observing conditions during photometric observations). One important point is that these observations were carried out in saturated mode (i.e., not using AGPM), so the pseudo-Zernike moment decomposition would be the key for a frame registration and selection (in addition to the centering and fitting of the stellar saturated PSF). The pseudo-Zernike moment decomposition can be used on any kind of image. For this reason, it is a perfect tool for frame registration. In the case of stellar saturated PSF, we can mask the saturation region (the non-linear regime and saturated pixels), to avoid issues and better characterize the inhomogeneities and speckles.

The case of SPHERE and other instruments:

In the case of SPHERE, frame selection also improved marginally the signal-to-noise of point sources. A more detailed description of how this test was carried out is presented in Appendix A.

Other instruments are using an AGPM-like coronagraph, and could benefit from the use of frame selection and centering as shown in this thesis. For example, VISIR/NEAR (Maire et al. 2020) uses an AGPM that operates in the N-band, and the circular aperture is at least partially visible, as shown in the report[1] delivered by the team. VISIR/NEAR has good performance and great stability (compared to NaCo), and applies a centering strategy that operates in situ by applying the same code as for Keck/NIRC2 (QACITS, Huby et al. 2016). However, it could be helpful to see if our centering technique can further improve astrometry at posteriori. On the other hand, the use of frame selection is something that should definitely be explored, given the large number of images produced for each observation sequence and the excellent stability of the instrument. Although frame selection was shown to have a marginal impact, this has not been explored at longer wavelengths, in this case at N-band. Considering the latter, it would be necessary to calibrate both the centering and the frame selection to be used in AGPM observations with VISIR/NEAR.

Another instrument that uses an AGPM-like coronagraph is ERIS, and it is further discussed in Section 5.5.

5.3 CenteR - re-visiting NaCo archival data

We have shown that the new technique and pipeline, called CenteR, can provide significant improvements on the final products. So far, its use has been limited mostly (if not only) to ISPY data. Objects on which CenteR has been applied, such as HD 34282, have shown that both centering and frame selection can even help to recover extended structures such as disks. The centering has the most impact on improving the signal-to-noise of point sources, as has been shown in this thesis. The band in which CenteR was used, L'-band, has a contrast that is much more favorable for the detection of planets. This is why re-visiting the archival observations of NaCo-AGPM could be of great benefit, and new discoveries could surprise us.

A preliminary plan would be to focus on archival data that have a large variability in weather conditions. This could be possible using the information downloaded from the ESO archive[2]. This table has both the names of the objects, as well as the dates and times of each observation (among other useful parameters). It is possible to extract this information and combine it with, for example, the Paranal Ambient Query Forms[3] (e.g., DIMM archive) to evaluate the different observing conditions of each observation. This strategy of focusing on datasets observed under varying conditions is based on the results obtained for R Cr A, where the impact in terms of improvements in signal-to-noise and astrometry was larger (also because the companion was closer in). A preview of the archived data shows that there are about 320 objects observed using AGPM in L', of which $\sim$ 160 correspond to ISPY observations and about 20 to technical time tests. The remainder 140 objects (around 30 programs) would serve to conduct a survey

[1] https://www.eso.org/sci/activities/vltsv/nearsd/ESO-331355_1_NEAR_Commissioning_Report.pdf
[2] http://archive.eso.org/eso/eso_archive_main.html
[3] http://archive.eso.org/cms/eso-data/ambient-conditions/paranal-ambient-query-forms.html

of NaCo-AGPM, reducing the data in a homogeneous way with the latest improvements implemented by CenteR. However, given the computational capacity, the analysis would focus on the inner region if all the frames were used, and may be extended regions if stacking is chosen (depending on the number of frames per target). In addition, the sample could be even larger if bands like M' are incorporated. However, CenteR's performance in terms of centering should be put to the test for this type of case. Furthermore, the algorithm works only with cases where the circular aperture is visible or partially visible, so a pre-selection of observations made with windowing should be carried out and therefore the sample could be smaller than these initial 140 objects.

5.4 SCALP - a perspective for the near future

The SCALP collaboration (led by Dr. Chauvin) has built a database based on the selection of stars that have indicators of planet-disc interaction. We can divide these indicators into the following groups: exocometary activity, exocomets in discs detected with CO emission, exocomets in binary systems, exocomets in systems with two belts, double belt systems, exozodiacal dust grains, and excentric debris disks. The original sample includes 48 objects classified within the aforementioned categories, of which only 7 have been observed. Of the remaining 41, 13 do not have preliminary observations with SPHERE (but none of the stars have previous archival observations in DB_K12, the core strategy adopted in SCALP). For this reason, it would be interesting to continue observing the full sample, but this time adding information such as the proper motion anomaly and the location of the disk (if any are detected from the SED). Both criteria would be of great help in selecting the most promising systems, where SPHERE (or some other instrument or facilities, such as ERIS or JWST) has a good chance of observing the planet predicted by the models. Re-analyzing the sample would be of great help to continue with the survey that, so far, is reduced to 7 objects out of the 48 that make up the original sample. This number of observed targets is insufficient to obtain results and conclusions from a statistical point of view.

5.5 Testing CenteR in ERIS-AGPM

ERIS[4] (Kenworthy et al. 2018) is a new-generation instrument that has been recently mounted at the VLT, Paranal observatory, Chile. ERIS has two science cameras: an IFU (SPIFFIER), and an imager (NIX) capable of observing from near to mid-infrared wavelengths. With SPIFFIER it is possible to observe in 12 configurations that cover from J- to K-bands, with a resolution ranging between 5 000 and 11 200. In addition, it has 3 possible plate scales with a field of view from $0.8'' \times 0.8''$ with a spaxel size of 12.5×25 mas, up to $8'' \times 8''$ with a spaxel of 125×250mas. The NIX (spectroscopy and imaging) can use a wide variety of observing modes, ranging from narrow and broad-band imaging with an option to use a coronagraph, and long-slit spectroscopy. It is possible to observe using one of the 17 narrow and board band filters in total, covering from J- to M'-bands. Depending on the configuration, it is possible to observe with a field of view of $26'' \times 26''$ or $55'' \times 55''$, with a pixel scale of 13 mas and 27 mas, respectively. Within the offered coronagraphs, we find the apodizing phase plate coronagraphy, the focal plane coronagraph, and the sparse aperture mask. The focal plane coronagraph (FPC) is very similar to

[4] https://www.eso.org/sci/facilities/paranal/instruments/eris/overview.html

a vortex AGPM-type coronagraph designed for L'- and M'-bands, operating with a pixel scale of 13 mas (as a reference, the pixel scale of NaCo was 27 mas).

The improvements shown for NaCo AGPM-L' using CenteR (in particular, the centering technique), can be very beneficial for ERIS AGPM in L'- and M'-bands. The centering is based on a calibration that is carried out with the observations themselves a posteriori, and its goal is to determine the position of the star behind the coronagraph. A key part of this technique is being able to observe the mask (the circular aperture), which up to now is not clear in the case of FPC observing mode. However, not observing this mask is not an impediment at all. It is possible to calibrate the technique using, for example, the dust and artifacts located in the optical path and/or camera. For this, it is necessary to study their motion and correlations using, for example, a resolved binary star (a benchmark study/test). So far, the FPC mode has not been offered for science verification (in this period), so this proposal for characterization of the centering and stability of the instrument could be proposed for the next verification phase.

Appendix A

Frame selection on SPHERE data

We also inspected the frame selection for the case of SPHERE data. We used the same procedure described in CenteR, a characterization based on pseudo-Zernike moment decomposition. We used observations of HD 165014, a star located in a crowded field (09:04:48.6 +00:18:04.1 galactic coordinates). Originally, this object was included in our sample due to its emission at infrared wavelength, indicative of having a warm debris disk, and was classified as a YSO (Lisse et al. 2015; Lisse et al. 2017). However, data from Gaia and analyses carried out by our team suggest that this star is a red giant (AGB star) with a mass of $5.8 M_{\odot}$ and a radius of $23 R_{\odot}$, located at a distance of $900\,pc$. The absorption and emission lines in the CO-bands at K-band (Lisse et al. 2015) indicate that it has a hot envelope, so it would be in a pre-planetary nebulae phase. Given its brightness, this star saturates in observations with, for example, VVV (Minniti et al. 2010), so its long-term variability (typical of an evolved AGB star) has been not confirmed yet.

Nontheless, given the number of point sources in the background this is an ideal target to investigate the improvement of frame selection at various separations from the central object. We use the pseudo-Zernike moment decomposition to obtain the Torus S/N and the homogeneity of all the 48 frames of HD 165014. Also, we extracted the weather conditions information for frame registration. Figure A.1 shows an example of a frame (left panel) and its reconstruction (right panel) using $m < 46$. Figure A.2 shows the result for the Torus S/N and the Homogeneity. The top-left panel shows the relation between the Torus S/N and the Homogeneity (color-coded with the time in the sequence), showing that both quantities provide the same kind of information about each frame. The rest of the panels show the Torus S/N as a function of time, color-coded using the seeing (top-right panel), the coherence time (bottom-left panel), and the wind speed (bottom-right panel). The quality of the frames decreases in time, resulting in a low Torus signal, as well as the quality of the weather conditions, decreases in time. We only kept the frames that have a torus S/N above 0.5, i.e. 40 frames of the original 48.

The post-processing was carried out for both datacubes (complete frames and frame selection), using the annular principal component analysis module `pca_annular` from `VIP` (Gomez Gonzalez et al. 2017b). The parameters used were `ncomp` set to *auto* for letting the algorithm define automatically the number of principal components for each patch by minimizing the change in the standard deviation of the residuals. We also used the module `vip.metrics.detection` to detect the sources in the field-of-view setting the background-σ in 2 and S/N threshold in 1.2. Afterwards we performed a visual inspection

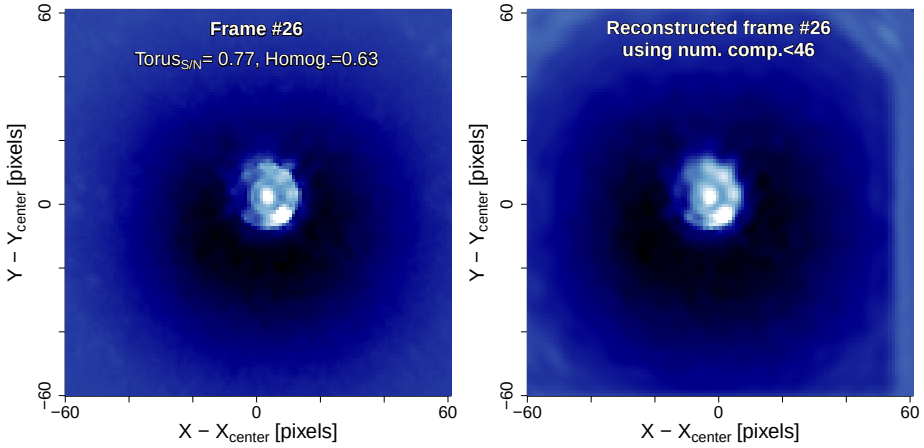

FIGURE A.1: Example of a single frame of SPHERE (left panel), and its reconstruction using the pseudo-Zernike moments with $0 < m < 46$ (left). The torus S/N and homogeneity of this frame correspond to 0.77 and 0.63, respectively. Both images (left and right), have the same color scale.

to remove artefacts, leaving us with 80 reliable sources in the field of view. Then, with the module `vip.metrics.snr` we measured the S/N of the sources, allowing for the low-number statistics to be accounted for (Mawet et al. 2014). In addition, we computed the contrast curve using the module `vip.metrics.contrast_curve`, which provides the sensitivity, throughput, and noise estimate at all angular separations.

Figure A.3 shows the S/N ratio of 80 sources between the frame selection and the complete dataset as a function of the angular separation. The circle sizes represent the S/N measured in the full dataset. Frame selection can change the S/N of objects in a typical range of −20% to 20%, negatively affecting the innermost region. Figure A.4 shows the flux ratio of the sources between the frame selection and the complete dataset. The purple line shows the noise ratio between frame selection and the full dataset and is obtained in the same manner as the denominator in the S/N (i.e., the "N" being the noise). The most impacted parameter corresponds to the noise, which undergoes random variations at different angular separations, while the signal of point sources is less affected (from −20% to 10% of improvements). As was mentioned before, typical SPHERE observations consist of less than 100 frames, and the removal of even a few frames leads to a significant impact on the source signal and in the self-subtraction due to the smaller rotational angle available. We concluded that the frame selection applied to SPHERE observations only leads to marginal improvements even under weather conditions that degrade over time for datacubes with a low number of frames (< 100 frames).

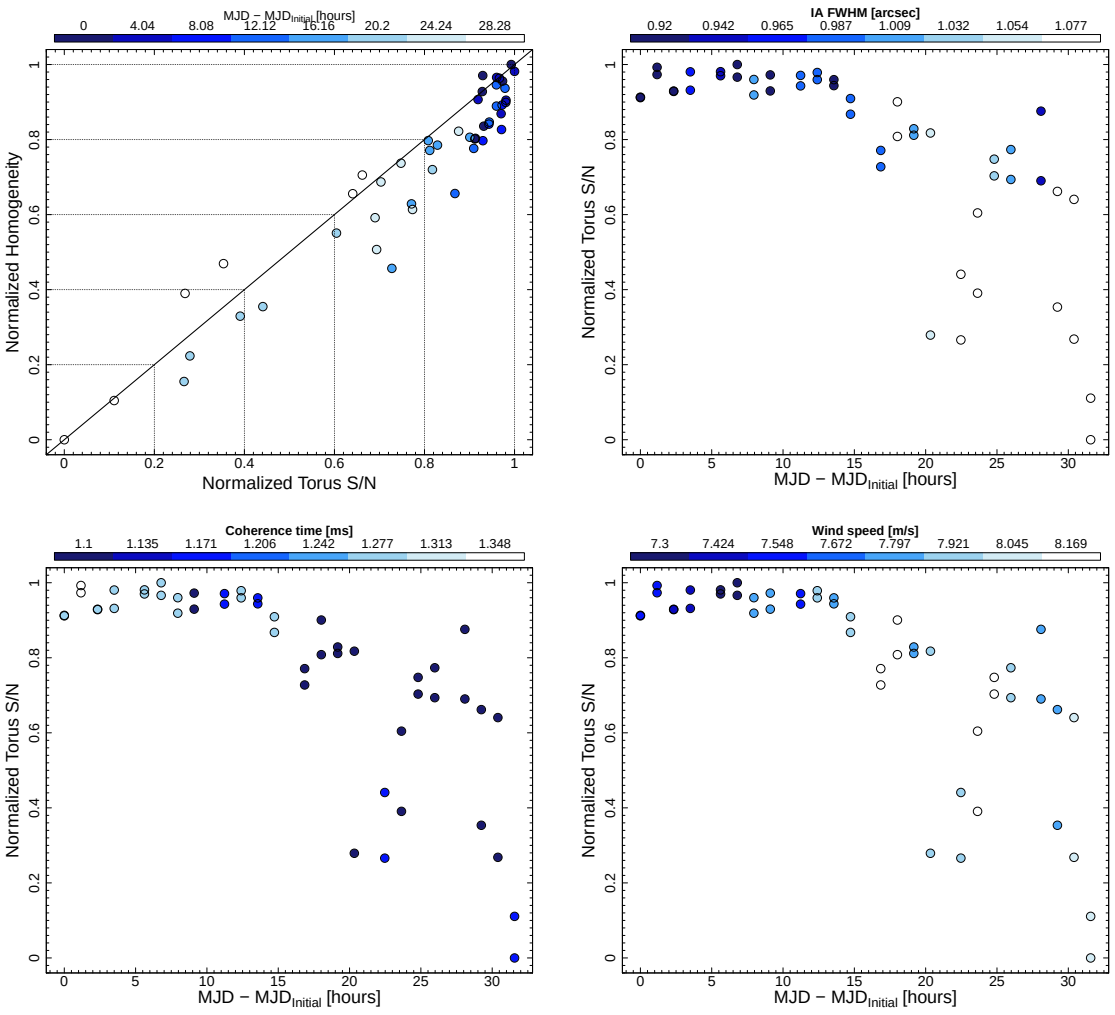

FIGURE A.2: Frame registration of the SPHERE observations of HD 165014. Top-left panel: Normalized homogeneity as a function of the normalized torus S/N. The color-coded corresponds to the time (hours). The panels top-right, bottom-left, and bottom-right correspond to the normalized torus S/N vs time, with color-coded the seeing, coherence time, and wind speed, respectively.

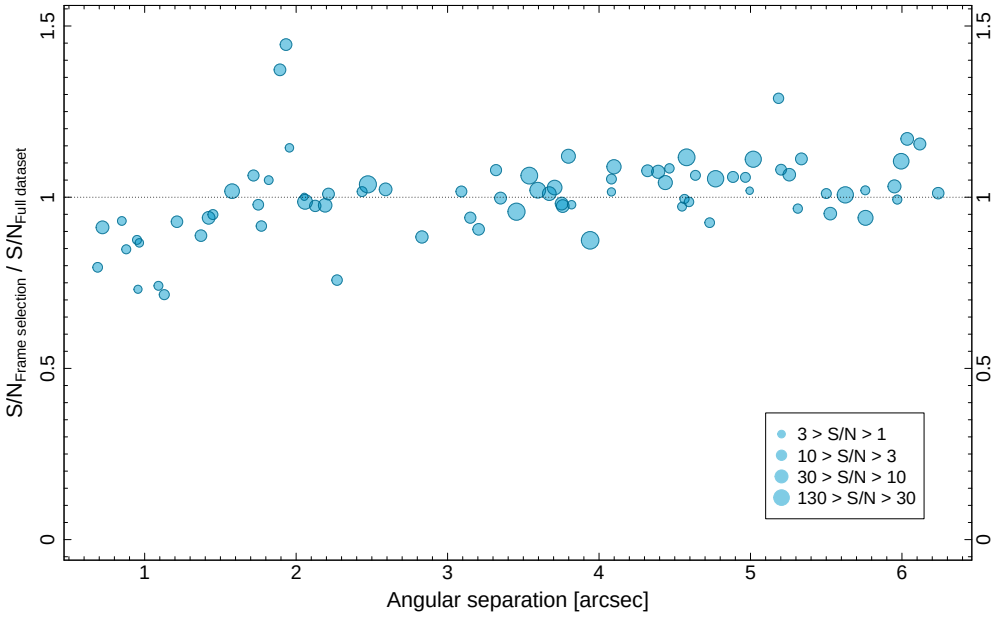

FIGURE A.3: S/N of frame selection over the S/N of the full dataset as a function of angular separation for each of the 80 point sources. The sizes of the circles highlight the S/N of each source.

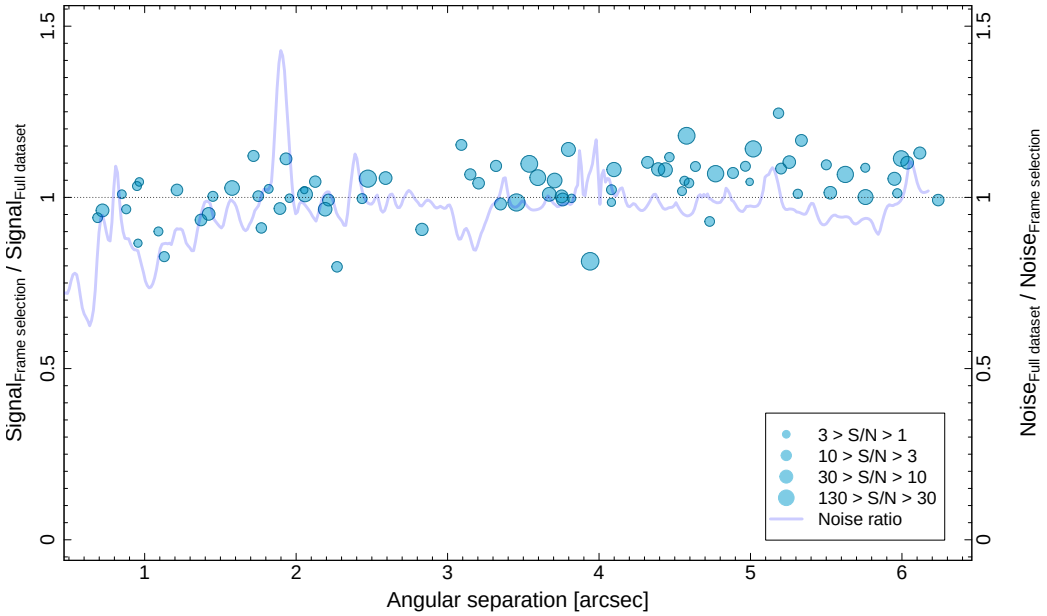

FIGURE A.4: Signal ratio (circles) and noise ratio (line) between frame selection and full dataset for each of the point sources as a function of the angular separation. The circles highlight the S/N of each point source.

References

Absil, O., Marion, L., Ertel, S., et al. 2021, A&A, 651, A45

Absil, O., Mawet, D., Delacroix, C., et al. 2014, in Society of Photo-Optical Instrumentation Engineers (SPIE) Conference Series, Vol. 9148, Adaptive Optics Systems IV, 91480M

Absil, O., Mawet, D., Karlsson, M., et al. 2016, in Society of Photo-Optical Instrumentation Engineers (SPIE) Conference Series, Vol. 9908, Ground-based and Airborne Instrumentation for Astronomy VI, ed. C. J. Evans, L. Simard, & H. Takami, 99080Q

Absil, O., Milli, J., Mawet, D., et al. 2013, A&A, 559, L12

Albrow, M. D., Beaulieu, J. P., Caldwell, J. A. R., et al. 2000, ApJ, 534, 894

Allard, F. 2014a, in Exploring the Formation and Evolution of Planetary Systems, ed. M. Booth, B. C. Matthews, & J. R. Graham, Vol. 299, 271–272

Allard, F. 2014b, in Exploring the Formation and Evolution of Planetary Systems, ed. M. Booth, B. C. Matthews, & J. R. Graham, Vol. 299, 271–272

Amara, A. & Quanz, S. P. 2012a, MNRAS, 427, 948

Amara, A. & Quanz, S. P. 2012b, MNRAS, 427, 948

Andre, P., Ward-Thompson, D., & Barsony, M. 1993, ApJ, 406, 122

Angus, R., Morton, T. D., Foreman-Mackey, D., et al. 2019, AJ, 158, 173

Asensio-Torres, R., Henning, T., Cantalloube, F., et al. 2021, A&A, 652, A101

Asensio-Torres, R., Janson, M., Bonavita, M., et al. 2018, A&A, 619, A43

Ataiee, S., Baruteau, C., Alibert, Y., & Benz, W. 2018, A&A, 615, A110

Ayliffe, B. A. & Bate, M. R. 2012, MNRAS, 427, 2597

Bakos, G. Á., Noyes, R. W., Kovács, G., et al. 2007, ApJ, 656, 552

Ballering, N. P., Rieke, G. H., & Gáspár, A. 2014, ApJ, 793, 57

Baraffe, I., Chabrier, G., Allard, F., & Hauschildt, P. H. 2002, A&A, 382, 563

Baraffe, I., Homeier, D., Allard, F., & Chabrier, G. 2015, A&A, 577, A42

Barge, P., Baglin, A., Auvergne, M., et al. 2008, A&A, 482, L17

Baruteau, C., Meru, F., & Paardekooper, S.-J. 2011, MNRAS, 416, 1971

Bayo, A., Rodrigo, C., Barrado Y Navascués, D., et al. 2008, A&A, 492, 277

Bennett, D. P., Udalski, A., Han, C., et al. 2018, AJ, 155, 141

Beust, H. & Morbidelli, A. 2000, Icarus, 143, 170

Beuzit, J. L., Vigan, A., Mouillet, D., et al. 2019, A&A, 631, A155

Bhatia, A. B. & Wolf, E. 1954, Mathematical Proceedings of the Cambridge Philosophical Society, 50, 40–48

Bibo, E. A., The, P. S., & Dawanas, D. N. 1992, A&A, 260, 293

Biller, B. A., Apai, D., Bonnefoy, M., et al. 2021, MNRAS, 503, 743

Biller, B. A., Close, L., Lenzen, R., et al. 2004, in Society of Photo-Optical Instrumentation Engineers (SPIE) Conference Series, Vol. 5490, Advancements in Adaptive Optics, ed. D. Bonaccini Calia, B. L. Ellerbroek, & R. Ragazzoni, 389–397

Biller, B. A., Close, L. M., Masciadri, E., et al. 2007, ApJS, 173, 143

Biller, B. A., Liu, M. C., Wahhaj, Z., et al. 2013, ApJ, 777, 160

Bitsch, B. & Johansen, A. 2017, in Astrophysics and Space Science Library, Vol. 445, Formation, Evolution, and Dynamics of Young Solar Systems, ed. M. Pessah & O. Gressel, 339

Bitsch, B., Lambrechts, M., & Johansen, A. 2015, A&A, 582, A112

Bitsch, B., Morbidelli, A., Johansen, A., et al. 2018, A&A, 612, A30

Boccaletti, A., Cossou, C., Baudoz, P., et al. 2022, arXiv e-prints, arXiv:2207.11080

Böhm, T., Catala, C., Balona, L., & Carter, B. 2004, A&A, 427, 907

Bohn, A. J., Ginski, C., Kenworthy, M. A., et al. 2021, A&A, 648, A73

Bohn, A. J., Kenworthy, M. A., Ginski, C., et al. 2019a, A&A, 624, A87

Bohn, A. J., Kenworthy, M. A., Ginski, C., et al. 2019b, A&A, 624, A87

Bohn, A. J., Kenworthy, M. A., Ginski, C., et al. 2020a, MNRAS, 492, 431

Bohn, A. J., Kenworthy, M. A., Ginski, C., et al. 2020b, ApJ, 898, L16

Bohn, A. J., Kenworthy, M. A., Ginski, C., et al. 2020c, ApJ, 898, L16

Bonavita, M. 2020, Exo-DMC: Exoplanet Detection Map Calculator, Astrophysics Source Code Library, record ascl:2010.008

Bonavita, M., Desidera, S., Thalmann, C., et al. 2016, A&A, 593, A38

Bond, I. A., Udalski, A., Jaroszyński, M., et al. 2004, ApJ, 606, L155

Bonnefoy, M., Marleau, G. D., Galicher, R., et al. 2014, A&A, 567, L9

Borucki, W. J., Koch, D., Basri, G., et al. 2010, Science, 327, 977

Bos, S. P., Miller, K. L., Lozi, J., et al. 2021, A&A, 653, A42

Boss, A. P. 1997, Science, 276, 1836

Bowler, B. P. 2016a, PASP, 128, 102001

Bowler, B. P. 2016b, PASP, 128, 102001

Bowler, B. P. & Nielsen, E. L. 2018, in Handbook of Exoplanets, ed. H. J. Deeg & J. A. Belmonte, 155

Brandt, G. M., Brandt, T. D., Dupuy, T. J., Li, Y., & Michalik, D. 2021a, AJ, 161, 179

Brandt, G. M., Brandt, T. D., Dupuy, T. J., Michalik, D., & Marleau, G.-D. 2021b, ApJ, 915, L16

Brandt, T. D. 2018, ApJS, 239, 31

Brandt, T. D. 2021, ApJS, 254, 42

Brandt, T. D., McElwain, M. W., Turner, E. L., et al. 2014, ApJ, 794, 159

Brouwers, M. G. & Ormel, C. W. 2020, A&A, 634, A15

Bryan, M. L., Ginzburg, S., Chiang, E., et al. 2020, ApJ, 905, 37

Burrows, A., Hubbard, W. B., Lunine, J. I., & Liebert, J. 2001, Reviews of Modern Physics, 73, 719

Burrows, A., Sudarsky, D., & Lunine, J. I. 2003, ApJ, 596, 587

Caffau, E., Ludwig, H. G., Steffen, M., Freytag, B., & Bonifacio, P. 2011, Sol. Phys., 268, 255

Cameron, P. B., Britton, M. C., & Kulkarni, S. R. 2009, AJ, 137, 83

Cantalloube, F., Farley, O. J. D., Milli, J., et al. 2020, A&A, 638, A98

Cantalloube, F., Mouillet, D., Mugnier, L. M., et al. 2015a, A&A, 582, A89

Cantalloube, F., Mouillet, D., Mugnier, L. M., et al. 2015b, A&A, 582, A89

Cantalloube, F., Por, E. H., Dohlen, K., et al. 2018, A&A, 620, L10

Carter, A. L., Hinkley, S., Kammerer, J., et al. 2022, arXiv e-prints, arXiv:2208.14990

Cassan, A., Kubas, D., Beaulieu, J. P., et al. 2012, Nature, 481, 167

Chambers, J. 2018, ApJ, 865, 30

Charbonneau, D., Brown, T. M., Latham, D. W., & Mayor, M. 2000, ApJ, 529, L45

Chauvin, G. 2018, in Society of Photo-Optical Instrumentation Engineers (SPIE) Conference Series, Vol. 10703, Adaptive Optics Systems VI, 1070305

Chauvin, G., Desidera, S., Lagrange, A. M., et al. 2017, A&A, 605, L9

Chauvin, G., Lagrange, A. M., Bonavita, M., et al. 2010, A&A, 509, A52

Chauvin, G., Lagrange, A. M., Dumas, C., et al. 2004, A&A, 425, L29

Chauvin, G., Thomson, M., Dumas, C., et al. 2003, A&A, 404, 157

Chauvin, G., Vigan, A., Bonnefoy, M., et al. 2015, A&A, 573, A127

Chiang, E. & Laughlin, G. 2013, MNRAS, 431, 3444

Chwolson, O. 1924, Astronomische Nachrichten, 221, 329

Claudi, R. U., Turatto, M., Gratton, R. G., et al. 2008, in Society of Photo-Optical Instrumentation Engineers (SPIE) Conference Series, Vol. 7014, Ground-based and Airborne Instrumentation for Astronomy II, ed. I. S. McLean & M. M. Casali, 70143E

Collier Cameron, A., Bouchy, F., Hébrard, G., et al. 2007, MNRAS, 375, 951

Collins, K. A., Collins, K. I., Pepper, J., et al. 2018, AJ, 156, 234

Contro, B., Horner, J., Wittenmyer, R. A., Marshall, J. P., & Hinse, T. C. 2016, MNRAS, 463, 191

Crivellari, L., Simón-Díaz, S., & Arévalo, M. J. 2019, Radiative Transfer in Stellar and Planetary Atmospheres

Cugno, G., Quanz, S. P., Launhardt, R., et al. 2019, A&A, 624, A29

Currie, T., Biller, B., Lagrange, A.-M., et al. 2022, arXiv e-prints, arXiv:2205.05696

Currie, T., Brandt, T. D., Kuzuhara, M., et al. 2020, ApJ, 904, L25

Currie, T., Brittain, S., Grady, C. A., Kenyon, S. J., & Muto, T. 2017, Research Notes of the American Astronomical Society, 1, 40

Currie, T., Burrows, A., Itoh, Y., et al. 2011, ApJ, 729, 128

Cushing, M. C., Kirkpatrick, J. D., Gelino, C. R., et al. 2011, ApJ, 743, 50

David, T. J. & Hillenbrand, L. A. 2015, ApJ, 804, 146

de Boer, J., Ginski, C., Chauvin, G., et al. 2021, A&A, 649, A25

Defrère, D., Absil, O., Hinz, P., et al. 2014, in Society of Photo-Optical Instrumentation Engineers (SPIE) Conference Series, Vol. 9148, Adaptive Optics Systems IV, ed. E. Marchetti, L. M. Close, & J.-P. Vran, 91483X

Delorme, P., Meunier, N., Albert, D., et al. 2017, in SF2A-2017: Proceedings of the Annual meeting of the French Society of Astronomy and Astrophysics, ed. C. Reylé, P. Di Matteo, F. Herpin, E. Lagadec, A. Lançon, Z. Meliani, & F. Royer, Di

Deng, H., Mayer, L., & Meru, F. 2017, ApJ, 847, 43

Dent, W. R. F., Wyatt, M. C., Roberge, A., et al. 2014, Science, 343, 1490

Desidera, S., Chauvin, G., Bonavita, M., et al. 2021a, A&A, 651, A70

Desidera, S., Chauvin, G., Bonavita, M., et al. 2021b, A&A, 651, A70

Desidera, S., Covino, E., Messina, S., et al. 2015, A&A, 573, A126

Dohlen, K., Langlois, M., Saisse, M., et al. 2008, in Society of Photo-Optical Instrumentation Engineers (SPIE) Conference Series, Vol. 7014, Ground-based and Airborne Instrumentation for Astronomy II, ed. I. S. McLean & M. M. Casali, 70143L

Dohnanyi, J. S. 1969, J. Geophys. Res., 74, 2531

D'Orazi, V., Desidera, S., Gratton, R. G., et al. 2017, A&A, 598, A19

Dorn, R. J., Anglada-Escude, G., Baade, D., et al. 2014, The Messenger, 156, 7

Doyon, R., Hutchings, J. B., Beaulieu, M., et al. 2012, in Society of Photo-Optical Instrumentation Engineers (SPIE) Conference Series, Vol. 8442, Space Telescopes and Instrumentation 2012: Optical, Infrared, and Millimeter Wave, ed. M. C. Clampin, G. G. Fazio, H. A. MacEwen, & J. Oschmann, Jacobus M., 84422R

Draine, B. T. 2003, ApJ, 598, 1026

Drazkowska, J., Bitsch, B., Lambrechts, M., et al. 2022, arXiv e-prints, arXiv:2203.09759

Dzib, S. A., Loinard, L., Ortiz-León, G. N., Rodríguez, L. F., & Galli, P. A. B. 2018, ApJ, 867, 151

Einstein, A. 1936, Science, 84, 506

Emsenhuber, A., Mordasini, C., Burn, R., et al. 2021, A&A, 656, A69

Ertel, S., Absil, O., Defrère, D., et al. 2014, A&A, 570, A128

Esparza-Borges, E., Oshagh, M., Casasayas-Barris, N., et al. 2022, A&A, 657, A23

Evans, Neal J., I., Dunham, M. M., Jørgensen, J. K., et al. 2009, ApJS, 181, 321

Faber, P. & Quillen, A. C. 2007, MNRAS, 382, 1823

Feigelson, E. D., Lawson, W. A., & Garmire, G. P. 2003, ApJ, 599, 1207

Fischer, D. A., Howard, A. W., Laughlin, G. P., et al. 2014, in Protostars and Planets VI, ed. H. Beuther, R. S. Klessen, C. P. Dullemond, & T. Henning, 715

Fischer, D. A. & Valenti, J. 2005, ApJ, 622, 1102

Flasseur, O., Denis, L., Thiébaut, É., & Langlois, M. 2018, A&A, 618, A138

Flasseur, O., Denis, L., Thiébaut, É., & Langlois, M. 2020, A&A, 637, A9

Fontanive, C., Mužić, , K., Bonavita, M., & Biller, B. 2019, MNRAS, 490, 1120

Forbrich, J., Preibisch, T., & Menten, K. M. 2006, A&A, 446, 155

Forgan, D., Parker, R. J., & Rice, K. 2015, MNRAS, 447, 836

Forgan, D. & Rice, K. 2013, MNRAS, 432, 3168

Fulton, B. J., Rosenthal, L. J., Hirsch, L. A., et al. 2021, ApJS, 255, 14

Fusco, T., Rousset, G., Sauvage, J. F., et al. 2006, Optics Express, 14, 7515

Gaia Collaboration, Arenou, F., Babusiaux, C., et al. 2022, arXiv e-prints, arXiv:2206.05595

Gaia Collaboration, Brown, A. G. A., Vallenari, A., et al. 2018, A&A, 616, A1

Gaia Collaboration, Brown, A. G. A., Vallenari, A., et al. 2021a, A&A, 649, A1

Gaia Collaboration, Brown, A. G. A., Vallenari, A., et al. 2021b, A&A, 650, C3

Gaia Collaboration, Prusti, T., de Bruijne, J. H. J., et al. 2016, A&A, 595, A1

Galicher, R., Boccaletti, A., Mesa, D., et al. 2018, A&A, 615, A92

Galicher, R., Marois, C., Macintosh, B., et al. 2016, A&A, 594, A63

Garcia, P. J. V., Benisty, M., Dougados, C., et al. 2013, MNRAS, 430, 1839

Gardner, J. P., Mather, J. C., Clampin, M., et al. 2006, Space Sci. Rev., 123, 485

Gaudi, B. S. 2012, ARA&A, 50, 411

Gerard, B. L. & Marois, C. 2016a, in Society of Photo-Optical Instrumentation Engineers (SPIE) Conference Series, Vol. 9909, Adaptive Optics Systems V, ed. E. Marchetti, L. M. Close, & J.-P. Véran, 990958

Gerard, B. L. & Marois, C. 2016b, in Society of Photo-Optical Instrumentation Engineers (SPIE) Conference Series, Vol. 9909, Adaptive Optics Systems V, ed. E. Marchetti, L. M. Close, & J.-P. Véran, 990958

Gerard, B. L., Marois, C., & Galicher, R. 2018, AJ, 156, 106

Girard, J. H., Leisenring, J., Kammerer, J., et al. 2022, in Society of Photo-Optical Instrumentation Engineers (SPIE) Conference Series, Vol. 12180, Space Telescopes and Instrumentation 2022: Optical, Infrared, and Millimeter Wave, ed. L. E. Coyle, S. Matsuura, & M. D. Perrin, 121803Q

Godoy, N., Olofsson, J., Bayo, A., et al. 2022, A&A, 663, A53

Gomez Gonzalez, C. A., Absil, O., Absil, P. A., et al. 2016, A&A, 589, A54

Gomez Gonzalez, C. A., Wertz, O., Absil, O., et al. 2017a, AJ, 154, 7

Gomez Gonzalez, C. A., Wertz, O., Absil, O., et al. 2017b, AJ, 154, 7

Gould, A., Dong, S., Gaudi, B. S., et al. 2010, ApJ, 720, 1073

Gould, A., Miralda-Escude, J., & Bahcall, J. N. 1994, ApJ, 423, L105

Gould, A., Yee, J. C., Bond, I. A., et al. 2013, ApJ, 763, 141

Grady, C. A., Woodgate, B., Torres, C. A. O., et al. 2004, ApJ, 608, 809

Grandjean, A., Lagrange, A. M., Meunier, N., et al. 2021, A&A, 650, A39

Groff, T. D., Kasdin, N. J., Limbach, M. A., et al. 2015, in Society of Photo-Optical Instrumentation Engineers (SPIE) Conference Series, Vol. 9605, Techniques and Instrumentation for Detection of Exoplanets VII, 96051C

Guillot, T., Fletcher, L. N., Helled, R., et al. 2022, arXiv e-prints, arXiv:2205.04100

Guyon, O., Pluzhnik, E. A., Kuchner, M. J., Collins, B., & Ridgway, S. T. 2006, ApJS, 167, 81

Hagelberg, J., Ségransan, D., Udry, S., & Wildi, F. 2016, MNRAS, 455, 2178

Henning, T. 2010, ARA&A, 48, 21

Henry, G. W., Marcy, G. W., Butler, R. P., & Vogt, S. S. 2000, ApJ, 529, L41

Hinkley, S., Oppenheimer, B. R., Soummer, R., et al. 2007, ApJ, 654, 633

Hori, Y. & Ikoma, M. 2011, MNRAS, 416, 1419

Houck, J. R., Roellig, T. L., van Cleve, J., et al. 2004, ApJS, 154, 18

Huby, E., Absil, O., Mawet, D., et al. 2016, in Society of Photo-Optical Instrumentation Engineers (SPIE) Conference Series, Vol. 9909, Adaptive Optics Systems V, ed. E. Marchetti, L. M. Close, & J.-P. Véran, 990920

Huby, E., Baudoz, P., Mawet, D., & Absil, O. 2015, A&A, 584, A74

Huby, E., Bottom, M., Femenia, B., et al. 2017, A&A, 600, A46

Hunziker, S., Quanz, S. P., Amara, A., & Meyer, M. R. 2018, A&A, 611, A23

Hwang, K. H., Choi, J. Y., Bond, I. A., et al. 2013, ApJ, 778, 55

Ida, S. & Lin, D. N. C. 2008, ApJ, 673, 487

Ida, S., Lin, D. N. C., & Nagasawa, M. 2013, ApJ, 775, 42

Iglesias, D., Bayo, A., Olofsson, J., et al. 2018, MNRAS, 480, 488

Jakobsen, P., Ferruit, P., Alves de Oliveira, C., et al. 2022, A&A, 661, A80

Janson, M., Lafrenière, D., Jayawardhana, R., et al. 2013, ApJ, 773, 170

Janson, M., Squicciarini, V., Delorme, P., et al. 2021, A&A, 646, A164

Jeong, G., Lee, B. C., Park, M. G., Bang, T. Y., & Han, I. 2022, A&A, 662, A12

Johansen, A. & Lambrechts, M. 2017, Annual Review of Earth and Planetary Sciences, 45, 359

Jorquera, S., Pérez, L. M., Chauvin, G., et al. 2021, AJ, 161, 146

Jovanovic, N., Martinache, F., Guyon, O., et al. 2015, PASP, 127, 890

Kaeufl, H.-U., Ballester, P., Biereichel, P., et al. 2004, in Society of Photo-Optical Instrumentation Engineers (SPIE) Conference Series, Vol. 5492, Ground-based Instrumentation for Astronomy, ed. A. F. M. Moorwood & M. Iye, 1218–1227

Kammerer, J., Cooper, R. A., Vandal, T., et al. 2022, arXiv e-prints, arXiv:2210.17528

Kenworthy, M. A., Hinz, P. M., Codona, J. L., et al. 2007, in In the Spirit of Bernard Lyot: The Direct Detection of Planets and Circumstellar Disks in the 21st Century, ed. P. Kalas, 23

Kenworthy, M. A., Snik, F., Keller, C. U., et al. 2018, in Society of Photo-Optical Instrumentation Engineers (SPIE) Conference Series, Vol. 10702, Ground-based and Airborne Instrumentation for Astronomy VII, ed. C. J. Evans, L. Simard, & H. Takami, 1070246

Kenyon, S. J. & Bromley, B. C. 2008, ApJS, 179, 451

Keppler, M., Benisty, M., Müller, A., et al. 2018, A&A, 617, A44

Kervella, P., Arenou, F., Mignard, F., & Thévenin, F. 2019, A&A, 623, A72

Kervella, P., Arenou, F., & Thévenin, F. 2022, A&A, 657, A7

Kiefer, F., Lecavelier des Etangs, A., Boissier, J., et al. 2014, Nature, 514, 462

Kiefer, S., Bohn, A. J., Quanz, S. P., Kenworthy, M., & Stolker, T. 2021, A&A, 652, A33

Kirkpatrick, J. D. 2005, ARA&A, 43, 195

Kokubo, E. & Ida, S. 2002, ApJ, 581, 666

Kouwenhoven, M. B. N., Brown, A. G. A., Zinnecker, H., Kaper, L., & Portegies Zwart, S. F. 2005, A&A, 430, 137

Kral, Q., Krivov, A. V., Defrère, D., et al. 2017, The Astronomical Review, 13, 69

Kraus, S., Hofmann, K. H., Malbet, F., et al. 2009, A&A, 508, 787

Krist, J. E., Golimowski, D. A., Schroeder, D. J., & Henry, T. J. 1998, PASP, 110, 1046

Krivov, A. V. & Booth, M. 2018, MNRAS, 479, 3300

Kuchner, M. J. & Traub, W. A. 2002, ApJ, 570, 900

Kuzuhara, M., Tamura, M., Kudo, T., et al. 2013, ApJ, 774, 11

Labiano, A., Argyriou, I., Álvarez-Márquez, J., et al. 2021, A&A, 656, A57

Lada, C. J. 1987, in Star Forming Regions, ed. M. Peimbert & J. Jugaku, Vol. 115, 1

Lafrenière, D., Doyon, R., Marois, C., et al. 2007a, ApJ, 670, 1367

Lafrenière, D., Marois, C., Doyon, R., & Barman, T. 2009a, ApJ, 694, L148

Lafrenière, D., Marois, C., Doyon, R., & Barman, T. 2009b, ApJ, 694, L148

Lafrenière, D., Marois, C., Doyon, R., Nadeau, D., & Artigau, É. 2007b, ApJ, 660, 770

Lagrange, A. M., Boccaletti, A., Langlois, M., et al. 2019a, A&A, 621, L8

Lagrange, A. M., Boccaletti, A., Langlois, M., et al. 2019b, A&A, 621, L8

Lagrange, A. M., Bonnefoy, M., Chauvin, G., et al. 2010, Science, 329, 57

Lagrange, A. M., Gratadour, D., Chauvin, G., et al. 2009a, A&A, 493, L21

Lagrange, A. M., Gratadour, D., Chauvin, G., et al. 2009b, A&A, 493, L21

Lagrange, A. M., Meunier, N., Desort, M., & Malbet, F. 2011, A&A, 528, L9

Lagrange, A. M., Meunier, N., Rubini, P., et al. 2019c, Nature Astronomy, 3, 1135

Lagrange, A. M., Rubini, P., Nowak, M., et al. 2020, A&A, 642, A18

Lambrechts, M. & Johansen, A. 2014, A&A, 572, A107

Lambrechts, M., Morbidelli, A., Jacobson, S. A., et al. 2019, A&A, 627, A83

Langlois, M., Gratton, R., Lagrange, A. M., et al. 2021a, A&A, 651, A71

Langlois, M., Gratton, R., Lagrange, A. M., et al. 2021b, arXiv e-prints, arXiv:2103.03976

Lannier, J., Delorme, P., Lagrange, A. M., et al. 2016, A&A, 596, A83

Launhardt, R., Henning, T., Quirrenbach, A., et al. 2020a, A&A, 635, A162

Launhardt, R., Henning, T., Quirrenbach, A., et al. 2020b, A&A, 635, A162

Launhardt, R., Queloz, D., Henning, T., et al. 2008, in Society of Photo-Optical Instrumentation Engineers (SPIE) Conference Series, Vol. 7013, Optical and Infrared Interferometry, ed. M. Schöller, W. C. Danchi, & F. Delplancke, 70132I

Lawson, K., Currie, T., Wisniewski, J. P., et al. 2021, AJ, 162, 293

Lazorenko, P. F., Mayor, M., Dominik, M., et al. 2009, A&A, 505, 903

Lazzoni, C., Desidera, S., Marzari, F., et al. 2018, A&A, 611, A43

Lebreton, J., van Lieshout, R., Augereau, J. C., et al. 2013, A&A, 555, A146

Lecavelier des Etangs, A. & Lissauer, J. J. 2022, New A Rev., 94, 101641

Lenzen, R., Hartung, M., Brandner, W., et al. 2003, in Society of Photo-Optical Instrumentation Engineers (SPIE) Conference Series, Vol. 4841, Instrument Design and Performance for Optical/Infrared Ground-based Telescopes, ed. M. Iye & A. F. M. Moorwood, 944–952

Lisse, C. M., Sitko, M. L., & Marengo, M. 2015, ApJ, 815, L27

Lisse, C. M., Sitko, M. L., Marengo, M., et al. 2017, AJ, 154, 182

Liu, B. & Ji, J. 2020, Research in Astronomy and Astrophysics, 20, 164

Lovis, C. & Fischer, D. 2010, in Exoplanets, ed. S. Seager, 27–53

Lowrance, P. J., Becklin, E. E., Schneider, G., et al. 2005, AJ, 130, 1845

Lubin, J., Van Zandt, J., Holcomb, R., et al. 2022, AJ, 163, 101

Ma, H., Qiao, Y., & Shen, C. 2017, in Society of Photo-Optical Instrumentation Engineers (SPIE) Conference Series, Vol. 10463, AOPC 2017: Space Optics and Earth Imaging and Space Navigation, 1046316

Macintosh, B., Graham, J. R., Barman, T., et al. 2015, Science, 350, 64

Macintosh, B., Graham, J. R., Ingraham, P., et al. 2014, Proceedings of the National Academy of Science, 111, 12661

Maire, A.-L., Huby, E., Absil, O., et al. 2020, Journal of Astronomical Telescopes, Instruments, and Systems, 6, 035003

Maire, A.-L., Langlois, M., Delorme, P., et al. 2021, Journal of Astronomical Telescopes, Instruments, and Systems, 7, 035004

Males, J. R., Close, L. M., Miller, K., et al. 2018, in Society of Photo-Optical Instrumentation Engineers (SPIE) Conference Series, Vol. 10703, Adaptive Optics Systems VI, 1070309

Manjavacas, E., Karalidi, T., Vos, J. M., Biller, B. A., & Lew, B. W. P. 2021, AJ, 162, 179

Marleau, G.-D., Coleman, G. A. L., Leleu, A., & Mordasini, C. 2019, A&A, 624, A20

Marley, M. S., Fortney, J. J., Hubickyj, O., Bodenheimer, P., & Lissauer, J. J. 2007, ApJ, 655, 541

Marois, C., Correia, C., Véran, J.-P., & Currie, T. 2014, in IAU Symposium, Vol. 299, Exploring the Formation and Evolution of Planetary Systems, ed. M. Booth, B. C. Matthews, & J. R. Graham, 48–49

Marois, C., Doyon, R., Racine, R., & Nadeau, D. 2000, PASP, 112, 91

Marois, C., Lafrenière, D., Doyon, R., Macintosh, B., & Nadeau, D. 2006, ApJ, 641, 556

Marois, C., Lafrenière, D., Macintosh, B., & Doyon, R. 2008a, ApJ, 673, 647

Marois, C., Macintosh, B., Barman, T., et al. 2008b, Science, 322, 1348

Marois, C., Macintosh, B., & Véran, J.-P. 2010, in Society of Photo-Optical Instrumentation Engineers (SPIE) Conference Series, Vol. 7736, Adaptive Optics Systems II, ed. B. L. Ellerbroek, M. Hart, N. Hubin, & P. L. Wizinowich, 77361J

Martin, D. V., El-Badry, K., Hodžić, V. K., et al. 2021, MNRAS, 507, 4132

Masciadri, E., Mundt, R., Henning, T., Alvarez, C., & Barrado y Navascués, D. 2005, ApJ, 625, 1004

Mason, B. D., Wycoff, G. L., Hartkopf, W. I., Douglass, G. G., & Worley, C. E. 2001, AJ, 122, 3466

Matthews, E., Hinkley, S., Vigan, A., et al. 2018, MNRAS, 480, 2757

Mawet, D., Absil, O., Delacroix, C., et al. 2013, A&A, 552, L13

Mawet, D., Milli, J., Wahhaj, Z., et al. 2014, ApJ, 792, 97

Mawet, D., Serabyn, E., Liewer, K., et al. 2010, ApJ, 709, 53

Mayer, L., Quinn, T., Wadsley, J., & Stadel, J. 2002, Science, 298, 1756

Mayor, M., Pepe, F., Queloz, D., et al. 2003, The Messenger, 114, 20

Mayor, M. & Queloz, D. 1995a, Nature, 378, 355

Mayor, M. & Queloz, D. 1995b, Nature, 378, 355

Merín, B., Montesinos, B., Eiroa, C., et al. 2004, A&A, 419, 301

Mesa, D., Bonnefoy, M., Gratton, R., et al. 2019, A&A, 624, A4

Mesa, D., Gratton, R., Zurlo, A., et al. 2015, A&A, 576, A121

Meshkat, T., Mawet, D., Bryan, M. L., et al. 2017, AJ, 154, 245

Meyer, M. R. & Wilking, B. A. 2009, PASP, 121, 350

Miles, B. E., Biller, B. A., Patapis, P., et al. 2022, arXiv e-prints, arXiv:2209.00620

Milli, J., Mouillet, D., Lagrange, A. M., et al. 2012, A&A, 545, A111

Minniti, D., Lucas, P. W., Emerson, J. P., et al. 2010, New A, 15, 433

Mizuno, H. 1980, Progress of Theoretical Physics, 64, 544

Morbidelli, A., Brasser, R., Tsiganis, K., Gomes, R., & Levison, H. F. 2009, A&A, 507, 1041

Mordasini, C., Alibert, Y., Georgy, C., et al. 2012, A&A, 547, A112

Morrison, S. & Malhotra, R. 2015, ApJ, 799, 41

Mouillet, D., Larwood, J. D., Papaloizou, J. C. B., & Lagrange, A. M. 1997a, MNRAS, 292, 896

Mouillet, D., Larwood, J. D., Papaloizou, J. C. B., & Lagrange, A. M. 1997b, MNRAS, 292, 896

Mugnier, L. M., Cornia, A., Sauvage, J.-F., et al. 2009, Journal of the Optical Society of America A, 26, 1326

Mulders, G. D., Mordasini, C., Pascucci, I., et al. 2019, ApJ, 887, 157

Murphy, S. J., Lawson, W. A., & Bessell, M. S. 2013, MNRAS, 435, 1325

Mustill, A. J. & Wyatt, M. C. 2009, MNRAS, 399, 1403

Mustill, A. J. & Wyatt, M. C. 2012, MNRAS, 419, 3074

Muterspaugh, M. W., Lane, B. F., Kulkarni, S. R., et al. 2010, AJ, 140, 1657

Ndugu, N., Bitsch, B., & Jurua, E. 2018, MNRAS, 474, 886

Nielsen, E. L. & Close, L. M. 2010, ApJ, 717, 878

Nielsen, E. L., De Rosa, R. J., Macintosh, B., et al. 2019a, AJ, 158, 13

Nielsen, E. L., De Rosa, R. J., Macintosh, B., et al. 2019b, AJ, 158, 13

Nielsen, E. L., De Rosa, R. J., Wang, J. J., et al. 2020, AJ, 159, 71

Nielsen, E. L., Liu, M. C., Wahhaj, Z., et al. 2013, ApJ, 776, 4

Noll, R. J. 1976, J. Opt. Soc. Am., 66, 207

Norfolk, B. J., Pinte, C., Calcino, J., et al. 2022, ApJ, 936, L4

Ogihara, M., Morbidelli, A., & Guillot, T. 2015, A&A, 578, A36

Olofsson, J., Juhász, A., Henning, T., et al. 2012, A&A, 542, A90

Olofsson, J., Samland, M., Avenhaus, H., et al. 2016, A&A, 591, A108

Ormel, C. W., Dullemond, C. P., & Spaans, M. 2010, ApJ, 714, L103

Ormel, C. W. & Klahr, H. H. 2010, A&A, 520, A43

Otten, G. P. P. L., Snik, F., Kenworthy, M. A., et al. 2017, ApJ, 834, 175

Pearce, T. D., Launhardt, R., Ostermann, R., et al. 2022, A&A, 659, A135

Pepe, F., Cristiani, S., Rebolo, R., et al. 2021, A&A, 645, A96

Petrus, S., Chauvin, G., Bonnefoy, M., et al. 2022, arXiv e-prints, arXiv:2207.06622

Pezzotti, C., Ottoni, G., Buldgen, G., et al. 2022, A&A, 657, A89

Phillips, M. W., Tremblin, P., Baraffe, I., et al. 2020, A&A, 637, A38

Pilbratt, G. L., Riedinger, J. R., Passvogel, T., et al. 2010, A&A, 518, L1

Poglitsch, A., Waelkens, C., Geis, N., et al. 2010, A&A, 518, L2

Pollack, J. B., Hubickyj, O., Bodenheimer, P., et al. 1996, Icarus, 124, 62

Pravdo, S. H., Shaklan, S. B., & Lloyd, J. 2005, ApJ, 630, 528

Pueyo, L. 2016a, ApJ, 824, 117

Pueyo, L. 2016b, ApJ, 824, 117

R Core Team. 2019, R: A Language and Environment for Statistical Computing, R Foundation for Statistical Computing, Vienna, Austria

Rajwa, B., Dundar, M., Irvine, A., & Dang, T. 2013, IM: Orthogonal Moment Analysis, r package version 1.0

Rameau, J., Chauvin, G., Lagrange, A. M., et al. 2013, A&A, 553, A60

Rebollido, I., Eiroa, C., Montesinos, B., et al. 2018, A&A, 614, A3

Ren, B., Pueyo, L., Chen, C., et al. 2020, ApJ, 892, 74

Ren, B., Pueyo, L., Zhu, G. B., Debes, J., & Duchêne, G. 2018, ApJ, 852, 104

Ricker, G. R., Winn, J. N., Vanderspek, R., et al. 2014, in Society of Photo-Optical Instrumentation Engineers (SPIE) Conference Series, Vol. 9143, Space Telescopes and Instrumentation 2014: Optical, Infrared, and Millimeter Wave, ed. J. Oschmann, Jacobus M., M. Clampin, G. G. Fazio, & H. A. MacEwen, 914320

Rieke, G. H., Wright, G. S., Böker, T., et al. 2015, PASP, 127, 584

Rieke, G. H., Young, E. T., Engelbracht, C. W., et al. 2004, ApJS, 154, 25

Rieke, M. J., Kelly, D., & Horner, S. 2005, in Society of Photo-Optical Instrumentation Engineers (SPIE) Conference Series, Vol. 5904, Cryogenic Optical Systems and Instruments XI, ed. J. B. Heaney & L. G. Burriesci, 1–8

Rouan, D., Riaud, P., Boccaletti, A., Clénet, Y., & Labeyrie, A. 2000, PASP, 112, 1479

Rousset, G., Lacombe, F., Puget, P., et al. 2003, in Society of Photo-Optical Instrumentation Engineers (SPIE) Conference Series, Vol. 4839, Adaptive Optical System Technologies II, ed. P. L. Wizinowich & D. Bonaccini, 140–149

Ruane, G., Ngo, H., Mawet, D., et al. 2019a, AJ, 157, 118

Ruane, G., Ngo, H., Mawet, D., et al. 2019b, AJ, 157, 118

Sahlmann, J., Henning, T., Queloz, D., et al. 2013a, A&A, 551, A52

Sahlmann, J., Lazorenko, P. F., Ségransan, D., et al. 2013b, A&A, 556, A133

Sajadian, S. & Jørgensen, U. G. 2022, A&A, 657, A16

Samland, M., Bouwman, J., Hogg, D. W., et al. 2021, A&A, 646, A24

Samland, M., Mollière, P., Bonnefoy, M., et al. 2017, A&A, 603, A57

Santos, N. C., Israelian, G., & Mayor, M. 2004, A&A, 415, 1153

Sauvage, J.-F., Fusco, T., Petit, C., et al. 2016, Journal of Astronomical Telescopes, Instruments, and Systems, 2, 025003

Schlaufman, K. C. 2018, ApJ, 853, 37

Schwarz, G. 1978, Annals of Statistics, 6, 461

Serabyn, E., Huby, E., Matthews, K., et al. 2017, AJ, 153, 43

Shannon, A., Bonsor, A., Kral, Q., & Matthews, E. 2016, MNRAS, 462, L116

Shao, M. & Colavita, M. M. 1992, ARA&A, 30, 457

Shkolnik, E. L., Allers, K. N., Kraus, A. L., Liu, M. C., & Flagg, L. 2017, AJ, 154, 69

Shu, F. H., Adams, F. C., & Lizano, S. 1987, ARA&A, 25, 23

Sicilia-Aguilar, A., Henning, T., Kainulainen, J., & Roccatagliata, V. 2011, ApJ, 736, 137

Sissa, E., Gratton, R., Alcalà, J. M., et al. 2019, A&A, 630, A132

Sivaramakrishnan, A., Soummer, R., Sivaramakrishnan, A. V., et al. 2005, ApJ, 634, 1416

Sivaramakrishnan, A., Tuthill, P., Lloyd, J. P., et al. 2022, arXiv e-prints, arXiv:2210.17434

Skemer, A. J., Hinz, P., Esposito, S., et al. 2014a, in Society of Photo-Optical Instrumentation Engineers (SPIE) Conference Series, Vol. 9148, Adaptive Optics Systems IV, ed. E. Marchetti, L. M. Close, & J.-P. Vran, 91480L

Skemer, A. J., Hinz, P., Esposito, S., et al. 2014b, in Society of Photo-Optical Instrumentation Engineers (SPIE) Conference Series, Vol. 9148, Adaptive Optics Systems IV, ed. E. Marchetti, L. M. Close, & J.-P. Vran, 91480L

Skowron, J., Udalski, A., Gould, A., et al. 2011, ApJ, 738, 87

Skrutskie, M. F., Jones, T., Hinz, P., et al. 2010, in Society of Photo-Optical Instrumentation Engineers (SPIE) Conference Series, Vol. 7735, Ground-based and Airborne Instrumentation for Astronomy III, ed. I. S. McLean, S. K. Ramsay, & H. Takami, 77353H

Smith, B. A. & Terrile, R. J. 1984a, Science, 226, 1421

Smith, B. A. & Terrile, R. J. 1984b, Science, 226, 1421

Snellen, I. A. G., Brandl, B. R., de Kok, R. J., et al. 2014, Nature, 509, 63

Snellen, I. A. G. & Brown, A. G. A. 2018, Nature Astronomy, 2, 883

Soummer, R., Ferrari, A., Aime, C., & Jolissaint, L. 2007, ApJ, 669, 642

Soummer, R., Hagan, J. B., Pueyo, L., et al. 2011a, ApJ, 741, 55

Soummer, R., Hagan, J. B., Pueyo, L., et al. 2011b, ApJ, 741, 55

Soummer, R., Pueyo, L., & Larkin, J. 2012, ApJ, 755, L28

Spanò, P., Delabre, B., Dekker, H., et al. 2012, in Society of Photo-Optical Instrumentation Engineers (SPIE) Conference Series, Vol. 8446, Ground-based and Airborne Instrumentation for Astronomy IV, ed. I. S. McLean, S. K. Ramsay, & H. Takami, 84467V

Sparks, W. B. & Ford, H. C. 2002a, ApJ, 578, 543

Sparks, W. B. & Ford, H. C. 2002b, ApJ, 578, 543

Spiegel, D. S. & Burrows, A. 2012, ApJ, 745, 174

Spiegel, D. S., Burrows, A., & Milsom, J. A. 2011, ApJ, 727, 57

Stetson, P. B. 1987, PASP, 99, 191

Stevenson, D. J. 1985, Icarus, 62, 4

Stolker, T., Bonse, M. J., Quanz, S. P., et al. 2019, A&A, 621, A59

Stone, J. M., Skemer, A. J., Hinz, P. M., et al. 2018a, AJ, 156, 286

Stone, J. M., Skemer, A. J., Hinz, P. M., et al. 2018b, AJ, 156, 286

Su, K. Y. L., Rieke, G. H., Stapelfeldt, K. R., et al. 2009, ApJ, 705, 314

Sucerquia, M., Alvarado-Montes, J. A., Zuluaga, J. I., Montesinos, M., & Bayo, A. 2020a, MNRAS, 496, L85

Sucerquia, M., Ramírez, V., Alvarado-Montes, J. A., & Zuluaga, J. I. 2020b, MNRAS, 492, 3499

Tamura, M. 2016, Proceedings of the Japan Academy, Series B, 92, 45

Taylor, K. N. R. & Storey, J. W. V. 1984, MNRAS, 209, 5P

Teh, C.-H. & Chin, R. T. 1988, IEEE Trans. Pattern Anal. Mach. Intell., 10, 496

Terebey, S., Shu, F. H., & Cassen, P. 1984, ApJ, 286, 529

Tobin, W., Barnes, S. I., Persson, S., & Pollard, K. R. 2019, MNRAS, 489, 574

Trapman, L., Miotello, A., Kama, M., van Dishoeck, E. F., & Bruderer, S. 2017, A&A, 605, A69

Udalski, A. 2003, Acta Astron., 53, 291

Ujjwal, K., Kartha, S. S., Mathew, B., Manoj, P., & Narang, M. 2020, AJ, 159, 166

van der Marel, N. 2015, PhD thesis, University of Leiden, Netherlands

van der Plas, G., Ménard, F., Canovas, H., et al. 2017, A&A, 607, A55

van Leeuwen, F. 2007a, A&A, 474, 653

van Leeuwen, F. 2007b, A&A, 474, 653

Vargas Catalán, E., Huby, E., Forsberg, P., et al. 2016, A&A, 595, A127

Vazan, A., Helled, R., Podolak, M., & Kovetz, A. 2016, ApJ, 829, 118

Venturini, J., Alibert, Y., & Benz, W. 2016, A&A, 596, A90

Vigan, A. 2020, vlt-sphere: Automatic VLT/SPHERE data reduction and analysis

Vigan, A., Bonavita, M., Biller, B., et al. 2017, A&A, 603, A3

Vigan, A., Fontanive, C., Meyer, M., et al. 2021a, A&A, 651, A72

Vigan, A., Fontanive, C., Meyer, M., et al. 2020, arXiv e-prints, arXiv:2007.06573

Vigan, A., Fontanive, C., Meyer, M., et al. 2021b, A&A, 651, A72

Vigan, A., Moutou, C., Langlois, M., et al. 2010, MNRAS, 407, 71

Vigan, A., Patience, J., Marois, C., et al. 2012, A&A, 544, A9

Vorobyov, E. I. & Basu, S. 2010, ApJ, 719, 1896

Wahhaj, Z., Liu, M. C., Nielsen, E. L., et al. 2013, ApJ, 773, 179

Wahhaj, Z., Milli, J., Romero, C., et al. 2021, A&A, 648, A26

Wang, J. J., Graham, J. R., Dawson, R., et al. 2018, AJ, 156, 192

Wells, M., Pel, J. W., Glasse, A., et al. 2015, PASP, 127, 646

Werner, M. W., Roellig, T. L., Low, F. J., et al. 2004, ApJS, 154, 1

Willott, C. J., Doyon, R., Albert, L., et al. 2022, PASP, 134, 025002

Winn, J. N. 2010, arXiv e-prints, arXiv:1001.2010

Wright, G. S., Wright, D., Goodson, G. B., et al. 2015, PASP, 127, 595

Wright, J. T. & Howard, A. W. 2009, ApJS, 182, 205

Xie, C., Choquet, E., Vigan, A., et al. 2022, arXiv e-prints, arXiv:2208.07915

Xuan, W. J., Mawet, D., Ngo, H., et al. 2018a, AJ, 156, 156

Xuan, W. J., Mawet, D., Ngo, H., et al. 2018b, AJ, 156, 156

Yoo, J., DePoy, D. L., Gal-Yam, A., et al. 2004, ApJ, 603, 139

Zernike, F. 1934, Monthly Notices of the Royal Astronomical Society, 94, 377

Zurlo, A., Gozdziewski, K., Mesa, C. L. D., et al. 2022, arXiv e-prints, arXiv:2207.10684